Modelling and Detecting Faults of Permanent Magnet Synchronous Motors in Dynamic Operations

Sveinung Attestog

UiA University of Agder

Doctoral Dissertations at the University of Agder 384

Sveinung Attestog

Modelling and Detecting Faults of Permanent Magnet Synchronous Motors in Dynamic Operations

Doctoral Dissertation for the Degree *Philosophiae Doctor (PhD)* at
the Faculty of Engineering and Science, Specialisation in Mechatronics

University of Agder
Faculty of Engineering and Science
2022

Doctoral Dissertations at the University of Agder 384
ISSN: 1504-9272
ISBN: 978-82-8427-095-1

Printed by 07 Media Sør
Kristiansand

Preface

This dissertation is based on research activities carried out at the University of Agder, Campus Grimstad, during the period October 2018 to February 2022. This PhD project is funded by the Ministry of Education in Norway. During the project I have learned from theoretical studies with different mathematical models and development of different fault-detection and identification scheme and put the theory into practice with my experimental work in the lab.

I will express my gratitude to everyone who has supported me along the way. First and foremost I would thank my supervisors Prof. Kjell G. Robbersmyr and Prof. Huynh Van Khang. Their guidance helped and guided me through over three years of research and writing of this dissertation. My sincere thanks to my main supervisor Prof. Kjell G. Robbersmyr for providing research directions, facilities and sometimes a joke to lighten the mood. Especially when the DC supply blew up and made a loud bang. I'm extremely grateful to my co-supervisor Prof. Huynh Van Khang for his supervision and teaching, not only during my PhD but also during my bachelor- and master-studies in Renewable Energy. A special thanks to Dr. Jagath Sri Lal Senanayaka who became my second co-supervisor this last year when the time was running out, and two more papers had to be published.

I am thankful to the Head of the Department Prof. Geir Grasmo and PhD-coordinator Emma E. Horneman for providing me with the necessary facilities and pleasant working environment for research activities. Special thanks to my colleagues at UiA for their warm welcome into the PhD-community at UiA and made every lunch-break something looking forward to. I hope that I did the same for those who started on their PhD-studies after me.

Last, but not least, I want to thank my family. Their support allowed me to focus fully on my research. Especially at the end, when my option for time off work to help on the farm became limited.

Sveinung Attestog
Grimstad, Norway
June 21. 2022

Forord

Denne avhandlinga er basert på forskingsarbeid utført på Universitet i Agder (Kampus Grimstad) i perioden frå oktober 2018 til februar 2022. Dette PhD arbeidet er sponsa av Kunnskapsdepartementet. I dette prosjektet har eg utført teoretiske studiar av ulike matematiske modeller og vore med på utvikle nye feilsøkingsmetodar og sett teori ut i praksis med laboratoriearbeid.

Eg vil hermed uttrykke mi takksemd til alle som har hjelpte undervegs i studiet. Først og fremst, vil eg takke rettleiarane mine Prof. Kjell G. Robbersmyr og Prof. Huynh Van Khang, for rettleiing under forskingsarbeid og artikkelskriving. Stor takk til hovudrettleiaren min Prof. Robbersmyr for gode råd, greie fasilitetar og av og til ein vits når det trongst å lette på stemninga. Spesielt den gongen likestraumstilførselen smalt svert høgt. Eg er særs takknemleg for all undervisning og hjelp frå medrettleiar Prof. Khang, ikkje berre i samband med doktorgraden, men også under bachelor- og mastergrads studiet i Fornybarenergi. Ei spesiell takk til kollegaen min Dr. Jagath Sri Lal Senanayaka, som blei min andre medrettleiar på slutten av arbeidet då tida begynte å bli knapp og hadde bruk for ekstra hjelp med dei siste publiseringane.

Eg vil også gjerne takke avdelingsleiar Prof. Geir Grasmo og PhD-koordinator Emma E. Horneman som har skaffa nødvendige fasilitetar og skapt eit triveleg forskingsmiljø. Ei stor takk til alle mine stipendiat- kollegaer for varm velkomst i doktorgradsmiljøet på UiA. Dei har absolutt vore med på å gjere samtalen under lunsjen til ei høgdepunkt i kvardagen. Eg håper at eg også klarte å gjere det same for kollegaene mine som starta etter meg.

Til slutt vil eg takke familien min, som gav meg ekstra stor støtte heime, slik at eg kunne fokusere fullt og heilt på forskinga. Spesielt mot slutten då eg ikkje hadde anledning til å hjelpe til så mykje på garden som eg eigentleg ønskja.

Sveinung Attestog
Grimstad, Noreg
21. juni 2022

Abstract

Permanent magnet synchronous motors (PMSMs) have played a key role in commercial and industrial applications, i.e. electric vehicles and wind turbines. They are popular due to their high efficiency, control simplification and large torque-to-size ratio although they are expensive. A fault will eventually occur in an operating PMSM, either by improper maintenance or wear from thermal and mechanical stresses. The most frequent PMSM faults are bearing faults, short-circuit and eccentricity. PMSM may also suffer from demagnetisation, which is unique in permanent magnet machines. Condition monitoring or fault diagnosis schemes are necessary for detecting and identifying these faults early in their incipient state, e.g. partial demagnetisation and inter-turn short circuit. Successful fault classification will ensure safe operations, speed up the maintenance process and decrease unexpected downtime and cost. The research in recent years is drawn towards fault analysis under dynamic operating conditions, i.e. variable load and speed. Most of these techniques have focused on the use of voltage, current and torque, while magnetic flux density in the air-gap or the proximity of the motor has not yet been fully capitalised.

This dissertation focuses on two main research topics in modelling and diagnosis of faulty PMSM in dynamic operations. The first problem is to decrease the computational burden of modelling and analysis techniques. The first contributions are new and faster methods for computing the permeance network model and quadratic time-frequency distributions. Reducing their computational burden makes them more attractive in analysis or fault diagnosis. The second contribution is to expand the model description of a simpler model. This can be achieved through a field reconstruction model with a magnet library and a description of both magnet defects and inter-turn short circuits.

The second research topic is to simplify the installation and complexity of fault diagnosis schemes in PMSM. The aim is to reduce required sensors of fault diagnosis schemes, regardless of operation profiles. Conventional methods often rely on either steady-state or predefined operation profiles, e.g. start-up. A fault diagnosis scheme robust to any speed changes is desirable since a fault can be detected regardless of operations. The final contribution is the implementation of reinforcement learning in an active learning scheme to address the imbalance dataset problem. Samples from a faulty PMSM are often initially unavailable and expensive to acquire. Reinforcement learning with a weighted reward function might balance the dataset to enhance the trained fault classifier's performance.

Abstrakt

Permanentmagnet-synkronmotorar (PMSM) har spela ei nøkkelrolle i kommersielle og industrielle applikasjonar, for eksempel når det gjeld elektriske køyretøy og vindturbinar. Dei er populære på grunn av sin høge effektivitet, framgang i reguleringteknikk og stort dreiemoment i forhold til storleiken, men dei er dyre. Ein feil vil eventuelt oppstå i ein PMSM, anten ved misleghald eller slitasje frå termiske og/eller mekaniske påkjenningar. Dei vanlegaste feilane i ein PMSM er lagerfeil, kortslutning og eksentrisitet. I ein PMSM kan det også skje demagnetisering, noko som er unikt for permanentmagnetmaskinar. Tilstandsovervaking eller feildiagnostisering er nødvendig for å oppdage og identifisere desse feila tidleg. Dette gjeld blant anna partiell demagnetisering og kortslutning. Vellykka klassifisering av feil vil sikre forsvarleg drift, framskunde vedlikehaldsarbeidet og redusere uventa nedetid og kostnader. Forskinga dei siste åra er retta mot feilanalyse under dynamiske driftsforhold, det vil seie variabel last og fart. Dei fleste av desse teknikkane har fokusert på målingar av spenning, straum og dreiemoment. Bruken av magnetisk flukstettleik i luftgapet eller i nærleiken av motoren for feilsøking er ennå ikkje fullt utforska.

Denne avhandlinga fokuserer på to forskingstema, modellering og diagnostisering av feil i PMSM med variabel fart og last. Det første problemet var å redusere ressursmengda som trengst for å modellere og analysere PMSM med feil. Dei første bidraga er nye og raskare metodar for å nytte seg av ein permeans-nettverksmodell og Cohens klassefunksjon. Denne ressursreduksjonen for å rekne med desse teknikkane vil føre til at dei blir meir attraktive når det gjeld analyse og feildiagnosering. Det andre bidraget er å utvikle ein feltrekonstruksjons-modell med eit magnetbibliotek som kan beskrive både magnetiske defektar og kortslutningar i ein PMSM.

Det andre temaet som er forska på, er å forenkle installasjonen av feildiagnostikkmetodar i PMSM. Målet er å redusere talet på sensorar, som er nødvendige for feildiagnostisering, uavhengig av drift. Konvensjonelle metodar er ofte avhengige av anten konstant fart eller forhandsdefinerte fartsprofilar for eksempel ved oppstart. Ein feildiagnoseteknikk som er motstandsdyktig mot fartsendringar er ønskjeleg sidan ein feil då kan oppdagast uavhengig av drift. Det siste bidraget er implementeringa av «Reinforcement Learning» i ein aktiv maskinlæringsmetodikk for å løyse problemet med ubalanserte datasett. Målingar frå ein defekt PMSM er ofte utilgjengeleg før installasjon, i tillegg er dei ressurskrevjande å skaffe. «Reinforcement Learning» med ein vekta belønningsfunksjon kan balansere datasettet og auke kor nøyaktig feilklassifiseraren kan bli etter treningsprosessen.

Publications

The following listed papers are based on research activities conducted by the author and have been published or submitted for publication in peer-reviewed journals and conference proceedings.

Paper A S. Attestog, H. V. Khang and K. G. Robbersmyr, "Detecting Eccentricity and Demagnetization Fault of Permanent Magnet Synchronous Generators in Transient State," 2019 22nd International Conference on Electrical Machines and Systems (ICEMS), Harbin, China, 2019, pp. 1-5, doi: 10.1109/ICEMS.2019.8921753.

Paper B S. Attestog, H. Van Khang and K. G. Robbersmyr, "Modelling Demagnetized Permanent Magnet Synchronous Generators using Permeance Network Model with Variable Flux Sources," 2019 22nd International Conference on the Computation of Electromagnetic Fields (COMPUMAG), Paris, France, 2019, pp. 1-4, doi: 10.1109/COMPUMAG 45669.2019.9032791.

Paper C S. Attestog, H. Van Khang and K. G. Robbersmyr, "Field Reconstruction for Modeling Multiple Faults in Permanent Magnet Synchronous Motors in Transient States," in IEEE Access, vol. 9, pp. 127131-127140, 2021, doi: 10.1109/ACCESS.2021.3112224.

Paper D S. Attestog, H. V. Khang and K. G. Robbersmyr, "Improved Quadratic Time-frequency Distributions for Detecting Inter-turn Short Circuits of PMSMs in Transient States," 2020 International Conference on Electrical Machines (ICEM), Gothenburg, Sweden, 2020, pp. 1461-1467, doi: 10.1109/ICEM49940.2020.9271050.

Paper E S. Attestog, J. S. L. Senanayaka, H. Van Khang, and K. G. Robbersmyr, "Mixed Fault Classification of Sensorless PMSM Drive in Dynamic Operations Based on External Stray Flux Sensors," Sensors, vol. 22, no. 3, p. 1216, Feb. 2022, doi: 10.3390/s22031216.

Paper F S. Attestog, J. S. L. Senanayaka, H. Van Khang, and K. G. Robbersmyr, "Robust Active Learning Multiple Fault Diagnosis of Sensorless PMSM Drives in Dynamic Operations Under Imbalanced Datasets", IEEE Transactions on Industrial Informatics (under revision).

Contents

List of Figures

List of Tables

Abbreviation

AL	Active learning
BLUE	Best linear unbiased estimator
BEMF	Back electromagnetic motive force
CWD	Choi-Williams distribution
CNN	Convolutional neural network
DF	Demagnetisation fault
DQN	Deep Q-network
EEC	Electric equivalent-circuit
EDT	Ensemble decision tree
EPVA	Extended Park's vector approach
DE	Dynamic eccentricity
FEA	Finite element analysis
FDI	Fault detection and identification
FFT	Fast Fourier transform
FN	False negative
FNN	Feedforward neural network
FP	False positive
FRM	Field reconstruction model
IPMSM	Interior permanent magnet synchronous motor
IGBT	Insulated-gate bipolar transistor
ITSC	Inter-turn short circuit
KNN	k-nearest neighbours
LOF	Local outlier factor
MCSA	Machine current signal analysis
MEC	Magnetic equivalent circuit
MMF	Magnetic motive force
MF	Mixed fault
ML	Machine learning
MST	Maxwell's stress tensor
NF	No-fault
OCC	One-class classifier
OL	Overlap
PM	Permanent magnet
PMSG	Permanent magnet synchronous generator
PMSM	Permanent magnet synchronous motor
PNM	Permeance network model
PWM	Pulse width modulation
ReLU	Rectified linear unit
RL	Reinforcement learning

SE	Static eccentricity
STFT	Short-time Fourier transform
SMOTE	Synthetic minority oversampling technique
SMPMSM	Surface mounted permanent magnet synchronous motor
SVM	Support vector machine
TFD	Time-frequency distribution
TNR	True negative rate
TPR	True positive rate
WVD	Wigner-Ville distribution
WSST	Wavelet synchrosqueezed transform
ZAM	Zao-Atlas-Marks distribution

Nomenclature

Several letters have been reused in the different publications of this dissertation. They are therefore listed multiple times with their respective descriptions and in line with the published papers.

$\boldsymbol{A}$	Magnetic vector potential
A	Fitting parameter for approximated F_{Class} (Paper A)
A	Action space (Paper F)
$A(l)$	Cross-sectional area as a function of length l (Paper B)
$A(\theta, \tau)$	Ambiguity function (Paper D)
a	Fitting parameter in F_{Class}
a_t	Action at step t
$\boldsymbol{B}$	Magnetic flux density field
$\boldsymbol{B_r}$	Remnant magnetic flux field
B	Fitting parameter for approximated F_{Class} (Paper A)
B	Friction coefficient (Paper C)
B_N	Normal component of magnetic flux density
$B_{nA:SC}$	Normal component of magnetic flux density induced by the unshorted turns in phase A
B_{nB}	Normal component of magnetic flux density induced by phase B
B_{nC}	Normal component of magnetic flux density induced by phase C
$B_{nK}(\theta)$	Normal component of magnetic flux density induced by phase k (a, b or c)
B_{nLoop}	Normal component of magnetic flux density induced by stator winding coil
B_{nPM}	Normal component of magnetic flux density induced by PM
B_{nS}	Normal component of magnetic flux density induced by stator winding
$B_{n1PM,k}$	Normal component of magnetic flux density induced by the kth magnet
B_T	Tangential component of magnetic flux density
$B_{tA:SC}$	Tangential component of magnetic flux density induced by the unshorted turns in phase A
B_{tB}	Tangential component of magnetic flux density induced by phase B

B_{tC}	Tangential component of magnetic flux density induced by phase C
$B_{tK}(\theta)$	Tangential component of magnetic flux density induced by phase k (a, b or c)
B_{tLoop}	Tangential component of magnetic flux density induced by stator winding coil
B_{tPM}	Tangential component of magnetic flux density induced by PM
B_{tS}	Tangential component of magnetic flux density induced by stator winding
$B_{t1PM,k}$	Tangential component of magnetic flux density induced by the kth magnet
b	Fitting parameter in F_{Class} (Paper A)
b	Bias in FNN fully connected layer (Paper E)
$C(t,\omega)$	Cohen class distribution function
C_m	Geometric factor for computing induced voltage
c	Constant
$d(n)$	Window function in discrete form
$d(P,o_n)$	Pair wise Euclidean distance between points P and o_n
$d_{\mathbf{ball}}$	Diameter of bearing ball
$d_{\mathbf{cage}}$	Diameter of bearing cage
$d_{\mathbf{mag}}$	Magnet thickness
$d_{\mathbf{tooth}}$	Thickness of stator tooth top
$\boldsymbol{E}$	Electric field intensity
e_a, e_b, e_c	Induced voltage in phase a, b and c
e_f	Induced voltage from faulty windings
e_n	Induced voltage phase n
$\boldsymbol{F_m}$	Magnetic scalar potential in PNM
$\mathcal{F}$	Fourier transform
$\mathcal{F}^{-1}$	Inverse Fourier transform
$F_{\mathbf{Class}}$	Fitting function for a first classifier
$F_{\mathbf{Det}}$	Fault detection indicator
$F(\omega)$	Function in frequency domain
$f(t)$	Time varying frequency (Paper A)
$f(t)$	Function in time domain (Paper D)
$f(\cdot)$	Activation function (Paper E)
f_s	Electrical synchronous frequency
$F(\omega)$	Function in frequency domain
f_1	Frequency of fundamental component
g_0	Average air-gap distance
$\boldsymbol{H}$	Magnetic flux intensity field
$H(x(t))$	Hilbert transform of $x(t)$
$h(t)$	The remainder function in F_{Class} (Paper A)
$h(t)$	Assumed shape of the fundamental component (Paper E)

I	Current measurement
$I(t)$	Function of three phase current
$I_k(t)$	Current of phase k (a, b or c)
I_a, I_b, I_c	Phase current of phases a, b and c
I_F	Current circulating in short circuit
I_P	Magnitude of Park's vector
$I_{\mathbf{ref}}$	Reference value for current
I_α, I_β	Stator current vector component in stationary reference frame
i	Integer
i_d, i_q	Direct and quadrature components of motor current
$\boldsymbol{J}$	Current density
$J_{\mathbf{rotor}}$	Inertia of rotor
j	Integer
k	Integer
$k_{\mathbf{BEMF}}$	BEMF constant
k_1	Fitting parameter in F_{Class}
k_2	Fitting parameter in F_{Class}
$\boldsymbol{L}$	Inductance matrix
L	Loss function
$L_{\mathbf{rotor}}$	Length or rotor
L_s	Self inductance
L_t	Label for sample at step t
$L_{\mathbf{tooth}}$	Length of stator tooth
$L_{\mathbf{yoke}}$	Thickness of stator yoke
l	Length
M	Number of samples in mini-batch
$\mathbf{MMF}_{\mathbf{Coil}}$	Magneto-motive force vector in PNM
M_s	Mutual inductance
m	Number of flux sources in PNM (Paper B)
m	Integer (Paper C)
$\boldsymbol{N_a}$,$\boldsymbol{N_b}$,$\boldsymbol{N_c}$	Vector description of number turns each slot in PNM
N	Number of elements in an array or sample (Papers B and D)
N	Number of turns per phase winding (Paper C)
N	Number of neurons in a FNN layer (Paper E)
$N_{\mathbf{Ball}}$	Number of balls in a bearing
$N_{\mathbf{epi}}$	Number of episode in training process
N_s	Number of stator slots
$N_{\mathbf{step}}$	Number of steps per episode
n_t, n_ω	Vectors with integers for computing Cohen's class function in discrete form
n_τ, n_θ	Vectors with integers for computing Cohen's class function in discrete form
$n_{\mathbf{rated}}$	Rated motor speed
n	Number of nodes in PNM (Paper B)
n	Integer (Papers C, D, E and F)
$n_{\mathbf{rated}}$	Rated motor speed

n_1, n_2	First and last sample per iteration of computing QTFD
o_n	n$^{\text{th}}$ neighbour to point P
$\boldsymbol{\mathcal{P}}$	Permeance matrix
P	New sample point
p	Number of pole pairs
Q	Critic function
Q_t	Target critic function
$\boldsymbol{R}$	Resistance matrix
$\mathcal{R}$	Reluctance
$\mathcal{R}_{\mathbf{AG}}$	Reluctance in air-gap
$\mathcal{R}_{\mathbf{Air\text{-}gap}}$	Reluctance in air-gap
$\mathcal{R}_{\mathbf{R}}$	Reluctance in rotor
$\mathcal{R}_{\mathbf{Rotor}}$	Reluctance in rotor
$\mathcal{R}_{\mathbf{S}}$	Reluctance in stator yoke
$\mathcal{R}_{\mathbf{Stator}}$	Reluctance in stator yoke
$\mathcal{R}_{\mathbf{ST}}$	Reluctance in a stator tooth
$\mathcal{R}_{\mathbf{Tooth}}$	Reluctance in a stator tooth
$\mathcal{R}_{\mathbf{M}}$	Reluctance in Magnet
$\mathcal{R}_{\mathbf{Magnet}}$	Reluctance in Magnet
R	Radial distance from rotor centre to middle of air-gap
$R(t,\tau)$	Auto correlation function in continuous form (Paper D)
$R(n_\tau, n_t)$	Auto correlation in discrete form (Paper D)
R_F	Short circuit resistance
$R_{\mathbf{mea}}$	Measured resistance
R_S	Per phase resistance (Paper C)
R_S	Strand resistance (Paper E)
R_1, R_2	Resistor after strand resistance is slit
r	Polar coordinate of FRM basis functions
r_r	Rotor radius
r_s	Stator inner radius
$r_{\mathbf{shaft}}$	Radius of rotor shaft
r_t	Reward to DQN agent at step t
$s(t)$	Analytic signal
s_t	Action perform by DQN agent at step t
s_1	First sample
T	Time window
t	Time
V_{C1}, V_{C2}	Induced voltage in search coil 1 and 2
v_a, v_b, v_c	Phase voltages
w_n	Weight matrix in FNN fully connected layer
w_1, w_2	Width measurements of stator tooth
$x(t)$	Input sample in continues form
$x(n)$	Input sample in discrete form
x_n	The nth feature input
y	Output of node in a FNN fully connected layer
y_t	Value function at step t
β	Contact angle between bearing ball
γ	Discount factor

δ	Threshold for fault detection
Θ	Critic network parameters
Θ_t	Target network parameters
θ	Angular position of motor (Paper A)
θ	Polar coordinate of FRM basis functions (Paper C)
θ	Kernal frequency domain (Paper D)
θ	Phase shift of fundamental component (Paper E)
$\theta_{\mathbf{ref}}$	Reference potion of rotor
$\theta_{\mathbf{mag}}$	Magnet pitch
θ_e	Electrical position of PMSM
θ_m	Mechanical position of PMSM
$\theta_{\mathbf{slot}}$	Stator slot pitch
λ	Imbalance ratio
λ_n	Flux linkage for phase n
$\mu(l)$	Permeability as a function of length l (Paper B)
μ	Short circuit severity (Paper C)
μ_f	Short circuit severity
μ_r	Relative permeability
$\mu_{\mathbf{rec}}$	Recoil permeability
μ_0	Permeability in vacuum
$\sigma_{\mathbf{Fe}}$	Diagonal matrix description of resistivity of iron core
σ	Adjusting parameter in kernel function of CWD and ZAM
$\sigma_{\mathbf{Cu20}}$	Resistivity of copper at 20 $^\circ C$
$\sigma_{\mathbf{samp}}$	Sample density
τ	Induced torque (Paper C)
τ	Running time (Paper D)
τ	Torque measurement (Paper E)
τ	Smoothing factor for updating target network (Paper F)
$\tau_{\mathbf{Ark}}$	Torque computed with Arkkio's method
$\tau_{\mathbf{load}}$	Load torque
$\Phi_{\mathbf{Coil}}$	Flux source representing influence by phase windings in PNM
$\mathbf{\Phi_s}$	Flux source vector in PNM
$\Phi_{\mathbf{Mag}}$	Flux source representing magnets in PNM
ϕ	Phase shift in F_{Class} (Paper A)
ϕ_i	Magnetic flux in stator tooth i (Paper C)
$\phi(\theta, \tau)$	Kernel function (Paper D)
ϕ	Stray Flux measurement (Paper E)
$\phi_{\mathbf{CWD}}$	Kernel function for Choi-Williams distribution
$\phi_{\mathbf{WVD}}$	Kernel function for Wignler-Ville distribution
$\phi_{\mathbf{ZAM}}$	Kernel function for Zhao-Atlas-Marks distribution
ω	Frequency domain (Paper D)
$\omega(t)$	Time varying angular velocity (Paper A)
ω_m	Motor angular speed
$\dot{\omega}_m$	Time derivative of ω_m

Chapter 1

Introduction

1.1 Background

The main principle of electrical motors and generators is the interaction between the magnetic fields in the rotor and stator to align or follow the path of least reluctance. The magnetic field of the rotor in a loaded permanent magnet synchronous motor (PMSM) will have an offset called the load angle relative to the fields of the stator [1]. Asynchronous motors got a rotor magnetic field induced by the current in the rotor bars induced by the stator fields. The rotor has a slip relative to the rotating fields in the motor, being called as asynchronous motors. For many years, they have been the workhorse in the industry due to their reliability and low-cost [2]–[5]. However, more energy-efficient components like PMSMs are a part of the solution to solve the problem of ever-increasing energy demand and climate change. Figure 1.1 shows a dismantled four-pole PMSM. This motor type has a high torque-to-size ratio, which depends on the strength of the permanent magnets (PM). Developments in frequent converters and sensorless PMSM drive strategies make PMSMs more desirable for industrial applications like pumps, fans, robotics, offshore wind turbines, and electric vehicles. The PMSM is exposed to mechanical and thermal stresses in dynamic operations. Consequently, faults in PMSMs for such applications occur more often than in industrial productions. These induced faults will cause hazardous conditions and production loss.

The fault rates reported in literature are 40-50 % on bearing faults, 30-40 % on stator faults and the rest on rotor faults [6], [7]. These numbers are related to reports from the 1980s on asynchronous motors [8]. It is assumed that bearing faults and stator faults are common in PMSMs. However, the rate of occurrence for demagnetisation faults (DF) is unclear. DF is unique to PM motors and will result in reduced efficiency and back electromagnetic motive force (BEMF), but the cogging torque increases [9], [10]. A magnet can be completely or partial demagnetised. The DF can be uniform on all poles or local on a single pole. Uniform DF is more difficult to detect because there is no magnetic asymmetry, but the PMSM has less available torque [6].

Many severe electrical faults, e.g., line-to-line and phase-to-ground short circuits, start with the deterioration of the insulation caused by wear or overloading. The incipient stage is called the inter-turn short circuit (ITSC). It might induce large currents, which generate excessive heat and deteriorate the insulation [11], [12]. Faults like ITSC and

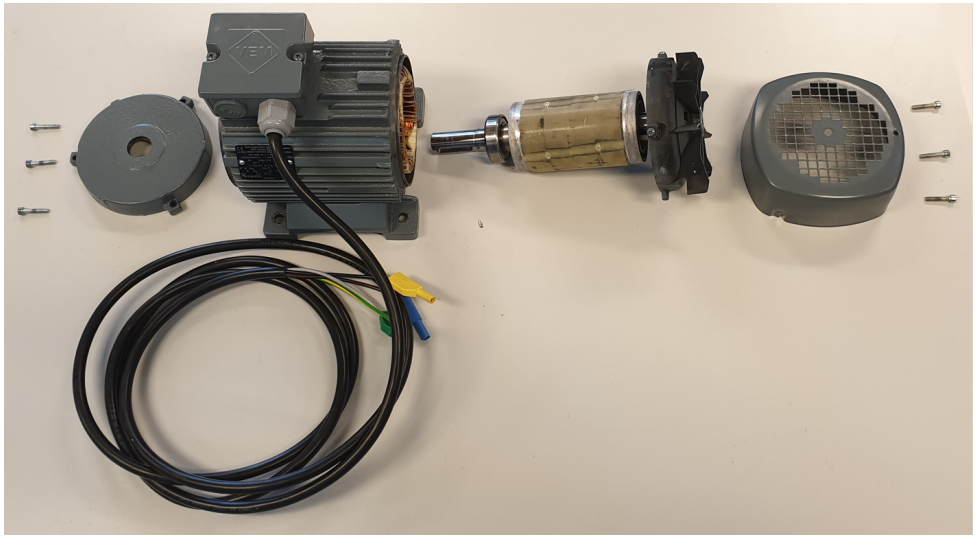

Figure 1.1: Dismantled PMSM - Model Type: "IE5-PS2R 90 L"

Table 1.1: List of faults in PMSM

Electrical	Mechanical	Magnetic
Inter-turn Short Circuit	Eccentricity	Uniform Demagnetisation
Line-to-line short circuit	Bearing fault	Non-uniform Demagnetisation
Phase-to-ground short circuit	Imbalance	Broken magnet
Open circuit fault	Loose foot	
High resistance connection		

DF will cause asymmetric pulls, causing mechanical faults like eccentricity. Mechanical faults include, but not limited to, bearing faults, rotor imbalance, shaft misalignment, bent shaft, and loose foot. These faults can be caused by poor lubrication, mistakes in installation, overload, or corrosion. Bearing faults can occur on the inner race, outer race, bearing cage or bearing balls. Eccentricity refers to the uneven air-gap distance between the rotor and stator [13]. Table 1.1 lists a few common PMSM faults under the categories electrical, mechanical, and magnetic faults.

Fault detection and identification (FDI) schemes are necessary for condition monitoring (CM) of PMSMs, ensuring safe operation and reducing unexpected downtime. Conventional FDI or CM methods applied in the industry are still limited to specific machine operations and often rely on steady-state operation, ideally with similar load and speed. The PMSMs in wind turbines, electric vehicles, and robotics operate with dynamic operations based on drive commands. Therefore, FDI schemes for PMSMs must be sufficiently robust against variable load and speed. The FDIs can be divided into three different categories, model-based, signal-based and machine learning (ML) based methods [9].

Model-based methods aim to identify fault signatures through mathematical models, i.e., electric equivalent-circuit (EEC), permeance network model (PNM), field reconstruction model (FRM) and finite element analysis (FEA). The latter is the most accurate, but simulating a few seconds of a PMSM in dynamic operation with a time-stepped FEA may

require several hours of computing. Extensive studies of machine models may reveal fault patterns for different faults in various operating conditions without damaging expensive motors. Alternative strategies with model-based fault detection are to estimate hard-to-measure parameters with an inverse problem or measure a residual between predicted and measured signals [14]. There is always a continuous effort to find simpler models with sufficient accuracy for online applications. This may involve simplifying model descriptions, making them faster to compute or giving a clearer overview of the model.

Signal-based methods rely on different signal processing techniques, which reveal fault signatures. The term signal-based method is a misnomer since all FDI techniques involve a level of signal processing of the measured signal. It refers, however, to fault diagnosis methods, which solely use signal processing techniques to highlight fault signatures from prior knowledge. They detect faults when a fault indicator exceeds a predefined threshold [6], e.g., the root mean square of a signal or the peak at a characteristic frequency. These indicators are often the results of extensive model-based studies. The time-series signal from a PMSM operating with variable speed often is transformed into frequency- or a time-frequency domain with techniques like fast Fourier-transform (FFT), Wavelet transforms, and quadratic time-frequency distributions (QTFD) [10]. An online FDI has the following key attributes: early detection, high accuracy, low computation burden, and low installation cost. Installation cost may include the required number of sensors and their location on the PMSM. FDIs scheme relying on measurements of stray flux may offer a non-invasive solution with more detailed information on the magnetic asymmetry than conventional methods using current and vibration sensors [5].

ML-based methods are data-driven models, being customisable for different applications, i.e., support vector machine (SVM), convolutional neural network (CNN), feedforward neural network (FNN) and reinforcement learning (RL). These are less demanding on prior knowledge of the PMSM but may require labelled data from both healthy and faulty cases for accurate classification [15]–[17]. Acquiring experimental data is a key part of fault diagnosis research for validating proposed techniques in model-based and signal-based FDI or training in ML approaches. Usually, training and testing samples of faulty PMSMs are unavailable or very expensive. Supervised ML algorithms have labelled training and testing datasets. These algorithms are faster to train but are highly specialised for a single task, e.g., discrimination between health classes. Unsupervised ML algorithms do not have labelled data but identify the clusters of the dataset in the feature space. These methods require more samples in the training dataset. Self-supervised ML, e.g., one-class SVM, local outlier factor (LOF) and auto-encoders, use only healthy case data. They have not been applicable for fault diagnosis [18]. They might be useful to combine with active learning (AL), which requires data from the faulty case after the first detected fault [16]. An ML classifier still faces a problem of imbalanced data when the samples of no-fault (NF) cases outnumber the faulty data samples. Severe data imbalance will make the classifier collapse, i.e., every sample is classified as a healthy case.

1.2 Objectives

This dissertation focuses on two main topics being actively researched. The first topic investigates reducing the computational burden in analysis of faulty PMSM in dynamic operations. Many mathematical models of PMSM focus on either accuracy or computational efficiency. FEA gives the highest accuracy but simulating a few seconds of an operating PMSM with transient loads and speeds may take several hours. Therefore, it is desirable to decrease the computational burden of models or signal processing techniques while maintaining sufficient accuracy.

The second objective is to develop FDI schemes of PMSM and investigate methods of reducing the effort required for implementing them. First, installing new sensors may affect the performance of the PMSM, and one should keep the numbers to a minimum and install them externally, e.g., measuring stray flux. Second, PMSM often operates with variable loads and speed, thus any FDI needs to adapt to the dynamic operation. Finally, all ML-based FDIs require training data from the different healthy classes. Historical data of faulty PMSM is very restricted in dynamic operations, while the data of healthy PMSM is abundant. This imbalanced data problem hinders the training of machine learners. Novel FDI schemes, requiring fewer faulty training samples, might be a more desirable option in fault diagnosis of PMSMs.

1.3 Contributions of the dissertation

The scientific contributions of this dissertation are withdrawn from six research papers published or submitted to international conferences proceedings and journals.

Paper A: Detecting Eccentricity and Demagnetisation Fault of Permanent Magnet Synchronous Generators in Transient State
Summary: In Paper A, the surface mounted PMSM is studied with FEA. The research builds on the work of Da et. al. [19], presenting a system of 12 search coils measuring air-gap flux for producing polar plots with different characteristics for different faults. The proposed FDI aims to find the minimum number of required search coils. In the case of a four-pole PMSM, the minimum number of search coils required to identify magnetic asymmetries are two. They are located on the opposite side in the stator. The induced search coil voltages during dynamic operation of a permanent magnet synchronous generator (PMSG) are analysed by FEA. A fault is detected if the difference stays below a threshold. In perfect magnetic symmetry, the voltage difference is equal to 0. This method is limited to machines with an even number of stator teeth. The change of magnitude obtained by enveloping the voltage difference can be used to diagnose demagnetisation and eccentricity. The FDI is verified with FEA results for a PMSM accelerating during start-up.

Contribution: A fault diagnosis scheme is proposed with three conditions in a decision tree obtained from an FEA of a four-pole PMSM. It discriminates between healthy case, DF, SE, and DE in dynamic operations based on input from two search coils mea-

suring magnetic flux in stator teeth.

This paper has been published as:
S. Attestog, H. V. Khang and K. G. Robbersmyr, "Detecting Eccentricity and Demagnetization Fault of Permanent Magnet Synchronous Generators in Transient State," 2019 22nd International Conference on Electrical Machines and Systems (ICEMS), Harbin, China, 2019, pp. 1-5, doi: 10.1109/ICEMS.2019.8921753.

Paper B: Modelling Demagnetised Permanent Magnet Synchronous Generators using Permeance Network Model with Variable Flux Sources
Summary: Paper B presents a method to describe the rotation of the rotor in a permeance network model (PNM) with variable magnetic flux sources. This method can lower the computational burden compared to the conventional methods with variable airgap permeance, which are empirically obtained. If the centre of the rotor does not change over time, it is not necessary to invert the permeance matrix in every time step. The proposed method does not require any variable permeance function for the airgap obtained numerically in an FEA. This allows more focus on the strategic design of the permeance network for accurate computation. The proposed model is verified by comparing it to an FEA with identical geometry.

Contribution: A PNM is proposed to replaces variable permeance for describing rotor revolution with variable flux sources. It replaces the air-gap permanence function, which is acquired empirically and is dependent on the rotor position. The new approach has a smaller computational burden since the permeance matrix does not need to be inverted every time-step in case of no dynamic eccentricity.

This paper has been published as:
S. Attestog, H. Van Khang and K. G. Robbersmyr, "Modelling Demagnetized Permanent Magnet Synchronous Generators using Permeance Network Model with Variable Flux Sources," 2019 22nd International Conference on the Computation of Electromagnetic Fields (COMPUMAG), Paris, France, 2019, pp. 1-4, doi: 10.1109/COMPUMAG 45669.2019.9032791.

Paper C: Field Reconstruction for Modelling Multiple Faults in Permanent Magnet Synchronous Motors in Transient States
Summary: Paper C presents a FRM to model faults in surface-mounted PMSM. This model type was first proposed and developed by Bahimi and Khoobroo [20]. However, Paper C gives a new feature for the FRM and verifies its strengths. The new feature is a magnet library, which stores basis functions describing magnets with different defects. The developed FRM also includes the description of ITSC, which has not been presented in previous papers. The developed model can simulate magnet defects and ITSC and has the potential to simulate both faults simultaneously. Further, the model can present detailed results of current, terminal voltage, EMF, torque, flux linkage, stator tooth flux density and induced search coil voltage. The model is verified with both FEA and exper-

imental data acquired from the in-house test bench.

Contribution: A FRM is developed implementing a basis function library of magnet defects and ITSC model description. The proposed library removes the need to compute a new rotor basis function in a static FEA for every combination of magnets with different defects. The basis function for each magnet defect is computed individually in static FEAs and later superimposed in the FRM.

This paper has been published as:
S. Attestog, H. Van Khang and K. G. Robbersmyr, "Field Reconstruction for Modeling Multiple Faults in Permanent Magnet Synchronous Motors in Transient States," in IEEE Access, vol. 9, pp. 127131-127140, 2021, doi: 10.1109/ACCESS.2021.3112224.

Paper D: Improved Quadratic Time-frequency Distributions for Detecting Inter-turn Short Circuits of PMSM in transient States
Summary: Paper D presents a new approach to compute QTFD with less computation burden. Previous implementations of QTFD can only be applied to signals lasting a few seconds. The proposed method allows generating spectrograms with Choi-Williams's distribution and Wigner-Ville distribution and is applied to samples of 120 s. They have been verified on a numerical example function and validated with experimental measurements. The time resolution is unaffected by window size, but frequency resolution sets a minimum limit for the window. A larger window space increases the computation time and sets the maximum limit in the case of online applications. The test on the experimental data proved that the proposed method could capture the signal components on noisy data with sharper peaks than STFT.

Contribution: An approach is proposed for producing QTFD (Cohen class functions), which reduces the computational burden. This expands the utility of QTFD for signal processing in online applications.

This paper has been published as:
S. Attestog, H. V. Khang and K. G. Robbersmyr, "Improved Quadratic Time-frequency Distributions for Detecting Inter-turn Short Circuits of PMSMs in Transient States," 2020 International Conference on Electrical Machines (ICEM), Gothenburg, Sweden, 2020, pp. 1461-1467, doi: 10.1109/ICEM49940.2020.9271050.

Paper E: Mixed Fault Classification of Sensorless PMSM Drive in Dynamic Operations Based on External Stray Flux Sensors
Summary: In Paper E, an FDI scheme for ITSC and DF is implemented for a surface mounted PMSM operating with both transient working conditions and mixed fault. It implements order tracking based on the rotor position, to estimate rotor position with an optimisation problem and a single stray flux sensor. The computed spectrograms normalise with respect to both amplitude and frequency of the fundamental component, which is sampled at every half harmonic up to the 40^{th} order. Any ML tool must discrim-

inate based on the harmonic content. The output features arrays computed from current, stray flux and torque are used to train four MLs: support vector machine (SVM), feed-forward neural network (FNN), ensemble decision tree (EDT), and k-nearest neighbours (KNN). The proposed algorithm is tested on experimental data from an in-house test bench.

Contribution: An FDI scheme is proposed based on a simple machine learner (SVM, FNN, EDT and KNN) and order tracking with an optimisation problem. The resulting scheme is robust to dynamic operating conditions and eliminates any need for a position sensor.

This paper has been published as:
S. Attestog, J. S. L. Senanayaka, H. Van Khang, and K. G. Robbersmyr, "Mixed Fault Classification of Sensorless PMSM Drive in Dynamic Operations Based on External Stray Flux Sensors," Sensors, vol. 22, no. 3, p. 1216, Feb. 2022, doi: 10.3390/s22031216.

Paper F: Robust Active Learning Multiple Fault Diagnosis of Sensorless PMSM Drives in Dynamic Operations Under Imbalanced Datasets
Summary: Paper F presents an FDI scheme for addressing the lack of faulty samples and imbalanced datasets. This method builds on the work from Paper E with order-tracking based on resampling the input signal at an equal angular increment. It is robust against transient working conditions and eliminates the need for the position sensor. LOF is used for anomaly detectors or detect faults when fault-signatures are unknown. The fault classifier part of the FDI starts its training when the first fault is detected by LOF and validated by an expert. The proposed fault classifier is developed based on the reinforcement learner deep Q-network. The most important with this reward function is to "rebalancing" the imbalance dataset without the need for any oversampling techniques.

Contribution: An FDI is proposed for discriminating between ITSC and local DF in PMSM in isolated and mixed fault cases with limited historical faulty data, using, local outlier factor, a density-based one-class classifier and reinforcement learning. It also implements the proposed order tracking method from Paper E. The resulting scheme is robust against the imbalanced datasets and dynamic load and speed.

This paper is under revison:
S. Attestog, J. S. L. Senanayaka, H. Van Khang, and K. G. Robbersmyr, "Robust Active Learning Multiple Fault Diagnosis of Sensorless PMSM Drives in Dynamic Operations Under Imbalanced Datasets", IEEE Transactions on Industrial Informatics (under revision).

1.4 Outline of dissertation

This dissertation consists of seven chapters. The introduction in Chapter 1 gives an overview of the dissertation and the research topics. Chapter 2 presents the state-of-art, and chapter 3 presents the in-house test bench developed for the research. Chapter 4 covers the topic of modelling faulty PMSM through Papers A, B and C. Chapter 5 summarise the implementation of the Cohen Class function with less computational burden in Paper D. The studies of FDI with ML are presented in Chapter 6 through Papers E and F. The final remarks and potential future improvements are in Chapter 7. Figure 1.2 shows the structure of this thesis and summarise the chapter contents.

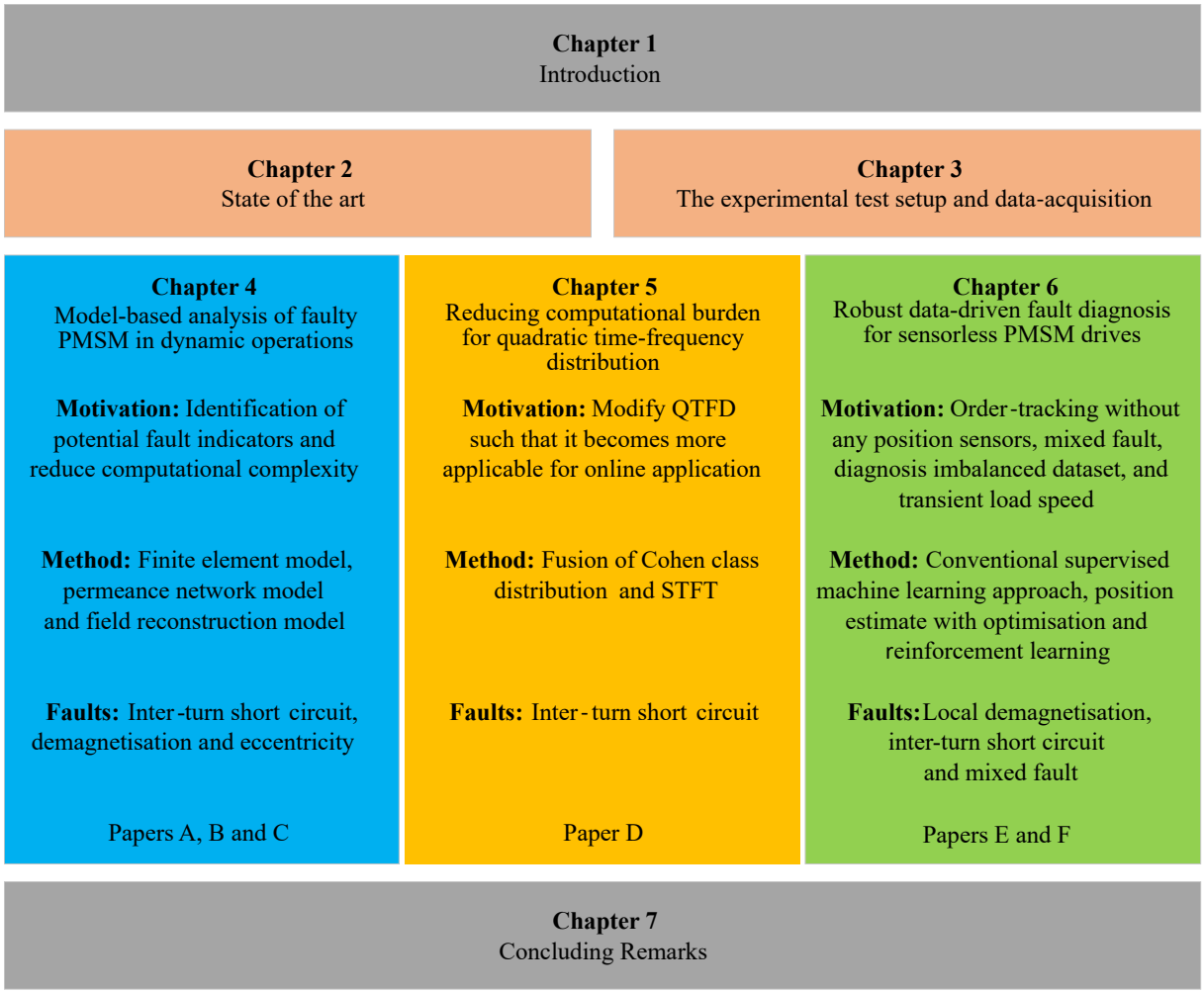

Figure 1.2: Summary of chapter contents

Chapter 2

State of the Art

This chapter presents state-of-the-art and identifies knowledge gaps for fault analysis of PMSM. The appended papers address problems in PMSM fault analysis by proposing new FDIs, or methods to model a faulty PMSM in dynamic operations. Fault analysis schemes fall into three categories model-, signal- and ML-based methods. The next frontier in the study of PMSM fault diagnosis is in dynamic operations. Many FDI schemes have been developed, relying on the steady-state operation or a predefined speed operation. The final goal is to propose FDIs, which could work well regardless of operation state and increase their versatility. Table 2.1 summarises measured parameters used in fault diagnosis of common PMSM faults. Literature reports fault diagnosis of PMSM in steady-state are saturated and there exist FDIs utilising measurement of voltage, current, torque, magnetic flux and vibration. An FDI scheme for PMSM operating in the transient state has been proposed for current and torque [21], [22]. However, magnetic flux density in the air-gap or stray flux has not been fully explored for PMSM in dynamic operations.

Table 2.1: Measured parameters used for fault diagnosis reported in literature

Measured	Demagnetisation		Eccentricity			Electrical	
Parameter	Partial	Uniform	Static	Dynamic	Mixed	ITSC	HRC
Voltage	x		x	x	x	✓	
Current	✓		x	x	✓	✓	
Active power					x	x	
Torque	✓	✓	x	x		✓	
Speed			x	x	x		
Magnetic flux	x	x	x	x	x	x	
Resistance						x	✓
Inductance						x	
Turns						✓	
Acoustics	x		x	x	x		
Vibration	x	x	x	x	x		
References	[19], [23]	[23]	[19], [24]	[19], [24]	[19], [24]	[19], [22]	[25]

* FDI validated for steady-state operation are marked with "x" and "✓" for transient-state operations.

2.1 Model-based analysis of faulty PMSM

Model-based methods revolve around mathematical descriptions of PMSM. The inverse problem is a collection of techniques which require accurate and fast-to-compute models. FDIs based on inverse problems can estimate hard-to-measure parameters like the number of shorted turns or determine faults based on the residual between estimated and measured parameters [26]. Alternatively, accurate models of faulty PMSM give us a deeper understanding of PMSM and how it behaves in different scenarios. Model studies lay the groundwork for developing new FDI schemes before any testing on real motors. The most accurate method to acquire knowledge of the behaviour inside a PMSM is to solve Maxwell's equation directly. However, electromagnetism is not the only subject required for accurate PMSM models. Stator windings current, friction, and hysteresis generate heat, and many material properties are temperature-dependent. Cooling of the motor with conduction and convection is described with thermodynamics and fluid dynamics. Changing magnetic fields induces forces and causes vibrations described with magnetostriction. Simulating an operating PMSM also requires knowledge of control theory on how to tune the controllers for a proper dynamic response, which also requires a description of the mechanics.

Solving differential equations for only describing the electromagnetic field is exhaustively cumbersome for simple structures and even impossible to solve analytically [10]. The second best option is to solve it numerically with FEA. The model geometry of a PMSM splits into a mesh where the governing equations are solved locally. The solution of the FEA depends on the mesh. Its "fineness" increases until the results converge. FEA provides the most detailed information on the PMSM, however simulating a couple of seconds may take hours to compute. This produces a drive for developing models with a smaller computationally burden but with sufficient accuracy. One modelling strategy for creating new models is to modify previous models to include more physical phenomena. The other one is to combine two modelling techniques to obtain individual merits or compensate for any shortcomings in each method. Many hybrid models use static FEA of PMSM to improve the accuracy of simpler models like EEC MEC and FRM [11]. Most EEC, which include the description of ITSC, split one phase into two parts, shorted and not shorted windings. A fault resistor connects in parallel across the shorted windings. It represents the remainder of the insulation where the short circuit has occurred. Winding function theory includes the description of geometric features and material properties [10] in the EEC. These models are best suited for electrical faults like a phase-phase short circuit, phase to ground, ITSC, open circuit, and high resistance connection [25], [27]. However, EEC can include the description of eccentricity and demagnetisation [18], [28]. These models are more demanding with the expertise of the PMSM's structure. Nevertheless, it is considered the model type for PMSM with the least computational burden.

Magnetic equivalent circuit (MEC) equates the flow of magnetic flux as the flow of current in EEC [29], [30]. Solving Kirchhoff's voltage and current laws gives sufficient accuracy for simple geometries. More complex structures are still solved with the same laws, but are often called the permeance network model (PNM). It is equivalent to the admittance matrix, which is applied to power flow problems and short circuit faults in

distribution networks. PNM is best suited for magnetic problems and describing magnetic asymmetries, e.g. eccentricity and demagnetisation. The main drawback of PNM is its description of rotor revolution. All of the nodes in the air-gap between the rotor and stator domains are connected, where their permeance depends on the rotor position [31]. All entries in the permanence matrix related to the nodes in the border layer between the rotor and stator need to update in each time step. The permeance matrix also needs to be inverted due to the updated entries, which usually are close to 0. It will become time-consuming for models with finer mesh. Gomez et al. proposed a PNM model that borderlines with an FEA in mesh fineness and needs to re-mesh in every angular increment [32].

The FRM technique recreates the air-gap magnetic flux density by superimposing and phase-shifting the radial and tangential components of air-gap magnetic flux density exported from the static FEA. Conventional FRM assumes no deformation in motor structure, no saturation, no end-coil effects, no hysteresis, and eddy current losses are negligible [33]. The conventional method computes the rotor basis function with all magnets defined in the static FEA. The linear assumption will allow for combining the basis functions of each magnet by superposisition. Basis magnet functions with different defects can be computed with static FEAs and stored in a library. New rotor basis functions are generated by superimposing different magnet basis functions without the need for a static FEA for every combination. No existing study has presented the possibility of a magnet library.

FRM maintains the accuracy of the FEA but is significantly faster to compute. It is especially well suited for time-stepping simulation, multi-physics problems or finding the optimal phase current waveform in a faulty PMSM [20], [34]. Kiani et. al. [35] investigated the vibration level of a PMSM at different speeds and loads in steady-state conditions. Each fault scenario required a computation time of 70 min in FRM, while an equivalent FEA would require 100 days. Khoobroo et. al. [36] proposed a detection scheme for ITSC faults in five-phase PMSMs based on flux observer. Torregrossa et. al. [37] included partial demagnetisation and static eccentricity (SE) in an extended FRM. It includes the description of the slotting effect and non-linear material by computing the basis functions at different rotor positions and current excitation. The look-up table generated from static FEAs enables the modelling of interior PMSM (IPMSM) with FRM. It is hard to find any publication on FRM simulating PMSM with implemented ITSC operating in transient-state or mixed with a DF.

2.2 Signal-based FDI

The term "signal-based" can be interpreted as a misnomer since all FDI techniques involve a level of signal processing of the signals measured from an operating PMSM. However, it is referred to as techniques that solely use signal processing techniques to highlight fault signatures from prior knowledge or estimate parameters, detecting faults when they exceed a set threshold [6]. It excludes techniques that require descriptive models of the specific PMSM. It separates from ML-based since no iterative training process is required, and

Table 2.2: Signature frequencies for different faults

Fault	Parameter	Frequency	Refrence
ITSC	I	$3f_s$ and $7f_s$	[38]
ITSC	I	$(2k-1)f_s$	[8], [39]
ITSC	I, Φ	$\left(\frac{kN_s}{p} \pm 1\right) f_s$	[38], [40]
ITSC	Φ	$\left(\frac{n}{p} + k\right) f_s$	[38], [41]
DF	I	f_s and $5f_s$	[42], [43]
DF	I	$\left(1 \pm \frac{k}{p}\right) f_s$	[43], [44]
Eccentricity	I	$\left(1 \pm \frac{2k-1}{p}\right) f_s$	[6]
Eccentricity	Vib., V, Φ	$\left(1 \pm \frac{k}{p}\right) f_s$	[45]
DE	I	$2kf_s$	[39]
Bearing outer race	Vib.	$\frac{N_{\text{ball}}}{2p} f_s \left(1 - \frac{d_{\text{ball}}}{d_{\text{cage}}} \cos(\beta)\right)$	[6], [46]
Bearing inner race	Vib.	$\frac{N_{\text{ball}}}{2p} f_s \left(1 + \frac{d_{\text{ball}}}{d_{\text{cage}}} \cos(\beta)\right)$	[6], [46]
Bearing ball	Vib.	$\frac{d_{\text{cage}}}{2pd_{\text{ball}}} f_s \left(1 - \left(\frac{d_{\text{ball}}}{d_{\text{cage}}} \cos(\beta)\right)^2\right)$	[6], [46]
Bearing cage	Vib.	$\frac{1}{2p} f_s \left(1 - \frac{d_{\text{ball}}}{d_{\text{cage}}} \cos(\beta)\right)$	[6], [46]
Bearing fault	I	$f_s \pm kf_v$	[10], [46]

the fault detection criterion is already known. The most common method is to extract the frequency components in a signal. Table 2.2 lists several characteristic frequencies found in literature for different faults. The letters/abbreviations I, V, Φ and Vib. refer to current, voltage, magnetic flux and vibration, respectively. All of the equations for fault signatures relate to the synchronous frequency of the motor f_s, which equals the mechanical frequency times the number of pole pairs p. N_s is the number of stator slots, and the parameters n and k are integers. Calculating fault characteristic frequencies requires the number of bearing balls N_{ball}, ball diameter d_{ball}, cage diameter d_{cage} and the contact angle β between the bearing ball and cage. The parameter f_v is side band frequencies in the current computed from the other equations related to bearing faults.

Fast Fourier-transform (FFT) can quickly compute the frequency composition of a signal, but it falls short when the speed of the PMSM is no longer constant. The peaks in the spectrogram are "smeared" over several frequencies, resulting in a spectrogram unsuited for fault diagnosis. A small step from FFT to the analysis of transient signals is to split the input signal and then compute a spectrogram for each "instant". This is short-time Fourier-transform (STFT). The main disadvantage of STFT is the compromise between the resolution of the time and frequency. Selecting short intervals improves the time resolution but decreases frequency resolution and vice versa. Other commonly used techniques are wavelet transform [47], Hibert-Huang transform [48], chirplet transform [49], and different techniques falling under the umbrella term QTFD or Cohen's class function [50], [51]. The first developed QTFD is the Wigner distribution, which was applied in the analysis of quantum physics. It is often called Wigner-Ville distribution

(WVD) in the field of signal processing [52]. The first major drawback to WVD is the cross-product problem [50], [53]. The solution is the filtering process from the kernel function. This includes, but is not limited to, Zhao-Atlus-Marks (ZAM), Choi-Williams distribution (CWD), and Gabor [51], [54], [55]. STFT computes the frequency composition for each time instant with a set interval. Cohen's class function uses the whole signal to compute each time instant. This allows it to plot signals with the variable frequency with high accuracy. However, computing time-frequency distributions (TFD) with the Cohen's Class function involve solving a triple integral [52]. Computation time increases with the length of the input sample and could be only applied to signals of a few seconds [55]. The computational burden prevents the QTFDs from implementation in online applications. A more computationally efficient method for computing QTFDs will enable them for online applications.

Another strategy against non-stationary signals is to order-normalise or track their harmonics. The procedure is done after transforming into the frequency domain for stationary signals by scaling the frequency axis. The equations in Table 2.2 is still applicable, but f_s equals 1. Empirical mode decomposition is a data-adaptive multi-resolution technique for decomposing non-linear and non-stationary signals. It separates the signal into intrinsic mode functions at different resolutions [56]. Vold-Kalman filters and Gabor order tracking are applicable for tracking the amplitude for a finite set of harmonics in a non-stationary signal. These methods are accurate, but the Vold-Kalman filter requires a model with information on the studied PMSM, and Gabor order tracking has a problem with order crossing [57], [58]. Another method for order-normalising the spectrogram is to re-sample the input signal based on the rotor position. One strategy is to use the position sensor, but this is not applicable to sensorless drives. Then the position or speed has to be estimated with for example Hilbert transform [59], sliding mode observer [60] and response analysis form high frequency signal injection [61]. Conventional methods often rely on current and voltage measurement, but an FDI scheme relying on stray flux has the potential of being less invasive. The unit responsible for condition monitoring of the PMSM can be separated and installed externally if the position is estimated by the same signal used for diagnosis, i.e. stray flux.

2.3 Machine learning-based FDI

2.3.1 Supervised and unsupervised machine learning

Supervised ML algorithms are trained and tested on fully labelled datasets. The training time is often short and requires few samples relative to unsupervised learning. These techniques are trained for a specific task, e.g. discriminating between a few healthy cases. The main drawback is the acquisition of labelled datasets, being resource-expensive or unavailable. Unsupervised ML algorithms do not require any labelled datasets and focus on recognising patterns in the datasets, dimension reduction and feature mining. The most common ML algorithms are support vector machines (SVM) [62], k-nearest neighbours (KNN) [63], decision tree [64], convolution neural network (CNN) [16] and artificial Neural network (ANN) [65].

An artificial neural network is an ML tool that resembles the human brain, where nodes represent the neurons and gains represent the strength of the signal in the synapses. The development of ANN has produced networks with many layers with thousands of parameters. These networks fall under the category of deep learning [66]. A large number of data samples of each class are required to train the network and optimise the parameter for the classification task. Ullah et. al. [67] trained deep neural networks under the principle of transfer learning. The majority of the network is pre-trained, but the last couple of layers retrain for a classification task. They are trained on the features computed from the pre-trained part of the network. In principle, a network trained to identify cats and dogs can retrain to discriminate between ITSC and DF. The field of PMSM fault classification has also been drawn back to ANN with few and simpler architectures. A highly specialised classifier may only need a few layers, being called as shallow learning [65]. Distinguishing between shallow and deep learning is defined by the number of layers. However, no exact limit has been specified.

2.3.2 Active learning and imbalance dataset problem

Labelled datasets are usually unavailable when a new ML-based FDI is installed on a PMSM. One approach to avoid the labelled data problem is using self-supervised MLs. They can be considered as a subset of unsupervised techniques since they work with unlabelled datasets. One type of self-supervised learning applied in the field of PMSM fault analysis is the one-class classifiers (OCC), which can be trained only on healthy datasets [68]. A trained OCC can quantify the deviation of a new data sample from the healthy samples. A large deviation from a healthy sample is considered a faulty case. There are four types of OCC; (1) Density-based methods e.g. local outlier factor (LOF) [69], (2) Reconstruction-based methods such as auto-encoder [70] and contrastive learning [71], (3) Boundary-based methods e.g., one-class SVM [16], (4) Ensemble-based methods which combine OCCs to form a more flexible data description model [68]. The best OCC in PMSM fault detection probably depends on the PMSM drive setup. However, comparing the OCCs has not been studied in literature.

Active learning (AL) is a semi-supervised ML algorithm where the training and testing datasets are partially labelled. These algorithms are trained on the labelled samples in the first iteration. Then they give a prediction on the unlabelled dataset with a confidence score. Predictions with high confidence are added to the labelled dataset in the next iteration. An expert (technician/engineer) will "actively" label the predictions with a low confidence score. AL is often called cooperative learning if it significantly relieves the workload for the expert [72], [73]. Jagath et. al. [16] proposed an active learning FDI which is combined a one-class SVM as the detector and CNN as the identifier. It avoids the need of no labelled samples in faulty cases but does not address the problem of imbalanced datasets. The training of the classifier is initiated after the first verified fault. However, the fault classifier may collapse and start classifying all cases as healthy since it still will achieve high accuracy. The problem occurs due to the data imbalance between the majority and minority classes in the training process. Normally, the imbalanced datasets are re-balanced by over- and under-sampling the datasets before the training process [74].

However, this adds another step of the signal processing before the training of any ML classifier. Under-sampling may resulting loss of useful information in the data set and oversampling makes over-fitting more likely.

Reinforcement learning (RL) may offer a solution to balance the datasets in the training process of the ML classifier. RL is a goal-orientated computational approach, in which an agent is trained to achieve a task inside an environment. The agent receives a reward or a penalty based on its state in the environment and actions. RL holds a vast array of possible applications. Song et. al. [75] implemented deep RL in a speed control strategy for a PMSM. Cao et. al. [76] proposed a method for finding the optimal multi-layer network through RL. They defined a set of 22 available layers in the RL algorithm to create the ML classifier. Li et. et. [77] proposed a method with a conditional generation adversarial network for expanding the ITSC dataset, consisting of negative sequence current and torque. It is an alternative to the synthetic minority oversampling technique (SMOTE) [74] applied to the dataset before training an ML classifier. The method is validated in the detection of ITSC in PMSM. Lin et. al. [78] proposed a deep Q-Network (DQN) with a weighted reward function for image classification. This approach offers a solution for PMSM fault classification, which integrates the dataset balancing into the training process of the classifier. However, this has not been validated for PMSM faults in dynamic operation or mixed fault (MF).

Chapter 3

Test-setup and data-acquisition

This chapter describes the in-house test-setup developed during the research period. It is difficult to obtain data from faulty PMSM, so the aim is to acquire measurements when such a motor operates with faults. The recorded data is used for training and validation of proposed algorithms in Papers D, E and F.

3.1 The developed in-house test-setup

The test setup revolves around the test motor, which is coupled to a load generator with a torque transducer in between. ITSC and DF are implemented on the test motor, operating under different operation profiles with variable load and speed. The test motor and load generated are mounted on a test bench made of duraluminium (AL-7075). The test bench has threaded holes and T-shaped slots-rails along its length and width. The ABB commercial drive supplying the test motor receives power from a 400 V power outlet. All operations are controlled via Dspace on an office laptop. Figure 3.1 shows a schematic overview of the setup and Figure 3.2 shows the test setup.

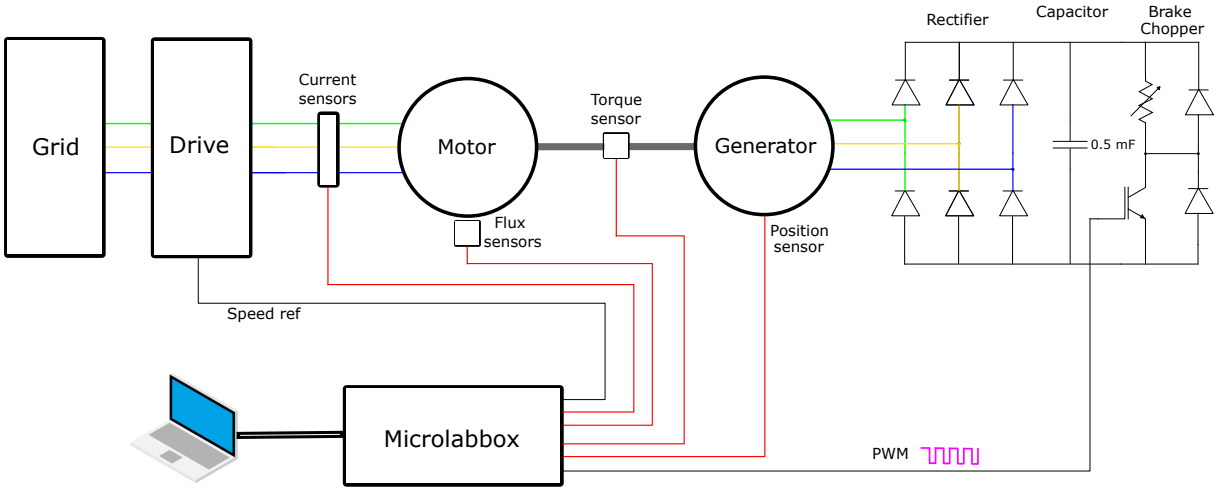

Figure 3.1: Schematic overview of the test setup

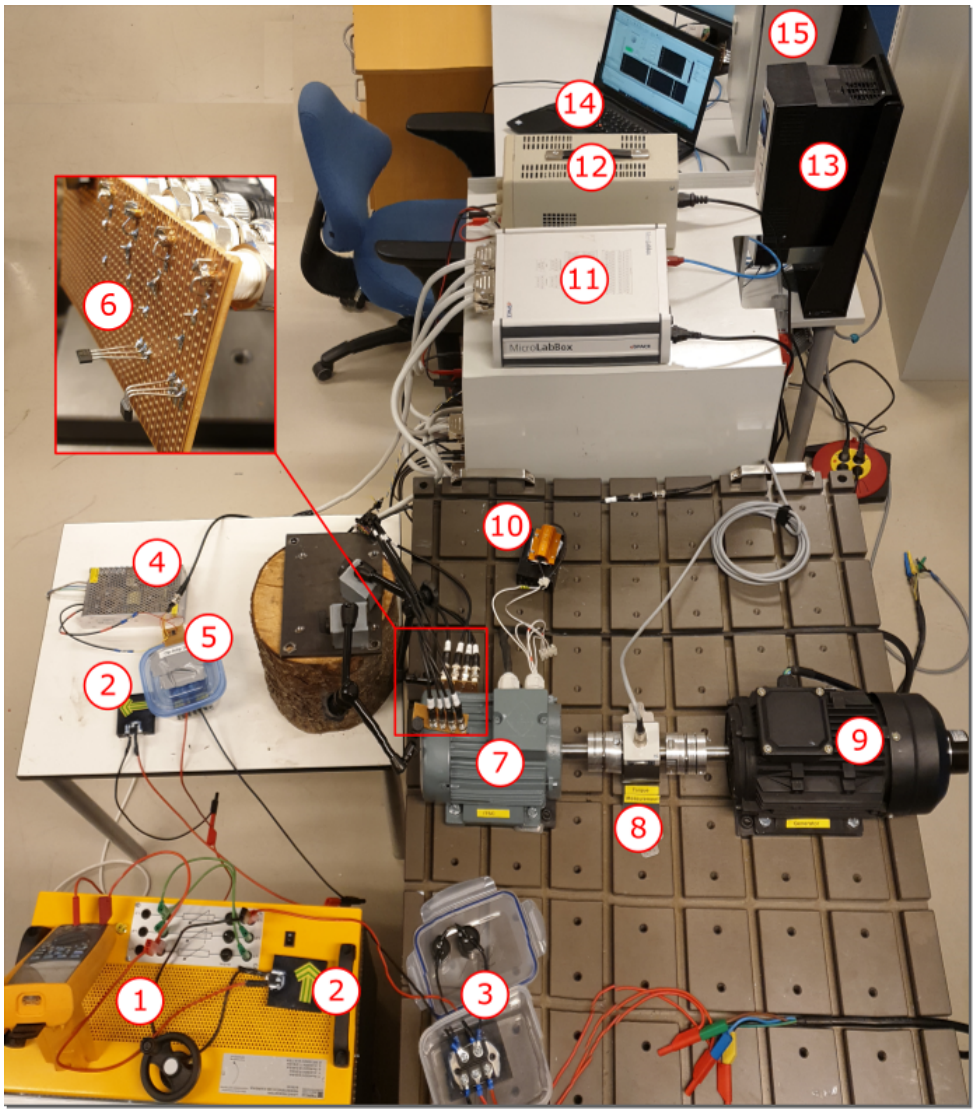

Figure 3.2: Overview of the test bench with (1) resistor bank, (2) flyback diode, (3) threephase rectifier with capacitor bank, (4) 12 V DC-supply, (5) IGBT brake chopper with OP-Amp, (6) hall sensors, (7) test motor, (8) torque sensor, (9) load generator, (10) short circuit resistor, (11) Microlabbox, (12) 24 V DC-supply, (13) ABB drive, (14) office laptop and (15) cabinet containing the current sensors

3.1.1 Motor and load generator

The electrical motors, surface-mounted PMSM "IE5-PS2R 90 L" are coupled to an IPMSM "90YSK-30FWJ302", which acts as the load generator. The two electrical machines are showcased in Figure 3.3 and respective nameplate parameters are listed in Table 3.1. The motor "IE5-PS2R 90 L" is selected because of easy access to stator winding and PMs for implementation of ITSC and local DF.

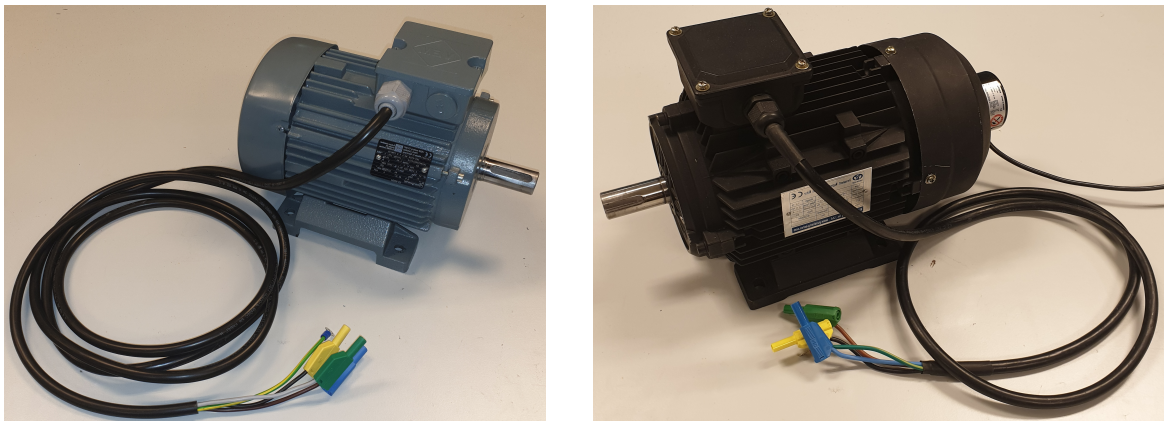

(a) (b)

Figure 3.3: The electrical machines of the test setup: (a) test motor and (b) load generator

Table 3.1: Test motor and load generator parameters

	Test motor	Load generator
Model	IE5-PS2R 90 L	90YSK-30FWJ302
Output power	2.2 kW	3 kW
Nominal voltage	280 V	400 V
Nominal current	5 A	6.4 A
Nominal speed	3000 rpm	3000 rpm
Nominal torque	7.0 Nm	9.6 Nm
Number of poles	4	4
Phase resistance	0.8 Ω	2.3 Ω
Direct axis inductance	6 mH	11.5 mH
Quadrature axis inductance	6 mH	27.5 mH
Nominal efficiency	90.2 %	92.6 %
Weight	18 kg	14 kg

3.1.2 Load regulator

A brake chopper in Figure 3.1 regulates the load consisting of the insulated-gate bipolar transistor (IGBT) "IXA70I1200NA" with a rated collector-emitter voltage of 1200 V. It breaks the circuit when turning ON and OFF at a switching frequency of 1 kHz. A 500 μF capacitor bank is connected across the output terminals of the three-phase full-bridge rectifier, removing the ripples from the voltage input of the brake chopper. The duty cycle used in the control of the brake chopper is a function obtained empirically by running the system at different speeds. An Op-Amp amplifies the PWM signal from the Microlabbox since its amplitude is insufficient to switch ON the IGBT. The resistor of the brake chopper is a variable 3.3 kW resistor bank set to 25 Ω. The brake chopper regulates the load with high precision for predefined dynamic load and speed profiles. Flyback diodes are connected across the resistor bank to give a path for the stored energy in the resistor bank.

3.1.3 Sensors

The three phase-currents are measured with the current sensors inside the electrical cabinet shown in Figure 3.2. The hall sensors, miniature ratio-metric linear solid-state sensors used to measure stray flux density, are placed in proximity to the PMSM. One sensor is bent 90° for measuring of both radial and tangential components. Each sensor is connected to the Microlabbox for 10 V supply and recording. Torque is measured with a torque transducer between the motor and the generator. Key parameters for all three sensors are listed in Table 3.2. The position sensor, mounted on the load generator, is an incremental encoder with a rated speed is 3000 rpm and requires a supply voltage of 24 V. Channels A and B of the incremental encoder transmit signals with 5000 pulses per revolution with a magnitude of 5 V and the third channel Z gives one pulse for every rotation.

Table 3.2: Key parameters for current-, torque-, and stray flux sensors

Parameter	Current	Torque	Stray flux
Model name	LTS 6-NP	T22	SS490
Supply voltage	5 V	11.5 V to 30 V	4.5 V to 10.5 V
Measuring range	± 19.2 A	± 50 Nm	± 67 mT
Sensitivity	104.16 $\frac{\text{mV}}{\text{A}}$	100 $\frac{\text{mV}}{\text{Nm}}$	31.25 $\frac{\text{mV}}{\text{mT}}$
Linearity error	<0.1 %	<0.3 %	<1.0 %
Max. temperature	80 °C	60 °C	125 °C
Min. temperature	-40 °C	0 °C	-40 °C

3.2 Inter-turn short-circuit - Implementation

The test motor "IE5-PS2R 90 L" has three parallel strands per phase winding, lowering self-inductance, phase resistance and BEMF. In the case of a short circuit on one single strand, the remaining two strands are unaffected. Therefore these motors are more tolerant to ITSC. Assuming copper resistivity at 25 °C, counting the number of turns and measuring the necessary geometric features of the PMSM will give an estimated phase resistance of 0.85 Ω. The nameplate value of 0.8 Ω verifies the observation of three parallel strands. Estimating the shorted turns between the end terminals compared to PMSM with single strand windings is less straightforward. The severity of an ITSC is defined as the number of shorted turns divided by the total number of turns in a phase winding. In the case of a single strand per phase, the severity level of ITSC is proportional to the measured resistance across the turns. In the case of parallel strands, however, the sum of the measured resistances between the tap and the two end terminals can be larger than the phase resistance measured between the end terminals. Another aspect of the ITSC in parallel strand PMSMs is that a short circuit may occur between two of the strands. When the two points on the strands have identical electrical positions relative to the end terminals. This ITSC has a severity of 0 % by the conventional definition of ITSC severity [27].

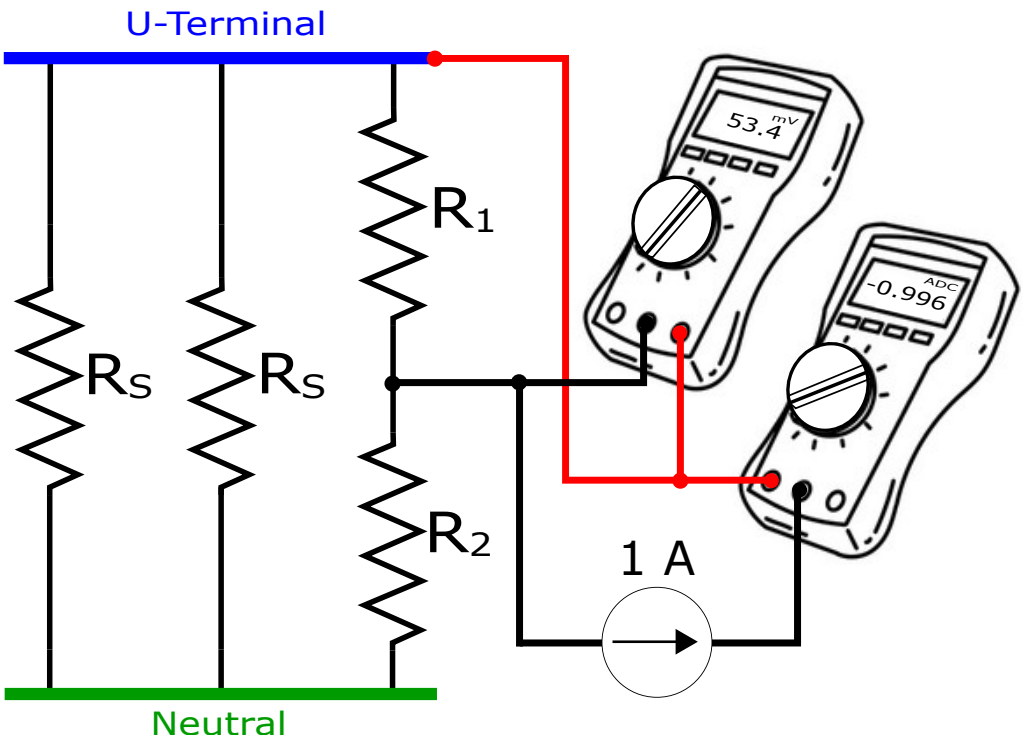

Figure 3.4: Sketch of sensitive resistance measurement

It is impossible to distinguish between the three parallel strands by visual inspection. To simplify the problem, the input phase terminal is chosen as one of the ends of the short circuit. It is a common point for all three strands. A short circuit tap is implemented on the phase winding by locally removing the coating on a single strand with sandpaper. Then the exposed copper surface is soldered with a wire, ensuring high electrical conductivity and easy access from outside the motor. The equivalent resistance between the tap and the end terminals is measured before soldering. The resistance of the shorted turns is in the magnitude of milliohms. A current of 1.0 A is passed through the phase winding, and the voltage drop is measured between the tap and end terminal. Figure 3.4 shows the schematic for the setup of sensitive resistance measurement. The circuit of a phase winding is described with three resistors R_s in parallel, where one of them splits into R_1 for shorted windings and R_2 for unsorted windings. Four taps are implemented in the stator, and the measured resistances are listed in Table 3.3.

The measured resistance is the equivalent resistance viewed by the multi-meters and is not equal to the resistance of the shorted windings. The parameter of interest is the ratio between R_1 and R_S, which is defined as the ITSC severity μ_f. A DC-circuit analysis results in the following description of the equivalent resistance:

$$R_\mathrm{mea} = \mu_\mathrm{f}\left(1 - \frac{2}{3}\mu_\mathrm{f}\right) R_\mathrm{s} \tag{3.1}$$

Solving for μ_f gives,

$$\mu_\mathrm{f} = \frac{3}{4} \pm \frac{1}{2}\sqrt{\frac{9}{4} - 6\frac{R_{mea}}{R_\mathrm{s}}}. \tag{3.2}$$

Table 3.3: Measurement of equivalent resistance in PMSM with implemented ITSC

Node 1	Node 2	Voltage (mV)	Current (A)	R_{mea} (mΩ)
U	1	53.4	0.9977	53.5
U	2	140.2	0.9977	140.5
U	3	375.8	0.9977	376.7
U	4	118.3	0.9977	118.6
N	1	859.3	0.9977	861.3
N	2	882.9	0.9977	884.9
N	3	887.6	0.9977	889.6
N	4	878.8	0.9977	880.8
U	N	841.4	0.9977	843.3

Table 3.4: Estimated value of μ_{f}

	U-teminal	Neutral	Total
Tap 1	2.2 %	97.8 %	100.0 %
Tap 2	5.8 %	94.5 %	100.3 %
Tap 3	6.0 %	93.3 %	99.3 %
Tap 4	4.8 %	95.1 %	99.9 %

One indicator for finding the correct solution for (3.2) is to identify which end terminal is closer to the short-circuit tap, i.e. is it more likely that the short circuit severity is larger or smaller than 75 %? The estimated severity levels μ_{f} implemented in the PMSM is estimated from the results in Table 3.3 and listed in Table 3.4. The equation derivation is proven correct since the estimated μ_{f} for R_1 and R_2 adds to 100 %. The final result of the circuit analysis is shown in Figure 3.5 with the placement of the implemented short-circuit taps. The measurement between the node is conducted to locate of each tap.

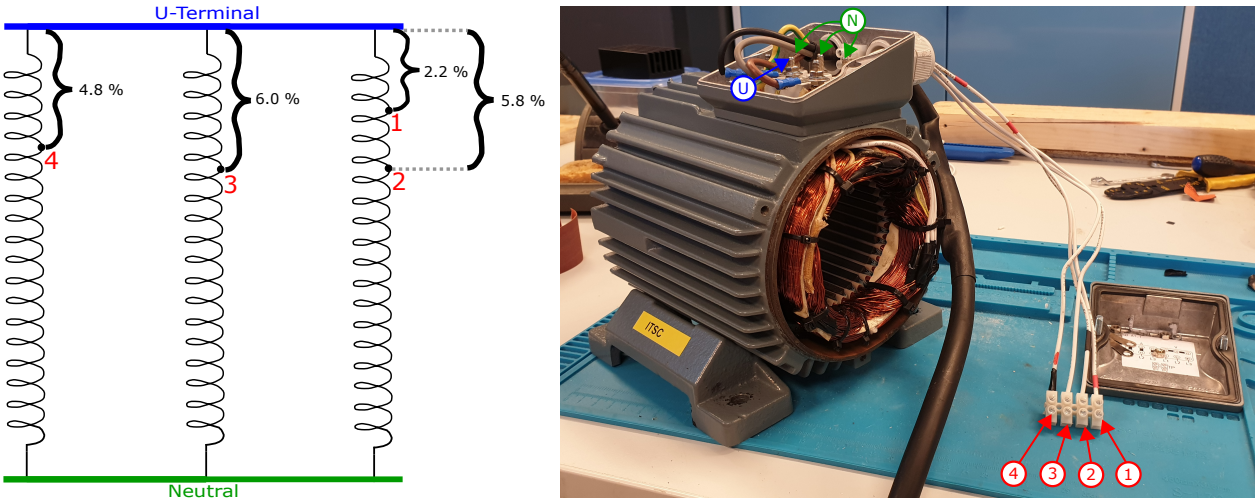

(a) (b)

Figure 3.5: Placement of short circuit taps in phase U in (a) circuit sketch and (b) image of the PMSM

3.3 Local partial demagnetisation - Implementation

Demagnetisation faults in PM machines are usually implemented by removing parts of the magnets [79] or replacing them with non-magnetic materials [80]. The latter results in an imbalance in the rotor. Another option is to install weaker magnets in the rotor through the manufacturers [42]. The mentioned methods do not mimic the demagnetisation caused by thermal cycling in dynamic operations of PMSM drives. The investigations by Fernandez et. al. [81] and Reigosa et. al. [82] show the temperature distribution of an IPMSM under different applied load currents. It is concluded that the hottest spot on average over time is in the middle of the magnet surface. This region is thus more likely to be affected by demagnetisation caused by overloading. The heat treatment proposed in Paper E involves local heating with a 1500 W electric cooktop. An aluminium block is placed on the iron hob. This allows for placement and removal of the PM rotor safely due to the low permeability of aluminium. The other rotor poles were cooled with a wet towel to ensure that they did not demagnetise during the heat treatment. Figure 3.6a shows the proposed heat treatment in progress. The rotor on the hot aluminium block is heated to 232 °C. The rotor is left on the hot surface for 10 minutes. Thermal paste is applied to the contact between the rotor and aluminium block to improve the heat transfer between the objects.

The magnetic field meter "Extech SDL900 AC/DC" measured the strength of the magnets before and after the heat treatment in the measurement setup in Figure 3.6b. The rotor is cooled to ambient temperature after the heat treatment. A wooden frame allowed the rotor to rotate while recording the measurement across its surface. It also kept the rotor axis horizontal while preventing any translational movement. The hall-sensor in the SDL900 is placed 3 mm above the rotor. Figure 3.7 shows the measured magnetic field surrounding the rotor before and after the heat treatment. The measurement is repeated three times to reduce measurement variations. A positive value indicates a North pole, while the South poles are negative. One North pole of the rotor lost 30 % of its original strength at two spots.

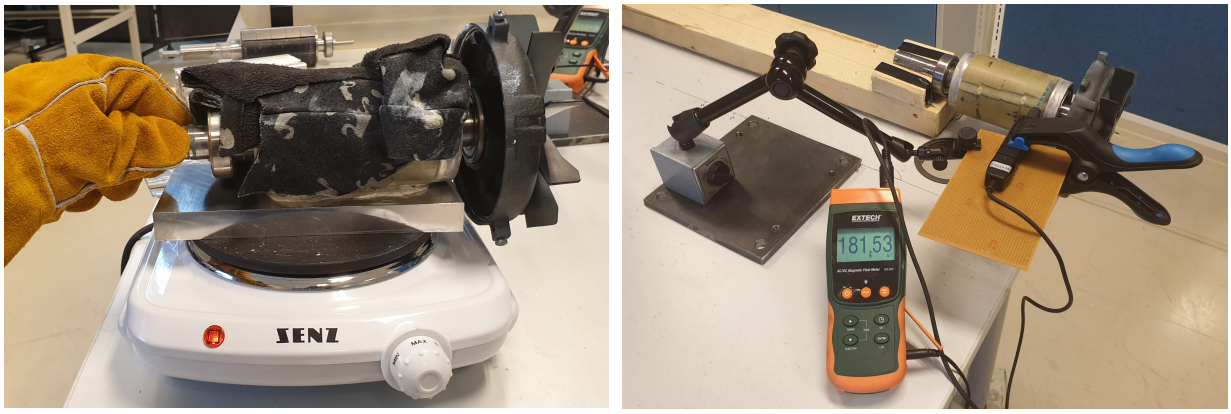

(a) (b)

Figure 3.6: The setups for (a) inducing local demagnetisation and (b) measuring magnetic field over the rotor surface

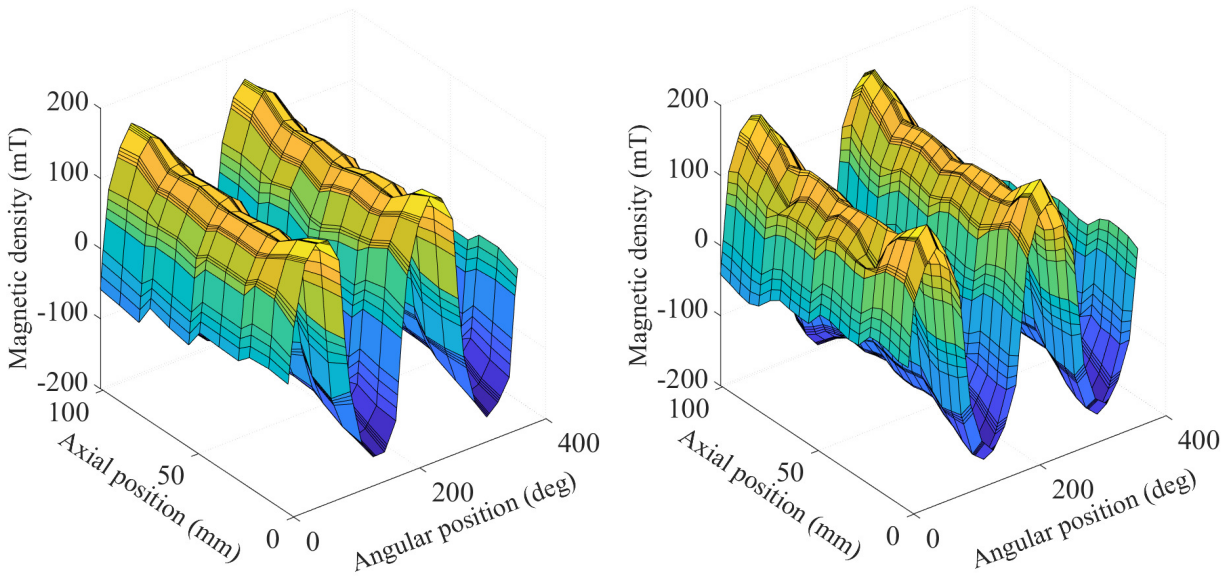

Figure 3.7: Measured magnetic field strength surrounding the PM rotor (a) before- and (b) after heat treatment

3.4 Operation profiles

Three different operation profiles are used in the experimental studies in Papers E and F. The first profile includes an operation with several combinations of loads and speeds, both constant or changing at a fixed rate. The two remaining profiles are generated by a random sequence of numbers and a first-order delay. Profile 2 keeps the load constant at 60 % of full load, while the speed constantly changes. The last profile keeps the reference speed constant at 1200 rpm, while the load changes unpredictably. The PMSM runs under these profiles with the health conditions: healthy, DF, 5 % ITSC and mixed fault (DF and ITSC). The Microlabbox records current, torque, stray flux, and rotor position with a sampling frequency of 10 kHz. For the proposed FDIs in Papers E and F, the measurements collected during the operation of Profile 1 are for both training and testing. The samples from Profile 2 and Profile 3 are for testing only.

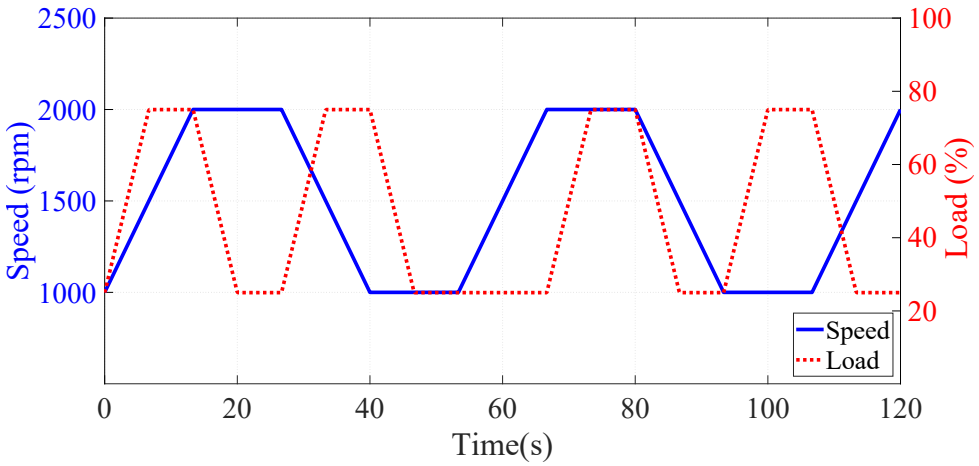

Figure 3.8: Profile 1: variable load and speed

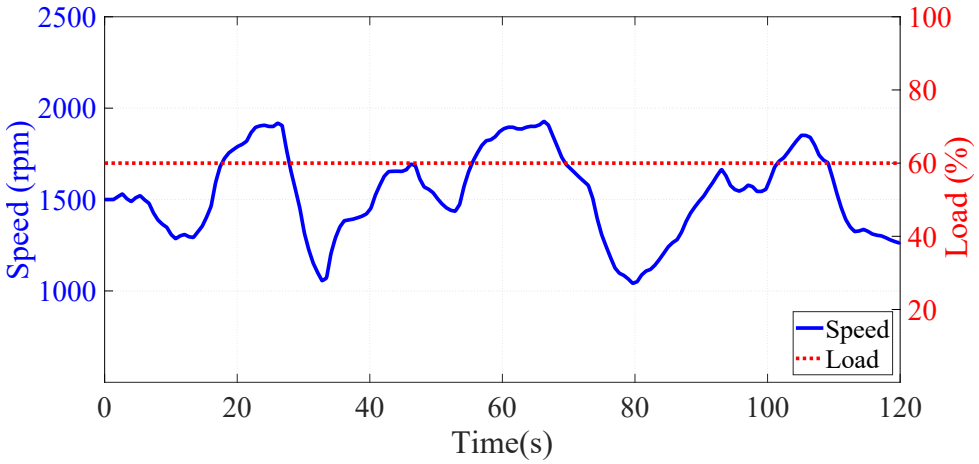

Figure 3.9: Profile 2: constant load and variable speed

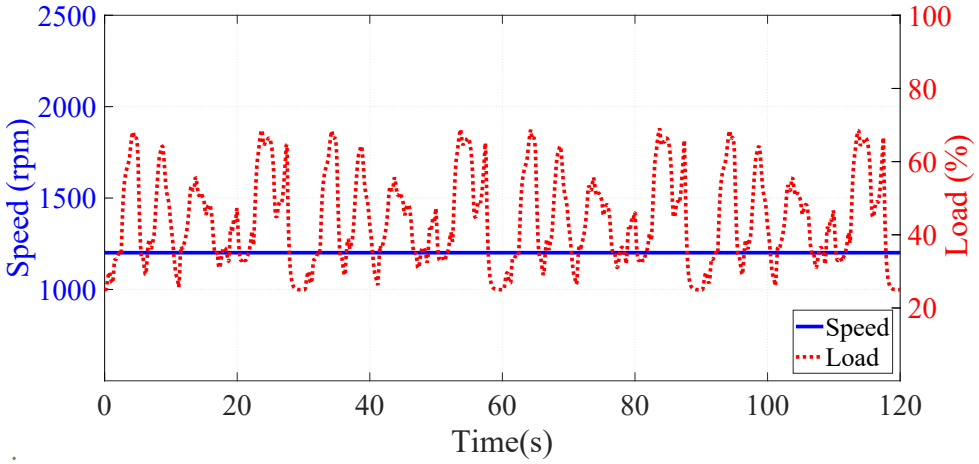

Figure 3.10: Profile 3: variable load and constant speed

Chapter 4

Model-based analysis of faulty PMSM in dynamic operations

Model-based analysis of faulty motors allows for estimating hard-to-measure parameters and development of new fault indicators and FDI schemes. The benefit of these analysis is to save cost by reducing the number of electrical motors required for testing. These analysis needs to be computationally efficient for simulating PMSM with magnetic asymmetries in dynamic operations. Faster models are more desirable, if they provide sufficient accuracy as compared to more computationally heavy models like FEA. This chapter summarises the work in the model-based analysis of faulty PMSM published in Papers A, B and C. Section 4.1 describes the FEA model of the faulty PMSG used for verifying the proposed FDI and PNM. The proposed FDI in Section 4.2 aims to minimise the required number of search coils. Estimated motor speed makes the FDI robust against speed changes. Section 4.3 presents a more computational-efficient PNM of faulty PMSM. It replaces the variable air-gap permeance with variable flux sources for describing rotor revolutions. The geometry in the FEA is updated to simulate a PMSM for the development and verification of the FRM in Section 4.4. The proposed FRM expands upon its utility with a magnet defect library and implements both DF and ITSC in the model description.

4.1 Developed FEA of PMSM for verification

The FEA of PMSM is built with commercial software for multi-physics analysis, COMSOL Multiphysics®. Figure 4.1 plots a quarter of the PMSM geometry, which is based on the design in [83]. The geometry is symmetrical with respect to the horizontal and vertical axis. Two search coils measuring magnetic flux (pink domains) are placed on separate stator teeth located at the top and bottom of the stator. The induced search coil voltages are computed and used for the verification of the FDI scheme proposed in Paper A and the PNM in Paper B. Table 4.1 lists the motor parameters.

Table 4.2 lists the properties of the material used in the model. The stator and rotor (grey) are made of iron. The electric conductivity is 11.2 $\frac{\mathrm{MS}}{\mathrm{m}}$ in the radial direction, but it is 1 $\frac{\mathrm{S}}{\mathrm{m}}$ along the axial direction for mimicking the lamination of the core. The iron is

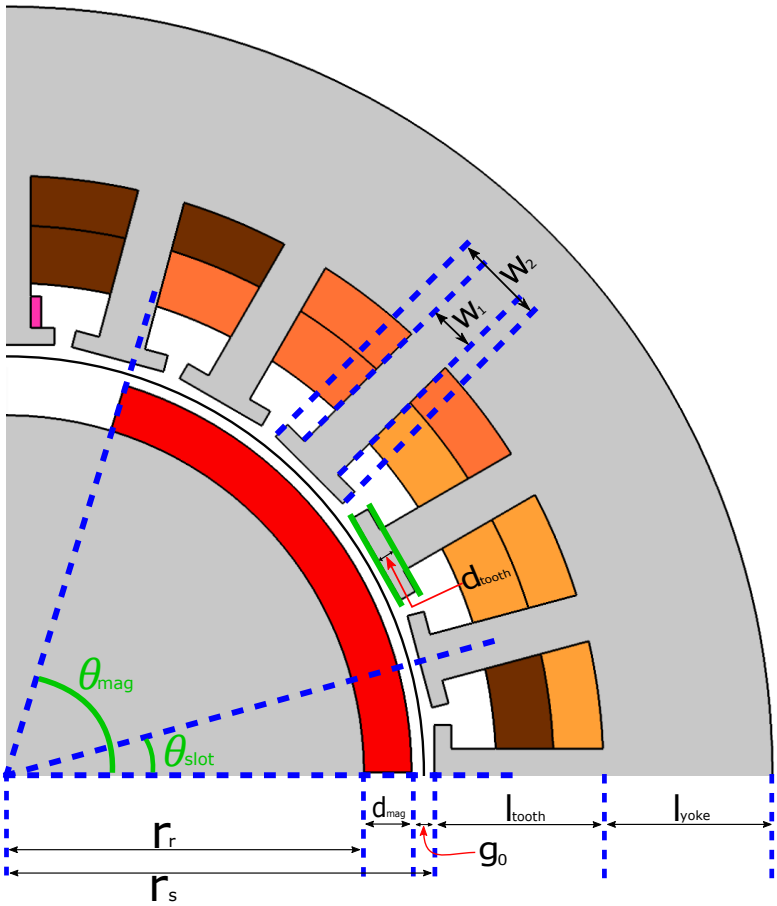

Figure 4.1: A quarter of PMSG geometry

Table 4.1: Parameters of PMSG model in Paper A and Paper B

Symbol	Quantity	Parameter description
p	2	Number of pole pairs
N_s	24	Number of stator slots
N	120	Number of turns per stator slot
d_{mag}	4.5 mm	Magnet thickness
d_{tooth}	5.9 mm	Thickness of stator tooth top
g_0	2.2 mm	Average air-gap distance
L_{rotor}	200 mm	Length of rotor
L_{tooth}	16.2 mm	Length of stator tooth
L_{yoke}	16.1 mm	Thickness of stator yoke
r_r	34.0 mm	Rotor radius
r_s	40.7 mm	Stator inner radius
w_1	4.5 mm	Width of stator tooth 1
w_2	9.0 mm	Width of stator tooth 2
θ_{slot}	15°	Stator slot pitch
θ_{mag}	73.1°	Magnet pitch
B	0.01 $\frac{\text{Nm}}{\frac{\text{rad}}{\text{s}}}$	Viscous friction
J_{Rotor}	0.1 kgm^2	Rotor inertia

Table 4.2: Material properties in the FEA

Material property	Soft Iron	Copper	Air	Unit
Relative permeability	Non linear see Figure 4.2	1	1	-
Relative permittivity	1	1	1	-
Electrical conductivity	11.2	60	0	$\frac{\text{MS}}{\text{m}}$

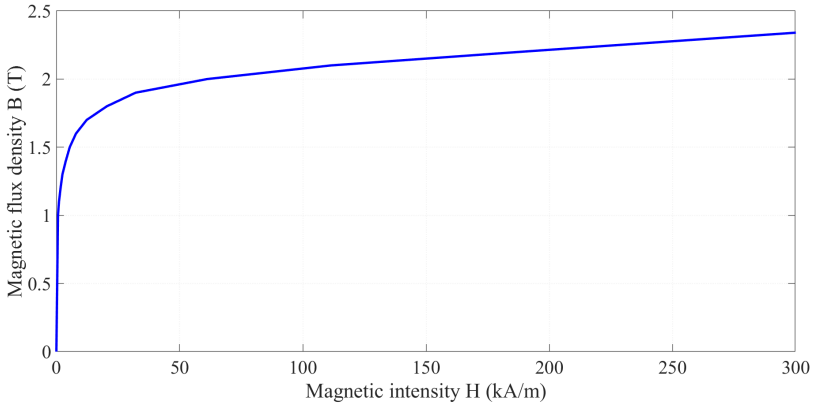

Figure 4.2: BH-curve of the iron core

a non-linear magnetic material, and Figure 4.2 shows its the BH-curve. Properties for copper define the phase windings (yellow, orange and brown) and the search coils (pink). The air domains are coloured in white, while the North pole domains is in red (South pole is not included in Figure 4.1. The linear model defines the magnets.

$$\mathbf{B} = \mu_0 \mu_{\text{rec}} \mathbf{H} + \mathbf{B}_{\text{r}} \tag{4.1}$$

where field of $\boldsymbol{B_r}$ points radial outward for North poles and inwards for South poles. It has a magnitude of 0.5 T and a uniform demagnetisation on one pole can be described by reducing the magnitude of $\boldsymbol{B_r}$. The parameter μ_0 is the permeability in vacuum and μ_{rec} is the recoil permeability of the magnet.

The domains related to the rotor are defined as rotating domain, governed by the following equation for a rigid body.

$$\dot{\omega}_m = \frac{\tau_{\text{Load}} - \tau_{\text{ARK}} - B\omega_m}{J_{\text{Rotor}}} \tag{4.2}$$

The motor angular speed ω_m increases due to applied load torque (τ_{Load}) of 10 Nm. A counter torque (τ_{ARK}) from the generator is computed with Arkkio's method [84]. Viscous friction is also included in the model description. The output terminal of the PMSG is Y-connected to a 50 Ω resistor per phase. Static eccentricity (SE) in the FEA model gives the centre of the rotating domain (RD) an offset relative to the geometric centre of the stator (S). The centre of the rotor (R) coincides with RD. On the other hand, the RD coincides with the centre of the stator and not R during dynamic eccentricity (DE). Figure 4.3 shows an exaggerated sketch illustrating the difference between the eccentricities. RD will coincide with neither the stator nor rotor axis during mixed eccentricity (ME), which is a mix of SE and DE.

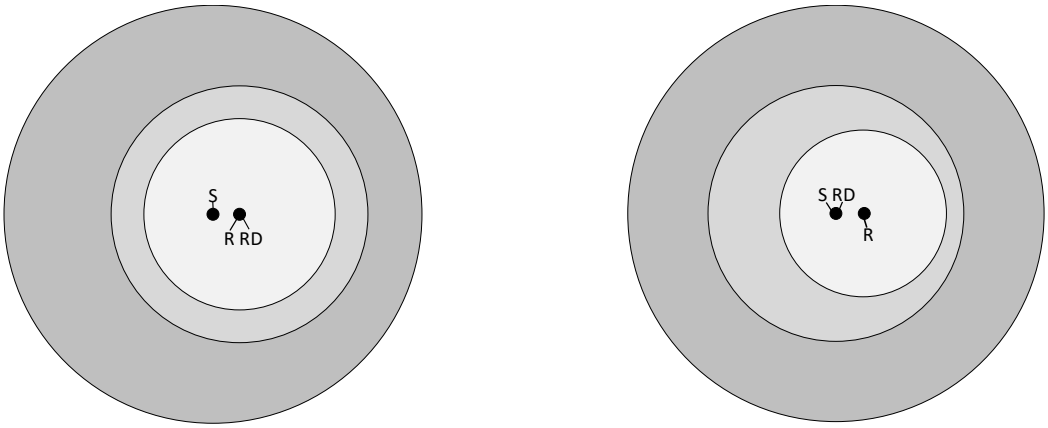

(a) (b)

Figure 4.3: Sketch of (a) static eccentricity and (b) dynamic eccentricity

4.2 Proposed FDI with reduced number of search coils

Da et. al. [19] proposed a fault diagnosis scheme with 12 search coils placed with equal angular distance in the stator. The magnitude of induced search coil voltages is presented in a polar plot. Different shapes in the polar plot represent different fault signatures. An FDI with only two search coils for detecting magnetic asymmetries like DF, SE and DE, is presented in Paper A. It is built on similar principles from Da et. al. [19], but fewer search coils will reduce the effort required for implementation. The FDI detects a fault if the square of the voltage difference between the search coils is greater than a threshold δ.

$$F_{\text{Det}} = (V_{C1} - V_{C2})^2 > \delta \tag{4.3}$$

The induced voltages in the strategically placed search coil will ideally be identical. The fault detection criterion is δ, which reduces the false positive rate due to noise. The work of Da et. al. [19] produced polar plots for different faults, e.g. eccentricity, short circuits, and DF. In a healthy case, the polar plot will be a perfect circle. In the case of eccentricity, the "circle" will be off centre. This offset will stay fixed in the case of SE or orbit around the geometric motor center axis in the case of DE. Uniform DF on one pole will cut off a part of the polar plot circle in the region of the demagnetised magnet. The shape will also rotate at the same speed as the motor. The proposed method aims to reduce the number of search coils, assuming that the envelope of the search coil voltage reflects the varying radius in the polar plot. Different faults produce different shapes on the envelope. The second assumption FDI scheme is to define shape in the polar plot with the equation for an ellipse.

$$F_{\text{Class}} = A\cos\left(2\omega(t)t + \phi\right) + B\cos\left(\omega(t)t + \phi\right) + h(t) \tag{4.4}$$

where ϕ is the phase shift and $h(t)$ is the remainder after the first and second harmonics are removed from the envelope function. Ideally, it is the local time average of the envelope and will be constant when the PMSG runs at constant speed. h(t) is propositional to the motor speed ($\frac{\omega(t)}{2}$ for a four-pole), if the PMSM operates in a non-saturated state. The fitting parameters for A and B were obtained in an optimisation problem, in which the

square error between the envelop and F_{Class} in (4.4) is minimised. Figure 4.4 shows the flowchart of the proposed FDI.

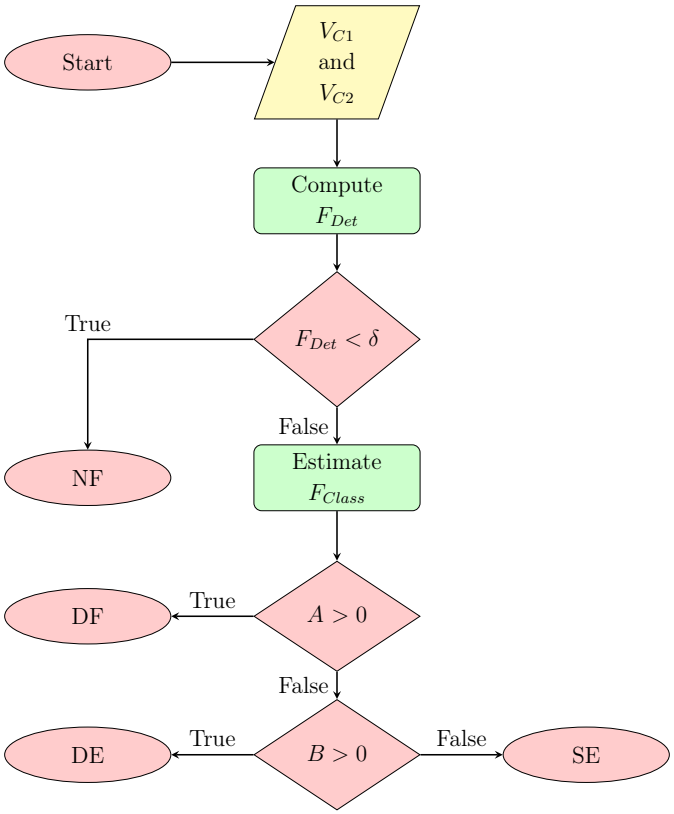

Figure 4.4: Flowchart of the proposed FDI

4.2.1 Verification of FDI with FEA

The FEA model in Section 4.1 is used for verifying the proposed method in Figure 4.4 (Paper A). Uniform demagnetisation over a single North pole is described by reducing its B_{r} from 0.5 T to 0.4 T. The FEA describes SE and DE with severity of 23.0 %. The PMSG is analysed with a prime mover torque of 10 Nm. Simulating 10 seconds in FEA takes 10 hours of computation time. Figures 4.5 and 4.6 show an absolute value of the induced search voltage with envelope in healthy case, SE, DE and DF.

In the healthy case and SE, the first (B) and second (A) harmonics of the envelope are negligible. A SE can still be detected if the static offset is towards either search coil because F_{Det} is no longer 0 and may exceed the set threshold δ. However, a SE has not been detected if the offset is perpendicular to the search coils. The distance between the rotor and search coils is equal, and the induced voltages have equal amplitudes.

A single search coil may suffice for classifying DE and DF. Table 4.3 shows the amplitude of the first and second harmonic of the envelope. The signature of a DE in a polar plot is a circle with an offset revolving around the origin [19]. This is reflected in amplitude modulation of the induced voltage. The envelope will have a first harmonic. Partial DF of a rotor pole cuts one side of the polar plots, which can be approximated as an ellipse with an offset. The envelope has the first and second harmonics as reported in

Table 4.3. The amplitudes A and B are estimated from (4.4) with an optimisation problem. It is dependent on the speed of the motor, which is measured by position sensors in a PMSG or PMSM drive setup.

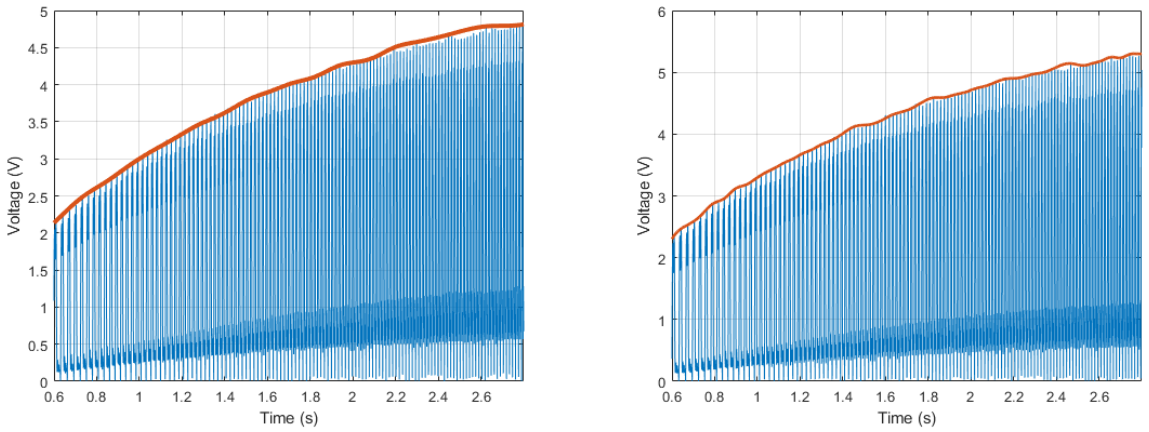

(a) (b)

Figure 4.5: Induced search coil with envelope in case of (a) no-fault and (b) SE

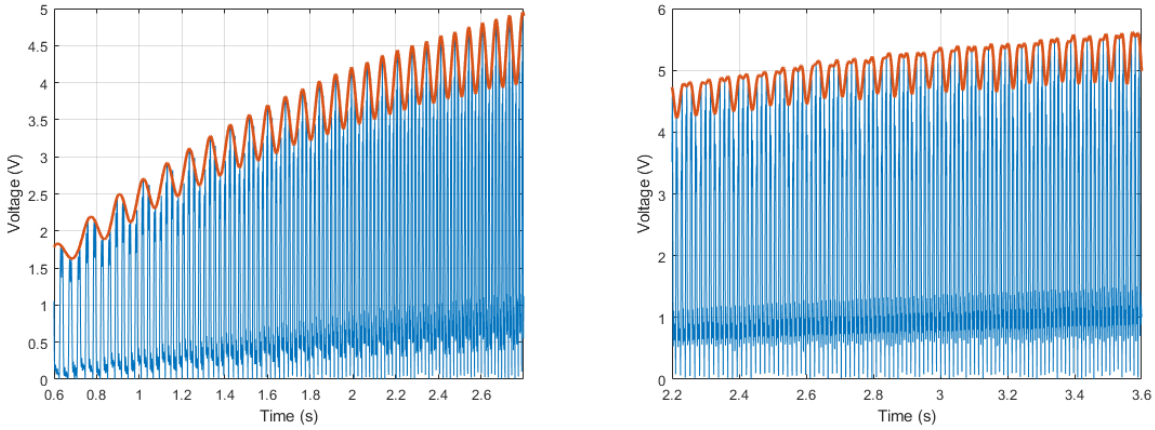

(a) (b)

Figure 4.6: Induced search coil with envelope in case of (a) DE and (b) DF

Table 4.3: Estimated amplitude of harmonics in the enveloped curve

Type of fault	A	B
NF	0.0	0.0
SE	0.0	0.0
DE	0.02	0.33
DF	0.11	0.25

4.3 PNM with variable flux sources

MEC has a similar description like an EEC, but magnetic flux, magnetic motive force (MMF), and reluctance respectively replace current, voltage, and resistance. The permeance matrix $\mathcal{P}$ in PNM is the magnetic equivalent to the admittance matrix. It is the matrix form of the node method derived from Kirchhoff's current law.

$$\boldsymbol{P}\boldsymbol{F}_{\boldsymbol{m}} = \boldsymbol{\Phi}_{\boldsymbol{s}}, \tag{4.5}$$

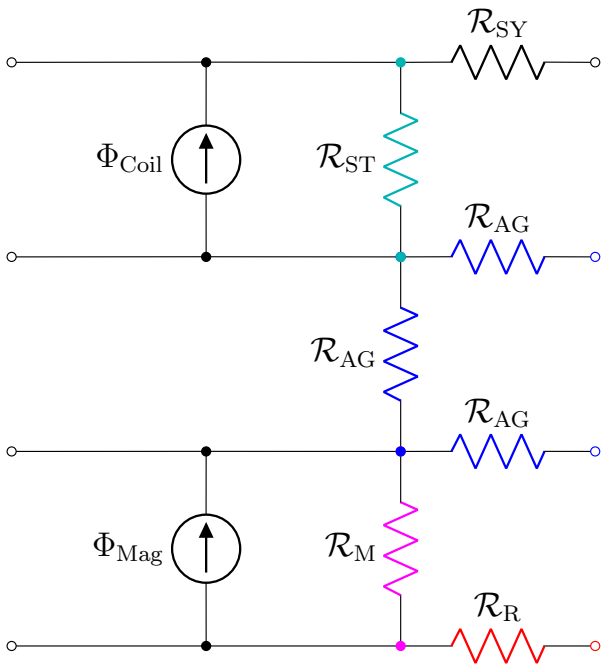

Figure 4.7: Unit equivalent circuit of PNM

The n$^{\mathrm{th}}$ diagonal entry is the sum of reciprocal of all the reluctances connected to the n^{th} node. The rest of the entries is the negative of the reciprocal of the reluctance connected between the two nodes. The enumeration represents the row and column number in $\mathcal{P}$. For example, the entry in row 1 and column 3 is $\frac{1}{\mathcal{R}_{1,3}}$. It is noted that the $\mathcal{P}$ is symmetrical since $\mathcal{R}_{1,3} = \mathcal{R}_{3,1}$. Normally, a PNM describes rotor revolutions with a variable permanence in the air-gap depending on the rotor position. All nodes in between the rotor and stator domains are then connected. The resulting $\mathcal{P}$ needs to be updated every time step, requiring inverting for computing the magnetic potential in each node. The new approach for describing rotation in a PNM is using variable flux sources.

Figure 4.7 shows the unit block for the MEC described in Paper B. The motor geometry splits into N_s sectors (stator slots). The unit circuits of each sector connect into a chain. The circuit completes when the ends of the chain are connected to make a ring. Figure 4.8 visualises the development of the PNM by redrawing the MEC into a network with an example of three MEC units (PMSM usually have more than three stator slots). The reluctances are highlighted in different colours in Figure 4.7. Each of the rotor reluctances R_{R} connects from one node to the next in the bottom left corner in Figure 4.8. The final

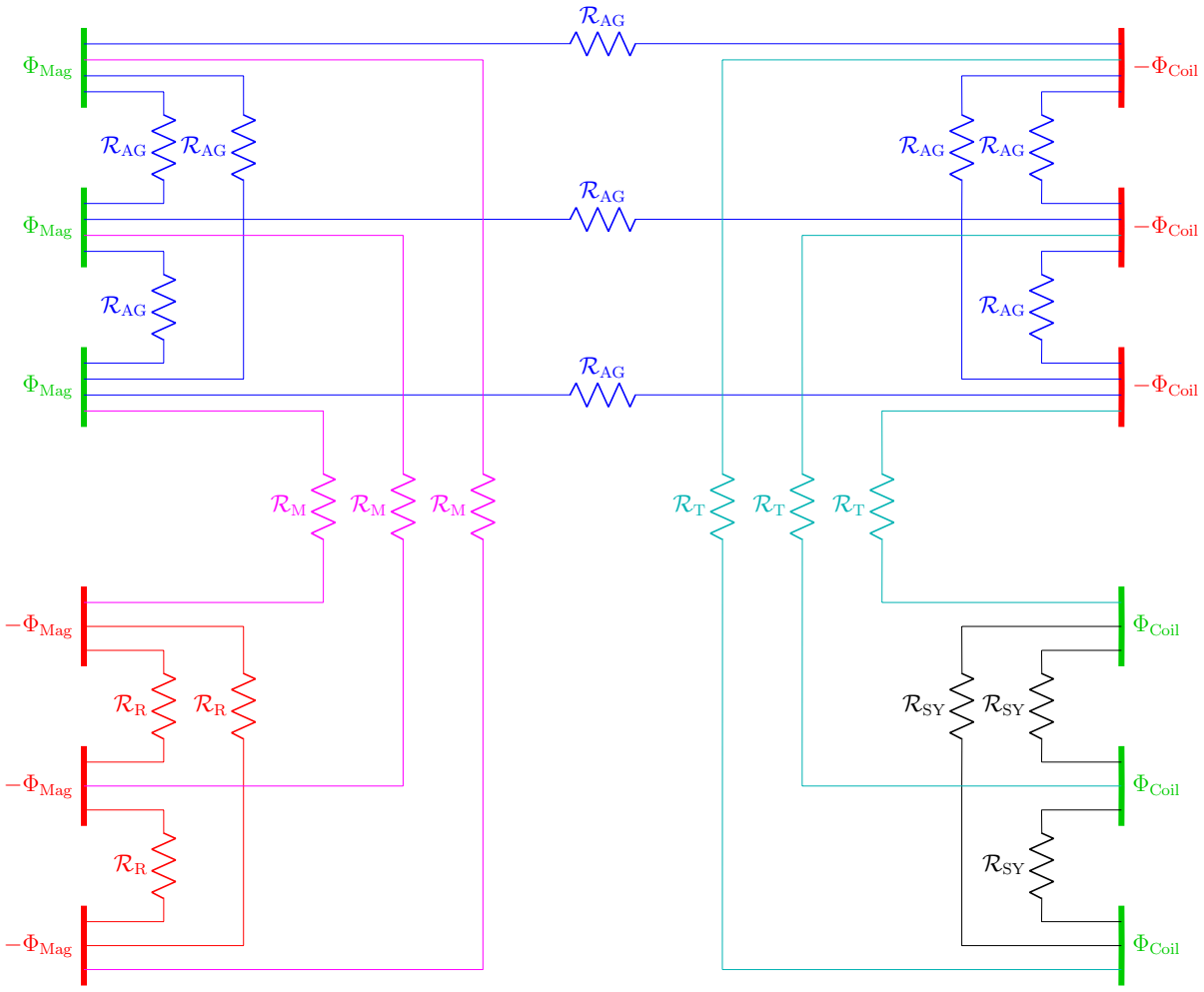

Figure 4.8: Example PNM with three elements redrawn in a network circuit

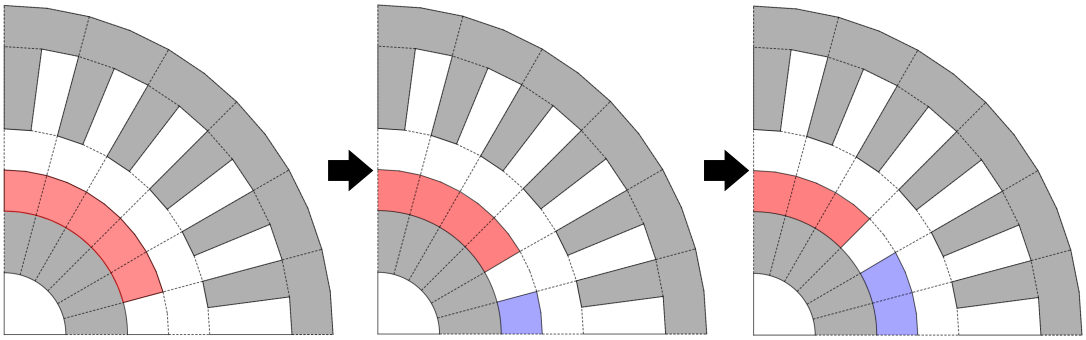

Figure 4.9: Illustration of moving rotor in PNM (counter clockwise)

R_{R} is connected from the last node to the first for completing the circle. There is a similar set-up for reluctances of the air-gap ($\mathcal{R}_{\mathrm{AG}}$) and stator yoke ($\mathcal{R}_{\mathrm{SY}}$).

The proposed PNM requires a N_s connection between the rotor and stator. A PNM describing rotor revolution with variable permeance needs N_s^2 connection across the air-gap. However, the proposed method makes the flux sources, representing the magnets vary when the motor is running. First, the function of the flux contribution from the magnets is defined for the initial position of the PMSM with no current excitation in the stator winding. The function is obtained from static FEA. This function is phase-shifted with respect to the rotor position. Figure 4.9 illustrates the principle, and the red and blue domains represent the North and South poles, respectively.

4.3.1 Verification of the proposed PNM with FEA

The proposed PNM is verified with the FEA described in Section 4.1. Figure 4.10 shows the polar plot of the magnetic flux density in the air-gap. The motor stands still with no current in the phase windings. The polar plots show the case of no demagnetisation in blue and complete demagnetisation on one North pole in red. The PNM captures the shape of the polar plot produced by the FEA. However, the mesh of the PNM model is too coarse to capture the finer details caused by the slotting effect. The magnetic field in the region of the demagnetised magnet has decreased, while the opposite has increased. In the setting of MEC, the flux sources at the demagnetised magnet are set to 0 Wb, but the remaining flux source is unchanged. Less magnetic flux flowing in the magnetic circuit explains why the magnitude of the air-gap magnetic flux over the remaining magnet (South poles) has decreased.

The second comparison between proposed PNM and time-stepping FEA is studied when the PMSG runs at 1300 rpm with a resistive load. The simulation studies compare the PMSG with no-fault and partial DF. The DF case is defined as one North pole losing 20 % of its original strength, i.e. decreasing B_{r} from 0.5 T to 0.4 T. The results from the PNM match well those from the FEA, showing the overall shape of the magnetic flux density in a stator tooth. The proposed PNM can compute ten seconds of simulated time in less than one second. Using FEA takes several minutes but provides more information. However, the PNM is sufficient if the average magnetic flux density in a stator is the parameter of interest.

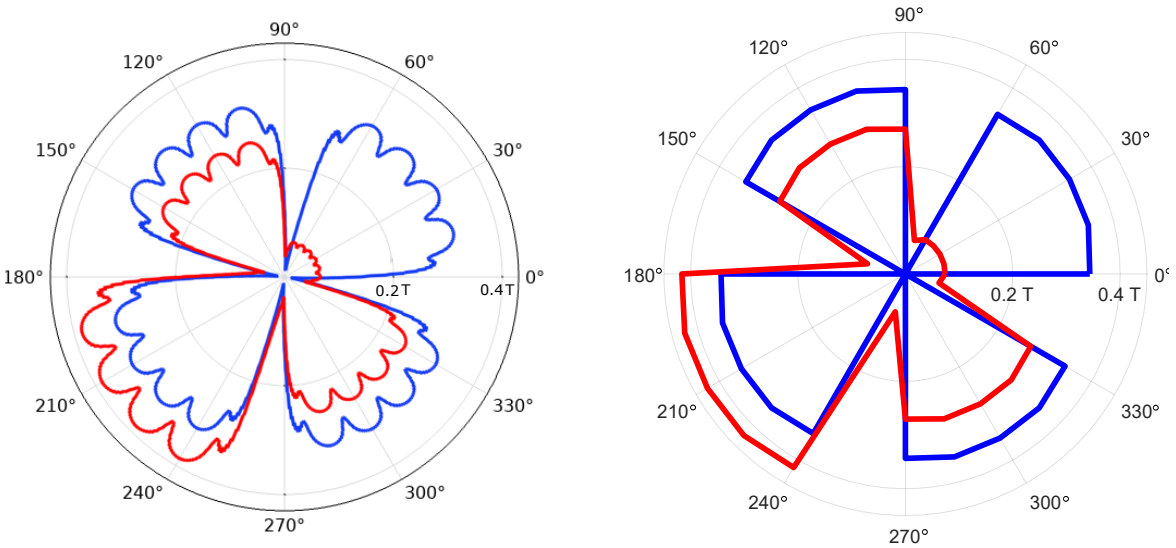

(a) (b)

Figure 4.10: Polar plot of the air-gap in stationary condition with no current from (a) FEA and (b) PNM

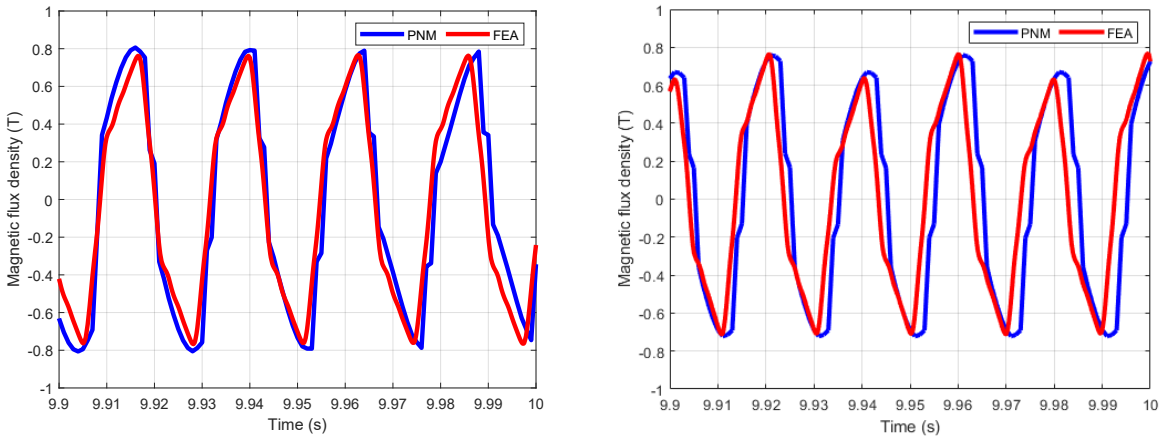

(a) (b)

Figure 4.11: Magnetic flux computed by FEA or PNM in a stator tooth for (a) healthy case and (b) one demagnetised magnet

4.4 Proposed FRM with magnet defect library

The FRM technique recreates the air-gap magnetic flux density by superimposing and phase-shifting the radial and tangential components of magnetic flux density exported from the static FEA. The conventional FRM for electrical machines has proved its main strength with efficient computations of magnetic fields and forces in healthy or faulty PMSM in steady-state [20], [35]. This model-based study aims to develop a magnet library of different magnet defects and include ITSC in the FRM framework. The developed FRM simulates a combined fault between ITSC and magnet defect in a PMSM in a transient state. FRM recreates the air-gap magnetic flux density based on superimposing and phase-shifting the contribution by magnets and stator windings. The basis functions are exported from static FEAs, and their normal (radial) and tangential components are written as:

$$\begin{aligned} B_N(\theta+\theta_m, I(t)) &= B_{nPM}(\theta+\theta_m) + B_{nS}(\theta, I(t)) \\ B_T(\theta+\theta_m, I(t)) &= B_{tPM}(\theta+\theta_m) + B_{tS}(\theta, I(t)) \end{aligned} \tag{4.6}$$

The air-gap magnetic flux density composes of the contribution from the PM and phase windings. A library containing the basis functions of magnets with different defects is developed in Paper C. The magnet library allows for the fast generation of new rotor basis functions with superposition and phase-shift. Flowchart in Figure 4.12 illustrates the developed FRM. Each magnet basis function (B_{nPM} and B_{tPM}) is computed in static FEA. The construction of $B_{nS}(\theta, I(t))$ and $B_{tS}(\theta, I(t))$ follows a similar procedure where a unit basis function. They are computed with an excitation current, e.g. 10 A (DC), and then used for recreating the basis function for phase A. However, this depends on the winding configuration. A second option is to include all windings for a phase in the static FEA. The other two phases are obtained by phase-shifting the basis function with 120° and 240°.

The basis function for the shorted windings is subtracted from the phase where the ITSC is located. The magnitude of the magnetic field contribution in the air-gap from the phase windings is proportional to its respective phase currents and the shorted windings are proportional to the fault current. All stator basis functions are normalised with respect to the excitation current used in the static FEA (10 A). The EEC part of the FRM is defined with the following equations [85]

$$\begin{bmatrix} v_a \\ v_b \\ v_c \\ 0 \end{bmatrix} = \mathbf{R} \begin{bmatrix} i_a \\ i_b \\ i_c \\ i_F \end{bmatrix} + \mathbf{L}\frac{d}{dt} \begin{bmatrix} i_a \\ i_b \\ i_c \\ i_F \end{bmatrix} + \begin{bmatrix} e_a \\ e_b \\ e_c \\ -e_F \end{bmatrix} \tag{4.7}$$

where $\mathbf{R}$ and $\mathbf{L}$ are the resistance and inductance matrices as:

$$\mathbf{R} = \begin{bmatrix} R_S & 0 & 0 & -\mu R_S \\ 0 & R_S & 0 & 0 \\ 0 & 0 & R_S & 0 \\ -\mu R_S & 0 & 0 & R_F + \mu R_S \end{bmatrix} \tag{4.8}$$

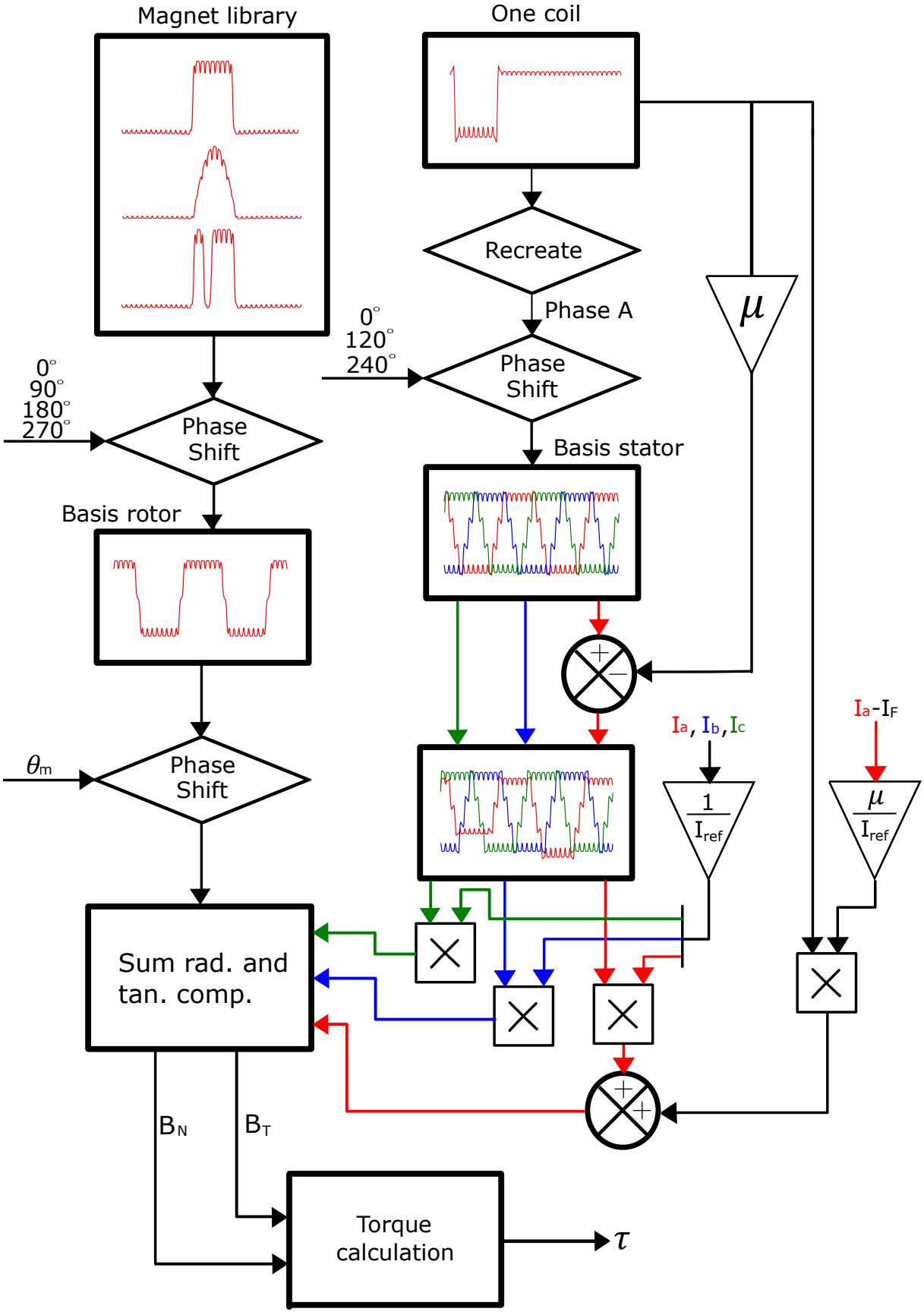

Figure 4.12: Flowchart of proposed FRM

and

$$\mathbf{L} = \begin{bmatrix} L_S & M_S & M_S & -\mu(1-\mu)L_S \\ M_S & L_S & M_S & -\mu M_S \\ M_S & M_S & L_S & -\mu M_S \\ -\mu L_S & -\mu M_S & -\mu M_s & \mu^2 L_S \end{bmatrix} \tag{4.9}$$

The FEA is crucial for the development of accurate FRM. The model geometry is based on the PMSM, "IE5-PS2R 90 L", from the in-house test bench. Figure 4.13 plots a quarter of the model geometry, but the whole geometry is needed to simulate the magnetic asymmetries. Table 4.4 lists key parameters of the PMSM. The FEA uses the material properties in Table 4.2.

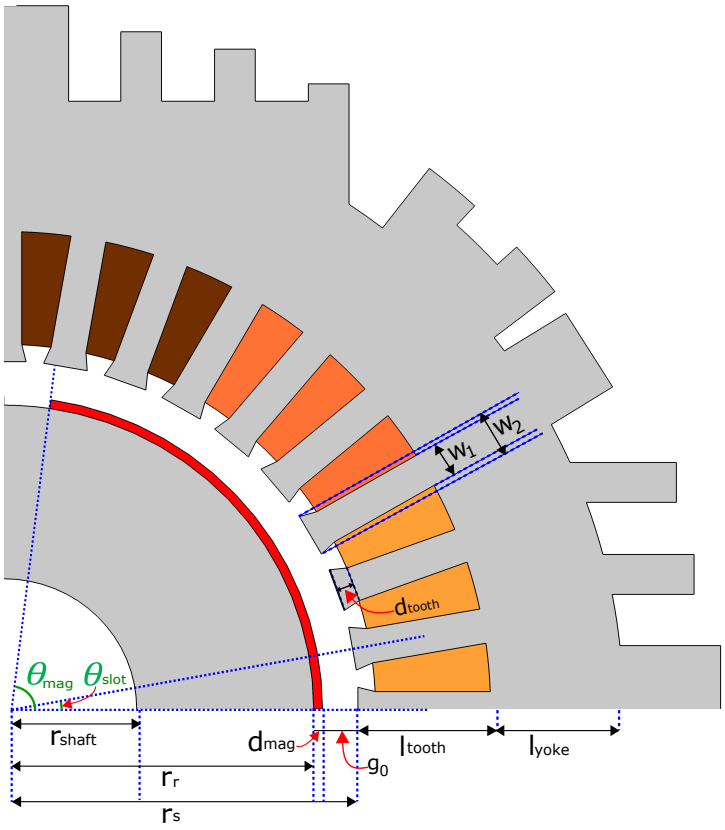

Figure 4.13: Geometry of the PMSM studied in Paper C

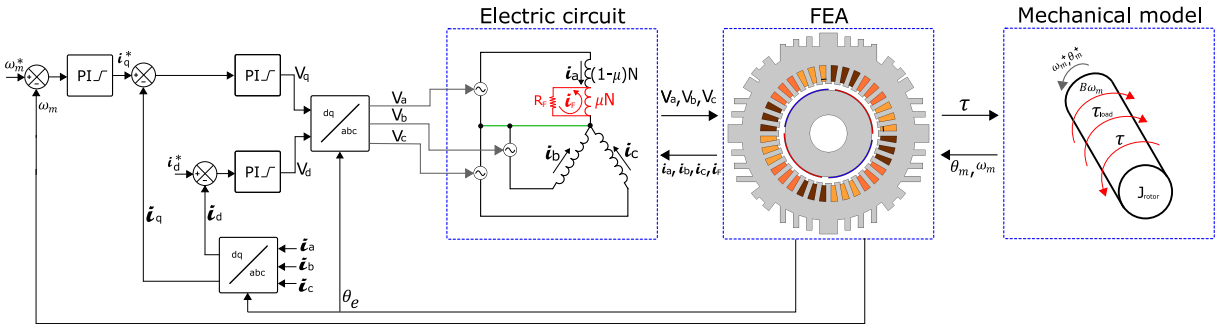

Figure 4.14: Block diagram of PMSM model system

Figure 4.14 shows the overall structure of the simulated PMSM with the integration of the field-oriented controllers and descriptions of the electrical and mechanical systems. The FRM description of the system is obtained by replacing the FEA part with its mathematical description.

Table 4.4: Geometric dimensions and parameters of the in-house motor

Symbol	Quantity	Parameter description
p	2	Number of pole pairs
N_s	36	Number of stator slots
N	80	Number of turns per stator slot
d_{mag}	1 mm	Magnet thickness
d_{tooth}	2 mm	Thickness of stator tooth top
g_0	4.0 mm	Average air-gap distance
L_{rotor}	100 mm	Length of rotor
L_{tooth}	14.5 mm	Length of stator tooth
L_{yoke}	9.1 mm	Thickness of stator yoke
r_{shaft}	15 mm	Rotor inner radius
r_r	35 mm	Rotor outer radius
r_s	40 mm	Stator inner radius
w_1	4 mm	Width of stator tooth 1
w_2	5 mm	Width of stator tooth 2
θ_{slot}	10°	Stator slot pitch
θ_{mag}	80.8°	Magnet pitch
n_{rated}	3000 rpm	Rated speed
k_{BEMF}	90 $\frac{\text{mV}}{\text{rpm}}$	Back EMF constant
R_s	2.1 Ω	Per phase resistance
L_s	36 mH	Self inductance
M_s	18 mH	Mutual inductance

4.4.1 Verification of FRM with FEA

The FRM is verified by comparing the results from the FRM and FEA simulating the PMSM in dynamic operations for 4 s. Table 4.5 lists the computation time of both models. The FEA has a computation time, which is three orders of magnitude larger than FRM.

Table 4.5: Computation time comparison between FEA and FRM

Fault condition	FEA	FRM	Ratio
Healthy	50906 s	49.9 s	1020
Missing magnet piece	54924 s	52.2 s	1052
ITSC (8 turns)	54877 s	49.3 s	1096
ITSC (72 turns)	55692 s	50.8 s	1080
Missing magnet piece and ITSC (8 turns)	64165 s	48.9 s	1312
Missing magnet piece and ITSC (72 turns)	64995 s	49.0 s	1326

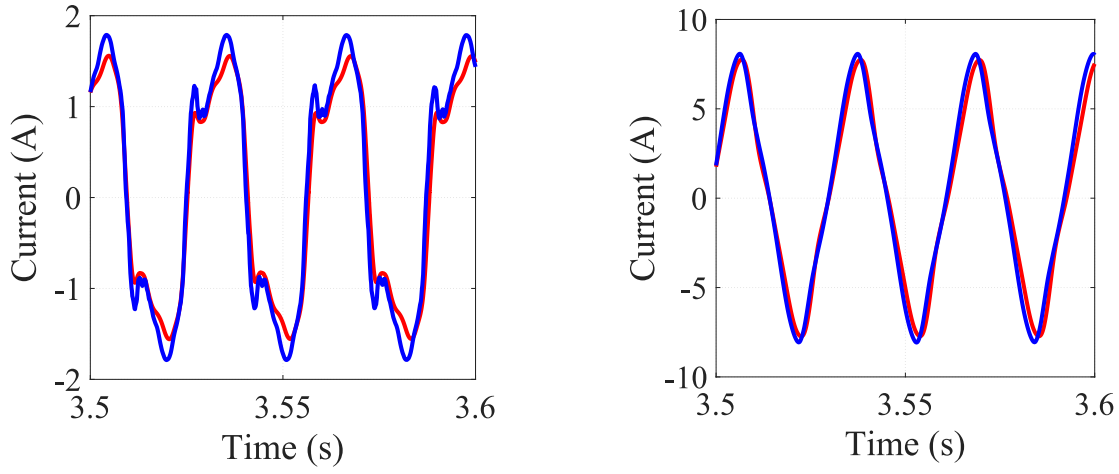

(a) (b)

Figure 4.15: Short circuit current with FEA (red) and FRM (blue) under different ITSC severities (a) 1.7 % and (b) 15 %

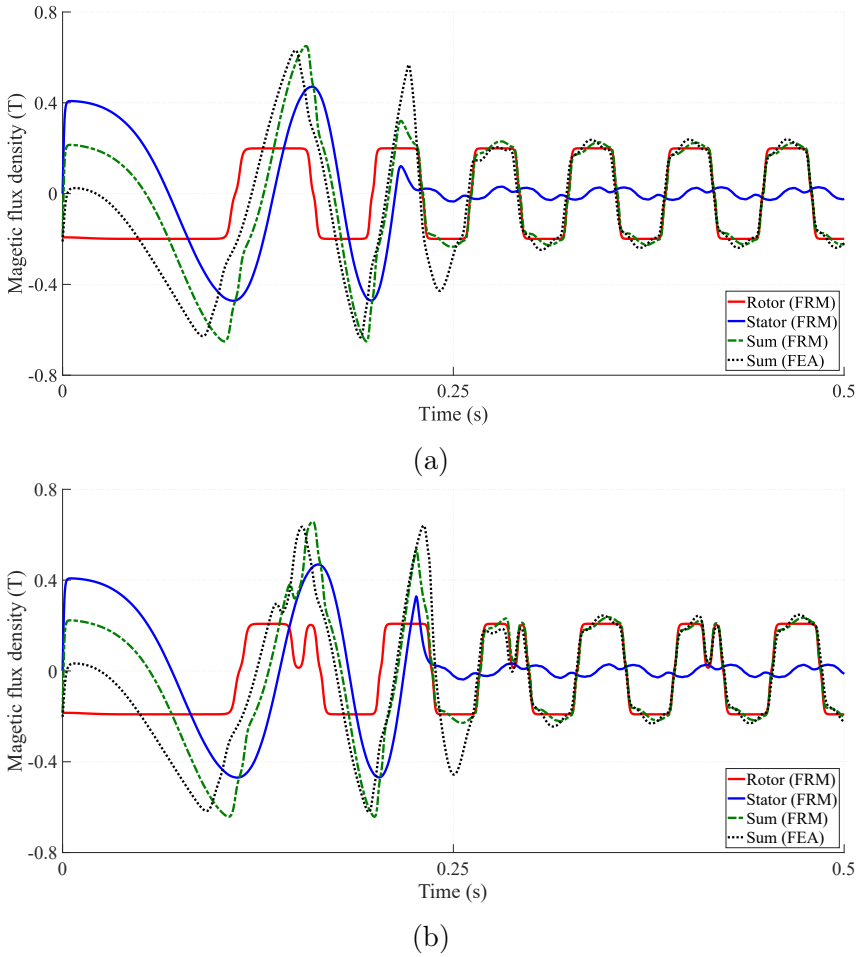

(a)

(b)

Figure 4.16: Decoupled contributions to the air-gap magnetic flux density in the (a) healthy case and (b) in case of missing a piece of one magnet

Figure 4.15 shows the current in the short circuit resistor computed with FEA and FRM for two different levels of the short circuit. They have similar waveforms, proving that the FRM can produce a similar result to FEA for a range of short circuit severity. Figure 4.16 shows the decoupling of magnetic flux densities recorded at a single point in the air-gap during the acceleration of the simulated PMSM. The rotor and stator contribution can easily separate in the FRM as compared to the FEA. This opportunity will allow the FRM to be used in inverse problems to diagnose magnet defects and their severity. The transient responses at the beginning have some deviations between the models, but they become similar in steady-state. This is probably due to the linear assumption in the FRM, which is not applied to the FEA.

4.4.2 Experimental validation of FRM

The FRM is validated with the current measurement extracted from the in-house test-bench. One fault signature for ITSC is an increase of the second harmonic of the extended Park's vector approach (EPVA) [86]. Stator currents are extracted from the proposed FRM and used to compute the Park's vector. The magnitude of the Park's vector, $|I_P|$, is used in time-frequency analysis and is defined as

$$|I_P| = \sqrt{I_\alpha^2 + I_\beta^2} \tag{4.10}$$

where I_α and I_β are the components of the current after the Clark transformation. The spectrograms of the I_P in cases of 0 % and 6 % at nominal speed (3000 rpm) are presented in Figure 4.17. The results from the FRM show a 4.4 dB higher peak of the second harmonic for the faulty PMSM than the healthy PMSM. This is shown in the measurement where the second harmonic increases by 3.2 dB. It is noted that the obtained result by FRM has a lower noise level than the experimental data but does show the general trend of the chosen fault indicator [86].

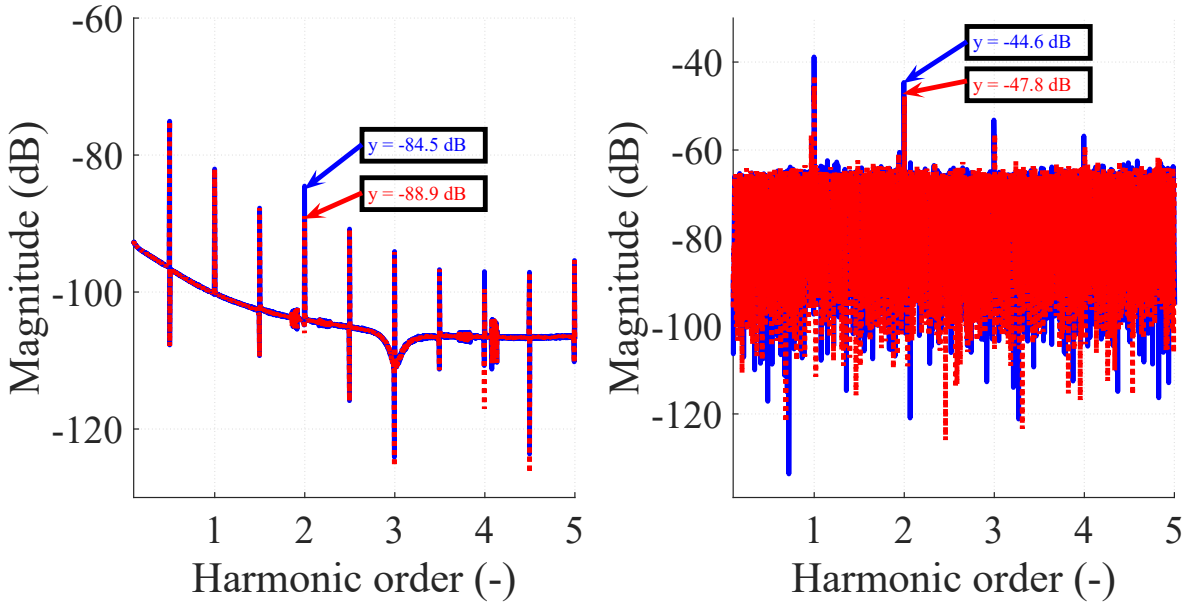

Figure 4.17: Spectrograms of I_P obtained from FRM (left) and experiment (right)

4.5 Summary

This chapter summarises the work done with the model-based approach for analysing faulty PMSM in dynamic conditions. An FDI scheme developed to to minimise the number of required installed search coils for detecting and identifying magnetic asymmetries is presented. The FDI identifies different fault signatures for DF, SE and DE and works with variable frequency, but requires information of the rotor positions. A more computational efficient PNM replacing variable air-gap permeance with variable flux sources is also presented. This eliminates the need to invert the permanence matrix in every time step due to rotor revolutions. The permeance matrix does not need to describe rotor revolution, making it easier to describe changes in the air-gap over time, e.g. DE. Section 4.4 presents a library of magnet basis functions. New combinations of magnets can combine to make a new rotor basis function without the need to compute in static FEA. The FRM is verified with FEA and validated with experimental results. Further, it allows for an easy decomposition of air-gap magnetic flux based on the contribution of the rotor and stator. This feature can be implemented in an inverse problem to diagnose DF and its severity. Finally, the proposed FRM can simulate a MF case with both ITSC and DF.

Chapter 5

Reducing computational burden for quadratic time-frequency distribution

Condition monitoring for electrical machines in dynamic operation requires the analysis of non-stationary signals. The conventional method of STFT applies the Fourier transform for a finite window. Its weakness is the relation between resolution and window size. A small window gives high time resolution but low frequency resolution, and vice versa for a large window size. The time resolution of the QTFD is not affected by the window size. This chapter summarises the work in Paper D, which presents a more computationally efficient method for computing QTFD. The proposed algorithm in Section 5.1 is verified on predefined multicomponent signals with variable frequencies and the effectiveness of the algorithm is tested on measurement from a PMSM setup with ITSC and variable speed conditions.

5.1 Proposed QTFD

Figure 5.1 illustrates the proposed implementation of QTFD for longer-lasting signals. The main principle is to implement QTFD in a similar approach as the STFT. Its signal is split into smaller intervals. In contrast to STFT, the window size has little effect on the time resolution of the spectrogram produced with QTFD. This spectrogram is noisy at the beginning and end. These parts are removed in each the input sample, which are overlapping. The output of each step is combined in a final spectrogram. The step by step of the algorithm is:

1. Extract a sample from the original array from entry n_1 to n_2. The initial values of n_1 and n_2 are 1 and f_sT (product of sampling frequency and time window)
2. Compute the QTFD with (5.5) for the sample
3. Cut off the first 20 % and last 20 % of the spectrogram (overlap)
4. Add the product of the overlap and f_sT to n_1 to n_2 and repeat the process
5. Repeat until end of signal

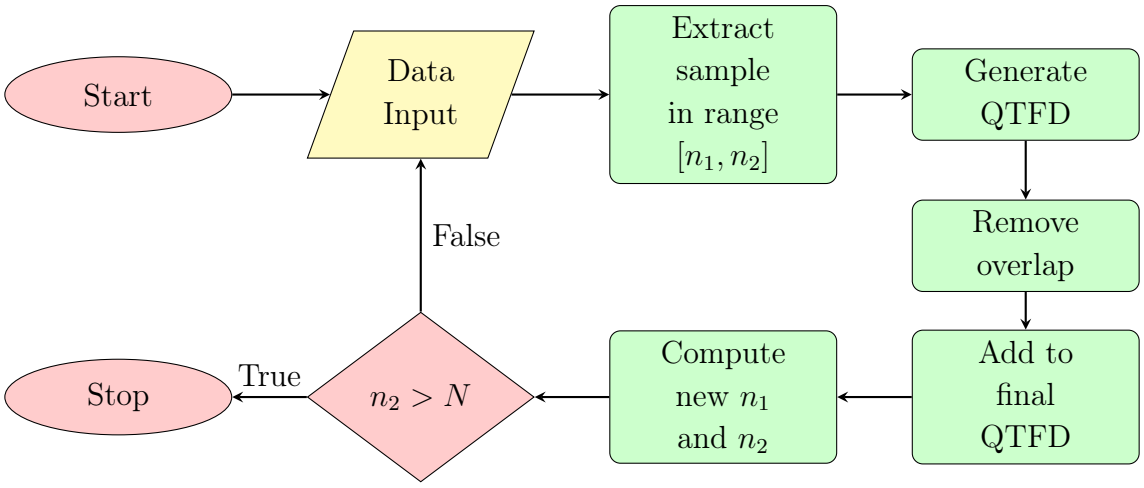

Figure 5.1: Flowchart of the proposed implementation of QTFD

QTFD is often called Cohen's class function in honour of Leon Cohen [52], who derived the generalised form to this family of distribution functions:

$$C(t,\omega) = \frac{1}{2\pi}\int_{-\infty}^{\infty}\int_{-\infty}^{\infty} A(\theta,\tau)\phi(\theta,\tau)e^{-j\theta t - j\tau\omega}d\theta d\tau, \tag{5.1}$$

where $A(\theta,\tau)$ is the ambiguity function, which is obtained by transforming the auto-correlation function into the ambiguity domain.

$$A(\theta,\tau) = \frac{1}{2\pi}\int_{-\infty}^{\infty} R(t,\tau)e^{j\theta t}dt \tag{5.2}$$

θ-domain refers to a frequency domain where the filtering by the kernel function is applied. On the other hand, ω is the frequency domain of the final QTFD. The auto-correlation function is defined as the product of the analytic function and its complex conjugate.

$$R(t,\tau) = s^*\left(t - \frac{\tau}{2}\right)s\left(t + \frac{\tau}{2}\right). \tag{5.3}$$

Finally, the analytic function is the Hilbert transform of input measurement. $R(t,\tau)$ is a function of time t and running time τ, resulting in that each time instant of the final QTFD is dependent on past and future events within the time sample.

The Cohen-class distribution may at first be intimidating because it requires solving a triple integral. However, it can be split into two Fourier- and one inverse Fourier transform and can be rewritten into

$$C(t,\omega) = \mathcal{F}_{\tau\to\omega}\mathcal{F}_{\theta\to t}\left(\phi(\theta,\tau)\mathcal{F}^{-1}_{t\to\theta}\left(R(t,\tau)\right)\right) \tag{5.4}$$

The subscript to $\mathcal{F}$ refers to the direction of transformation between the domains. Cohen's class function in discrete form in (5.5) is derived in detail in Paper D.

$$C(n_t,n_\omega) = \mathrm{FFT}_{n_\tau\to n_\omega}\left(\mathrm{FFT}_{n_\theta\to n_t}\left(\phi(n_\theta,n_\tau)\odot\mathrm{FFT}^{-1}_{n_t\to n_\theta}\left(R(n_t,n_\tau)\right)\right)\right) \tag{5.5}$$

The proposed algorithm was first tested on function with variable frequency and no additive noise. Then it was tested on measurement from the PMSM setup in [59].

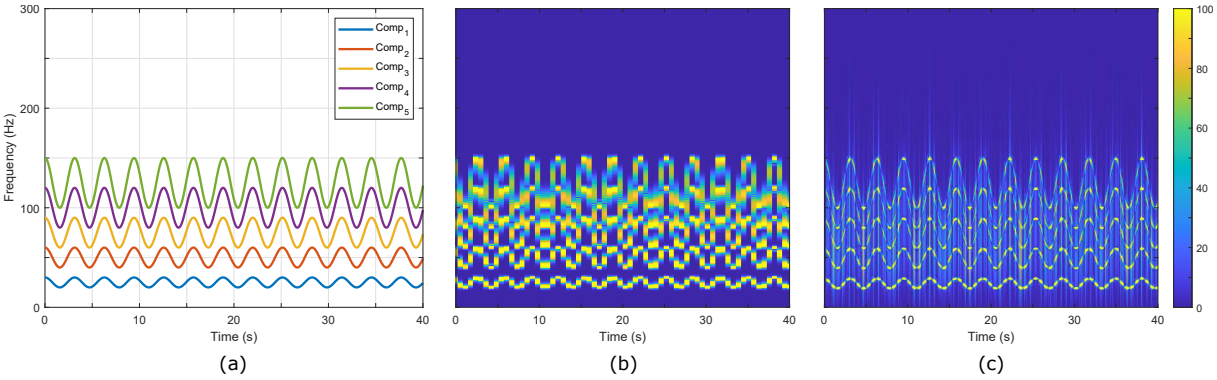

Figure 5.2: Numerical test with (a) instantanouse frequencies of the original signal, (b) spectrogram computed with STFT and (c) spectrogram computed with CWD

5.1.1 Numerical verification of the method

The performance of the proposed algorithm is first verified against the function

$$x(t) = \sum_{k=1}^{5} \sin\left(2\pi k\left(\frac{5}{2}\sin(2t) + 25t\right)\right) \tag{5.6}$$

Figure 5.2(a) shows the frequency component function (5.6), having an amplitude equal to 1. Both STFT and the proposed QTFD have a window size of 1 s and 20 % overlap. The STFT uses a Hanning window, and the proposed QTFD uses the CWD kernel function. Both algorithms capture the waveform of the components, but the separation of the fourth and fifth components, having the largest frequency modulation, becomes blurry for STFT. Changing the time window did not improve the TFD produced by the STFT. The resolution for the proposed is not affected by the change in window size but does greatly affect the computation time. The waveforms in CWD have a smoother shape due to the finer time resolution in the spectrogram.

5.1.2 Experimental validation of the method

Figures 5.3a shows the spectrogram generated by STFT for a phase current of the PMSM in the healthy case. The sampling rate and window sizes are 1 kHz and 1 s, respectively. The Hanning window function is applied to the window with an overlap of 20 %. STFT is used as a benchmark to compare with the spectrograms generated by CWD. Figure 5.3b shows the spectrogram generated from CWD. The harmonic peaks were captured and proved that CWD is capable of capturing harmonic peaks. The fundamental frequency is much more dominant in CWD as compared to the STFT. Element-wise square root balance the size difference between the peaks but makes the spectrogram noisy.

Figure 5.4 shows the spectrograms obtained by STFT and CWD of the phase current for the same PMSM operating under an ITSC. Both STFT and CWD can pick up the third harmonic, which is the indicator for electrical faults. These experimental results prove that CWD can pick up the same harmonic peaks as STFT. The fundamental component is much more dominant in the CWD. The proposed method processes a time-series signal of length 2 minutes (sampling frequency 1 kHz) in less than ten seconds.

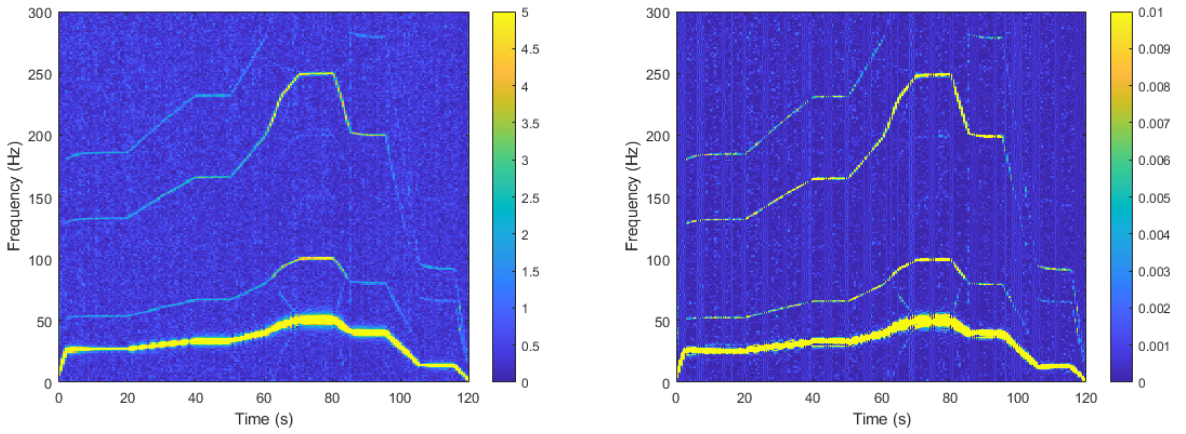

(a) (b)

Figure 5.3: Spectrogram of phase current for healthy PMSM operating at variable speed, (a) STFT and (b) CWD

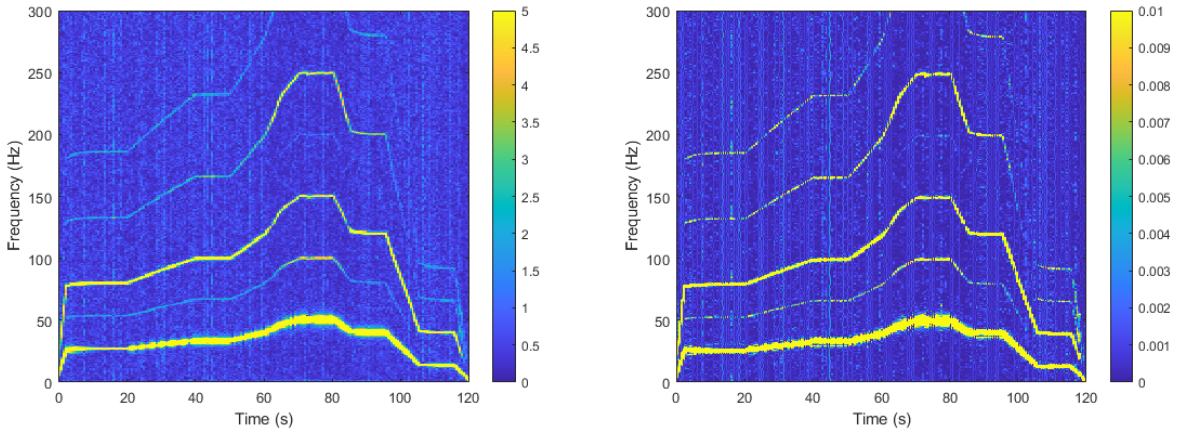

(a) (b)

Figure 5.4: Spectrogram of phase current for PMSM with 10 % ITSC operating at variable speed, (a) STFT and (b) CWD

5.2 Summary

In this chapter, a modified QTFD is presented for implementation in online monitoring. The time resolution of the spectrogram produced with the proposed algorithm seems to be unaffected by the window size. However, the computational burden increases with a larger window, which is a limitation in online applications. The proposed method can process a time-series signal in two minutes (sampling frequency 2 kHz) in less than ten seconds. It does produce smoother components in the spectrogram than STFT, being easier to distinguish. In the experimental test, the proposed method performs on par with STFT but has sharper peaks in the spectrogram.

Chapter 6

Robust data-driven fault diagnosis for sensorless PMSM drives

Both model- and signal-based FDI schemes require accurate information about the monitored motor or system. However, acquiring data on faulty operations is often scarce, resulting in imbalanced datasets. Classifiers trained on datasets with the healthy case in the overwhelming majority will collapse and classify all input samples as a healthy class. A desirable classifier should counter the imbalance dataset problem regardless of operation profile. This chapter presents the two proposed FDIs based on ML and stray flux sensors published in Paper E and Paper F. Both algorithms are trained and tested on PMSM in dynamic operations. The proposed FDI in Section 6.1 aims to classify local DF and ITSC on sensorless PMSM in transient states based on external stray flux and ML classifier. The input signal is order-normalised with the rotor position estimated from one hall sensor with an optimisation problem. Four supervised ML algorithms are tested in a comparison study: EDT, KNN, SVM and FNN. Section 6.2 presents an FDI, aiming to solve the imbalance training datasets problem in an AL framework. The proposed method combines the self-supervised anomaly detector based on a LOF and a DQN classifier. The proposed FDI is trained to classify healthy cases, ITSC, local DF and MF. The robustness of the proposed method is validated experimentally from dynamic operations with ML and imbalanced training datasets measured from the in-house test setup.

6.1 Order tracking with optimisation problem

The data-driven FDI using ML algorithm trained on data from stray flux sensors is presented in Paper E. The diagnosis scheme is suited for sensorless drives robust against dynamic operations. FDI based on stray flux sensors will allow post-installation placed externally on the PMSM. Stray flux has recently gained popularity in literature for fault detection of ITSC, demagnetisation, and mechanical faults due to its sensitivity [5]. Existing research focuses on the model- or signal-based algorithms, requiring multiple stray flux sensors and speed measurements for detecting faults in variable speed conditions. The proposed algorithm is trained and tested on an operation profile with changing load and speed. Two additional profiles are used for testing. Demagnetised magnets are inappro-

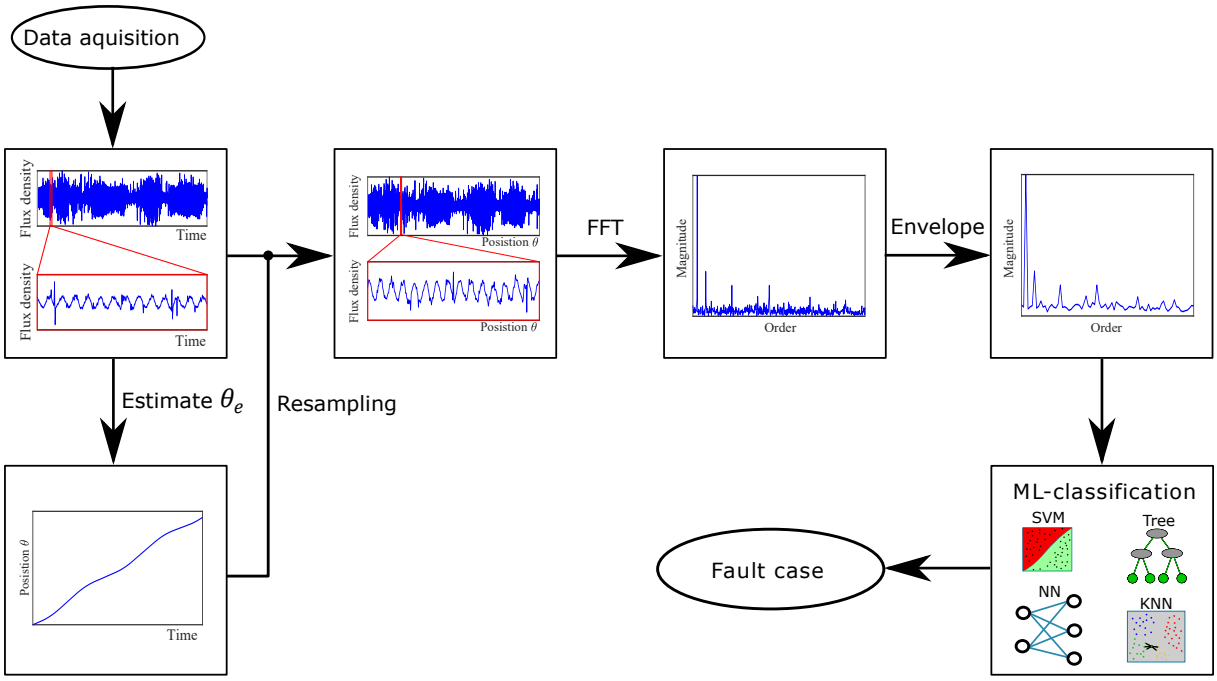

Figure 6.1: Block diagram of preparation of features

priately implemented in the existing research, causing imbalances or damage to magnets. Heat treatment with an electric hob is presented in Paper E for inducing local DF.

The block diagram in Figure 6.1 shows the proposed pre-treatment of the input signal for computing features before passing it on to the ML classifier. Data samples were order-normalised by resampling from a set time step to a fixed angular increment. Rotor position is estimated by splitting the signal into sections before an optimisation problem estimates the fundamental frequency f_1. The objective function is:

$$[f_1, \theta] = \arg\min_{f_1,\theta} \left((x(t) - h(t))^2 \right) \tag{6.1}$$

where h(t) is the assumed function of the fundamental component,

$$h(t) = \sin(2\pi f_1 t + \theta_1). \tag{6.2}$$

The phase angle θ_1 is required for an accurate estimate of f_1. Algorithm 1 describes the process for estimating f_1.

The estimated position dictates the resampling process of the original datasets with linear interpolation. The original signal has a sampling frequency of 10 kHz, whereas the output has 400 samples per rotor revolution. Figure 6.2 visuals the benefit of the resampling process for order-tracking. The first cycle of the chirp function has more samples than the last cycle. Transformation performed by the resampling balances the number of samples per cycle, and the chirp function appears as a sine wave plotted against the rotor position. The signal is split into intervals with a fixed number of rotor revolutions before computing the spectrogram for each window with FFT. Both amplitude and "frequency" of the spectrogram are normalised with the fundamental frequency. Any fault classification approach based on analysing these spectrograms needs to study the composition of

Algorithm 1 Training Algorithm for DQN

Require: One stray flux measurement

while Computing position **do**

Step 1: Extract a small time sample with period T from the original time series data.

Step 2: Compute the objective function for frequencies in the interval $[0, 100]$ Hz with an incremental step of 5 Hz. The optimal ϕ for a given f_1 is found by the Golden Section Search in the interval $[0, 2\pi]$. The values for f_1 and ϕ, that yield the smallest value of (6.1) are the initial guesses in step 3.

Step 3: Find the optimal solution for f_1 and ϕ by the Simplex Search method with the initial guesses given in step 2.

Step 4: Repeat for next time step

end while

the harmonics. The final step of the pre-treatment is to envelop the spectrogram. The spectrogram splits into intervals with a length of a half order centred around the half harmonics [0, 0.5, 1,..., 39, 39.5, 40] to find the maximum in each interval. The resulting envelopes of the spectrograms are chosen as the selected features for classifications. The results prove the effectiveness in the comparative study of the ML algorithms EDT, KNN, SVM and FNN. They are tested on PMSM with no-fault, DF, ITSC or MF operating with changing load and speed.

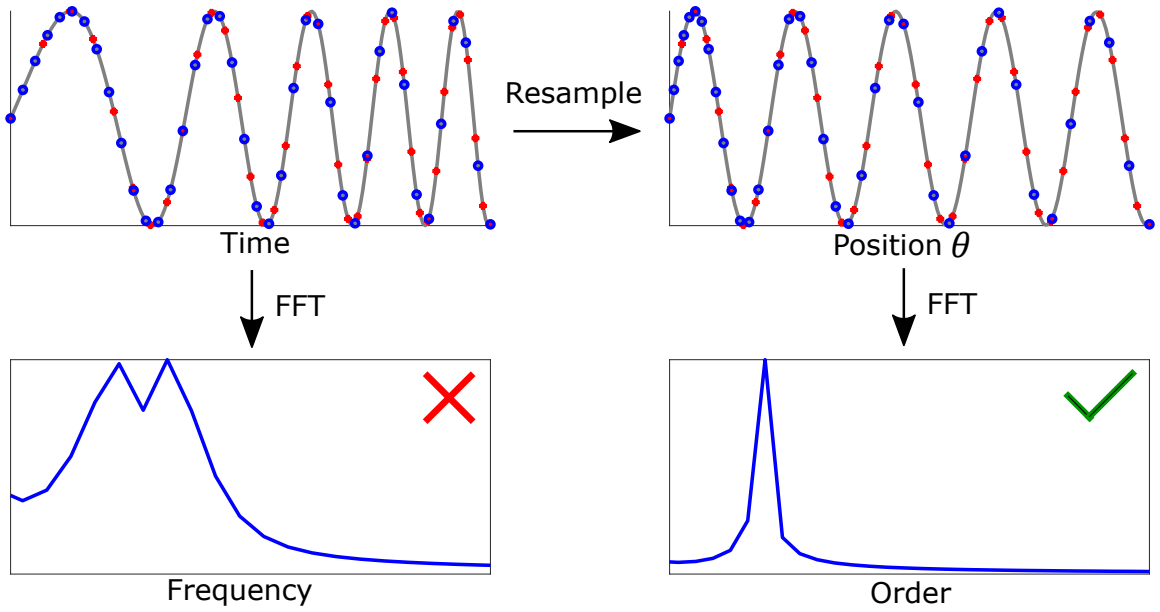

Figure 6.2: Visualising the benefit of the resampling process from time- to θ-domain

6.1.1 Experimental validation of FDI

The performance of the four learning classifiers, EDT, KNN, SVM, and FNN, is investigated with experimental data from the in-house test bench described in Chapter 3. The recorded data of operation Profile 1 with regular changes in speed and load is split into

80 % for training and 20 % for testing. The observation in Profile 1 is shuffled randomly before the split to prevent over-fitting of the classifiers. The algorithms use all samples from Profile 2 and Profile 3 for testing. An average achieved accuracy and training time is obtained by a Monte Carlo analysis, where the algorithm is repeatedly trained and tested 100 times. All the algorithms have a training time of less than 3 s. However, the computation times of EDT and FNN are two orders of magnitude larger than the other KNN and SVM.

Table 6.1: Average classification accuracy (%) for detecting DF, ITSC, and MF

Machine	Operation	DF			ITSC			MF		
Learner	Profile	1 τ	3 I	2 Φ	1 τ	3 I	2 Φ	1 τ	3 I	2 Φ
SVM	1	85.6	82.5	**99.5**	69.6	72.6	**93.9**	58.5	59.4	87.8
	2	76.9	66.1	**99.4**	65.9	53.7	84.7	48.2	38.8	78.7
	3	76.3	64.5	**96.4**	60.6	55.8	81.1	45.2	38.7	73.7
KNN	1	66.2	69.6	**98.2**	63.9	69.7	88.5	50.0	53.5	81.8
	2	58.4	56.2	**98.3**	54.3	50.6	75.2	31.6	30.1	66.1
	3	56.0	60.5	**96.5**	50.7	53.5	80.0	28.2	31.2	69.2
EDT	1	87.4	82.9	**98.5**	70.9	68.2	**91.6**	59.2	57.4	86.3
	2	80.8	61.2	**98.0**	62.3	57.3	78.5	46.6	33.6	71.1
	3	80.8	71.1	**93.7**	64.7	54.4	84.0	48.2	41.1	73.2
FNN	1	85.4	83.5	**99.6**	72.7	75.1	**96.6**	58.5	60.6	89.9
	2	74.1	68.1	**99.9**	58.8	56.0	85.0	42.0	41.2	77.7
	3	71.2	66.5	**97.5**	55.9	56.0	86.3	38.7	39.0	75.4

Table 6.1 reports the average achieved accuracy from all four algorithms. The letters "τ", "I", and "Φ" refer to the use of torque, current, and stray flux signals to compute the features in the training and test data. The numbers in front of the letters refer to how many sensors are included in the computed features.

In the case of single fault case, the ML algorithms are trained and tested on datasets with negative samples (no-fault) and positive samples (fault), in the case of either DF, ITSC with 5 % severity or both (MF). All four algorithms achieve the highest accuracy with stray flux data for detecting DF, while the accuracy for detecting ITSC stays above 80 %. All algorithms reach an average accuracy of over 90 % for detecting DF with stray flux, regardless of the test profile. The accuracy is significantly lower for ML algorithms trained on current or torque data. It ranges between 87.4 % and 56.0 %. The latter has a significant disadvantage since there is only one torque transducer in the test setup. KNN trained on a balanced dataset achieves the lowest accuracy overall. All algorithms have a lower prediction accuracy for ITSC. However, SVM and FNN keep an accuracy above 80 %. The winding configuration of the PMSM with parallel strands makes it harder to detect ITSC compared with single strand phase windings. Shorting 5 % of the turns on one of three strands is less severe since the other two strands in parallel are unaffected. The installed current sensors measure the sum of the three parallel strands, reducing any influence from the shorted turns.

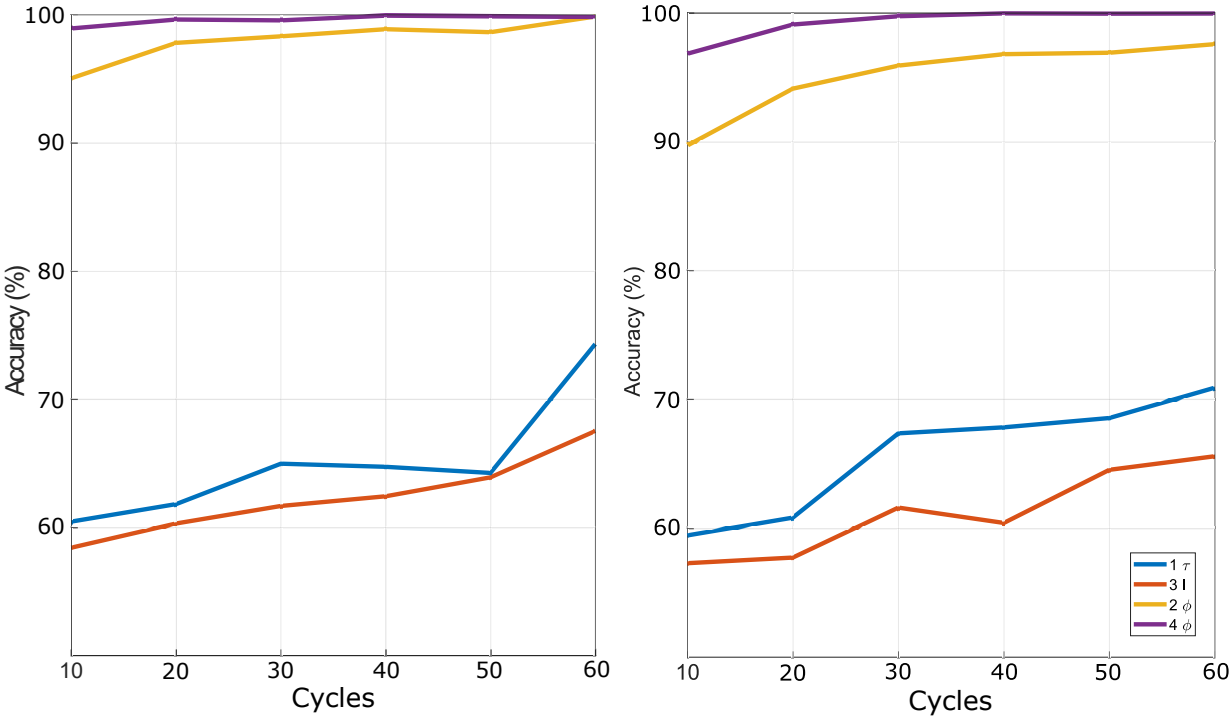

(a) (b)

Figure 6.3: Performance of FNN-classifier for detecting local DF with spectrograms computed from different numbers of cycles in operations of (a) Profile 2 and (b) Profile 3

The ML algorithms are, in addition to fault detection, also trained for discrimination among no-fault, local DF, local ITSC and MF. There is an equal number of observations in each fault case. A classifier with an accuracy below 25 % is worse than random chance. The EDT, SVM and FNN-based classifiers have the highest accuracy among the studied algorithms. The accuracy of all the classifiers increases by including more signals in the training data. The KNN-based classifier has an accuracy of just above 25 % when trained and tested using current or torque data on Profile 2 and Profile 3. However, FNN reaches an accuracy above 75.4 %, which is the best performance of the four tested algorithms.

The second analysis done in Paper E is to find the ideal length for the samples. Larger samples give spectrograms with sharper peaks but take longer time to measure. The sample length is defined in cycles because the input signal is resampled based on the estimated rotor position. Figure 6.3 shows line plots of the detection accuracy of local demagnetisation achieved by the FNN-classifier with the best performance in the previous analysis. The study investigates the achieved accuracies in cases of features computed from one torque sensor (1 τ), three current sensors (3 I), two hall sensors (2 ϕ) and four hall sensors (4 ϕ). Combining the three different physical parameters did not give significantly higher accuracy than the case of four flux sensors. The accuracy increases with longer samples as shown in Figure 6.3. However, only the two cases with stray flux converge with an accuracy above 90 %. The accuracy of FNN trained on samples from four hall sensors converges at 20 cycles, but the ideal length is 30 cycles if the FNN only uses two hall sensors.

6.2 Balancing datasets with reinforcement learning

The imbalance dataset problem results in a higher possibility for false negatives (FN) or even a collapse of the classifier. Noise, overlapping classes, and one class represented by multiple clusters will amplify the problem [87]. The imbalance datasets normally are rebalanced by oversampling the minority class or undersampling the majority class. Alternatively, the minority class can generate new samples with different variations of SMOTE [88]. The proposed FDI scheme implementing RL in an AL setup would provide another option to balance the classes in the dataset. The overall scheme proved robust against variable load and speed operation with MF.

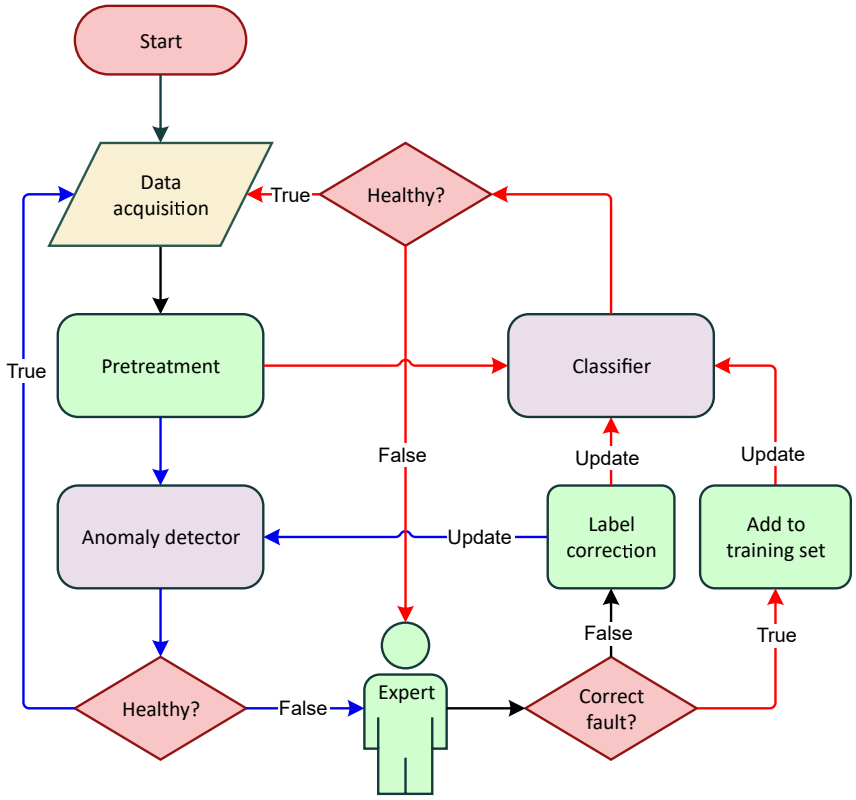

Figure 6.4: Flowchart of the proposed FDI scheme. Note: Arrows coloured in red, blue and black represent information flow related to classifier, detector or both; green objects represent processes/actions; purple boxes represent detector and classifier, red diamonds represent decisionss

The proposed FDI scheme shown in Figure 6.4 is developed based on an online fault diagnosis scheme in [16]. The input signals are resampled with the same pre-treatment described in Paper E. There is no available labelled sample in the faulty case in the first stage of development. However, the anomaly detector is an OCC, which only requires samples from the healthy case. If the anomaly detector gives a false positive (FP), it needs to update its competence with these FPs. The LOF is the chosen anomaly detector, which is a density-based OCC. LOF for a new point P for its k nearest neighbouring points o_n is defined as:

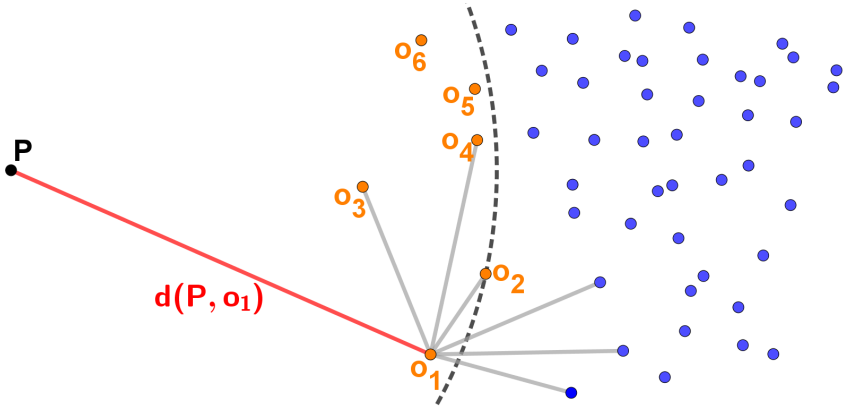

Figure 6.5: Illustration of LOF in a 2D-feature space

$$\mathrm{LOF}(P) = \frac{1}{k}\sum_{n=1}^{k}\frac{\rho_{\mathrm{samp}}(o_n)}{\rho_{\mathrm{samp}}(P)} \tag{6.3}$$

The density of point P, $\rho_{\mathrm{samp}}(P)$, is defined as:

$$\rho_{\mathrm{samp}}(P) = \left(\frac{1}{k}\sum_{n=1}^{k} d(P, o_n)\right)^{-1} \tag{6.4}$$

where $d(P, o_n)$ is the Euclidean distance between point P and its neighbouring point o_n. Figure 6.5 illustrates the principle of LOF.

The exploration of true positive samples marks the end of the first stage of the FDI scheme. The classifier only knows one fault in the first iteration, and the anomaly detector works alongside the fault classifier. Further exploration of new fault samples will make the FDI more knowledgeable and accurate. The aim is to narrow down the fault search during maintenance. Jagath et. al. [16] used a CNN as a classifier, which is not necessarily well suited for unbalanced dataset. The proposed algorithm replaced the CNN with a DQN due to its potential in the weighted reward function for rebalancing the datasets [78].

$$r_t = \begin{cases} 1, & a_t = L_t = \text{Healthy} \\ -1, & a_t \neq L_t = \text{Healthy} \\ \lambda, & a_t = L_t = \text{Faulty} \\ -\lambda, & a_t \neq L_t = \text{Faulty} \end{cases} \tag{6.5}$$

Imbalance in a dataset is measured by the ratio between negative (healthy) and positive (faulty) samples, λ. RL often uses the analogy of teaching an agent to play a game [89]. In the case of fault classification, the game is a "Quiz". We ask the agent, "What class does this 1D-array of features belong to?". The weighted reward function gives a point if the agent correctly classifies the healthy class and penalises one point due to misclassification. The magnitude of the reward and penalty for the faulty class is increased with a factor λ. The purpose of r_t is to prevent the collapse of the classifier due to a severe imbalance dataset, where all new samples will be classified as the majority class (healthy).

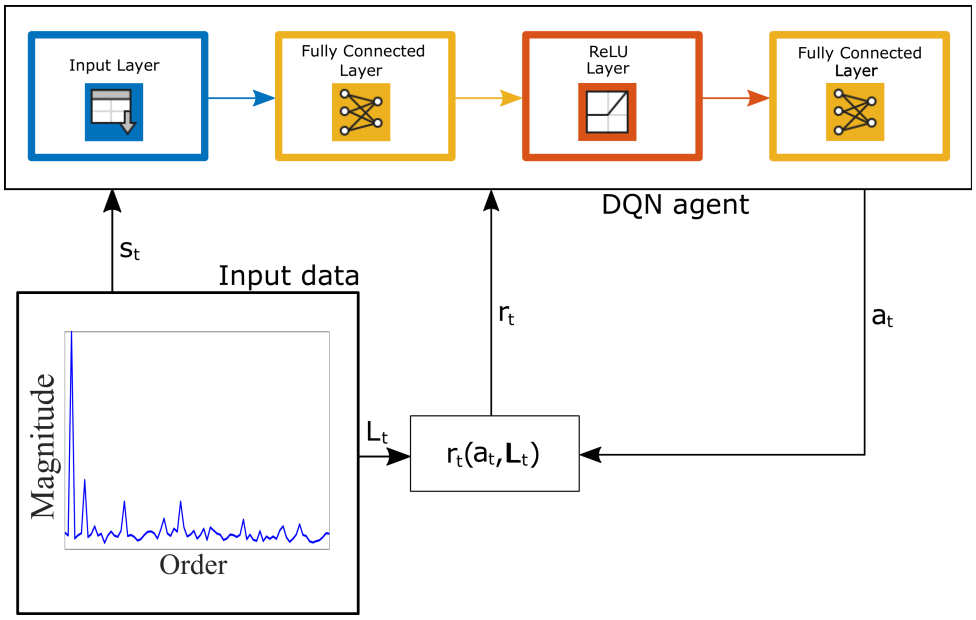

Figure 6.6: Block diagram of DQN agent interacting with the environment

The agent has four possible actions (answers). They are defined in the action space $A = \{[0,0],[0,1],[1,0],[1,1]\}$. The entries in A represent NF, DF, ITSC and MF, respectively. The encoding of the labels is for the DQN. The prediction output is decoded for a human reader. Figure 6.6 shows the interaction between DQN-agent and its environment where the agent answers one question at a time. The schematics inside the agent represent the layers of the critic network: input layer with 243 nodes, fully connected layer with 100 nodes, a rectified linear unit (ReLU) layer and a second fully connected layer with 2 or 4 nodes depending on the number of classes in datasets.

6.2.1 Experimental validation of FDI with DQN

The one-class SVM and LOF need to define their respective criterion for anomaly identification. The outlier factor determines the sensitivity of the one-class SVM, which is 10 %. The output of the trained one-class SVM under testing is a numeric score, which is less than 0 in case of an anomaly, as suggested in [16]. The LOF does require trial and error to determine a suitable threshold. A value close to 1 will make the detector more sensitive but has a greater FP rate. The selected threshold is 1.1. A new sample point in feature space is identified as an anomaly/fault if the regions of its k^{th} nearest neighbours are, on average 10 % more densely populated than its neighbourhood. Parameter k of the LOF equals 5.

The one-class SVM and LOF classifiers are first trained on the healthy datasets from Profile 1, 250 samples, with the result shown in Table 6.2 and Table 6.3. The testing dataset from Profile 1 consists of 50 samples. All samples from each faulty class from any operation profile were in the test dataset, 900 samples in total. Initially, the training set includes only samples from Profile 1. The accuracy of the one-class SVM anomaly detector in [16], when testing on each of the fault cases, varies between 57 % and 98.3 %. The proposed LOF anomaly detector predicts all the fault cases as anomalies almost

perfectly, but it gets a higher FP rate than one-class SVM. The training dataset increases with additional samples from healthy classes operating in Profiles 2 and 3. It is noted that the number of extra samples in the table headers is the number added from each profile. As a result, the accuracy of the proposed LOF anomaly detector is improved, but the one-class SVM overall accuracy suffers from this addition. This proves that the proposed LOF anomaly detector can effectively identify anomalies better than the existing one-class SVM when more knowledge of the healthy class is presented.

Table 6.2: Accuracy of one-class SVM outlier detector

Fault test case	Test	Extra samples from Profiles 2 and 3					
(Criterion)	Pro.	0	50	100	150	200	250
Healthy	1	84.0	82.0	80.0	80.0	80.0	80.0
(Score $\geqslant 0$)	2	80.0	98.0	98.0	98.0	98.0	98.0
	3	46.0	70.0	80.0	80.0	84.0	90.0
DF	1	71.7	55.3	56.0	56.0	51.7	53.0
(Score < 0)	2	57.0	46.0	45.7	44.3	41.0	41.0
	3	84.0	58.3	54.7	51.0	44.7	44.3
ITSC	1	82.3	55.3	53.7	53.0	46.3	45.7
(Score < 0)	2	90.7	54.3	48.0	39.7	22.7	21.7
	3	98.3	77.0	74.7	67.0	59.0	57.0
MF	1	66.7	44.0	46.0	43.0	39.7	38.7
(Score < 0)	2	73.3	32.0	30.3	23.7	16.3	15.0
	3	93.0	62.3	58.7	51.7	42.7	37.0

Table 6.3: Accuracy of LOF outlier detector

Fault test case	Test	Extra samples from Profiles 2 and 3					
(Criterion)	Pro.	0	50	100	150	200	250
Healthy	1	86.0	86.0	88.0	88.0	80.0	98.0
(LOF $\leqslant 1.1$)	2	14.0	72.0	94.0	80.0	86.0	84.0
	3	8.0	52.0	88.0	80.0	82.0	90.0
DF	1	100	100	98.0	98.0	100	100
(LOF > 1.1)	2	100	98.0	100	100	100	100
	3	100	92.0	94.0	94.0	98.0	98.0
ITSC	1	100	100	100	100	100	100
(LOF > 1.1)	2	100	100	100	100	100	100
	3	100	100	100	94.0	100	100
MF	1	100	98.0	100	96.0	100	100
(LOF > 1.1)	2	100	94.0	96.0	100	100	98.0
	3	100	92.0	84.0	92.0	96.0	96.0

The CNN and proposed DQN fault classifiers are trained to discriminate between NF and a fault case (DF or ITSC). However, they are tested on all four healthy classes (NF,

DF, ITSC and MF). Table 6.4 lists the results from this comparative study with true positive rate (TPR) and true negative rate (TNR). Green numbers indicate a rate above 98 %, and red numbers are less than 50 %. Increasing the imbalance ratio λ is achieved by decreasing the number of positive samples in the training set. All negative samples from the PMSM operating with Profile 1 are in the training datasets, but 50 of these samples are randomly selected for testing. The test datasets are balanced between the health classes and have 50 randomly selected samples from each class. They are sampled from the dataset, which is not used for training when $\lambda > 1$. This selection is only for the test dataset from Profile 1. All samples from Profile 2 and Profile 3 are in the test (300 samples per health class per profile).

Both CNN and the proposed DQN classifiers achieve a TPR higher than 90 % for the fault case the classifier has seen before with $\lambda = 1$. The lowest TPR for DQN and CNN trained for ITSC is 82.0 % and 76.1 %, respectively. This is the case of the test samples from Profile 3 with constant speed and variable loads. The DQN classifier for DF maintains a TPR above 97.8 %. However, the TNR for the NF drops to 72.8 %. The CNN classifier improves its hit rate for NF by increasing λ. A lower FP rate is a positive quality in a classifier, but the TPR for the CNN drops to below 50 % when increasing λ. The CNN collapses since all inputs are classified as NF. The proposed DQN classifier, on the other hand, reduces the possibility of FN but has overcompensated slightly with more FPs. Neither FP nor FN is desirable in FDI. However, FN and FP rates can be compensated in the proposed AL scheme by correct relabeling by an expert. The proposed DQN fault classifier has the second option with the weighted reward function.

The MF case includes DF and ITSC, thus DQN and CNN may classify it as either health class. The results in Table 6.4 reveal that both DQN and CNN classifiers trained for DF, identify MF as a fault. The TPR of MF is lower than that of DF. The CNN also classifies MF as NF at a higher rate with larger λ. These results indicate a high possibility for DF and MF sharing similar fault signatures. A fault classifier trained on all four healthy classes may find it difficult to separate between DF and MF. Neither DQN nor CNN classifier identifies MF as a fault when they are trained to identify ITSC fault.

The final comparative study between DQN and CNN are implemented on all four classes: NF, DF, ITSC and MF. Figure 6.7 shows the hit rates (TNR and TPR) of the DQN and CNN fault classifiers using the test dataset in Profile 3. The figure also shows the overall accuracy. DQN and CNN classifiers have lower accuracy than four-class classifiers. They start with an overall accuracy of 75 %, then decrease with increasing λ. The accuracy of the CNN declines at a higher rate than DQN and heads towards a collapse. Its hit rate for NF increases towards 100 %.

There are 12 miss rates in total for a four-class classifier. Figure 6.8 plots the miss rates for both DQN and CNN fault classifiers, which are not close to 0. The comparison still uses the test dataset from Profile 3. It is noted that the first and last letters in the labels denote the predicted and true classes, respectively. Figure 6.8 reveals that the proposed DQN fault classifier is confused between DF and MF, which were predicted in the analysis of the two-class classifiers. The DQN classifier confuses ITSC with NF and MF, while NF is generally confused with all health classes. This demonstrates that the reward function may have overcompensated and needs adjustment. A combined decision

between fault classifier and anomaly detector may also reduce the rate of FPs since Table 6.3 reports a high accuracy for LOF. The CNN fault classifier does not misclassify NF with any fault class. The confusion between DF and MF decreases with increasing λ and is classified as NF instead. CNN starts to misclassify all ITSC as NF.

Table 6.4: Comparing TPR and TNR of DQN and CNN classifiers when trained for identifying either DF or ITSC

		Local Demagnetisation								Inter-turn short circuit							
		DQN				CNN				DQN				CNN			
Test Pro.	Imb. ratio	TPR DF	TNR NF	TPR MF	TNR ITSC	TPR DF	TNR NF	TPR MF	TNR ITSC	TPR ITSC	TNR NF	TPR MF	TNR DF	TPR ITSC	TNR NF	TPR MF	TNR DF
1	1	100	99.9	95.8	100	97.2	98.4	73.7	99.9	98.5	97.9	12.8	99.4	95.4	96.6	2.9	99.8
	1.25	100	99.9	97.6	99.8	96.3	98.1	71.2	99.9	95.7	97.2	9.4	99.6	93.2	93.6	6.7	98.6
	1.67	100	99.7	99.6	100	95.8	98.9	71.0	100	97.1	98.1	11.5	98.8	89.1	97.9	5.8	98.8
	2.5	100	99.9	99.5	98.8	95.5	99.3	69.8	99.9	98.2	96.5	14.9	98.4	81.6	97.9	1.6	99.9
	5	100	98.7	99.6	99.1	92.9	98.6	64.3	99.9	96.4	95.6	14.7	98.9	67.6	96.9	2.1	99.8
	10	100	96.1	99.9	97.9	82.1	99.8	49.8	100	96.2	92.8	19.0	97.7	55.4	96.7	3.0	99.7
	15	99.9	93.4	99.6	95.8	69.4	97.5	35.8	99.7	93.4	90.3	15.7	98.5	43.5	99.7	2.0	99.5
	30	100	88.6	100	93.1	46.9	99.8	23.9	99.9	90.1	84.7	27.2	95.5	23.6	99.7	0.2	100
2	1	99.4	100	95.8	99.9	92.3	93.4	74.3	99.4	91.4	85.1	28.9	95.4	80.0	94.0	3.0	99.9
	1.25	99.6	99.9	97.9	100	94.8	93.7	77.1	99.5	92.7	85.1	24.6	96.6	77.8	91.0	4.8	99.7
	1.67	99.9	99.6	98.8	100	95.3	93.2	75.8	99.4	90.0	85.7	24.9	96.2	72.8	95.1	4.4	99.6
	2.5	99.8	99.1	99.5	99.7	95.2	94.8	75.9	99.4	94.6	77.9	35.1	92.3	65.0	95.9	2.0	100
	5	99.9	97.9	99.6	99.3	91.3	95.0	65.8	99.5	94.4	72.5	35.7	91.2	47.4	96.4	1.7	99.9
	10	99.9	91.6	99.8	96.4	75.4	97.5	47.3	99.9	88.0	69.9	35.1	91.7	37.6	96.3	1.4	99.8
	15	100	85.0	99.9	93.8	66.7	93.2	37.6	98.6	84.6	68.8	30.7	91.2	23.4	99.4	0.6	99.8
	30	100	72.8	100	89.8	49.1	97.6	32.2	99.3	79.6	72.3	33.2	88.0	13.2	99.5	0.3	100
3	1	97.9	99.9	89.0	100	99.0	97.1	91.6	100	82.0	91.6	12.4	99.3	76.1	94.6	5.4	99.1
	1.25	97.8	99.9	90.9	100	98.5	95.4	90.8	99.7	83.2	90.2	10.1	99.3	81.0	87.9	11.8	96.9
	1.67	98.9	99.8	94.0	99.9	99.1	96.4	93.7	100	83.8	90.1	10.9	99.3	76.9	94.6	9.4	96.6
	2.5	99.5	98.2	96.5	99.5	98.3	98.0	88.1	99.8	85.9	87.7	11.4	99.0	64.4	97.1	2.0	99.9
	5	99.6	97.0	97.5	98.9	97.5	97.6	85.9	99.8	86.6	84.8	11.4	98.8	53.9	95.3	2.0	99.8
	10	99.8	93.1	98.4	97.8	88.4	99.6	71.0	100	86.9	80.2	14.1	98.8	39.1	95.9	1.9	99.1
	15	99.7	88.4	98.4	96.3	78.0	96.3	57.2	98.6	85.2	79.0	13.3	98.2	22.5	98.4	2.6	99.0
	30	99.8	82.2	99.1	95.1	46.8	99.6	30.8	100	83.9	73.2	20.5	95.0	18.2	99.3	0.4	100

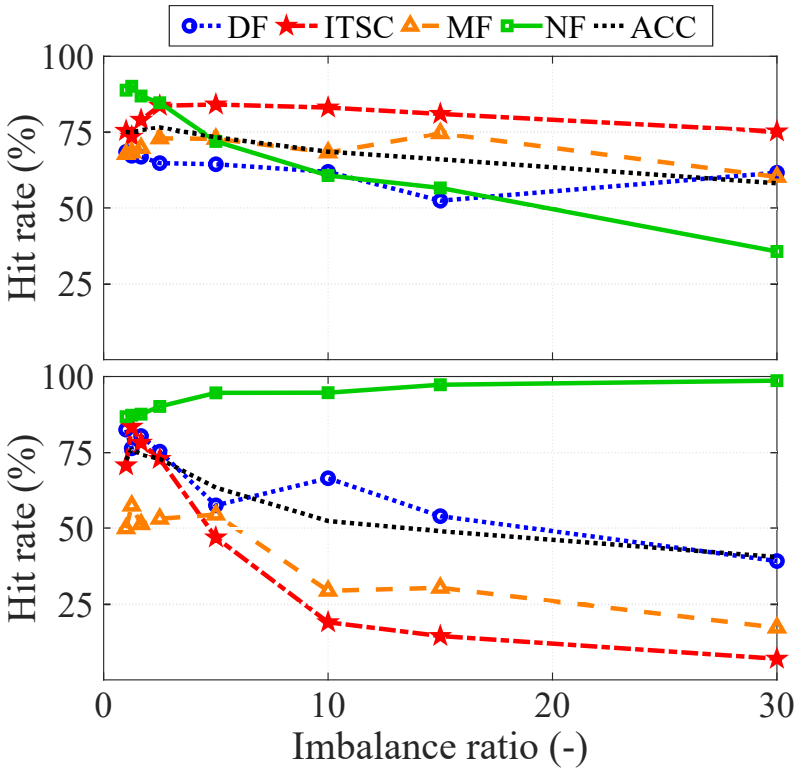

Figure 6.7: Hit rates of DQN (top) and CNN (bottom) fault classifiers

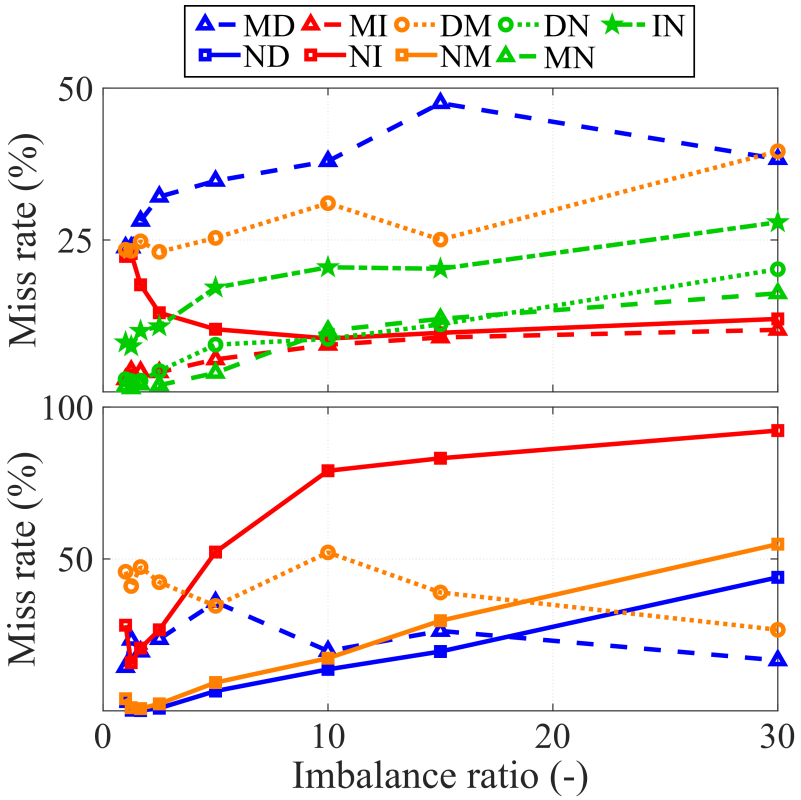

Figure 6.8: Miss rates of DQN (top) and CNN (bottom) fault classifiers

6.3 Summary

This chapter presented two FDI schemes based on ML. First, FDI scheme is proposed for single and MFs of a sensorless PMSM drive in dynamic operations with two external stray flux sensors. An order tracking method based on position estimation is proposed for resampling the measurement before generating features for ML algorithms. Eliminating the need for position sensors makes the proposed FDI applicable in sensorless PMSM drives. The fault classifiers are trained using data from Profile 1 and achieve high accuracy for detecting magnet defects or ITSC faults when being tested on the datasets in Profiles 2 and Profile 3. This work also introduces a method of inducing local demagnetisation through heat treatments, resulting in less physical damage to the rotor.

The second FDI scheme has an AL framework with RL, which is built on Paper E. It is trained and tested with dynamic operating conditions and MFs, where labelled training samples are initially unavailable. Training and testing datasets are collected from the in-house test-bench. The LOF anomaly detector trained only with data from Profile 1 gives a high FP rate. Nevertheless, the proposed AL framework allows it to improve prediction accuracy when adding new healthy case samples. Training of the DQN classifier starts after the faulty class has been discovered. The reward function is weighted and depends on the dataset imbalance ratio λ. The comparative study shows that the DQN fault classifier is more robust against data imbalance than the CNN and can overcompensate the weight of the minority class.

Chapter 7

Concluding remarks

7.1 Conclusions

The first research topic involvs mathematical models of faulty PMSM, which are fast to compute with sufficient accuracy. Two improved models including a PNM in Paper B and FRM in Paper C. Previous versions of PNM used variable permeance to model the revolution of the rotor. This becomes computationally heavy for detailed PNMs with a higher number of nodes. The proposed PNM replaces the variable permanence in the air-gap with variable flux sources describing the magnets of the PMSM. It simplifies the overview of the model, which can be used to model demagnetisation and has the potential to be implemented in the short-circuit model. The computation burden decreases significantly when the PNM does not simulate DE. Nevertheless, the proposed approach makes the PNM easier to understand by separating the description of rotor revolution from the permeance matric.

The FRM in Paper C is developed based on the principle of field reconstruction, superimposing magnetic field contribution from the rotor and stator. The basis function is computed with static FEA, but the computation time of the FEA is three orders of magnitude larger than FRM. The proposed FRM has a magnet library with the basis function of different magnet defects included. A new rotor basis function is generated by superimposing magnet basis functions from the proposed library, which is faster than to compute all the combinations in static FEAs. The proposed FRM is also the first reported FRM with the implementation of a short circuit.

An approach to reduce the computation cost of acquiring QTFD is presented in Paper D. The time resolution is less affected by the window size than STFT because each time instant in the spectrogram takes the whole signal into account. One of the main drawbacks is that the computational burden increases with the length of the processed data sample. Therefore, previous work only worked with short time samples (a few seconds). The proposed method splits the signal into smaller parts and combines them in a single spectrogram. The proposed QTFD algorithm can transform a time sample with a length of 120 s into a time-frequency domain in a few seconds. The resulting spectrogram had sharper peaks, and the time resolution was unaffected by the selected window.

The second research topic focuses on implementing FDIs on PMSM in dynamic operating conditions. An FDI with fewer flux sensors is presented in Paper A. The study

is developed based on the previous publication [19], which used 12 search coils equally spaced in the stator. The proposed method can reduce the number of required search coils to 2. The envelope of the induced search coil voltages has different frequency compositions, which separates the health classes: NF, DF, SE and DE. The method is verified with FEA, simulating the acceleration phase of a PMSG during start-up. It is limited to PM machines with mirror symmetry and is dependent on the rotor position. A data-driven diagnosis scheme utilising stray flux sensors is presented in Paper E. Spectrogram, being order-normalised, is implemented to make the FDI robust against dynamic operations and the time-series data are re-sampled at a fixed angular increment. The proposed method eliminates the need of any position sensor by estimating the relative position with a stray flux sensor and an optimisation problem. This makes it possible for the FDI to be installed externally on a sensorless drive.

The problem with unavailable training samples of faulty PMSM and imbalanced datasets, which is a challenge for implementing data-driven FDI, is investigated in Paper F. The study is built on the framework of AL with a fault detector and a fault classifier. LOF is used as a fault detector, being more effective against data samples with overlapping classes than one-class SVM. DQN is implemented as the classifier, which introduces another approach to balance the dataset than under- and oversampling. The proposed reward function is overcompensated with a slight increase of FP in datasets with a larger imbalance.

7.2 Limitations and future work

The fault diagnosis scheme in Paper A with time-stepped FEA did reduce the number of required sensors to the bare minimum. However, motor geometry (symmetry) might limit this FDI application. In a four-pole motor, the sensors need to be placed on the opposite side of the stator. The number of stator teeth needs to be even. In this case, the search coils are perfectly placed 360° (electrical degrees) apart. In a two-pole motor, the search coils should have opposite polarities since the induced voltages will be identical in theory. However, no motors is perfectly symmetric, and a certain noise level is unavoidable. This is why the difference in the induced voltages needs to exceed a set threshold for detecting a fault.

The proposed model PNM does reduce computational burden since the permeance matrix does not need to be inverted every time step. However, this benefit disappears with a DE that needs to be modelled. Nevertheless, the new approach makes it easier for the engineer to develop the new PMSM model with eccentricity. It separates the mathematical description of the revolution of the rotor and the variation of air-gap distance. The proposed PNM may describe the rotation with the variable flux sources and change eccentricity with the permeance matrix. Further development of the proposed PNM should include more fault cases and address the computational burden.

The accuracy of the FRM, which is the second proposed model of a faulty PMSM, is limited by the accuracy of the static FEA describing PMSM. However, the benefit of reduced computational burden justifies its implementation. It can model any magnet

defects and ITSC, but its versatility can be increased by the description of eccentricity faults.

The proposed method to compute QTFT is effective in numerical examples where the images of the signal components had smoother shapes as compared to spectrograms computed with STFT. However, the difference in performance is less clear with measurement from a PMSM with ITSC fault. The noise made it unclear, and the cross-product problem makes WVD unattractive. This topic can be extended by filtering from the kernel function of CWD or ZAM.

In Paper F a comparison of OCCs is performed between LOF and one-class SVM. However, it would be beneficial to do an extensive comparison study of more OCCs to reveal their strength and weaknesses. LOF is in this work more effective than one-class SVM, due to the overlap between the health classes. However, LOF becomes more memory intensive if more healthy case samples need to be added. Strategic removal of the sample may help to maintain the computation burden of LOF and keep it attractive for online applications. Reconstruction-based OCC like auto-encoders is widely popular in the machine learning community and may be a competitive option, but it was not successfully executed in this work. A second option is the fourth OCC type, or the hybrid class, combining the three other categories for making use of their respective strength and compensating for their weaknesses.

The compensation in the reward function is assumed to be the ratio between the majority and minority classes. It is reported in the literature as being the most effective for rebalancing the weights in imbalanced datasets, validated in an image classification scheme. However, this assumption may be incorrect since the results in Paper F show that the reward function is overcompensating, resulting in classifiers with higher FP rate. It is reasonable to assume that reducing the ratio can be beneficial since the current value is overcompensated and rebalancing healthy cases can result in a collapsing classifier. Studying the "best" ratio in the reward function and maximising the overall accuracy of the proposed FDI in Paper F might be a good topic for future work.

References

[1] S. J. Chapman, *Electric Machinery Fundamentals*, 5th ed. New York: McGraw-Hill, 2012, ISBN: 9780071086172.

[2] J. Lee, S. Moon, H. Jeong, and S. W. Kim, "Robust Diagnosis Method Based on Parameter Estimation for an Interturn Short-Circuit Fault in Multipole PMSM under High-Speed Operation," *Sensors*, vol. 15, no. 11, pp. 29 452–29 466, Nov. 2015. DOI: 10.3390/s151129452.

[3] L. Wu, Y. Du, Z. Chen, Y. Guo, H. Wen, and Y. Fang, "Influence of Load Characteristics on Three-Phase Short Circuit and Demagnetization of Surface-Mounted PM Synchronous Motor," *IEEE Transactions on Industry Applications*, vol. 56, no. 3, pp. 2427–2440, Jan. 2020. DOI: 10.1109/TIA.2020.2968036.

[4] M. E. Iglesias Martínez, J. A. Antonino-Daviu, P. F. de Córdoba, J. A. Conejero, and L. Dunai, "Automatic Classification of Winding Asymmetries in Wound Rotor Induction Motors Based on Bicoherence and Fuzzy C-Means Algorithms of Stray Flux Signals," *IEEE Transactions on Industry Applications*, vol. 57, no. 6, pp. 5876–5886, Nov. 2021. DOI: 10.1109/TIA.2021.3108413.

[5] I. Zamudio-Ramirez, R. A. Osornio-Rios, J. A. Antonino-Daviu, H. Razik, and R. d. J. Romero-Troncoso, "Magnetic Flux Analysis for the Condition Monitoring of Electric Machines: A Review," *IEEE Transactions on Industrial Informatics*, vol. 18, no. 5, pp. 2895–2908, May 2022, ISSN: 19410050. DOI: 10.1109/TII.2021.3070581.

[6] Y. Chen, S. Liang, W. Li, H. Liang, and C. Wang, "Faults and Diagnosis Methods of Permanent Magnet Synchronous Motors: A Review," *Applied Sciences*, vol. 9, no. 10, Mar. 2019. DOI: 10.3390/app9102116.

[7] S. S. Moosavi, Q. Esmaili, A. Djerdir, and Y. A. Amirat, "Inter-Turn Fault Detection in Stator Winding of PMSM Using Wavelet Transform," in *2017 IEEE Vehicle Power and Propulsion Conference (VPPC)*, Dec. 2017, pp. 1–5. DOI: 10.1109/VPPC.2017.8330891.

[8] M. Zafarani, E. Bostanci, Y. Qi, T. Goktas, and B. Akin, "Interturn Short-Circuit Faults in Permanent Magnet Synchronous Machines: An Extended Review and Comprehensive Analysis," vol. 6, no. 4, pp. 2173–2191, Dec. 2018. DOI: 10.1109/jestpe.2018.2811538.

[9] E. A. Bhuiyan, M. M. A. Akhand, S. K. Das, and et. al., "A Survey on Fault Diagnosis and Fault Tolerant Methodologies for Permanent Magnet Synchronous Machines," *Int. J. Autom. Comput.*, vol. 17, no. 6, pp. 763–787, Nov. 2020. DOI: 10.1007/s11633-020-1250-3.

[10] H. A. Toliyat, S. Nandi, S. Choi, and H. Meshgin-Kelk, *Electric Machines : Modeling, Condition Monitoring, and Fault Diagnosis*. Boca Raton, USA (FL): Taylor & Francis, 2017, ISBN: 9781138073975.

[11] Y. Qi, E. Bostanci, V. Gurusamy, and B. Akin, "A Comprehensive Analysis of Short-Circuit Current Behavior in PMSM Interturn Short-Circuit Faults," *IEEE Transactions on Power Electronics*, vol. 33, no. 12, pp. 10 784–10 793, Dec. 2018. DOI: 10.1109/TPEL.2018.2809668.

[12] K.-C. Kim, S.-B. Lim, D.-H. Koo, and J. Lee, "The Shape Design of Permanent Magnet for Permanent Magnet Synchronous Motor Considering Partial Demagnetization," *IEEE Transactions on Magnetics*, vol. 42, no. 10, pp. 3485–3487, Oct. 2006. DOI: 10.1109/TMAG.2006.879077.

[13] Y. Zhongming and W. Bin, "A review on induction motor online fault diagnosis," in *Proceedings IPEMC 2000. Third International Power Electronics and Motion Control Conference (IEEE Cat. No.00EX435)*, Aug. 2000, pp. 1353–1358. DOI: 10.1109/IPEMC.2000.883050.

[14] Z. Gao, C. Cecati, and S. X. Ding, "A Survey of Fault Diagnosis and Fault-Tolerant Techniques—Part I: Fault Diagnosis With Model-Based and Signal-Based Approaches," *IEEE Transactions on Industrial Electronics*, vol. 62, no. 6, pp. 3757–3767, Jun. 2015. DOI: 10.1109/TIE.2015.2417501.

[15] D. Neupane and J. Seok, "Bearing Fault Detection and Diagnosis Using Case Western Reserve University Dataset With Deep Learning Approaches: A Review," *IEEE Access*, vol. 8, pp. 93 155–93 178, Apr. 2020. DOI: 10.1109/ACCESS.2020.2990528.

[16] J. S. L. Senanayaka, H. V. Khang, and K. G. Robbersmyr, "Toward Self-Supervised Feature Learning for Online Diagnosis of Multiple Faults in Electric Powertrains," *IEEE Transactions on Industrial Informatics*, vol. 17, no. 6, pp. 3772–3781, Aug. 2021. DOI: 10.1109/TII.2020.3014422.

[17] C.-F. Tsai and W.-C. Lin, "Feature Selection and Ensemble Learning Techniques in One-Class Classifiers: An Empirical Study of Two-Class Imbalanced Datasets," *IEEE Access*, vol. 9, pp. 13 717–13 726, Jan. 2021. DOI: 10.1109/ACCESS.2021.3051969.

[18] M. Krichen, E. Elbouchikhi, N. Benhadj, M. Chaieb, M. Benbouzid, and R. Neji, "Motor Current Signature Analysis-Based Permanent Magnet Synchronous Motor Demagnetization Characterization and Detection," *Machines*, vol. 8, no. 3, pp. 1–28, Jun. 2020. DOI: 10.3390/MACHINES8030035.

[19] Y. Da, X. Shi, and M. Krishnamurthy, "A New Approach to Fault Diagnostics for Permanent Magnet Synchronous Machines Using Electromagnetic Signature Analysis," *IEEE Transactions on Power Electronics*, vol. 28, no. 8, pp. 4104–4112, Aug. 2013.

[20] B. Fahimi and A. Khoobroo, "Method and apparatuses for fault management in permanent magnet synchronous machines using the field reconstruction method," pat., U.S. Patents 8,314,576 B2, Nov. 2012. [Online]. Available: https://patents.google.com/patent/US8314576B2/en.

[21] Z. Chen, R. Qi, and H. Lin, "Inter-turn Short Circuit Fault Diagnosis for PMSM Based on Complex Gauss Wavelet," in *2007 International Conference on Wavelet Analysis and Pattern Recognition*, vol. 4, Nov. 2007, pp. 1915–1920. DOI: 10.1109/ICWAPR.2007.4421769.

[22] J. Faiz, H. Nejadi-Koti, and Z. Valipour, "Comprehensive Review on Inter-Turn Fault Indexes in Permanent Magnet Motors," *{IET} Electric Power Applications*, vol. 11, no. 1, pp. 142–156, Jan. 2017. DOI: 10.1049/iet-epa.2016.0196.

[23] J. Faiz and E. Mazaheri-Tehrani, "Demagnetization Modeling and Fault Diagnosing Techniques in Permanent Magnet Machines Under Stationary and Nonstationary Conditions: An Overview," *IEEE Transactions on Industry Applications*, vol. 53, no. 3, pp. 2772–2785, 2017. DOI: 10.1109/TIA.2016.2608950.

[24] J. Faiz and S. Moosavi, "Eccentricity fault detection – From induction machines to DFIG—A review," *Renewable and Sustainable Energy Reviews*, vol. 55, pp. 169–179, Mar. 2016. DOI: https://doi.org/10.1016/j.rser.2015.10.113.

[25] J. Zhang, J. Hang, S. Ding, and M. Cheng, "Online Diagnosis and Localization of High-Resistance Connection in PMSM With Improved Fault Indicator," *IEEE Transactions on Power Electronics*, vol. 32, no. 5, pp. 3585–3594, May 2017. DOI: 10.1109/TPEL.2016.2587670.

[26] J. De Bisschop, A. A. E. Abdallh, P. Sergeant, and L. Dupré, "Analysis and Selection of Harmonics Sensitive to Demagnetisation Faults Intended for Condition Monitoring of Double Rotor Axial Flux Permanent Magnet Synchronous Machines," *IET Electric Power Applications*, vol. 12, no. 4, pp. 486–493, 2018. DOI: 10.1049/iet-epa.2017.0568.

[27] V. Gurusamy, E. Bostanci, C. Li, Y. Qi, and B. Akin, "A Stray Magnetic Flux-Based Robust Diagnosis Method for Detection and Location of Interturn Short Circuit Fault in PMSM," *IEEE Transactions on Instrumentation and Measurement*, vol. 70, Jul. 2021. DOI: 10.1109/TIM.2020.3013128.

[28] A. Aggarwal, I. M. Allafi, E. G. Strangas, and J. S. Agapiou, "Off-Line Detection of Static Eccentricity of PMSM Robust to Machine Operating Temperature and Rotor Position Misalignment Using Incremental Inductance Approach," *IEEE Transactions on Transportation Electrification*, vol. 7, no. 1, pp. 161–169, Jun. 2021. DOI: 10.1109/TTE.2020.3006016.

[29] G. Forstner, A. Kugi, and W. Kemmetmüller, "A Magnetic Equivalent Circuit Based Modeling Framework for Electric Motors Applied to a PMSM With Winding Short Circuit," *IEEE Transactions on Power Electronics*, vol. 35, no. 11, pp. 12 285–12 295, Apr. 2020. DOI: 10.1109/TPEL.2020.2986042.

[30] M. Zhang, A. Macdonald, K. J. Tseng, and G. M. Burt, "Magnetic Equivalent Circuit Modeling for Interior Permanent Magnet Synchronous Machine under Eccentricity Fault," *Proceedings of the Universities Power Engineering Conference*, pp. 1–6, Sep. 2013. DOI: 10.1109/UPEC.2013.6715044.

[31] W. Bai, D. Qin, Y. Wang, and T. C. Lim, "Dynamic Characteristics of Motor-Gear System under Load Saltations and Voltage Transients," *Mechanical Systems and Signal Processing*, vol. 100, pp. 1–16, Feb. 2018. DOI: 10.1016/j.ymssp.2017.07.039.

[32] D. Gómez, A. Rodríguez, I. Villar, A. López-de-Heredia, I. Etxeberria-Otadui, and Z. Zhu, "Experimental Validation of an Enhanced Permeance Network Model for Embedded Magnet Synchronous Machines," *Electric Power Systems Research*, vol. 140, pp. 836–845, Nov. 2016. DOI: https://doi.org/10.1016/j.epsr.2016.04.022.

[33] A. Khoobroo and B. Fahimi, "Magnetic Flux Estimation in a Permanent Magnet Synchronous Machine using Field Reconstruction Method," *IEEE Transactions on Energy Conversion*, vol. 26, no. 3, pp. 757–765, May 2011. DOI: 10.1109/TEC.2011.2140115.

[34] J. Luznar, J. Slavič, and M. Boltežar, "Structure-Borne Noise at PWM Excitation using an Extended Field Reconstruction Method and Modal Decomposition," *Strojniski Vestnik/Journal of Mechanical Engineering*, vol. 65, no. 9, pp. 471–481, 2019. DOI: 10.5545/sv-jme.2019.6115.

[35] M. Kiani, D. Torregrossa, B. Fahimi, F. Peyraut, and A. Miraoui, "Detection of faults in PMSM using Field Reconstruction Method and Mechanical Impulse Response," in *2011 Twenty-Sixth Annual IEEE Applied Power Electronics Conference and Exposition (APEC)*, Fort Worth, USA (TX), Mar. 2011, pp. 1896–1901. DOI: 10.1109/APEC.2011.5744854.

[36] A. Khoobroo and B. Fahimi, "A New Method of Fault Detection and Treatment in Five Phase Permanent Magnet Synchronous Machine using Field Reconstruction Method," in *2009 IEEE International Electric Machines and Drives Conference, IEMDC 09*, Miami, FL, USA, May 2009, pp. 682–688. DOI: 10.1109/IEMDC.2009.5075279.

[37] D. Torregrossa, A. Khoobroo, and B. Fahimi, "Prediction of Acoustic Noise and Torque Pulsation in PM Synchronous Machines with Static Eccentricity and Partial Demagnetization using Field Reconstruction Method," *IEEE Transactions on Industrial Electronics*, vol. 59, no. 2, pp. 934–944, May 2012. DOI: 10.1109/TIE.2011.2151810.

[38] J. A. Rosero, L. Romeral, J. A. Ortega, and E. Rosero, "Short-Circuit Detection by means of Empirical Mode Decomposition and Wigner-Ville Distribution for PMSM Running under Dynamic Condition," *IEEE Transactions on Industrial Electronics*, vol. 56, no. 11, pp. 4534–4547, Jan. 2009. DOI: 10.1109/TIE.2008.2011580.

[39] J. K. Park and J. Hur, "Detection of Inter-Turn and Dynamic Eccentricity Faults Using Stator Current Frequency Pattern in IPM-Type BLDC Motors," *IEEE Transactions on Industrial Electronics*, vol. 63, no. 3, pp. 1771–1780, Jan. 2016. DOI: 10.1109/TIE.2015.2499162.

[40] P. Tian, C. A. Platero, K. N. Gyftakis, and J. M. Guerrero, "Stray Flux Sensor Core Impact on the Condition Monitoring of Electrical Machines," *Sensors (Switzerland)*, vol. 20, no. 3, pp. 1–14, 2020. DOI: 10.3390/s20030749.

[41] L. Frosini, C. Harlisca, and L. Szabo, "Induction Machine Bearing Fault Detection by Means of Statistical Processing of the Stray Flux Measurement," *IEEE Transactions on Industrial Electronics*, vol. 62, no. 3, pp. 1846–1854, 2015. DOI: 10.1109/TIE.2014.2361115.

[42] J. R. Riba Ruiz, J. A. Rosero, A. Garcia Espinosa, and L. Romeral, "Detection of Demagnetization Faults in Permanent-Magnet Synchronous Motors under Nonstationary Conditions," *IEEE Transactions on Magnetics*, vol. 45, no. 7, pp. 2961–2969, Jun. 2009. DOI: 10.1109/TMAG.2009.2015942.

[43] Z. Ullah and J. Hur, "A Comprehensive Review of Winding Short Circuit Fault and Irreversible Demagnetization Fault Detection in PM Type Machines," *Energies*, vol. 11, no. 12, p. 3309, Nov. 2018. DOI: 10.3390/en11123309.

[44] J. Rosero, L. Romeral, J. A. Ortega, and J. C. Urresty, "Demagnetization Fault Detection by means of Hilbert Huang Transform of the Stator Current Decomposition in PMSM," *IEEE International Symposium on Industrial Electronics*, pp. 172–177, Jun. 2008. DOI: 10.1109/ISIE.2008.4677217.

[45] I. Zamudio-Ramirez, J. A. Ramirez-Nunez, J. Antonino-Daviu, *et al.*, "Automatic Diagnosis of Electromechanical Faults in Induction Motors Based on the Transient Analysis of the Stray Flux via MUSIC Methods," *IEEE Transactions on Industry Applications*, vol. 56, no. 4, pp. 3604–3613, Apr. 2020. DOI: 10.1109/TIA.2020.2988002.

[46] S. Nandi, H. Toliyat, and X. Li, "Condition Monitoring and Fault Diagnosis of Electrical Motors—A Review," *IEEE Transactions on Energy Conversion*, vol. 20, no. 4, pp. 719–729, Dec. 2005. DOI: 10.1109/TEC.2005.847955.

[47] J. Hang, J. Zhang, M. Xia, S. Ding, and W. Hua, "Interturn Fault Diagnosis for Model-Predictive-Controlled-PMSM Based on Cost Function and Wavelet Transform," *IEEE Transactions on Power Electronics*, vol. 35, no. 6, pp. 6405–6418, Nov. 2020. DOI: 10.1109/TPEL.2019.2953269.

[48] A. G. Espinosa, J. A. Rosero, J. Cusidó, L. Romeral, and J. A. Ortega, "Fault Detection by means of Hilbert-Huang Transform of the Stator Current in a PMSM with Demagnetization," *IEEE Transactions on Energy Conversion*, vol. 25, no. 2, pp. 312–318, Feb. 2010. DOI: 10.1109/TEC.2009.2037922.

[49] B. Yang, Z. Yang, R. Sun, Z. Zhai, and X. Chen, "Fast Nonlinear Chirplet Dictionary-Based Sparse Decomposition for Rotating Machinery Fault Diagnosis under Nonstationary Conditions," *IEEE Transactions on Instrumentation and Measurement*, vol. 68, no. 12, pp. 4736–4745, Mar. 2019. DOI: 10.1109/TIM.2019.2900886.

[50] Y. Guan, M. Liang, and D.-S. Necsulescu, "Velocity synchronous bilinear distribution for planetary gearbox fault diagnosis under non-stationary conditions," *Journal of Sound and Vibration*, vol. 443, pp. 212–229, Mar. 2019. DOI: https://doi.org/10.1016/j.jsv.2018.11.039.

[51] S. Rajagopalan, J. A. Restrepo, J. M. Aller, T. G. Habetler, and R. G. Harley, "Nonstationary Motor Fault Detection using Recent Quadratic Time-Frequency Representations," *IEEE Transactions on Industry Applications*, vol. 44, no. 3, pp. 735–744, May 2008. DOI: 10.1109/TIA.2008.921431.

[52] L. Cohen, *Time-Frequency Analysis*, ser. Prentice Hall signal processing series. Englewood Cliffs, N.J: Prentice Hall PTR, 1995, ISBN: 0135945321.

[53] R. Sharma and R. B. Pachori, "Improved Eigenvalue Decomposition-Based Approach for Reducing Cross-Terms in Wigner–Ville Distribution," *Circuits, Systems, and Signal Processing*, vol. 37, no. 8, pp. 3330–3350, 2018.

[54] W. Liu and X. Guo, "Detection of Transient Power Quality Disturbances based EMD Combined with Choi-Williams Distribution," in *2012 IEEE International Conference on Automation and Logistics*, pp. 588–591.

[55] A. L. Martinez-Herrera, L. M. Ledesma-Carrillo, M. Lopez-Ramirez, S. Salazar-Colores, E. Cabal-Yepez, and A. Garcia-Perez, "Gabor and the Wigner-Ville transforms for Broken Rotor Bars Detection in Induction Motors," in *2014 International Conference on Electronics, Communications and Computers (CONIELECOMP), Cholula*, May 2014, pp. 83–87.

[56] F. Zhou, L. Yang, H. Zhou, and L. Yang, "Optimal Averages for Nonlinear Signal Decompositions—Another Alternative for Empirical Mode Decomposition," *Signal Processing*, vol. 121, pp. 17–29, Apr. 2016. DOI: https://doi.org/10.1016/j.sigpro.2015.10.022.

[57] J. C. Urresty, J. R. Riba, and L. Romeral, "Diagnosis of Interturn Faults in PMSMs Operating under Nonstationary Conditions by Applying Order Tracking Filtering," *IEEE Transactions on Power Electronics*, vol. 28, no. 1, pp. 507–515, May 2013. DOI: 10.1109/TPEL.2012.2198077.

[58] M.-C. Pan, S.-W. Liao, and C.-C. Chiu, "Improvement on Gabor Order Tracking and Abjective Comparison with Vold–Kalman Filtering Order Tracking," *Mechanical Systems and Signal Processing*, vol. 21, no. 2, pp. 653–667, Feb. 2007. DOI: https://doi.org/10.1016/j.ymssp.2006.01.006.

[59] J. S. L. Senanayaka, V. K. Huynh, and K. G. Robbersmyr, "Fault detection and classification of permanent magnet synchronous motor in variable load and speed conditions using order tracking and machine learning," *Journal of Physics: Conference Series*, vol. 1037, no. 3, 2018.

[60] H. Kim, J. Son, and J. Lee, "A High-Speed Sliding-Mode Observer for the Sensorless Speed Control of a PMSM," *IEEE Transactions on Industrial Electronics*, vol. 58, no. 9, pp. 4069–4077, Dec. 2011. DOI: 10.1109/TIE.2010.2098357.

[61] D. Kim, Y.-C. Kwon, S.-K. Sul, J.-H. Kim, and R.-S. Yu, "Suppression of Injection Voltage Disturbance for High-Frequency Square-Wave Injection Sensorless Drive with Regulation of Induced High-Frequency Current Ripple," *IEEE Transactions on Industry Applications*, vol. 52, no. 1, pp. 302–312, Sep. 2016. DOI: 10.1109/TIA.2015.2478887.

[62] S. Liang, Y. Chen, H. Liang, and X. Li, "Sparse Representation and SVM Diagnosis Method for Inter-Turn Short-Circuit Fault in PMSM," *Applied Sciences*, vol. 9, no. 2, Jan. 2019. DOI: 10.3390/app9020224.

[63] P. Pietrzak and M. Wolkiewicz, "On-line Detection and Classification of PMSM Stator Winding Faults Based on Stator Current Symmetrical Components Analysis and the KNN Algorithm," *Electronics*, vol. 10, no. 15, Jul. 2021. DOI: 10.3390/electronics10151786.

[64] J. C. Quiroz, N. Mariun, M. R. Mehrjou, M. Izadi, N. Misron, and M. A. Mohd Radzi, "Fault Detection of Broken Rotor Bar in LS-PMSM using Random Forests," *Measurement*, vol. 116, pp. 273–280, Feb. 2018. DOI: https://doi.org/10.1016/j.measurement.2017.11.004.

[65] P. Ewert, T. Orlowska-Kowalska, and K. Jankowska, "Effectiveness Analysis of PMSM Motor Rolling Bearing Fault Detectors Based on Vibration Analysis and Shallow Neural Networks," *Energies*, vol. 14, no. 3, Jan. 2021. DOI: 10.3390/en14030712.

[66] F. Arellano-Espitia, M. Delgado-Prieto, V. Martinez-Viol, J. J. Saucedo-Dorantes, and R. A. Osornio-Rios, "Deep-Learning-Based Methodology for Fault Diagnosis in Electromechanical Systems," *Sensors*, vol. 20, no. 14, Jul. 2020. DOI: 10.3390/s20143949.

[67] Z. Ullah, B. A. Lodhi, and J. Hur, "Detection and Identification of Demagnetization and Bearing Faults in PMSM Using Transfer Learning-Based VGG," *Energies*, vol. 13, no. 15, Jul. 2020. DOI: 10.3390/en13153834.

[68] B. Krawczyk, M. Galar, M. Woźniak, H. Bustince, and F. Herrera, "Dynamic Ensemble Selection for Multi-Class Classification with One-Class Classifiers," *Pattern Recognition*, vol. 83, pp. 34–51, Nov. 2018. DOI: 10.1016/j.patcog.2018.05.015.

[69] S. Liu, Y. Zhao, Z. Lin, *et al.*, "Data-Driven Event Detection of Power Systems Based on Unequal-Interval Reduction of PMU Data and Local Outlier Factor," *IEEE Transactions on Smart Grid*, vol. 11, no. 2, pp. 1630–1643, Mar. 2020. DOI: 10.1109/TSG.2019.2941565.

[70] T. Zhang, J. Chen, S. He, and Z. Zhou, "Prior Knowledge-Augmented Self-Supervised Feature Learning for Few-shot Intelligent Fault Diagnosis of Machines," *IEEE Transactions on Industrial Electronics*, pp. 10 573–10 584, Jan. 2022. DOI: 10.1109/TIE.2022.3140403.

[71] Y. Ding, J. Zhuang, P. Ding, and M. Jia, "Self-Supervised Pretraining via Contrast Learning for Intelligent Incipient Fault Detection of Bearings," *Reliability Engineering and System Safety*, vol. 218, p. 108 126, Feb. 2022. DOI: https://doi.org/10.1016/j.ress.2021.108126.

[72] C. Huang, "Featured Anomaly Detection Methods and Applications," Doctor of Philosophy in Computer Science, University of Exeter, 2018, pp. 115–124. [Online]. Available: https://ore.exeter.ac.uk/repository/%20bitstream/handle/10871/34351/HuangC.pdf?sequence=1.

[73] M. Chen, K. Zhu, R. Wang, and D. Niyato, "Active Learning-Based Fault Diagnosis in Self-Organizing Cellular Networks," *IEEE Communications Letters*, vol. 24, no. 8, pp. 1734–1737, Aug. 2020. DOI: 10.1109/LCOMM.2020.2991449.

[74] R. Blagus and L. Lusa, "SMOTE for High-Dimensional Class-Imbalanced Data," *BMC Bioinformatics*, vol. 14, no. 1, Mar. 2013. DOI: https://doi.org/10.1186/1471-2105-14-106.

[75] Z. Song, J. Yang, X. Mei, T. Tao, and M. Xu, "Deep Reinforcement Learning for Permanent Magnet Synchronous Motor Speed Control Systems," *Neural Computing and Applications*, vol. 33, no. 10, pp. 5409–5418, May 2021. DOI: 10.1007/s00521-020-05352-1.

[76] J. Cao, J. Ma, D. Huang, and P. Yu, "Finding the Optimal Multilayer Network Structure through Reinforcement Learning in Fault Diagnosis," *Measurement: Journal of the International Measurement Confederation*, vol. 188, p. 110 377, Jan. 2021. DOI: 10.1016/j.measurement.2021.110377.

[77] F. Li, Y. Wang, S. Xu, and Y. Li, "Fault Diagnosis of Permanent Magnet Synchronous Motor Inter Turn Short Circuit Based on Deep Reinforcement Learning," *Journal of Physics: Conference Series*, vol. 2137, no. 1, p. 012 004, Oct. 2021. DOI: 10.1088/1742-6596/2137/1/012004.

[78] E. Lin, Q. Chen, and X. Qi, "Deep Reinforcement Learning for Imbalanced Classification," *Applied Intelligence*, vol. 50, no. 8, pp. 2488–2502, Mar. 2020. DOI: 10.1007/s10489-020-01637-z.

[79] Y. Park, D. Fernandez, S. B. Lee, *et al.*, "Online Detection of Rotor Eccentricity and Demagnetization Faults in PMSMs Based on Hall-Effect Field Sensor Measurements," *IEEE Transactions on Industry Applications*, vol. 55, no. 3, pp. 2499–2509, Dec. 2019. DOI: 10.1109/TIA.2018.2886772.

[80] S. Moon, J. Lee, H. Jeong, and S. W. Kim, "Demagnetization Fault Diagnosis of a PMSM Based on Structure Analysis of Motor Inductance," *IEEE Transactions on Industrial Electronics*, vol. 63, no. 6, pp. 3795–3803, Feb. 2016. DOI: 10.1109/TIE.2016.2530046.

[81] D. Fernandez, D. Reigosa, T. Tanimoto, T. Kato, and F. Briz, "Wireless Permanent Magnet Temperature & Field Distribution Measurement System for IPMSMs," *2015 IEEE Energy Conversion Congress and Exposition, ECCE 2015*, pp. 3996–4003, Sep. 2015. DOI: 10.1109/ECCE.2015.7310224.

[82] D. D. Reigosa, D. Fernandez, T. Tanimoto, T. Kato, and F. Briz, "Permanent-Magnet Temperature Distribution Estimation in Permanent-Magnet Synchronous Machines Using Back Electromotive Force Harmonics," *IEEE Transactions on Industry Applications*, vol. 52, no. 4, pp. 3093–3103, Mar. 2016. DOI: 10.1109/TIA.2016.2536579.

[83] B. N. Cassimere, S. D. Sudhoff, and D. H. Sudhoff, "Analytical Design Model for Surface-Mounted Permanent-Magnet Synchronous Machines," *IEEE Transactions on Energy Conversion*, vol. 24, no. 2, pp. 347–357, Jun. 2009.

[84] A. Lehikoinen, *Arkkio's method for torque computation*, Smeklab Motors and Magnetics Consulting, 2016, Downloaded: 12.11.2018. [Online]. Available: https://www.anttilehikoinen.fi/research-work/arkkios-method-torque-computation/.

[85] B. Vaseghi, B. Nahid-Mobarakeh, N. Takorabet, and F. Meibody-Tabar, "Experimentally Validated Dynamic Fault Model for PMSM with Stator Winding Inter-Turn Fault," in *2008 IEEE Industry Applications Society Annual Meeting*, Edmonton, AB, Canada, Oct. 2008, pp. 1–5. DOI: 10.1109/08IAS.2008.24.

[86] P. Pietrzak and M. Wolkiewicz, "Comparison of Selected Methods for the Stator Winding Condition Monitoring of a PMSM Using the Stator Phase Currents," *Energies*, vol. 14, no. 6, Mar. 2021. DOI: 10.3390/en14061630.

[87] Y. Lu, Y.-M. Cheung, and Y. Y. Tang, "Bayes Imbalance Impact Index: A Measure of Class Imbalanced Data Set for Classification Problem," *IEEE Transactions on Neural Networks and Learning Systems*, vol. 31, no. 9, pp. 3525–3539, Nov. 2020. DOI: 10.1109/TNNLS.2019.2944962.

[88] R. Razavi-Far, M. Farajzadeh-Zanjani, and M. Saif, "An Integrated Class-Imbalanced Learning Scheme for Diagnosing Bearing Defects in Induction Motors," *IEEE Transactions on Industrial Informatics*, vol. 13, no. 6, pp. 2758–2769, Sep. 2017. DOI: 10.1109/TII.2017.2755064.

[89] I. Oh, S. Rho, S. Moon, S. Son, H. Lee, and J. Chung, "Creating Pro-Level AI for a Real-Time Fighting Game Using Deep Reinforcement Learning," *IEEE Transactions on Games*, pp. 1–1, Jan. 2021. DOI: 10.1109/TG.2021.3049539.

Appended Papers

Paper A

Detecting Eccentricity and Demagnetization Fault of Permanent Magnet Synchronous Generators in Transient State

Sveinung Attestog, Huynh Van Khang, Kjell G. Robbersmyr

This paper has been published as:

S. Attestog, H. V. Khang and K. G. Robbersmyr, "Detecting Eccentricity and Demagnetization Fault of Permanent Magnet Synchronous Generators in Transient State," 2019 22nd International Conference on Electrical Machines and Systems (ICEMS), Harbin, China, 2019, pp. 1-5, doi: 10.1109/ICEMS.2019.8921753.

A.1 Abstract

Eccentricity and demagnetization fault of a four-pole 1.5 kW surface mounted permanent-magnet synchronous-generator (PMSG) were modelled by using time-discretised finite element analysis (FEA). Both fault types are caused by magnetic asymmetry in the generator. The faulty behaviour of a PMSG under transient operating condition is studied with FEA. Two search coils were wound around stator teeth on opposite sides of the rotor. The induced voltage from these coils will be equal in healthy case. A fault is detected when the induced voltages are non-identical. The simulation results revealed that the envelope of the induced search coil voltage had sinusoids during dynamic eccentricity and demagnetization. Finally, a novel fault scheme is proposed to detect the mentioned faults during transient state.

A.2 Introduction

Wind turbine systems are usually based on doubled-fed induction generators or permanent magnet synchronous generators (PMSG). PMSG is gaining in popularity thanks to its simple structure, efficient energy conversion and low noise [1]. Offshore wind has been of interest for a long time. One of the main barriers is the cost of maintenance. Faults in permanent magnet synchronous machines are often caused by contamination, humidity, mechanical tensions, overloading, high temperature, vibrations, and the partial discharge of high-frequency switching from frequency converters [2]. The detection and identification of faults in PMSGs in earlier stages is critical for safe, profitable and reliable operation of offshore wind turbines.

The most common fault types in PMSGs are inter-turn short circuit, irreversible demagnetisation, and rotor eccentricity. The most popular fault detection technique in commercial use is machine current signal analysis (MCSA) where Fast Fourier Transform is used for processing the machine current signal. The faults is identified according to certain harmonic patterns. The technique is limited to stationary operating condition. Motors in electric vehicles and generators in wind turbine often operate with varying speed and load. Short-Time Fourier−, Wavelet-, and Hilbert Huang Transform are then used for analysis in transient operating conditions. Alternatively, the data generated is fed into an artificial neural network, being trained to classify the different fault patterns [3].

One of the best indicators for detecting mechanical faults like static and dynamic eccentricity is vibration signatures. The fault is detected by analysing the measured vibrations using signal processing techniques to identify the signature for a certain fault [4]. Another methods for detecting local demagnetisation and eccentricity is using analytical model based on an inverse problem [5]. A well design analytical or lumped magnetic circuit model can detect faults based on the measured terminal voltage, current and torque. An online detection method was presented in [6], which could detect local demagnetisation and dynamic eccentricity based on measurement from the Hall sensor [6].

Fault detection schemes involving search coils are intensively developed. The authors in [7] presented a fault detection scheme to detect asymmetry in the magnetic circuit of

a permanent magnet synchronous motor (PMSM). Twelve search coils are placed evenly spaced in the stator wound around their own stator tooth. The fault detection scheme used linear time-invariant filter for tracking of the fundamental component of the induced search coil voltage. This is then used to produce polar plots. The radius represents the amplitude of the induced voltage in the search coil and the angle represents the locations of the search coils. The shape of the polar plot indicated what type of faults was occurring in the electrical machine [7]. The amplitude of the induced search coil voltage is dependent on the speed of the electrical machine. This does not affect the overall shape of the polar plots, but false alarms may occur due to transient operating conditions. Unless all induced search coil voltages increase at the same rate simultaneously, keeping the shape of the polar plot.

This paper will investigate the possibility of a fault classifier for differentiating demagnetisation, static eccentricity and dynamic eccentricity. It is inspired by the fault detection scheme in [7]. The main contribution is to propose a detection scheme to detect the mentioned faults by using a fewer search coils.

A.3 Finite Element Analysis PMSG

A 1.5 kW 4-pole surface-mounted PMSG with sinusoidally distributed double layer windings was simulated. The geometry of the model is shown in Figure A.1 and is based on the motor design in [8]. The windings in each slot are divided into two coil-domains, where each of them represents a bundle of 40 turns. The model is first solved in a stationary solver where the rotor is standing still (Without applied torque or terminal voltage). This result is used as the initial conditions for the time-stepping finite element analysis (FEA). The governing equations of the electromagnetic model are below

$$\nabla \times \boldsymbol{H} = \boldsymbol{J}, \tag{A.1}$$

$$\boldsymbol{B} = \nabla \times \boldsymbol{A}, \tag{A.2}$$

$$\boldsymbol{E} = -\frac{\partial \boldsymbol{A}}{\partial t}, \tag{A.3}$$

and

$$\nabla \cdot \boldsymbol{B} = 0. \tag{A.4}$$

where $\boldsymbol{H}$ is the magnetic flux intensity, $\boldsymbol{J}$ is the current density, $\boldsymbol{B}$ is the magnetic flux density, $\boldsymbol{A}$ is the magnetic vector potential and $\boldsymbol{E}$ is the electric field intensity. The magnets are described with the linear model[9]

$$\boldsymbol{B} = \mu_r \mu_0 \boldsymbol{H} + \boldsymbol{B_r}. \tag{A.5}$$

where μ_0 is the permeability in vacuum and the relative permeability μ_r is set to 1. The remanence magnetic flux $\boldsymbol{B_r}$ is set to 0.5 T and is reduced to 0.4 T for modelling demagnetised magnet.

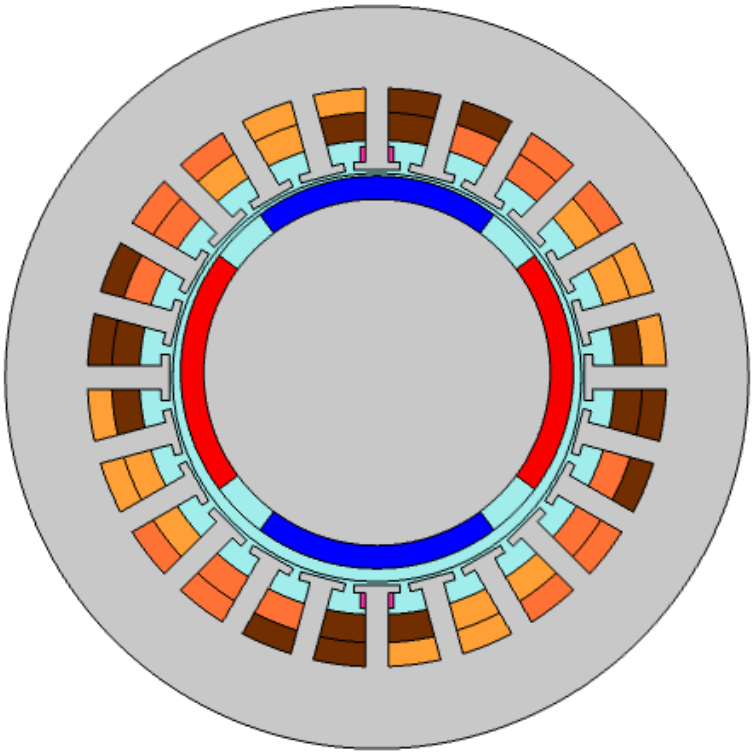

Figure A.1: PMSG Model geometry

A.4 Proposed fault detection and classification scheme

A.4.1 Fault indicator

The proposed method for fault detection is to compare the signal of two strategically placed search coils. The first search coil can be wound around any stator tooth. The second coil needs to be wound around the stator tooth located on the opposite side of the rotor. The voltage signal from these two search coils will theoretically be identical due to the geometry. Due to this criterion, this method works best on electrical machines with even number of stator teeth. The proposed fault indicator is:

$$F_{\text{Det}} = (V_{C1} - V_{C2})^2. \tag{A.6}$$

where V_{C1} and V_{C2} are the induced voltage in search coil 1 and 2, respectively. If F_{Det} is 0, then no fault is detected, and if it is not equal to 0 a magnetic asymmetry is detected. This is the case when the measurement has no noise. Measurements from a real sensor will of course have noise. In this case, a threshold δ needs to be selected based on an estimated variance in the signal. A fault is detected when F_{Det} is greater than δ.

A.4.2 Fault Classifier

Originally the suggested classifier for this paper was:

$$F_{\text{Class}} = ((a\sin(\omega(t)t+\phi)+k_1)^2 + (b\cos(\omega(t)t+\phi)+k_2)^2)^{0.5}. \tag{A.7}$$

where a, b, k_1 and k_2 are shape fitting parameters of the envelope. The time varying angular frequency $\omega(t)$ can be written as $f(t)$, where $f(t)$ is time varying frequency. The fundamental frequency of the envelope is approximately a half of the fundamental frequency to the original induced search coil voltage. This is shown later in the results. Neither $\omega(t)$ or phase angle ϕ are used for classification of the faults in the generator, but are important for fitting the curve. Equation (A.7) is inspired by the polar plots in [7]. If no fault was present in the machine, the shape of the polar plots was a perfect circle. In the case of static eccentricity, the circle was move off centre. Assuming that the speed was constant, the envelope of the induced search coil voltage will be constant over time in both cases. The polar plots in the cases of dynamic eccentricity and demagnetisation had a rotating movement over time. This will also be reflected in the envelop pattern in the induced search coil voltage.

All the parameters used to classify faults in (A.7) have a physical meaning in terms of the dynamic eccentricity and demagnetisation. Dynamic eccentricity is detected if $k_1 \neq 0$ or $k_2 \neq 0$ and demagnetisation is detected if a $\neq$ b. The equation is difficult to work with, thus it is replaced with:

$$F_{\text{Class}} = A\cos(2\omega(t)t+\phi) + B\cos(\omega(t)t+\phi) + h(t). \tag{A.8}$$

Derivation of the expression inside the square root in (A.7) will result in an equation with similar shape as (A.8). Both equation can fit the envelop of the induced search coil voltage equally well. Some information is lost in the simplification, but (A.8) is still sufficient for fitting the envelope curve for classification of faults. The parameters A and B is still loosely related to the original classification parameter a, b, k_1 and k_2. The classification algorithm based on (A.8) is shown in Figure A.2. The classification of fault types depends on whether amplitude A or B is larger than 0. It is assumed that $h(t)$ is proportional to the speed of the rotor. In this study case, it has the shape of a step response of the first order system. Both steady state value and time constant of $h(t)$ can be estimated by minimizing the square error between the envelope curve and $h(t)$. A and B is then estimated by minimizing the square error between data and (A.8) with respect to A, B, ϕ and steady state value of $\omega(t)$. Function $\omega(t)$ is assumed to be the step response of a first order system with same time constant as $h(t)$. Alternative methods for detecting the presence of the sinusoids in the envelope could have been short time Fourier transform or the best linear unbiased estimator (BLUE).

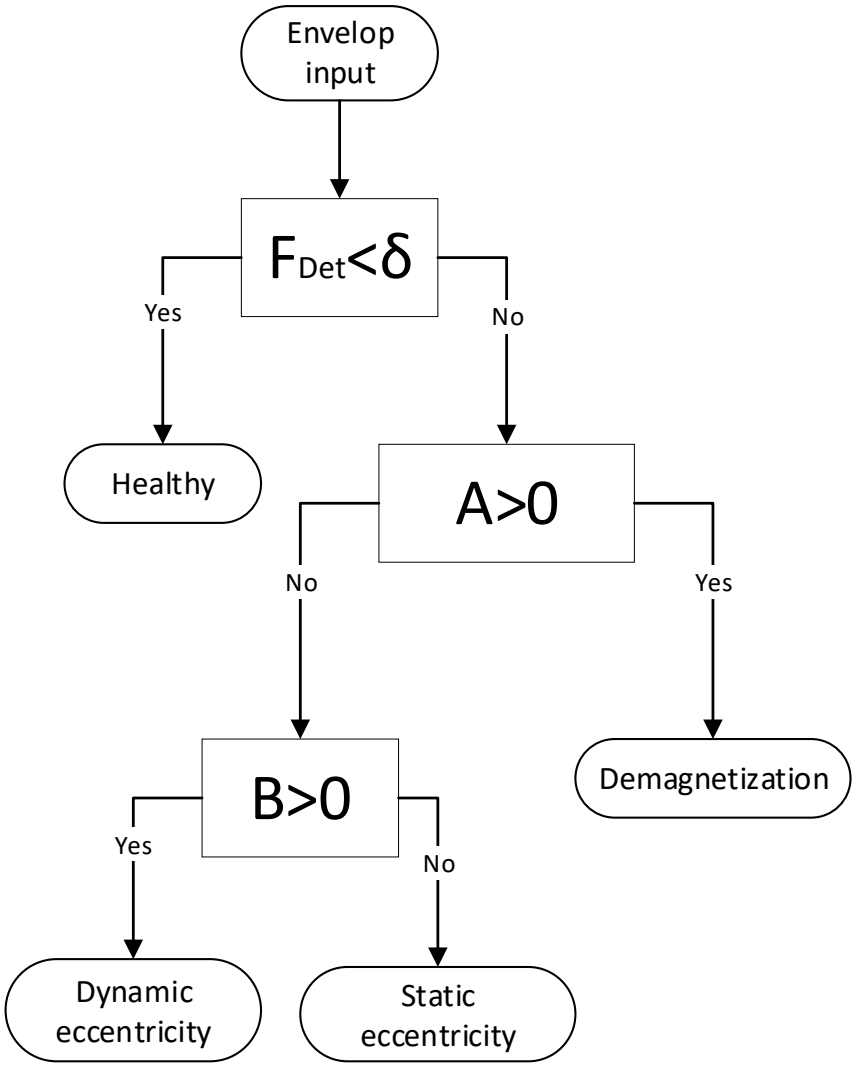

Figure A.2: Suggested fault classification scheme

A.4.3 Simulation

The fault classifier proposed in this paper was tested against simulation training data. The finite element model of the PMSG was run in four different scenarios:

- Healthy: Rotor and stator are concentric and no demagnetised magnets.
- Demagnetisation: Rotor and stator are concentric, but B_r for one South pole is reduced to 0.4 T.
- Static eccentricity: No demagnetised magnet. Rotor and stator are eccentric, but rotating domain shares centre with rotor. The severity is 23.0 %
- Dynamic eccentricity: No demagnetised magnets. Rotor and stator are eccentric, but rotating domain shares centre with stator. The severity is 23.0 %.

In all four scenarios, the rotor had a 10 Nm applied prime mover torque, and the terminals were star-connected to a resistive load of 50 Ω on each phase. Figure A.3 illustrates the difference between the static and dynamic eccentricity. S, R and RD indicates the centres for the stator-, rotor- and rotating domain, respectively. The sketch is exaggerated for better illustrating the difference between the two types of eccentricities.

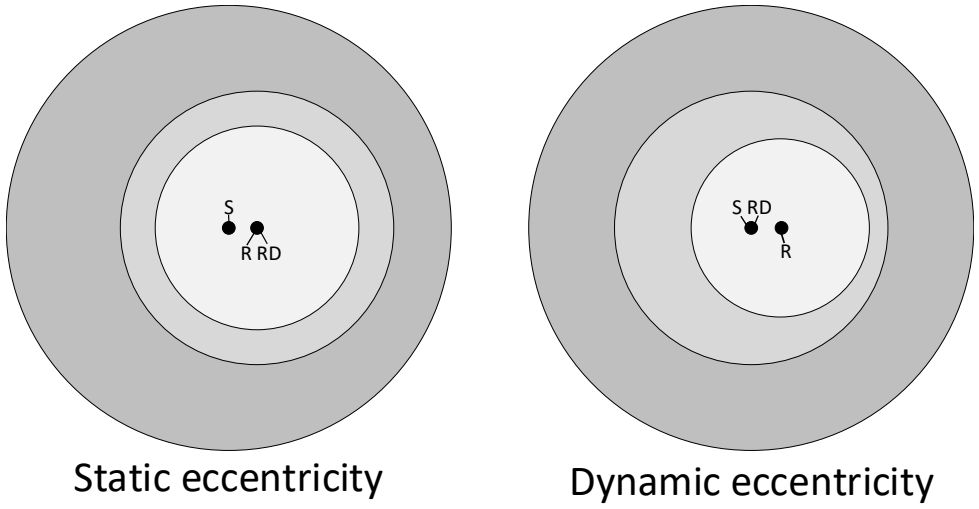

Figure A.3: Simple sketch of modelled eccentricities

A.5 Results and Discussion

Figs. A.4, A.5 and A.6 show the voltage difference between two search coils and the phase current of the PMSG in the beginning of the simulation. The search coils are located on top and bottom of the stator wound around their own stator tooth. The plots on the left side of these figures reveal that the magnetic asymmetry can effectively be detected by the voltage difference between two strategically placed search coils. The phase current is not that simple. A sinusoid is generated in all three faulty cases, which looks similar to the healthy case.

Figs. A.7a and A.7b show the plots of the absolute value of the search coils voltage in healthy case and with static eccentricity fault, respectively. The measurement period plotted in the figures was picked early in the simulation. The induced voltage has some transient behaviour and both the amplitude and frequency are increasing. Both the envelopes of the healthy case and static eccentricity case is increasing steadily. No sinusoidal components is present in the envelope signal. On the other hand, the sinusoidal components are clearly present in the case of demagnetisation and dynamic eccentricity. This is observed in Figs. A.8a and A.8b. The amplitude and frequency of the envelope seem to increase over time when the amplitude and frequency of the original voltage signal also increase. The main frequency component of the envelope curve seems to be a half of fundamental frequency of the original signal. In the case of dynamic eccentricity, the peaks of envelope curve appears at every fourth peaks of the absolute value of the induced search coil voltage. Note that two peaks indicate one period for the absolute value of the

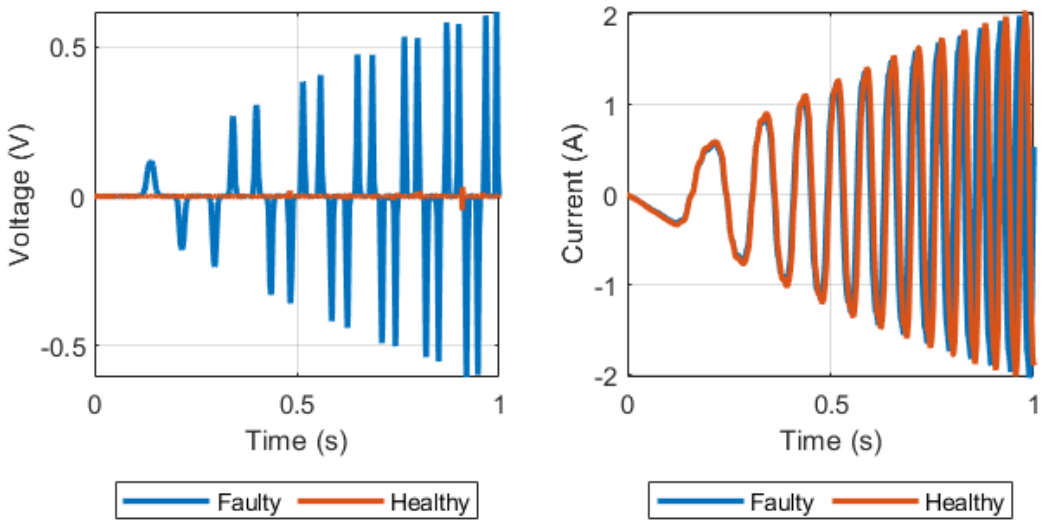

Figure A.4: Demagnetisation - Voltage difference between two strategically placed search coils (left) and phase current (right)

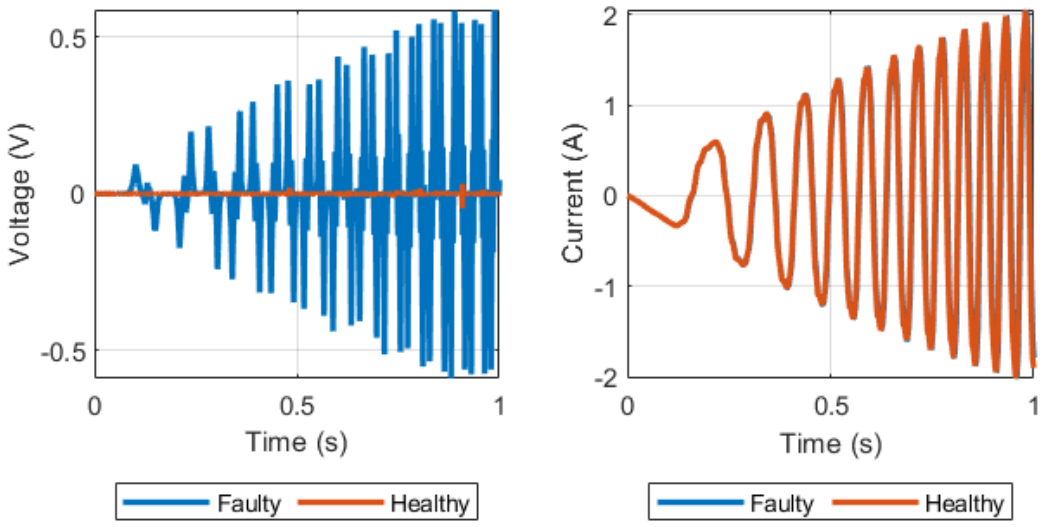

Figure A.5: Static eccentricity - Voltage difference between two strategically placed search coils (left) and phase current (right)

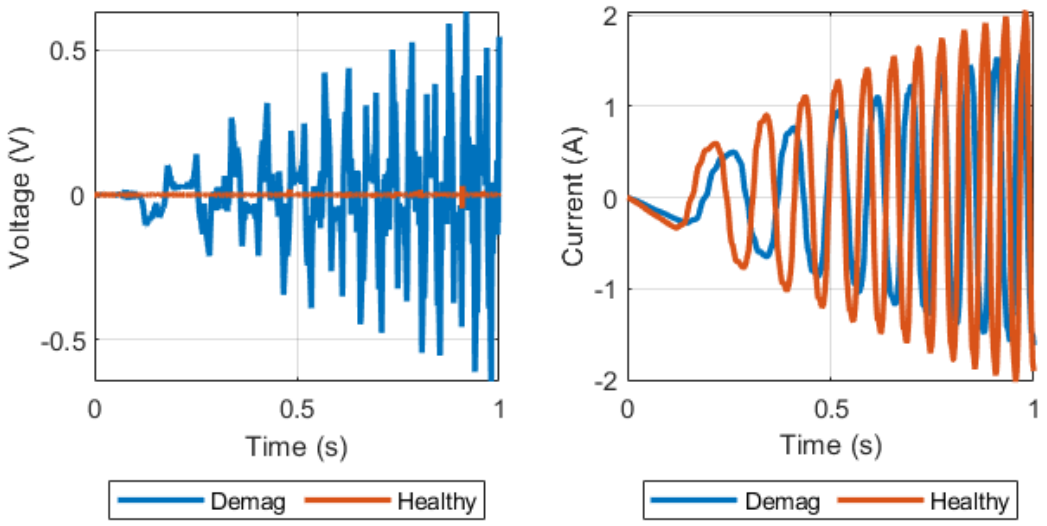

Figure A.6: Dynamic eccentricity - Voltage difference between two strategically placed search coils (left) and phase current (right)

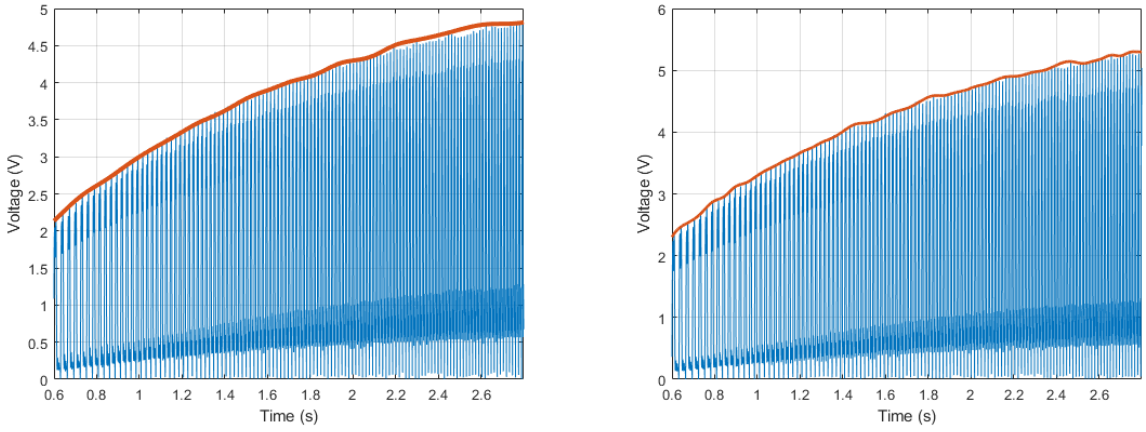

(a) (b)

Figure A.7: Envelope of absolute value of search coil voltage with (a) no faults and (b) static eccentricity fault

search coil voltage, thus the fundamental frequency of the envelope curve is half of the fundamental frequency of the induced search coil voltage.

The envelope curve in Figs. A.7a to A.8a is computed by the "envelope" function in MATLAB. The technique, being proved to be most effective, was the peak value technique. It tracks the maximum values (peaks) of a certain number of last data points. This number was set as 80, but this can vary depending on the data. The number can not be too large or too small. Neither case will not track the envelope and capture its characteristics.

Table A.1 shows the values of the amplitudes A and B from (A.8) in the voltage signal generated from the simulation. The parameters are estimated by minimising the

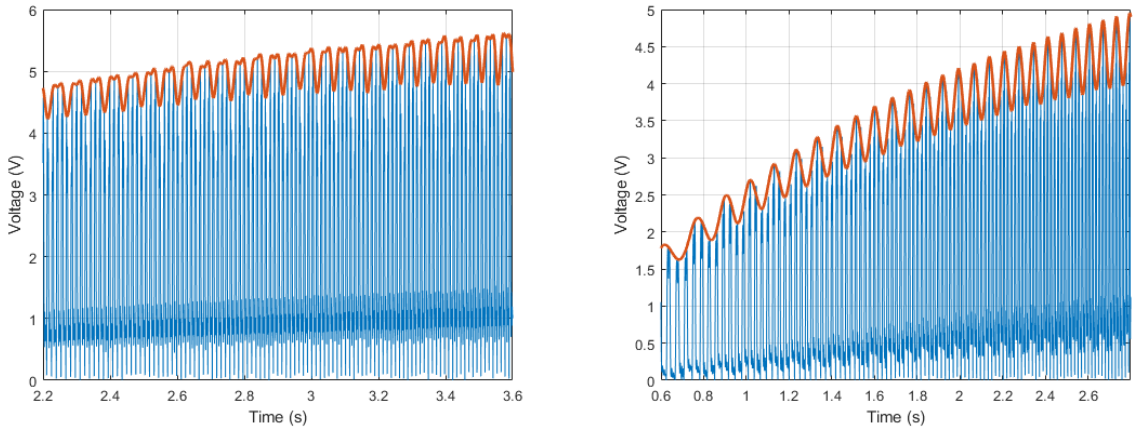

(a) (b)

Figure A.8: Envelope of absolute value of search coil voltage with (a) demagnetisation fault and (b) dynamic eccentricity

Table A.1: Estimated amplitude of sinusoids in the envelope curve

Type of fault	A	B
No-fault	0.0	0.0
Static Eccentricity	0.0	0.0
Dynamic Eccentricity	0.02	0.33
Demagnetisation	0.11	0.25

two objective functions. In the case of demagnetisation, the dataset shown in Figure A.4 includes 18001 data points in the period between 2.20 s and 2.66 s. This set was used to estimate the parameters in function $h(t)$. A smaller subset of 4596 data point was used to estimate A and B. The dataset of the envelope curve from the remaining study cases are shown in Figs. A.7a, A.7b and A.8b including 14001 data points each. A smaller subset of 3096 data points in period between 1.40 s and 1.71 seconds were used to estimate A and B. Both A and B were equal to 0 in healthy case and static eccentricity case. B was present during dynamic eccentricity and both A and B had a larger value than 0 when the PMSG was demagnetised.

The critical point for the fault classifier is the computing of the envelope. If the signal is too noisy, then the fault of the PMSG can not be classified. The noise can be reduced by filtering the signal, low pass filter, moving average filter or Savitzky-Golay filter. The current method for computing the envelope is by taking the maximum from the last data points. The envelope is captured at some parts of the dataset. Figure A.7a to Figure A.8b show some examples where the envelope was captured. The issue with the current simple method is that it will not capture the characteristics of the envelope when the fundamental frequency of the induced voltage is too small or too large. This could be solved with an algorithm where the number of data-points used for computing the envelope varies over time depending on the current fundamental frequency of the induced voltage. This will depend on the speed of the rotor.

A.6 Conclusion

In this paper, a new fault detection scheme was proposed using only 2 search coils. The difference in voltage signals from two strategically placed search coils, being in opposite sides of the rotor, can in theory detect magnetic asymmetry in the generator. The criterion for placing the search coils limits this method to permanent magnet machines with even number of stator teeth. The fault classification scheme was tested on simulations from a finite element model of a PMSG, but will probably also work for a PMSM. Datasets of the induced search coil voltage during transient state operation of the PMSG were extracted, and sinusoidal components in the envelope was identified by minimising two objective functions. Both study cases, with static eccentricity and no fault, had no sinusoidal components. Either one or two sinusoidal component were present during dynamic eccentric case or demagnetisation case, respectively.

Future work will involve experimental verification of the fault classifier and a change in the algorithm that makes it more automatic. This will make the classifier able to classify the fault faster. The alternatives may be to use BLUE or an artificial neural network which is trained to recognise envelope patterns discussed in this paper.

References

[1] B. Yang, T. Yu, H. Shu, *et al.*, "Passivity-based sliding-mode control design for optimal power extraction of a PMSG based variable speed wind turbine," *Renewable Energy*, vol. 119, pp. 577–589, Apr. 2018.

[2] N. Nishiyama, H. Uemura, and Y. Honda, "Highly Demagnetization Performance IPMSM Under Hot Environments," *IEEE Transactions on Industry Applications*, vol. 55, no. 1, pp. 265–272, Feb. 2019.

[3] Z. Ullah and J. Hur, "A Comprehensive Review of Winding Short Circuit Fault and Irreversible Demagnetization Fault Detection in PM Type Machines," *Energies*, vol. 11, no. 12, Nov. 2018.

[4] F. Cira, "Detection of eccentricity fault based on vibration in the PMSM," *Results in physics*, vol. 10, pp. 760–765, Sep. 2018.

[5] J. De Bisschop, A. A. E. Abdallh, P. Sergeant, and L. Dupré, "Analysis and selection of harmonics sensitive to demagnetisation faults intended for condition monitoring of double rotor axial flux permanent magnet synchronous machines," *IET Electric Power Applications*, vol. 12, no. 4, pp. 486–493, Apr. 2018.

[6] Y. Park, D. Fernandez, S. B. Lee, *et al.*, "Online Detection of Rotor Eccentricity and Demagnetization Faults in PMSMs Based on Hall-Effect Field Sensor Measurements," *IEEE Transactions on Industry Applications*, vol. 55, no. 3, pp. 2499–2509, May 2019.

[7] Y. Da, X. Shi, and M. Krishnamurthy, "A New Approach to Fault Diagnostics for Permanent Magnet Synchronous Machines Using Electromagnetic Signature Analysis," *IEEE Transactions on Power Electronics*, vol. 28, no. 8, pp. 4104–4112, Aug. 2013.

[8] B. N. Cassimere, S. D. Sudhoff, and D. H. Sudhoff, "Analytical Design Model for Surface-Mounted Permanent-Magnet Synchronous Machines," *IEEE Transactions on Energy Conversion*, vol. 24, no. 2, pp. 347–357, Jun. 2009.

[9] S. Ruoho, E. Dlala, and A. Arkkio, "Comparison of Demagnetization Models for Finite-Element Analysis of Permanent-Magnet Synchronous Machines," *IEEE Transactions on Magnetics*, vol. 43, no. 11, pp. 3964–3968, Nov. 2007.

Paper B

Modelling Demagnetized Permanent Magnet Synchronous Generators using Permeance Network Model with Variable Flux Sources

Sveinung Attestog, Huynh Van Khang, Kjell G. Robbersmyr

This paper has been published as:

S. Attestog, H. Van Khang and K. G. Robbersmyr, "Modelling Demagnetized Permanent Magnet Synchronous Generators using Permeance Network Model with Variable Flux Sources," 2019 22nd International Conference on the Computation of Electromagnetic Fields (COMPUMAG), Paris, France, 2019, pp. 1-4, doi: 10.1109/COMPUMAG 45669.2019.9032791.

B.1 Abstract

The partial demagnetisation in a four-pole 1.5 kW surface mounted permanent-magnet synchronous-generator was modeled by permeance network model (PNM). The results were compared to a 2-D time-stepping finite element analysis (FEA). Both models where simulated in scenarios where one of the magnets where 20 % and 100 % demagnetised and when none of the magnets where demagnetised. The results showed that the proposed PNM with variable magnetic flux sources matched the results of the FEA. The proposed method only need to invers the permeance matrix once before the time simulation, while the traditinal PNM need to invers it in every time step. This make the proposed model less computationally heavy when modeling electrical machines in healthy and faulty conditions, like demagnetisation, short circuit, and static eccentricity. The difference is smaller when modeling dynamic eccentricity, becuase the geometry of the airgap changes over time.

B.2 Introduction

Demagnetisation normally occurs in a permanent-magnet synchronous-generator (PMSG) due to low magnetic flux in high coercivity under high-temperature environments, being the result of poor cooling or overloading [1]. Finding the best indicators for this phenomenon is important for controlling and maintenance of the PMSG. Measured parameters, namely currents, voltages, torques, or output powers, are normally analysed using signal processing techniques in fault diagnosis. This conventional approach is fast, but treats the generator like a black box. Further, run-to-failure tests or seeded faults are often difficult, expensive and infeasible in certain machines. Understanding physical background of a fault allows finding the best measured parameters or fault indicators. Finite element analysis (FEA) has been a useful approach for modelling motors with faults and providing numerical data for testing fault diagnosis algorithm. However, computational burden is the main disadvantage of FEA. Processing powers of modern computers are increasing, but avoiding heavy computation is still important. Further, models and algorithms used in condition monitoring need to be fast to solve, thus a too detailed model is not suited for this purpose. Using permeance network models (PNM) or called magnetic equivalent circuit is a promising solution, but modelling rotation in PNM was identified as a main challenge to be addressed further [2]–[4].

One way to model rotation of the rotor in the PNM is the use of variable resistors in the airgap domain [2]. The nodes connecting between the rotating domain (rotor) and stationary domains (stator) are all connected to one another. Authors in [3] and [4] focused on induction motors and permanent magnet synchronous machines, respectively. The principle is that the permeance in the airgap will change over time when the rotor moves. The permeance depending on rotor position is usually obtained by FEA. If the network has n number of nodes both in the rotor and stator, which are all connected, then $2n^2 + 2n$ entries in the permeance matrix need to be updated, because of the change in rotor position. Another approach is to re-mesh the network in the airgap domain when the rotor moves as detailed in [5], which is almost like a FEA. The permeance matrix

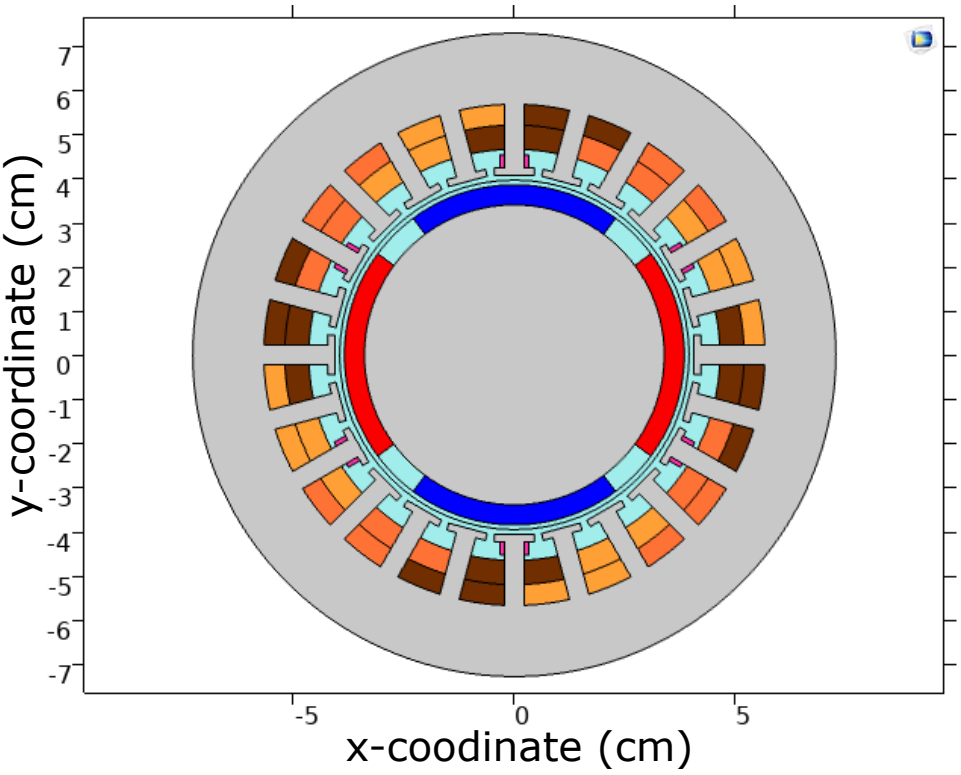

Figure B.1: Model geometry of permanent magnet synchronous generator

need to be inverted in every time step, because of the re-meshing. This is the majority of the computational complexity. Other methods involve hybrid models between PNM and FEA [6].

This work proposes a method to model rotation of the rotor in a PNM. The suggested method involves adjusting the magnetic flux sources representing the magnets and changing their direction over time. This method would be less complex as compared to the existing methods because it does not require any change of the entries in the permeance matrix over time due to the rotation of the rotor. The time depended parameters will be in the vector describing the magnetic flux sources in the network. Furthermore, the developed PNM is used to model a PMSG under healthy and demagnetised conditions.

B.3 Permeance Network Model

This section will describe and explain the proposed method for describing the PNM with variable magnetic flux sources. The geometry of a four-pole 1.5 kW surface mounted PMSG with double layer distributed windings is shown in Figure B.1, which is also used in the FEA for a comparative study.

B.3.1 Reluctance and Permeance

Permeance is the inverse of reluctance. The PMSG in Figure B.1 is subdivided into smaller elements called flux tubes. The general equation for computing the reluctance of the flux tube connected between nodes i and j is:

$$\mathcal{R} = \int_i^j \frac{1}{\mu(l)\mathrm{A}(l)} dl, \tag{B.1}$$

where μ is the permeability and $A(l)$ is the cross-sectional area along length l. The equations for the permeance of a few specific geometries are given in [7]. The permeance for stator teeth was computed by the equations for box shape flux tubes while the remaining flux tubes are calculated by the equations for trapezoids, which is different depending on direction of the flux [7].

B.3.2 Magnetic Flux Sources

The equivalent circuit of a permanent magnet or other sources of magnetic motive force (MMF) is a voltage source connected in series with a reluctance. A sketch of the equivalent circuit is shown in Figure B.5. This circuit can be replaced with a current source connected parallel with a reluctance [5] as shown in Figure B.3.

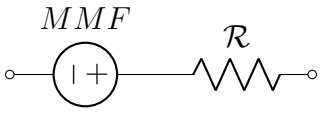

Figure B.2: Equivalent circuit of a magnetic motive force source

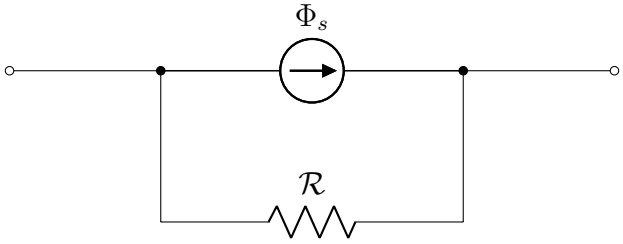

Figure B.3: Equivalent circuit of a magnet flux source

The relation between MMF and Φ_s is given by

$$\Phi_s = \frac{\mathrm{MMF}}{\mathcal{R}}. \tag{B.2}$$

The MMF sources induced by the phase currents I_a, I_b and I_c are computed by

$$\mathrm{MMF}_{\mathbf{Coil}} = N_a I_a + N_b I_b + N_c I_c, \tag{B.3}$$

where $\boldsymbol{N_a}$, $\boldsymbol{N_b}$ and $\boldsymbol{N_c}$ are vectors describing the number of turns in each stator slot and direction of the windings of phase a, b and c, respectively. The first entry of $\mathbf{MMF}_{\mathbf{Coil}}$ is the MMF source induced by the phase currents in the windings of stator slot number 1.

The value of Φ_s for a permanent magnet is equal to the product of its coercive force and height [5]. A second approach is to select the magnetic flux density induced by the magnet and multiply by the cross-sectional area of the flux tube in the PNM containing

the magnet. The flux sources describing the magnets of a healthy permanent magnet machine is defined as

$$\Phi_{mag}(\theta) = \begin{cases} \Phi_s & \text{if } \theta - \theta_{ref} \in [0, \frac{5\pi}{12}] \cup [\pi, \frac{17\pi}{12}] \\ -\Phi_s & \text{if } \theta - \theta_{ref} \in [\frac{\pi}{2}, \frac{11\pi}{12}] \cup [\frac{3\pi}{2}, \frac{23\pi}{12}] \\ 0 & \text{else} \end{cases} \tag{B.4}$$

The reference angle θ_{ref} is with respect to the position of the stator teeth in the model. The position of the rotor needs to have a value between 0 and 2π. Alternatively, (B.4) can be replaced by a single continuous equation obtained from Fourier transform, which has the similar shape. If (B.4) is used, sudden jumps in the estimated flux density over time will occur. Demagnetisation can be modelled by decreasing the magnitude of the magnetic flux density from portions of the magnet.

B.3.3 Model Setup

Magnetic flux sources are used instead of MMF sources, because this reduces the size of the matrix describing the network [5]. The governing equation of the PNM is

$$\boldsymbol{\mathcal{P}} \boldsymbol{F_m} = \boldsymbol{\Phi_s}, \tag{B.5}$$

where

$$\boldsymbol{\mathcal{P}} = \begin{bmatrix} \mathcal{P}(1,1) & \mathcal{P}(1,2) & \cdots & \mathcal{P}(1,n) \\ \mathcal{P}(2,1) & \mathcal{P}(2,2) & \cdots & \mathcal{P}(2,n) \\ \vdots & \vdots & \ddots & \vdots \\ \mathcal{P}(n,1) & \mathcal{P}(n,2) & \cdots & \mathcal{P}(n,n) \end{bmatrix}, \tag{B.6}$$

$$\boldsymbol{F_m} = \begin{bmatrix} F_m(1) \\ F_m(2) \\ \vdots \\ F_m(n) \end{bmatrix} \tag{B.7}$$

and

$$\boldsymbol{\Phi_s} = \begin{bmatrix} \Phi_s(1) \\ \Phi_s(2) \\ \vdots \\ \Phi_s(n) \end{bmatrix}. \tag{B.8}$$

The diagonal entries in permanence matrix $\boldsymbol{\mathcal{P}}$ are the sum of permeances connected to a node and the remain entries are the permeance between 2 different nodes multiplied by -1. In the case of a PNM with n number of nodes and m number of magnetic flux sources, the size of $\boldsymbol{\mathcal{P}}$ is $n \times n$. If the magnets and the MMF induced by the phase currents was represented by the equivalent circuit in Figure B.2, the size of the matrix describing the network would increase to $(n+m) \times (n+m)$.

Previous papers showed how rotation could be modelled by variable airgap permeances [2] or re-meshing the network in the airgap [5]. These strategies must change the entries

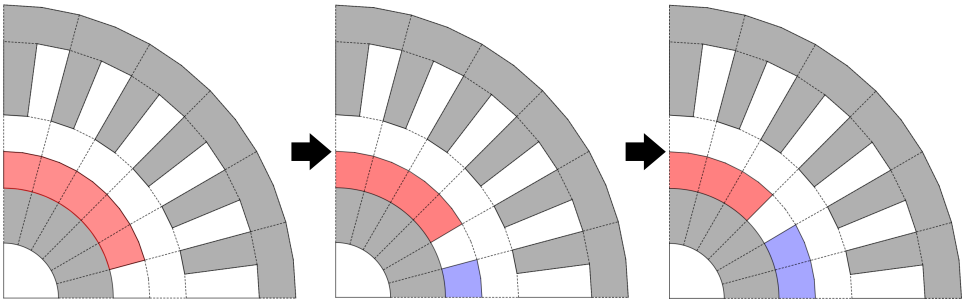

Figure B.4: Illustration of moving rotor (counter clockwise rotation)

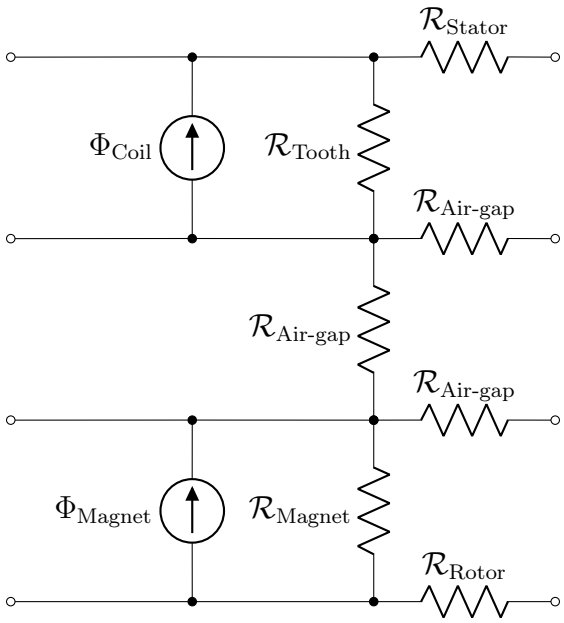

Figure B.5: Unit equivalent circuit of permeance network

of the permeance matrix and invert it in every time step. It is proposed in this paper to change the direction of flux sources representing the magnets instead. Figure B.4 shows a sketch of a quarter of the motor at different rotor positions. The whole motor geometry is subdivided into 24 sectors. Each of them includes one stator tooth, one stator slot and parts of airgap, magnet, rotor and stator yoke. One of these sections can be described with the magnetic circuit in Figure B.5. Within Figure B.4, the red domain is the North pole with magnetic flux point radially outwards, and the blue domain is the South pole with magnetic flux source pointing radially inwards. The magnetic flux in the source switches between a positive value (North pole) and a negative value (South pole). The flux sources in the domains without magnets between the North and South pole are equal to 0 Wb. Variable magnetic flux sources can mimic the rotation of the rotor, and no entry in the permeance matrix needs to change due to the rotation of the rotor and the matrix only need to be inverted once before the time simulation. The exception is dynamic eccentricity where the geometry of in the airgap change over time.

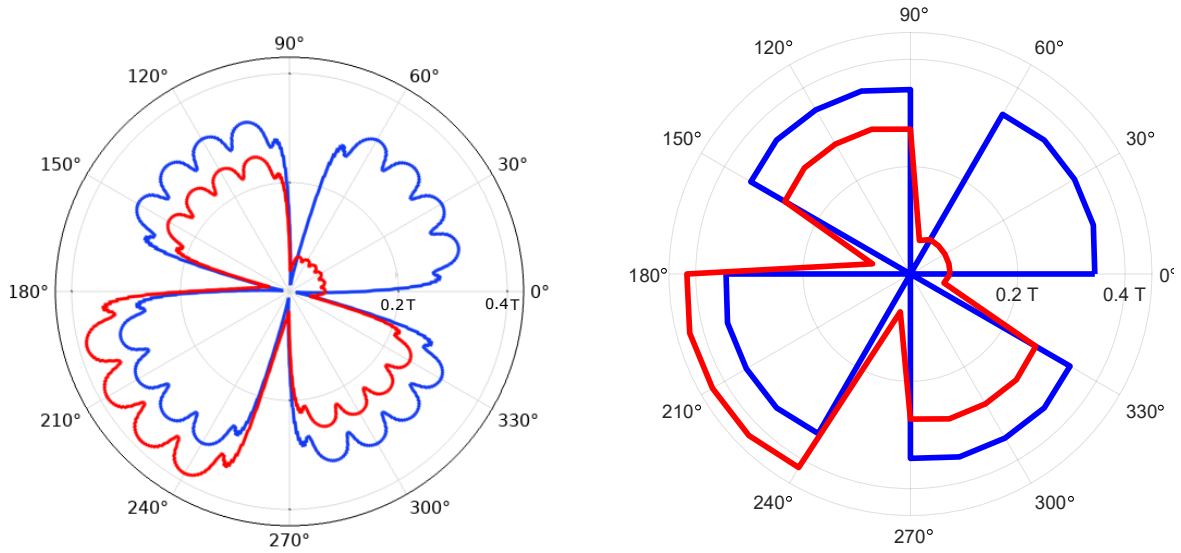

(a) (b)

Figure B.6: Caption place holder

B.4 Results and Discussions

This section will present and discuss the simulation results. A adaptive time-stepping FEA defined by Maxwell's equations were used as a benchmark comparison. The magnets in the FEA were described with the linear model [8]. First simulation was a stationary study with motor speed equal to 0 rpm, and the phase current amplitudes were 0 A. This first simulation generates the initial conditions for time-stepping FEA simulations. The machine was analysed in the generator mode. The terminals were connected to resistive loads of 50 Ω, and the applied prime mover torque was 10 Nm. The achieved steady state speed from the FEA was 1300 rpm and this was set as motor speed in the PNM. Both in the stationary- and time-stepping simulations of the PMSG were modelled in two scenarios, no fault and with one magnet with 20 % demagnetisation and 100 % demagnetisation.

Figure B.6a shows the initial value of magnetic flux density in the middle of the air-gap in the polar coordinate system for a healthy generator (blue) and a demagnetised generator (red). The variation in amplitude in the area covered by magnets is due to variation of air-gap length. It is shown that the magnetic flux density in the middle of the airgap near the demagnetised magnets is much smaller compared to the non-demagnetised magnet. The magnetic flux densities at South poles are also reduced, but increased at the remaining healthy North pole. Therefore, search coils [9] or hall sensors [10] should be installed for monitoring the condition of demagnetisation. The PNM has a coarser resolution but the characteristics the airgap magnetic flux density is still captured in Figure B.6b.

The magnetic flux density from one stator tooth in a healthy case was extracted in the time domain as shown in Figure B.7a, in which the waveforms from the PNM and the FEA have a good agreement. The resulting plots from the PNM have some sudden jumps, but they occur when the the time derivative of the magnetic flux is large. The

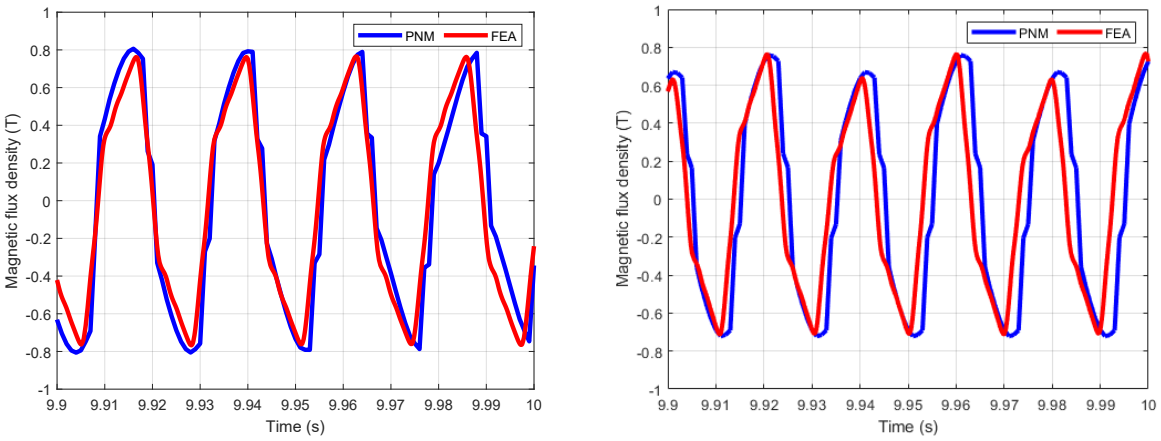

(a) (b)

Figure B.7: Magnetic flux density in stator tooth computed with FEA and PNM with (a) no fault and (b) 20 % demagnetisation on one magnet

magnetic flux sources in magnets are not defined by a continuous function, and at some point the change in magnetic flux density is infinity large. This is not an issue because the network does not include any inductors or capacitor, which would create some dynamic responses. Figure B.7b shows the magnetic flux density through a stator tooth when one of the North poles is demagnetised about 20 %. In other word, the strength of the magnet is reduced to 80 % of original strength. The result from the PNM matches the curve from the FEA.

From simulation time point of view, both PNM and FEA simulated 10 seconds of operation, but the FEA accelerated from 0 to 1300 rpm and the PNM was operating in steady state at a speed of 1300 rpm. The PNM could solve in less than 0.7 s, while the FEA used several hours to complete a 10-second operation. The FEA model used a free triangular mesh with 6609 element with average skewness of 0.78. When the rotor domain moved in each time step, the rotor-mesh did not necessary align with the stator-mesh in the boundary between them. The interpolation across this border boundary is one of the main reason behind the large computational burden. The time step of the FEA decreased when the rotor speed increased, but reducing the tolerance of the solver can improve the computation time.

Saturation was not included in the current model, but the main purpose of this paper was to show how variable magnetic flux sources could represent the rotations of the motor. Saturation can easily be included by setting up a recursive algorithm and iteratively updating the relative permeability of the non-linear material. To achieve this, the first step is to obtain the magnetic flux flowing between the nodes in the network based on an initial guess of the relative permeabilities of the materials defined in the model. Then, the magnetic flux density and magnetic flux intensity are computed, updating of relative permeability and repeating the process until it converges [5].

B.5 Conclusion

This paper proposed a method to model rotation of the rotor in a permeance network model (PNM) with variable magnetic flux sources. This method can lower the computational burden significantly as compared to the traditional models with variable airgap permeances or re-meshing of the network in the airgap. If the centre of rotor does not change over time, it is not necessary to invert the permeance matrix in very time step. The proposed method does not require any special variable permeance function computed in a FEA, which allows more focus on strategic design of the permeance network for accurate computation.

The proposed method was tested on a coarse PNM example, and a comparative study was presented by comparing the results from the proposed model and a FEA, showing that the proposed PNM is able to simulate an PMSG in healthy and faulty condition quickly. The simulated results confirm that the demagnetisation can be detected effectively based on the polar plot of magnetic flux density in the middle of the airgap of the generator by using search coils or hall sensors.

References

[1] N. Nishiyama, H. Uemura, and Y. Honda, "Highly Demagnetization Performance IPMSM Under Hot Environments," *IEEE Transactions on Industry Applications*, vol. 55, no. 1, pp. 265–272, 2019.

[2] C. Delforge and B. Lemaire-Semail, "Induction machine modeling using finite element and permeance network methods," *IEEE Transactions on Magnetics*, vol. 31, no. 3, pp. 2092–2095, 1995.

[3] A. Mahyob, P. Reghem, and G. Barakat, "Permeance Network Modeling of the Stator Winding Faults in Electrical Machines," *IEEE Transactions on Magnetics*, vol. 45, no. 3, pp. 1820–1823, 2009.

[4] D. Faustner, W. Kemmetmüller, and A. Kugi, "Magnetic Equivalent Circuit Modeling of a Saturated Surface-Mounted Permanent Magnet Synchronous Machine," *IFAC-PapersOnLine*, vol. 48, no. 1, pp. 360–365, 2015.

[5] D. Gómez, A. Rodríguez, I. Villar, A. López-de-Heredia, I. Etxeberria-Otadui, and Z. Zhu, "Experimental validation of an enhanced permeance network model for embedded magnet synchronous machines," *Electric Power Systems Research*, vol. 140, pp. 836–845, 2016.

[6] G. Devornique, J. Fontchastagner, D. Netter, and N. Takorabet, "Hybrid Model: Permeance Network and 3-D Finite Element for Modeling Claw-Pole Synchronous Machines," *IEEE Transactions on Magnetics*, vol. 53, no. 6, pp. 1–4, 2017.

[7] M. Zhang, A. Macdonald, K. Tseng, and G. Burt, "Magnetic equivalent circuit modeling for interior permanent magnet synchronous machine under eccentricity fault," *2013 48th International Universities' Power Engineering Conference (UPEC)*, 1–6, Dublin, 2013.

[8] S. Ruoho, E. Dlala, and A. Arkkio, "Comparison of Demagnetization Models for Finite-Element Analysis of Permanent-Magnet Synchronous Machines," *IEEE Transactions on Magnetics*, vol. 43, no. 11, pp. 3964–3968, 2007.

[9] Y. Da, X. Shi, and M. Krishnamurthy, "A New Approach to Fault Diagnostics for Permanent Magnet Synchronous Machines Using Electromagnetic Signature Analysis," *IEEE Transactions on Power Electronics*, vol. 28, no. 8, pp. 4104–4112, 2013.

[10] Y. Park, D. Fernandez, S. B. Lee, *et al.*, "Online Detection of Rotor Eccentricity and Demagnetization Faults in PMSMs Based on Hall-Effect Field Sensor Measurements," *IEEE Transactions on Industry Applications*, vol. 55, no. 3, pp. 2499–2509, 2019.

Paper C

Field Reconstruction for Modelling Multiple Faults in Permanent Magnet Synchronous Motors in Transient States

Sveinung Attestog, Huynh Van Khang, Kjell G. Robbersmyr

This paper has been published as:

S. Attestog, H. Van Khang and K. G. Robbersmyr, "Field Reconstruction for Modeling Multiple Faults in Permanent Magnet Synchronous Motors in Transient States," in IEEE Access, vol. 9, pp. 127131-127140, 2021, doi: 10.1109/ACCESS.2021.3112224.

C.1 Abstract

Conventional field reconstruction model (FRM) for electrical machines has proved its main strength in efficient computations of magnetic fields and forces in healthy permanent magnet synchronous machines (PMSM) or faulty machines in steady states. This study aims to develop a magnet library of different magnet defects and include inter-turn short-circuit (ITSC) in the FRM for PMSM. The developed FRM can model a combination fault between ITSC, and magnet defect in a PMSM in transient states. Within the framework, an 8-turn ITSC was modelled in both finite element analysis (FEA) and FRM, and then identified by the extended Park's vector approach. The air-gap magnetic field reproduced by the FRM shows a good agreement with the result from time-stepping FEA. The computation speed is over 1000 times faster than an equivalent time-stepping FEA. The suggested FRM allows for quickly understanding effect of faults in the rotor and stator on the air-gap magnetic flux density and identifying unique signatures for such defects.

C.2 Introduction

Modelling and simulation allow for a profound understanding of electrical machines in healthy and faulty conditions. Usually, modelling of electrical machines requires a trade-off among computational burden, complexity and accuracy. Electrical equivalent circuit (EEC), winding function theory, magnetic equivalent circuit, and finite element analysis (FEA) have been the most common modelling methods for electrical machines for many decades. One modelling strategy of creating new models is to modify previous models to include more physical phenomena. The other one is to combine two modelling techniques to obtain individual merits or compensate for any shortcoming in each method. Among others, field reconstruction model (FRM) is very efficient in computing magnetic fields and forces in electrical machines [1]. This method was first developed about one and a half decades ago, being briefly discussed hereafter.

The FRM technique recreates the airgap magnetic flux density by superimposing and phase-shifting the radial and tangential components of magnetic flux density, exported from the static FEA. It maintains the accuracy of FEA, but is significantly faster to compute, especially in time-stepping simulation or solving multi-physics problems. The authors in [2] investigated the vibration level of a permanent magnet synchronous motor (PMSM) at different speeds, and loads in steady-state conditions. Within the work, each fault scenario required a computation time of 70 min in FRM, while the equivalent FEA would require 100 days. The authors in [3] published many papers on using FRM to deal with fault detection of five-phase PMSMs and optimal current excitation.

Conventional FRMs have two variable inputs: rotor position and currents. This linear model fits well surface-mounted permanent magnet synchronous motor (SMPMSM) because those machines do not work much in saturation conditions. The conventional FRMs [4] must respect the following assumptions:

- No deformation in stator or rotor core structures due to internal forces

- No saturation condition
- Zero flux density in the axial direction
- No end-coil effect
- Hysteresis and eddy currents are neglected

To improve the existing FRMs, three versions of the FRMs have been proposed in [5]–[7] during the last decade. These FRMs included the interaction between the magnets and stator teeth, and slotting effect. The first one combined relative and differential permeabilities, being obtained numerically in static FEA. The second one simplified the motor geometry by employing conformal mapping and transforming the slotted stator to a slotless stator. However, the permeability in the airgap requires a more complicated equation, depending on the x- and y-coordinate. The last one considers the slotting effect and non-linear material by computing the basis functions at different rotor positions and current excitation. A look-up table is generated from the static FEAs. This allows the FRM to model interior permanent magnet synchronous motors. Towards fault diagnosis, the authors in [8] predicted partial demagnetisation and static eccentricity by FRM. In this framework of static eccentricity, the non-uniform airgap has to be taken into account by generating the basis functions for each stator phase separately, and then computing the rotor basis function for all rotor positions. To our best knowledge, no existing FRM is able to model multiple faults in a SMPMSM in transient states.

This work aims to develop a FRM for modelling SMPMSMs in transient states, allowing for quickly investigating multiple faults in dynamic operations. The first contribution is to build a magnet library for the FRM to model SMPMSMs in faulty conditions. One magnet is quickly studied at a time in static FEAs. The suggested library consists of several faulty magnets, which can be combined in any way for recreating the rotor basis functions for the FRM. The second contribution is to include the effect of short circuit in the FRM. A FRM was initially used for detecting inter-turn short circuit (ITSC) in five-phase machines [9], but to the authors' knowledge, this has not been fully explored in transient states or mixed faults. The two modifications allow the proposed FRM to model SMPMSMs with combined magnet defects and inter-turn short circuit in transient states. The performance of the proposed FRM is verified by using time-stepping FEA.

C.3 Developed Field Reconstruction Model

The principle of the FRM is to create a set of basis functions for the magnetic field in the airgap. In case of SMPMSMs, this includes the magnets in the rotor and armature current in the stator. They are studied separately and exported from static FEAs and later superimposed in the FRM [10].

$$\begin{aligned} B_N(\theta+\theta_m, I(t)) &= B_{nPM}(\theta+\theta_m) + B_{nS}(\theta, I(t)) \\ B_T(\theta+\theta_m, I(t)) &= B_{tPM}(\theta+\theta_m) + B_{tS}(\theta, I(t)). \end{aligned} \tag{C.1}$$

The basis functions are extracted from the airgap at the distance R from the center. The static FEA generates the x- and y-components of the flux density, but they need to be converted to polar coordinate r and θ for the FRM. However, the rotor basis function is phase shifted by the rotor position θ_m. The exported functions of flux density depend on both r and θ. For a simplification, r is chosen to be constant, thus is not needed in the description in (C.1). The stator basis function is excited by the three phase currents $I_a(t)$, $I_b(t)$, and $I_c(t)$ represented by $I(t)$ in (C.1). A block diagram of the proposed FRM is shown in Figure C.1.

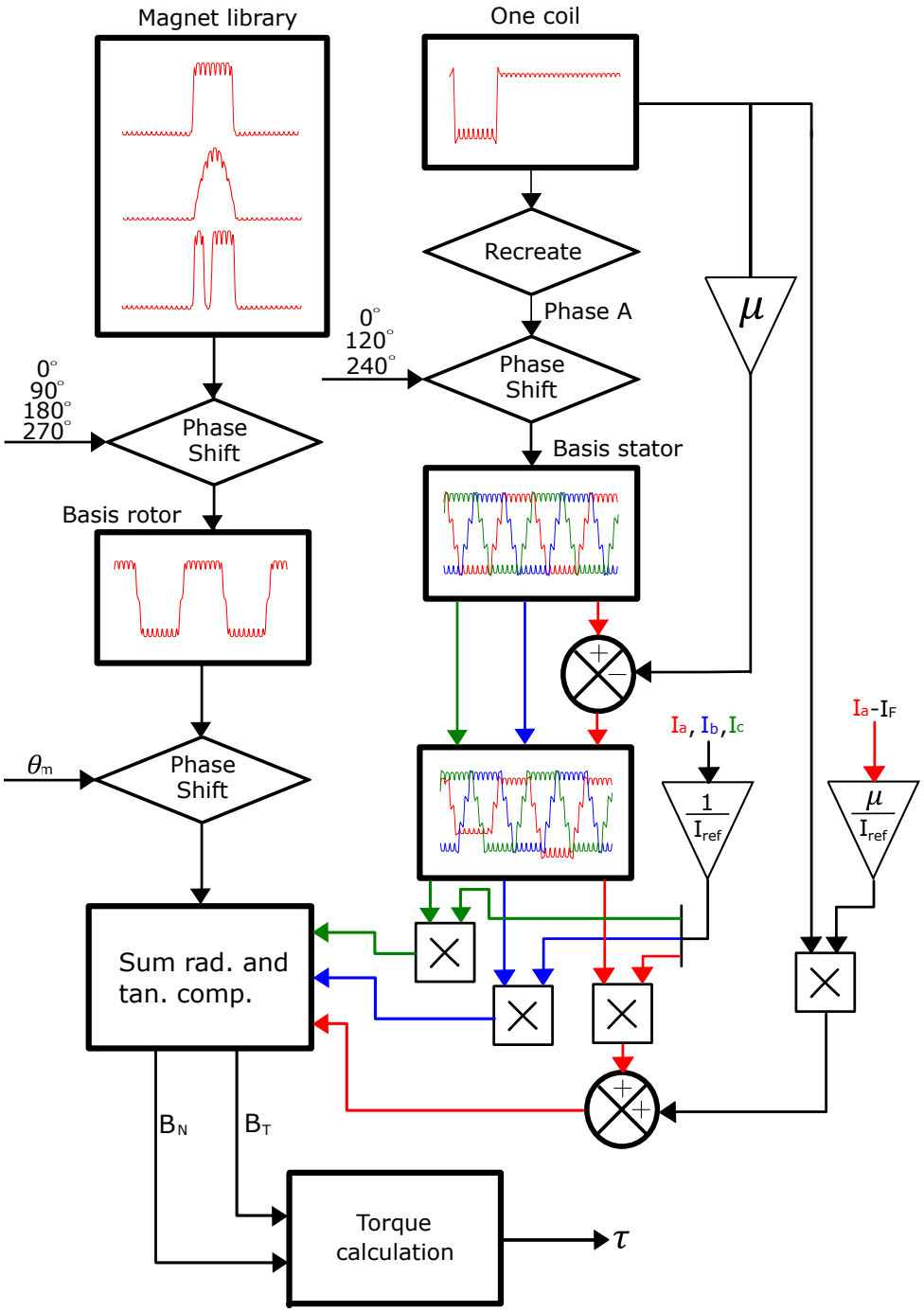

Figure C.1: The suggested diagram of field reconstruction model

C.3.1 Rotor Basis Function and Magnet Library

The rotor basis function is obtained by setting the phase currents to 0 A. Conventionally, all the magnets are defined in FEA when computing the rotor basis function. It is proposed to only let one of the magnets be active and export radial ($B_{r1PM,k}$) and tangential ($B_{t1PM,k}$) components for the single magnet basis functions to the FRM. The complete rotor basis functions (B_{rPM} and B_{tPM}) are then recreated in (C.2).

$$\begin{aligned} B_{nPM}(\theta) &= \textstyle\sum_{k=1}^{2p}(-1)^{k-1}B_{n1PM,k}\left(\theta + \frac{\pi(k-1)}{p}\right) \\ B_{tPM}(\theta) &= \textstyle\sum_{k=1}^{2p}(-1)^{k-1}B_{t1PM,k}\left(\theta + \frac{\pi(k-1)}{p}\right), \end{aligned} \tag{C.2}$$

The integer $k = [1, 2p]$, where p is the pole pair. In this study, a North pole was selected as the active magnet, but the South pole can easily be computed by multiplying with -1. The sign of the magnets is taken into consideration in (C.2), but is not included in Figure C.1. A collection of individual magnet basis functions with different defects is put into the magnet library. The radial components of different magnets are shown in the top left corner of Figure C.1, but both radial and tangential components are included in pairs. Any magnet can be replaced with any term in (C.2), thus any sets of magnets can be combined and rearranged in the FRM without the need to study every set in static FEAs. This is very time-saving in term of combinatorics and factorial function. Figure C.2 shows the magnetic flux density at the rotor positions of 0° and 10°, being as an example of a reconstructed rotor including three healthy magnets and one faulty magnet, in which a piece is missing [11].

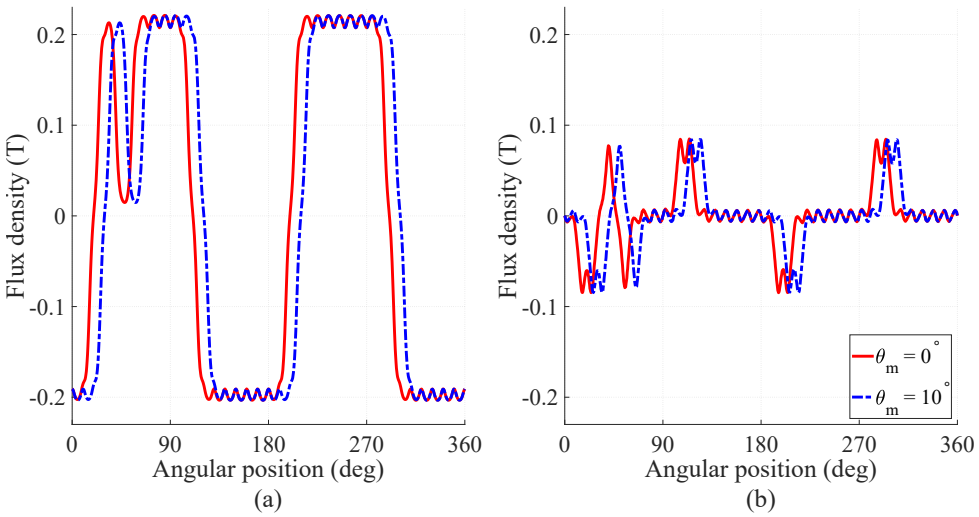

Figure C.2: Recreated rotor function at two different rotor positions with parts removed from one magnet, (a) radial component and (b) tangential component

The single magnet basis function is computed at multiple angles of 1° increment in the interval $[0°, 10°]$, being used as a look-up table in the model. The contribution from the rotor is computed by interpolation in the look-up table at an angle between 0° and 10°. This angle is the remainder after subtracting the position θ_m by the closest multiple of slot

pitch (10° for 36 slots motor), which is still smaller than θ_m. The output function is phase-shifted by that slot pitch multiple. Switching the order between these two operations will increase the computational burden. For example, when $\theta_m = 73.6°$, a function is extracted by interpolating between 3° and 4°, then phase-shifting that output function by 70°. The purpose of the look-up table is to include the slotting effect as described in [7].

The phase-shift process is conducted by removing parts of the basis function vector at the beginning, which are added at the end or in the other way around, depending on the direction of rotation. This can be done by using a look-up table. The rotor basis functions are repeated two times in the interval of $[0, 4\pi]$. The air-gap field basis function is extracted with an interpolation for the interval of $[\theta_{r,min}, \theta_{r,min} + 2\pi]$. The angle $\theta_{r,min}$ equals θ_m mod 360°. In other words, the smallest positive remainder of the fraction is $\frac{\theta_m}{360°}$.

The accuracy of a FRM significantly depends on the original static FEA. The mesh in the model can affect the final FRM. It is important to select the number of elements along the air-gap equal to a multiple of 360° divided by the angular increment. This will ensure that the meshes in the rotor and stator will perfectly align in every increment. The rotor basis function will become noisy due to interpolation performed in FEA if the nodes of the rotor and stator meshes are not perfectly aligned.

C.3.2 Stator Basis Function and Inter-turn Short Circuit

The conventional FRMs place only one wire in a stator slot with a current of 1 A [10], and the stator basis function is recreated by phase-shifting and superimposition with respect to winding distribution. When developing this model, placing only one wire did not produce the accurate reproduction of the magnetic flux in the air-gap. The motor studied in this paper has concentrated windings, thus a coil of 80 turns occupying two stator slots is used as unit basis functions (B_{nLoop} and B_{tLoop}) for the stator. Figure C.3 highlights which coil in phase A is used to compute the unit basis function for the stator and its current direction.

The first step to recreate the basis function for phase A is to phase-shift B_{nLoop} and B_{tLoop} by 10° and 20° (1 and 2 slot pitches). Superimposing these functions gives the contribution from half of the windings in phase A. The second half is obtained through phase-shifting the first half by 180° and adding it to the first half. The procedure for recreating the basis function for one phase will be different, depending on stator geometry or winding configuration. However, the principle is the same: identifying a repeatable part of the windings (preferably a coil) and recreating the stator basis function from this unit function by phase-shifting and superimposing. Alternatively, generating the stator basis functions can be done by defining all the windings [7]. Different stator geometries can be defined in the FEA, which can be used for constructing a library of stator basis functions. The remaining phases are obtained by phase-shifting the basis functions by 120° and 240°. Figure C.4 shows the final stator basis functions of the studied motor with healthy windings, which can be defined as follows.

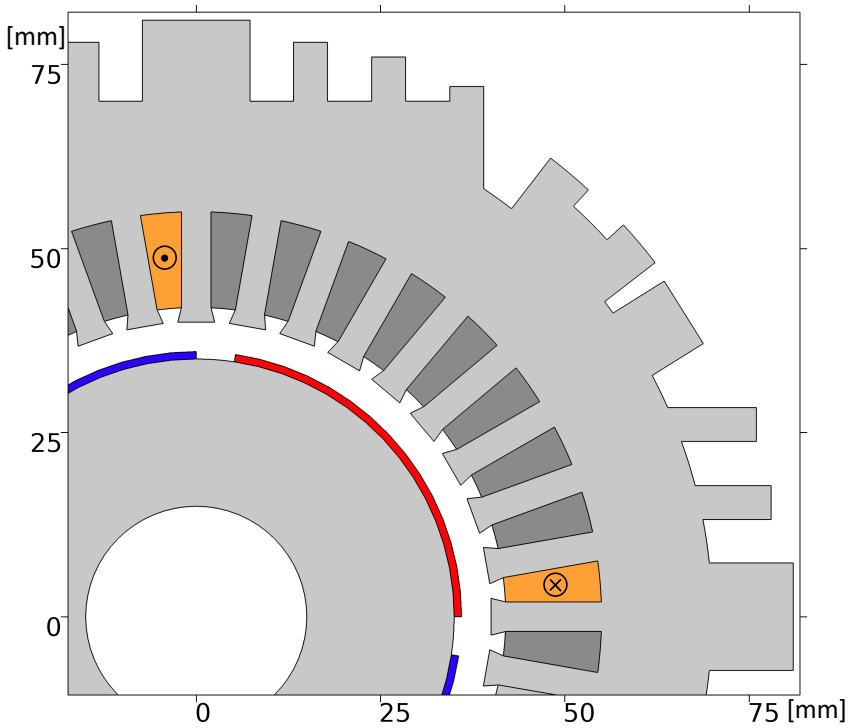

Figure C.3: Highlighting the used coil in generating stator basis function

$$\begin{aligned} B_{nS}(\theta, I(t)) &= \tfrac{1}{I_{ref}} \textstyle\sum_{k=a,b,c} I_k(t) B_{nk}(\theta) \\ B_{tS}(\theta, I(t)) &= \tfrac{1}{I_{ref}} \textstyle\sum_{k=a,b,c} I_k(t) B_{tk}(\theta) \end{aligned} \tag{C.3}$$

For a machine with an ITSC in phase A, a fault can be described with the following modification written in (C.4).

$$\begin{aligned} B_{nS}(\theta, I(t)) &= \tfrac{I_a(t)}{I_{ref}} B_{nA:SC}(\theta) + \tfrac{I_b(t)}{I_{ref}} B_{nB}(\theta) \\ &+ \tfrac{I_c(t)}{I_{ref}} B_{nC}(\theta) + \mu \tfrac{I_a(t) - I_F(t)}{I_{ref}} B_{nLoop}(\theta) \\ B_{tS}(\theta, I(t)) &= \tfrac{I_a(t)}{I_{ref}} B_{tA:SC}(\theta) + \tfrac{I_b(t)}{I_{ref}} B_{tB}(\theta) \\ &+ \tfrac{I_c(t)}{I_{ref}} B_{tC}(\theta) + \mu \tfrac{I_a(t) - I_F(t)}{I_{ref}} B_{tLoop}(\theta) \end{aligned} \tag{C.4}$$

where $\mu_t extf$ is the ratio of shorted turns in one coil and the total number of turn in that coil (i.e. 80 turns in the studied motor). It is noted that the ITSC is a local phenomenon. The block diagram in Figure C.1 illustrates how the ITSC is implemented in phase A. The location of the ITSC faults can be re-positioned by phase-shifting B_{nLoop} and B_{tLoop}. The right side of Figure C.1 illustrates how the basis function is modified in the suggested block diagram. The shorted windings are excited by the current $I_a - I_F$. An ITSC fault can be introduced to any phase, but the basis function for the fault windings needs to be phase-shifted to a valid location. The shorted windings for one phase need to be located where that phase is defined. It is not physically reasonable for an ITSC to occur in phase B if the shorted windings are located in phase C.

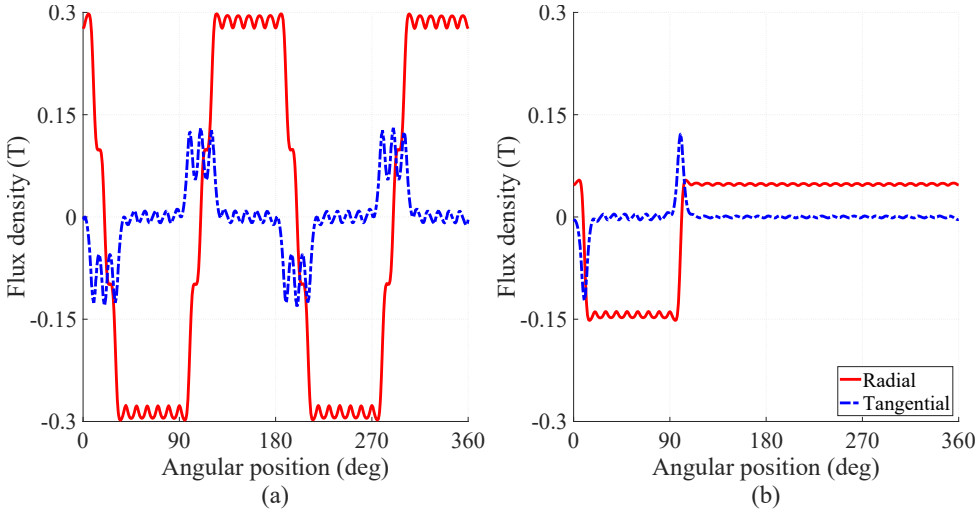

Figure C.4: Stator basis function for (a) the recreated function for phase A and (b) one 80-turn coil

C.3.3 Torque Computation

The torque is computed by Maxwell's stress tensor (MST).

$$\tau = \frac{L_{\text{rotor}} R^2}{\mu_0} \int_0^{2\pi} B_T(\theta + \theta_m, I) B_N(\theta + \theta_m, I) d\theta, \tag{C.5}$$

where L_{Rotor} is the length of the rotor, μ_0 is the permeability in free space, and R is the distance from the center of the motor to middle of the air-gap, where the magnetic flux density is extracted. Keeping it constant for all angular positions θ allows for a simpler expression. The torque in the developed FEA was computed with Arkkio's method.

C.3.4 Flux Linkage and Electromotive Force

It is assumed that the radial component of the magnetic flux density in the airgap goes through the stator teeth and contributes to the flux linkage.

$$\phi_i = L \int_{\frac{2\pi}{N_s}(i-1)-\frac{\pi}{N_s}}^{\frac{2\pi}{N_s}(i)-\frac{\pi}{N_s}} B_N(\theta + \theta_m, I) d\theta, \tag{C.6}$$

where N_s is the number of stator teeth. The following summation results in the magnetic flux linkage for each phase,

$$\lambda_n = \sum_{k=1}^{3} \sum_{i=1}^{9} \left(\phi_{i+k+3(n-1)} + \phi_{i+k+18+3(n-1)} \right) \tag{C.7}$$

The flux linkages for phases A, B and C are obtained by replacing n with 1, 2 or 3, respectively. Note that (C.7) is specific for the geometry and winding distribution of the motor model analysed in this paper. A different geometry will have a different equation, but the principle is the same, summing the magnetic flux contribution within the cross-section of the coil. The induced voltage is then computed by:

$$e_n = -C_M \frac{d(\lambda_n)}{dt} \tag{C.8}$$

The constant C_M is the geometric factor depending on the number of turns, winding distribution, motor geometry and flux leakage. In this paper, C_M was set to 3. A simple way to obtain C_M is to perform a time-step simulation at a constant speed (i.e. 1000 rpm) at no load in both FEA and FRM. The geometric factor C_M is adjusted for matching the amplitude of the excitation voltage.

C.3.5 Electrical model

The electric circuit model in the abc-reference frame is used in this study [12]. This circuit allows the FRM to use a voltage input instead of a current input. In this work, the SMPMSM operates in motor mode, thus the electric circuit model is shown as (C.9).

$$\begin{bmatrix} v_a \\ v_b \\ v_c \\ 0 \end{bmatrix} = \mathbf{R} \begin{bmatrix} i_a \\ i_b \\ i_c \\ i_F \end{bmatrix} + \mathbf{L}\frac{d}{dt} \begin{bmatrix} i_a \\ i_b \\ i_c \\ i_F \end{bmatrix} + \begin{bmatrix} e_a \\ e_b \\ e_c \\ -e_F \end{bmatrix} \tag{C.9}$$

where $\mathbf{R}$ and $\mathbf{L}$ are the resistance and inductance matrices given as:

$$\mathbf{R} = \begin{bmatrix} R_S & 0 & 0 & -\mu R_S \\ 0 & R_S & 0 & 0 \\ 0 & 0 & R_S & 0 \\ -\mu R_S & 0 & 0 & R_F + \mu R_S \end{bmatrix} \tag{C.10}$$

and

$$\mathbf{L} = \begin{bmatrix} L_S & M_S & M_S & -\mu(1-\mu)L_S \\ M_S & L_S & M_S & -\mu M_S \\ M_S & M_S & L_S & -\mu M_S \\ -\mu L_S & -\mu M_S & -\mu M_s & \mu^2 L_S \end{bmatrix} \tag{C.11}$$

The mutual inductance between the phase windings is neglected, but the mutual inductance between the healthy and faulty windings in phase A is considered as in [13], [14]. Some entries in the matrices are divided by 6 because the ITSC is applied to only one sixth of the windings. All the excitation voltages are computed with (C.8), but the flux linkage for e_F is only for faulty turns. Normally, e_F can be defined to be proportional to the phase excitation voltages, depending on which phase the fault was located [13]. However, the FRM allows for computing the flux linkage in the faulty turns, being used to compute the e_F. It is also possible to estimate the back EMF constant for the motor and assume that the electromotive force is sinusoidal like in [13], but this will dismiss details in the model and reduce the model accuracy.

$$e_f = -\mu C_M \frac{d}{dt}\left(\sum_{i=2}^{10} \phi_i\right) \tag{C.12}$$

C.4 Developed Finite element model

The motor studied in this paper is a SMPMSM with concentrated windings. The motor was disassembled for measuring key geometric parameters. They are listed in Table C.1 with other key parameters needed in the simulation. Only a quarter of the model is shown in Figure C.5, but the geometry of the whole motor was simulated, due to asymmetries caused by faults. The different colours (yellow, orange and brown) indicate the different phase windings (phase A, B and C) in the stator. The electromagnetic model in the FEA is defined by Maxwell's equations.

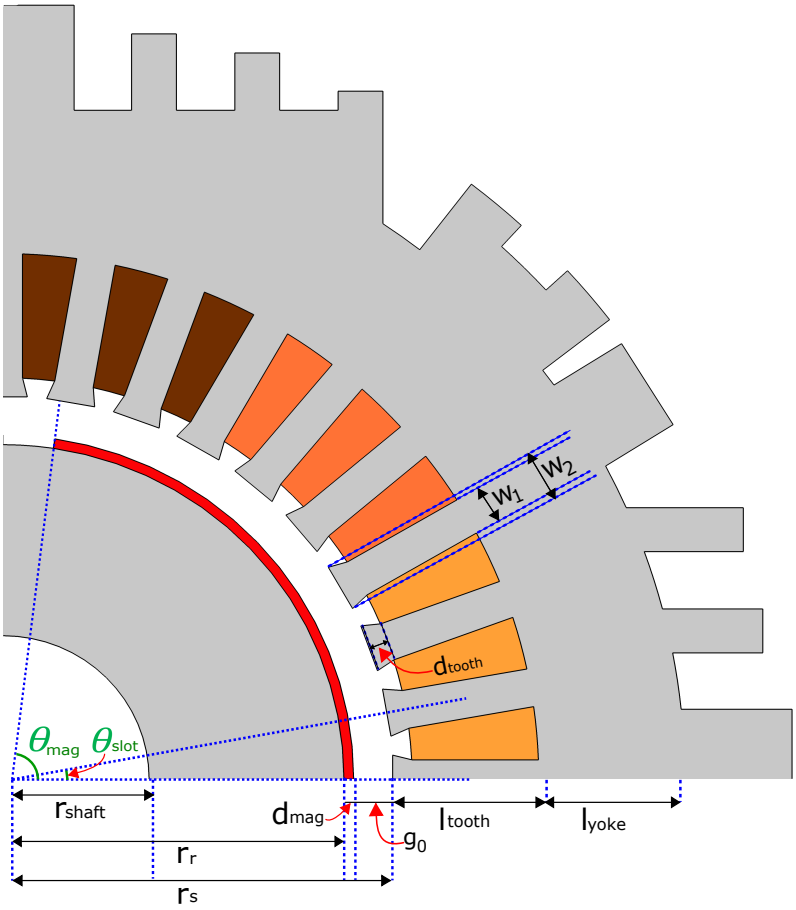

Figure C.5: Geometry of a quarter of the studied SMPMSM

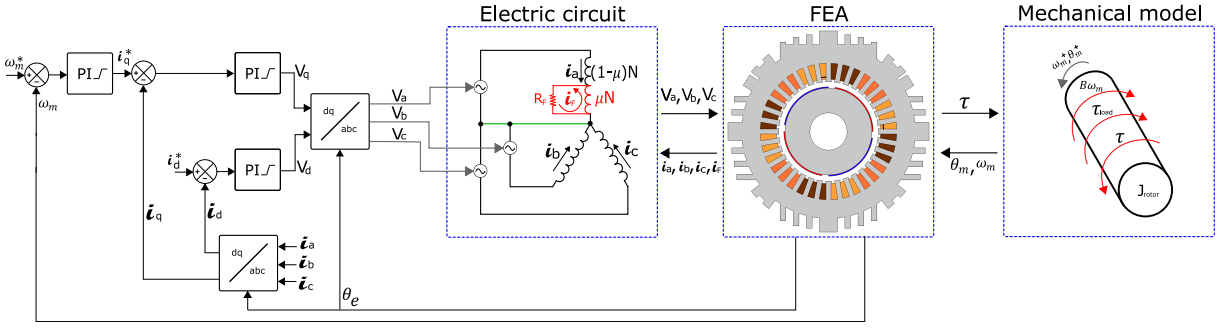

Figure C.6: Block diagram of FE model

The motor is controlled by PI-controllers with a inner current loop, which controls the d- and q-components separately. The speed controller defines the reference value for the I_q, while the reference value for I_d is set as 0 A. No voltage modulation like space-vector modulation of hysteresis is included in the model. The main focus of this paper is compare the FRM with FEA when modelling faulty motors.

Figure C.6 illustrates the block diagram of the FEA model used as benchmark for the FRM. The dynamics of the mechanical parts in the model is described by a simple cylinder with applied torques and viscous friction.

$$\dot{\omega}_m = \frac{\tau - \tau_{load} - \mathrm{B}\omega_m}{J_{\mathrm{rotor}}} \tag{C.13}$$

The inertia of the rotor J_{rotor} and the viscose friction B are set at 0.05 $\mathrm{kg} \cdot \mathrm{m}^2$ and 0.01 $\frac{\mathrm{N}\cdot\mathbf{m}\cdot\mathrm{s}}{\mathrm{rad}}$, respectively. No load torque (τ_{Load}) was required in this static FEA as mentioned earlier.

Table C.1: Geometric dimensions and parameters of the in-house motor

Symbol	Quantity	Parameter description
p	2	Number of pole pairs
N_s	36	Number of stator slots
N	80	Number of turns per stator slot
L_{rotor}	100 mm	Length of rotor
R	38.0 mm	Radius used to compute torque by MST
r_{shaft}	15.0 mm	Rotor inner radius
r_r	35.0 mm	Rotor outer radius
r_s	40.0 mm	Stator inner radius
d_{mag}	1.0 mm	Magnet thickness
g_0	4.0 mm	Average air-gap distance
L_{tooth}	14.5 mm	Length of stator tooth
d_{tooth}	2.0 mm	Thickness of stator tooth top
w_1	4.0 mm	Width of stator tooth 1
w_2	5.0 mm	Width of stator tooth 2
L_{yoke}	9.1 mm	Thickness of stator yoke
θ_{slot}	10°	Stator slot pitch
θ_{mag}	80.8°	Magnet pitch
n_{rated}	3000 rpm	Rated speed
k_{BEMF}	90 $\frac{\mathrm{mV}}{\mathrm{rpm}}$	Back EMF constant
R_s	2.1 Ω	Per phase resistance
L_s	36 mH	Self inductance
M_s	18 mH	Mutual inductance

The self-inductance on the real motor is 6 mH. The inductances computed in FEA is used in FRM for the best comparison between the two simulation methods.

C.5 Results and Discussions

C.5.1 Comparison between FEA and FRM

The primary purpose of this paper is to investigate the performance of the suggested FRM on modelling a faulty SMPMSM with the minimum requirement for the basis functions. First, a static analysis was conducted for a comparison between FRM and FEA. The induced torque was computed in the interval 0° and 360° with 1° increments and the current excitation $I_a = 10$ A, $I_b = 0$ A, and $I_c = 0$ A. The computed torques by FEA and the proposed FRM are plotted in Figure C.7, showing an almost perfect agreement between the two methods. The faulty case is the case of a missing piece on one magnet. This verifies the validity of superimposing contributions from the rotor and stator to the magnetic field. The FEA takes 12 min 25 s to complete a simulation while the suggested FRM takes 0.103 s to compute or 7233 times faster than FEA under the same simulation requirement. This in turn is one order of magnitude larger than the existing FRM in [15]. However, the computational burden of the suggested FRM significantly increases when including the calculation of flux linkages and back EMF. This issue will be discussed further in detail when presenting the results of time-stepping simulations.

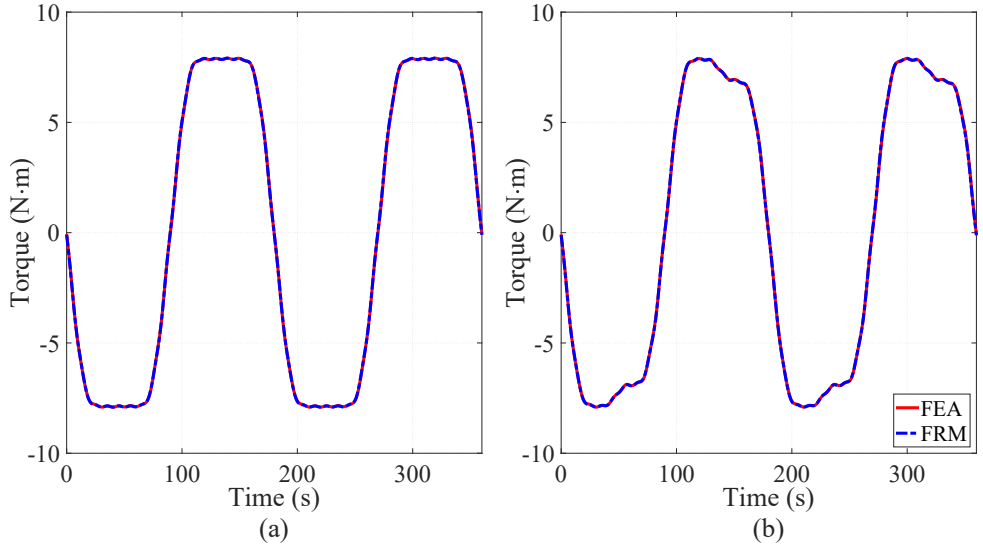

Figure C.7: Induced torque at any rotor positions with the current excitation $I_a = 10$ A, $I_b = 0$ A and $I_c = 0$ A in (a) healthy case and (b) missing magnet piece

The second analysis is implemented with time-stepping simulations in variable speeds. The reference speed jumps between 50 rad/s and 100 rad/s as shown in Figure C.8, where only the speed prediction from the FEA and FRM in the healthy case is plotted. The speed responses from the faulty condition are close to identical. The following faults were investigated in time-stepping simulations:

- Magnet defect: A piece of a one of the North pole is removed in the middle og the magnet.
- An ITSC is applied to one of the unit coils in phase A with severity 1.7 % and 15 %. This is 1.6 % and 5.6 % of the total number of turns in phase A, respectively.

- Combination between the magnet defect and ITSC fault as previously listed.

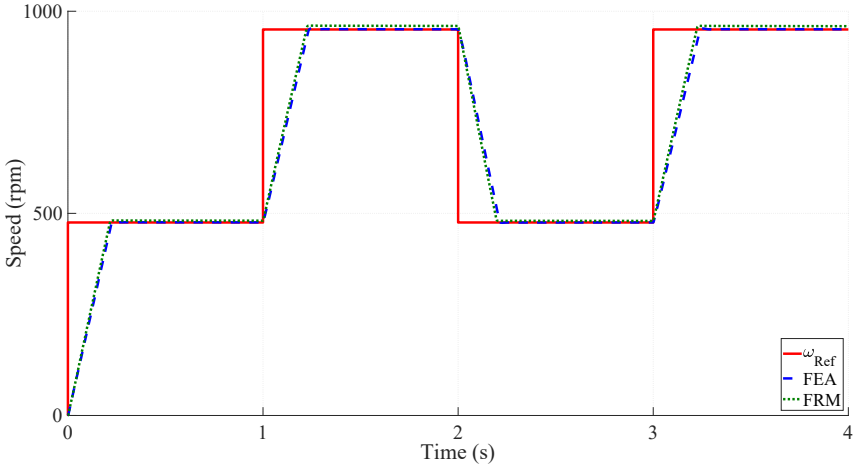

Figure C.8: Variable speed profile of SMPMSM computed by FEA and FRM in healthy case

The time-consuming computation of the FEA model with the PI-controllers is carried out for a comparative study in this paper, being listed in Table C.2. The time-stepping FEA computed in 14 to 15 hours with a office laptop. Implementation of the faults in the FEA increase the computation time, due to slight changes the geometry and increased number of element in the mesh. The proposed FRM completes the time-stepping simulation in about 50 s, with the same simulation requirements like FEA. The applied fault has a little effect on the FRM computation. The ratio of computing time between FEA and the proposed FRM is also given in Table C.2, indicating the difference in the computational burden. All the simulation cases studied in this paper prove that the proposed FRM is three orders of magnitude faster than FEA, verifying statements from previous published papers on FRM [15]. Furthermore, the developed FRM allows for fast extracting results of parameters, terminal voltage, armature current, torque, flux linkage, back EMF and induced search coil voltage wound around a stator tooth, and flux density from any point in the airgap. The FRM model does also have the potential to reproduce the signal of the stray flux, but it is necessary to export results from outside of the SMPMSM, and not just from the airgap.

Table C.2: Computation time comparison between FEA and FRM

Fault condition	FEA	FRM	Ratio
Healthy	50906 s	49.9 s	1020
Missing magnet piece	54924 s	52.2 s	1052
ITSC (8 turns)	54877 s	49.3 s	1096
ITSC (72 turns)	55692 s	50.8 s	1080
Missing magnet piece and ITSC (8 turns)	64165 s	48.9 s	1312
Missing magnet piece and ITSC (72 turns)	64995 s	49.0 s	1326

The torque is computed with different fault scenarios and plotted in Figure C.9. The suggested FRM is able to compute a similar electromagnetic torque like FEA with similar

average value and level of torque ripples with the reference magnet. The reference magnet is described with a remnant magnetic flux density of 1.08 T. The missing magnet piece gives a slight decrease of torque, but the overall torque ripples are the same in the healthy case as observed in Figure C.9a and Figure C.9b. The induced torque estimated by the FRM is close to that of FEA with an error of less than 3 %. The ITSC fault results in an increase of the torque ripples estimated by FEA and FRM, as shown in Figure C.9c. Figure C.10 shows the corresponding d- and q-components when the SMPMSM is operating under healthy conditions. Both the components in FEA and FRM have a close agreement, but some spikes and dynamic responses in the FEA results were not captured by the FRM. However, SMPMSMs are usually fed by a well-controlled converter, allowing for limiting such spikes in a current regulator.

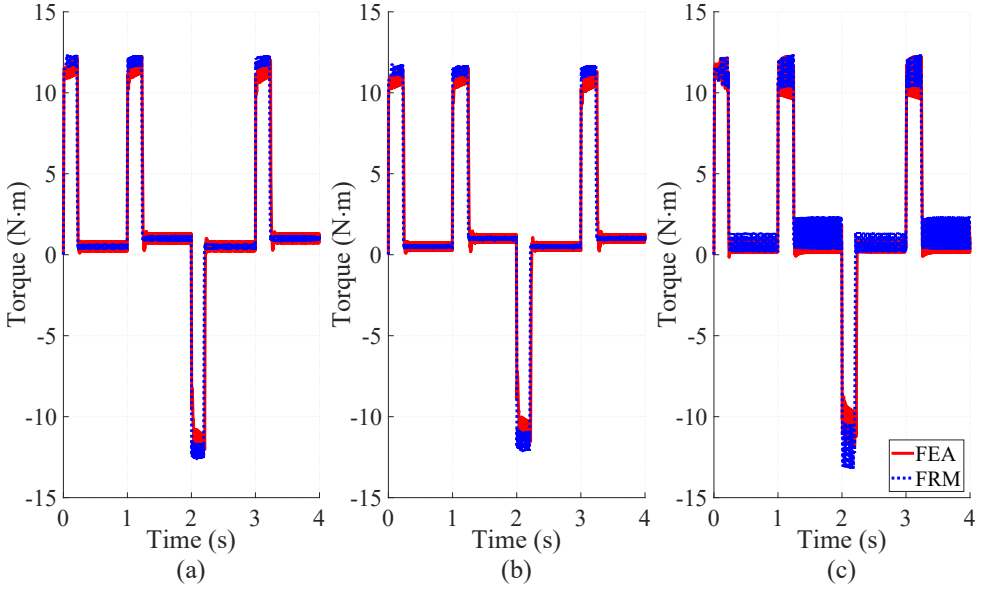

Figure C.9: Comparison of torque estimation by FEA and FRM in case of (a) healthy motor, (b) missing magnet piece, and (c) ITSC in one coil with severity 15 %

An ITSC was applied to one coil in phase A with the severity levels of 1.7 % (8 turns) and 15 % (72 turns). The short circuit current I_{sc}, which is equal to the difference between I_a and I_F, flowing through the fault resistor R_F is plotted in Figure C.11. The predicted I_{sc} by FRM is close to that of FEA in the severe case, but less agreed in the lower severity. Results from the FRM are time-shifted slightly for better highlighting the similarity between the current waveforms. Minor differences in the induced torque cause the peaks imperfectly in phase. The simplified electrical model probably is the main reason behind the deviation from FEA in less severe ITSC faults. RMS of I_{sc} is not deviated significantly between the two models. However, I_{sc} is not a suitable fault indicator in fault diagnosis, because typically only in-house tests or numerical simulations have the possibility of estimating this quantity [14], [16]. Conventionally, SMPMSM drives cannot measure I_{sc}, but the presented result aims at confirming of the FRM's capabilities of reproducing the results from FEA.

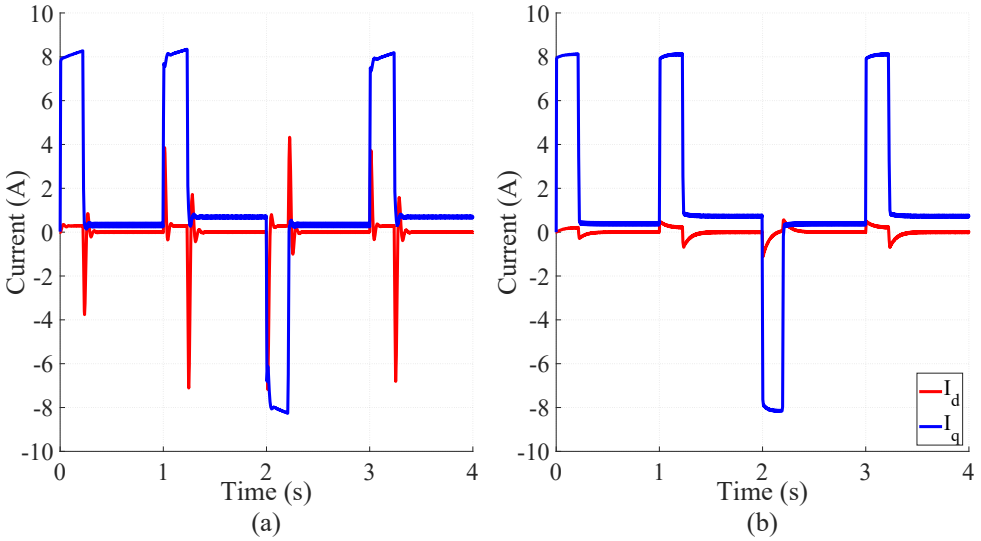

Figure C.10: The d- and q-component of the armature current in healthy case computed by (a) FEA and (b) FRM

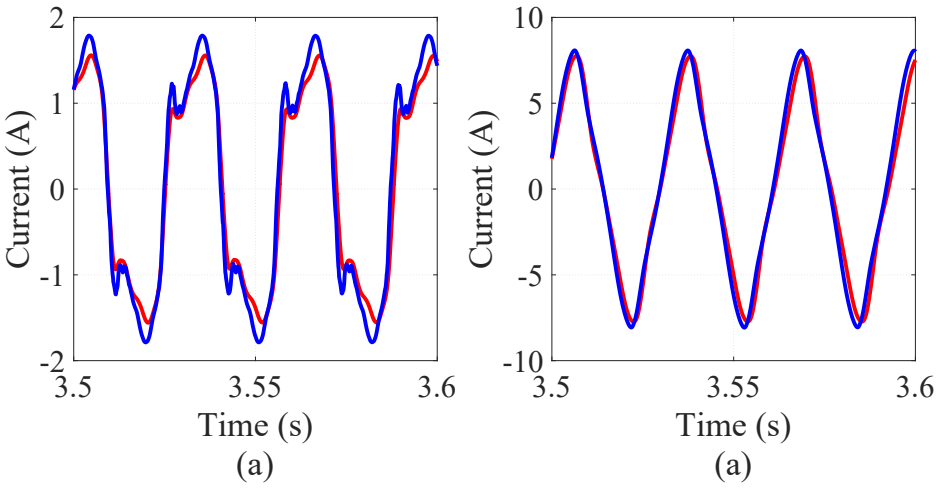

Figure C.11: Short circuit current I_{sc} in case of ITSC in one coil with severity (a) 1.7 % and (b) 15 %

C.5.2 Fault indicators identified by FRM

The radial and tangential components of the magnetic flux density in the air-gap in the healthy case are plotted in Figure C.12 for the first half second of the time-stepping simulations, proving that the FRM can easily decouple the contribution to air-gap flux given by rotor and stator. During the acceleration within the first 0.25 s, the contribution from the stator field is more dominating than that from the rotor. However, the magnitude decreases when the motor reaches a constant speed of 478 rpm (50 rad/s), but would increase again if the motor needs to change speed or if load is applied to the rotor. The sum of the field contributions shows a close agreement with the result from FEA, both in magnitude and shape of the waveform.

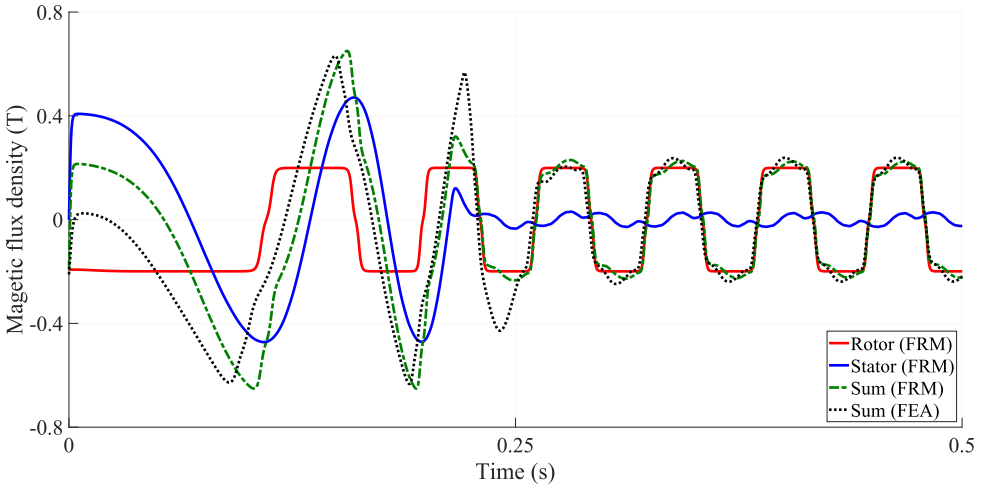

Figure C.12: Decoupling the contribution to the radial component of the air-gap magnetic flux density from the rotor and stator in case of no fault and comparison between FRM and FEA

The magnets of the SPMSM are defined with a constant remnant magnetic flux, resulting in the radial component of the magnetic flux density contributed by the rotor as a trapezoidal shape or red curve in Figure C.12a. Therefore, a flux sensor located in air-gap can track the shape of the magnetic flux density at no load conditions, and compare the shape in later operations. If the shape begins to deviate over time, a magnet defect can be detected. In case of magnet defects like missing magnet piece or partial demagnetisation, this may appears as a period dip in the trapezoidal waveform as shown in Figure C.13. This is the same principle as using search coil for detecting magnet faults as described in [17]. A magnet defect like partial demagnetisation can be decoded with only one sensor. Other asymmetries in the magnetic circuit like eccentricity would need at least a minimum two sensors.

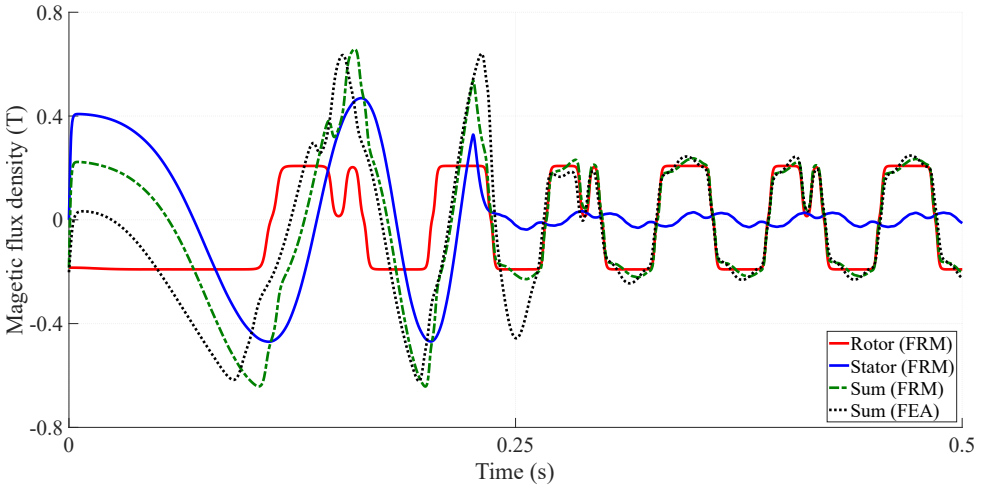

Figure C.13: Decoupling the contribution to the normal component of the air-gap magnetic flux density from the rotor and stator in the case of missing magnet piece and comparison between FRM and FEA

Stator short-circuit faults in electrical machines are often detected by an increase of the third harmonic of the armature current. Within this work, the extended Park's vector approach (EPVA) [18] is chosen. Stator currents are extracted from the proposed FRM and used to compute the Park's vector. The magnitude of the Park's vector, $|I_P|$, is used in a time-frequency analysis and is defined as

$$|I_P| = \sqrt{I_\alpha^2 + I_\beta^2} \tag{C.14}$$

where I_α and I_β are the components of the stator current vector in the stationary reference frame (α, β). Under an ITSC, the second harmonic of the current space vector increases in the spectrogram obtained by the wavelet synchrosqueezed transform (WSST) [18]. In case of missing magnetic, no second harmonic is visible in the Figure C.14.

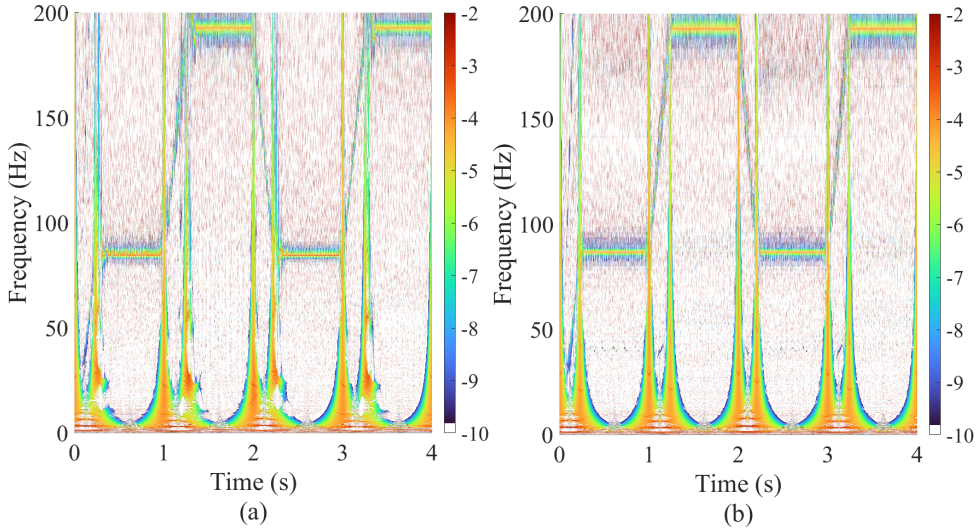

Figure C.14: Spectrogram of I_P in log scale with missing magnet piece computed in (a) FEA and (b) FRM

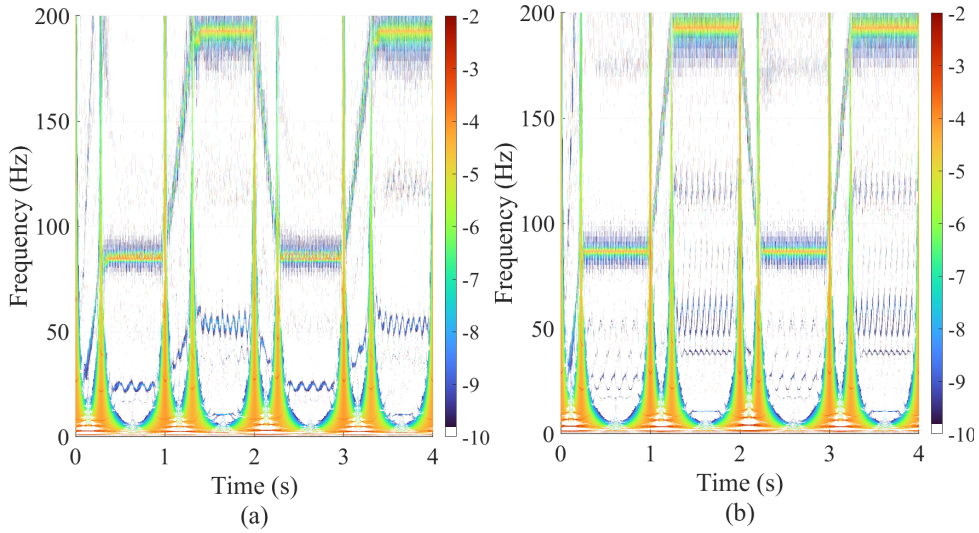

Figure C.15: WSST of amplitude of state space vector I_S in log scale with both 8 shorted turns and missing magnet piece. Computed in (a) FEA and (b) FRM

Figure C.15 shows the results from the simulation where the SPMSM has 8 shorted turns and missing magnet piece. The second harmonic is present at the frequencies 32 Hz and 64 Hz, depending on the motor speed profile in Figure C.8. This highlights the $2 \cdot f_s$ peak in Figure C.15, which is not present in either of the subfigures in Figure C.14. Missing magnet piece does not generate thus second harmonic, thus it is caused by the ITSC fault. The amplitude of the second harmonic becomes more viable when the severity of ITSC fault increases. The result in Figure C.15 confirms the efficacy of the EPVA and shows that magnet defects has little effect on the second harmonic.

The developed FRM in this work focuses on 2 electrical faults in PMSMs, namely demagnetisation and ITSC, which were not addressed in literature. FRMs can also be modified for other fault types like high resistance connection, line-to-line short circuit, phase-to-ground short circuit and eccentricities faults as discussed in [8].

C.5.3 Experimental Validation

Experimental validations were conducted on a 4-pole 2.2 kW SMPMSM of an in-house test setup. The motor is coupled to a generator (3 kW 4-pole SMPMSM) with a torque sensor in between. The generator is wye-connected to a three-phase restive load. Figure C.16 shows an overview of the in-house test bench. The whole setup was controlled via a Dspace controller installed on office laptop. The Microlabbox sent out the control signal to the ABB commercial drive and record signals of torque, current, and position. The sensors were powered by the 24 V DC-power supply. The test motor got multiple taps that can be used for ITSC. The available severity are 2 %, 5 % and 6 %. The taps related for each specific fault severities were connected to an external fault resistor (1 Ω). It makes the artificial ITSC more realistic, since it represents the degeneration of the insulation and limits the fault current. The current through the fault resistor reached 6.4 A at nominal speed in no-load condition.

The motor was run at 1500 rpm and 3000 rpm (nominal speed), at 50 % of rated load. The load was estimated by the ABB-drive. The loading condition was increased by decreasing the resistance in the resistor bank. First, no ITSC was implemented on the motor. Measurements were recorded for 120 s at a sampling frequency of 10 kHz. The motor was stopped for safe rewiring and implementation the ITSC. The resistance of the resistor bank was also increased to the maximum when increasing the steady-state speed from 1500 rpm to 3000 rpm since a larger speed translates to larger output load when the resistance is kept constant. Identical scenarios were simulated in the FRM. The results of the chosen fault indicator, second harmonic of I_P is presented in Table C.3, being obtained by Fast Fourier transform of two minutes long measurements, which were normalised by their respected DC-component of I_P. The general trend is that the second harmonic is increasing with increasing severity of ITSC, but the trend has a greater slope at higher speed.

The spectrograms of the I_P in cases of 0 % and 6 % at nominal speed are presented in spectrograms of Figure C.17. The simulation shows that the second harmonic of I_P will increase by 4.4 dB when a short circuit is implemented. This is also shown in the experimental measurement where the second harmonic increased by 3.2 dB. It is noted

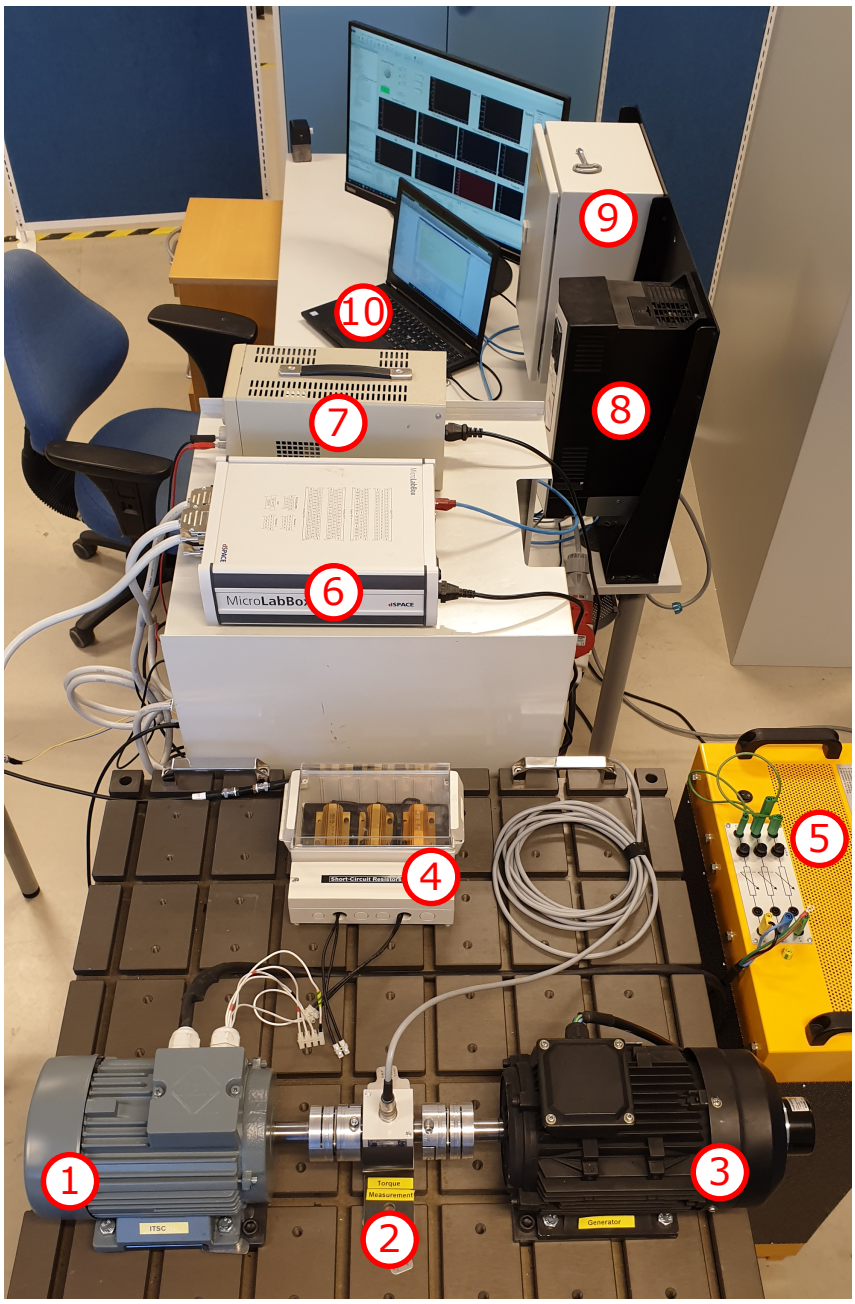

Figure C.16: In-house test setup with (1) motor, (2) torque sensor, (3) generator, (4) fault resistor, (5) resistor bank, (6) Microlabbox, (7) low voltage DC-supply, (8) ABB motor drive, (9) cabinet containing current sensors, and (10) laptop

Table C.3: Amplitude of second harmonic of $|I_P|$ at different short circuit serveries

ITSC	1500 rpm	3000 rpm
0 %	-48.7 dB	-47.8 dB
2 %	-46.0 dB	-46.7 dB
5 %	-46.1 dB	-45.5 dB
6 %	-46.3 dB	-44.6 dB

that the obtained result by FRM has a lower noise level than the experimental data, but does show the general trend of the chosen fault indicator [18].

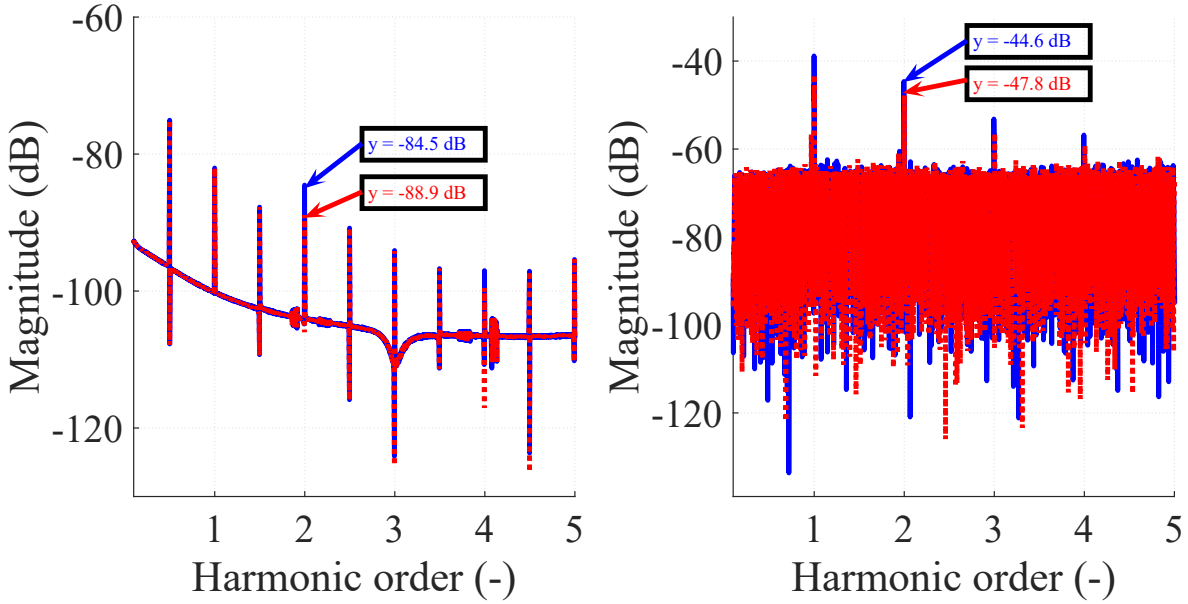

Figure C.17: Comparison between spectrogram of I_P obtained from (a) FRM or (b) experiment

C.6 Conclusion

This paper develops a field reconstruction model to model faults in SMPMSM. The key features of the new model includes a developed magnet library and the implementation of ITSC in FRM. The developed model can simulate magnet defects, ITSC and has the potential to easy implement both faults in the same simulation. Further, the model can present detailed results of current, terminal voltage, EMF, torque, flux linkage, stator tooth flux density and induced search coil voltage.

The model presented in this paper performed over 1000 times faster than the compared commercial FEA and was able to reproduce signals that can be analysed with fault indicator for magnet defects and ITSC. If the model did not include the computation of flux linkages and EMF, it is over 7000 times faster. Therefore, the integration of the flux linkage increases computational burden significantly. This faster computing FRM (without computation of flux linkage and EMF) may have potential for developing condition monitoring of torque or magnetic flux density.

References

[1] J. Luznar, J. Slavič, and M. Boltežar, "Structure-borne noise at pwm excitation using an extended field reconstruction method and modal decomposition," *Strojniski Vestnik/Journal of Mechanical Engineering*, vol. 65, no. 9, pp. 471–481, 2019. DOI: 10.5545/sv-jme.2019.6115.

[2] M. Kiani, D. Torregrossa, B. Fahimi, F. Peyraut, and A. Miraoui, "Detection of faults in PMSM using Field Reconstruction Method and Mechanical Impulse Response," in *2011 Twenty-Sixth Annual IEEE Applied Power Electronics Conference and Exposition (APEC)*, Fort Worth, USA (TX), Mar. 2011, pp. 1896–1901. DOI: 10.1109/APEC.2011.5744854.

[3] B. Fahimi and A. Khoobroo, "Method and apparatuses for fault management in permanent magnet synchronous machines using the field reconstruction method," pat., U.S. Patents 8,314,576 B2, Nov. 2012. [Online]. Available: https://patents.google.com/patent/US8314576B2/en.

[4] A. Khoobroo and B. Fahimi, "Magnetic flux estimation in a permanent magnet synchronous machine using field reconstruction method," *IEEE Transactions on Energy Conversion*, vol. 26, no. 3, pp. 757–765, May 2011. DOI: 10.1109/TEC.2011.2140115.

[5] B. J. Deken and S. D. Pekarek, "Enhanced field reconstruction method for the efficient analysis of permanent magnet synchronous machines," *IEEE Transactions on Energy Conversion*, vol. 27, no. 3, pp. 661–669, Jul. 2012, ISSN: 08858969. DOI: 10.1109/TEC.2012.2204755. [Online]. Available: https://ieeexplore.ieee.org/document/6236115.

[6] L. Gu, S. Wang, D. Patil, B. Fahimi, and M. Moallem, "An improved conformal mapping aided field reconstruction method for modeling of interior permanent magnet synchronous machines," in *ECCE 2016 - IEEE Energy Conversion Congress and Exposition, Proceedings*, Milwaukee, WI, USA, 2016, pp. 1–7. DOI: 10.1109/ECCE.2016.7854845. [Online]. Available: https://ieeexplore.ieee.org/document/7854845.

[7] P. Chen, T. Chen, J. Liang, B. Fahimi, and M. Moallem, "Torque ripple mitigation via optimized current profiling in interior permanent magnet synchronous motors," in *2019 IEEE International Electric Machines and Drives Conference (IEMDC)*, San Diego, CA, USA, 2019, pp. 240–247, ISBN: 9781538693490. DOI: 10.1109/IEMDC.2019.8785352. [Online]. Available: https://ieeexplore.ieee.org/document/8785352.

[8] D. Torregrossa, A. Khoobroo, and B. Fahimi, "Prediction of acoustic noise and torque pulsation in PM synchronous machines with static eccentricity and partial demagnetization using field reconstruction method," *IEEE Transactions on Industrial Electronics*, vol. 59, no. 2, pp. 934–944, May 2012. DOI: 10.1109/TIE.2011.2151810.

[9] A. Khoobroo and B. Fahimi, "A new method of fault detection and treatment in five phase permanent magnet synchronous machine using field reconstruction method," in *2009 IEEE International Electric Machines and Drives Conference, IEMDC 09*, Miami, FL, USA, May 2009, pp. 682–688. DOI: 10.1109/IEMDC.2009.5075279.

[10] W. Zhu, B. Fahimi, and S. Pekarek, "A field reconstruction method for optimal excitation of permanent magnet synchronous machines," *IEEE Transactions on Energy Conversion*, vol. 21, no. 2, pp. 305–313, Jun. 2006, ISSN: 08858969. DOI: 10.1109/TEC.2005.859979. [Online]. Available: https://ieeexplore.ieee.org/document/1634576.

[11] Y. Park, D. Fernandez, S. B. Lee, *et al.*, "Online Detection of Rotor Eccentricity and Demagnetization Faults in PMSMs Based on Hall-Effect Field Sensor Measurements," *IEEE Transactions on Industry Applications*, vol. 55, no. 3, pp. 2499–2509, 2019, ISSN: 0093-9994. DOI: 10.1109/TIA.2018.2886772.

[12] B. Vaseghi, B. Nahid-Mobarakeh, N. Takorabet, and F. Meibody-Tabar, "Experimentally Validated Dynamic Fault Model for PMSM with Stator Winding Inter-Turn Fault," in *2008 IEEE Industry Applications Society Annual Meeting*, Edmonton, AB, Canada, Oct. 2008, pp. 1–5. DOI: 10.1109/08IAS.2008.24.

[13] Y. Qi, E. Bostanci, V. Gurusamy, and B. Akin, "A Comprehensive Analysis of Short-Circuit Current Behavior in PMSM Interturn Short-Circuit Faults," *IEEE Transactions on Power Electronics*, vol. 33, no. 12, pp. 10 784–10 793, Dec. 2018, ISSN: 0885-8993. DOI: 10.1109/TPEL.2018.2809668. [Online]. Available: https://ieeexplore.ieee.org/document/8302979.

[14] Y. Qi, E. Bostanci, M. Zafarani, and B. Akin, "Severity estimation of interturn short circuit fault for pmsm," *IEEE Transactions on Industrial Electronics*, vol. 66, no. 9, pp. 7260–7269, 2019, ISSN: 02780046. DOI: 10.1109/TIE.2018.2879281.

[15] D. Torregrossa, B. Fahimi, F. Peyraut, and A. Miraoui, "Fast computation of electromagnetic vibrations in electrical machines via field reconstruction method and knowledge of mechanical impulse response," *IEEE Transactions on Industrial Electronics*, vol. 59, no. 2, pp. 839–847, Apr. 2012, ISSN: 02780046. DOI: 10.1109/TIE.2011.2143375. [Online]. Available: https://ieeexplore.ieee.org/document/5754577.

[16] J. C. Urresty, J. R. Riba, and L. Romeral, "Diagnosis of interturn faults in PMSMs operating under nonstationary conditions by applying order tracking filtering," *IEEE Transactions on Power Electronics*, vol. 28, no. 1, pp. 507–515, 2013, ISSN: 08858993. DOI: 10.1109/TPEL.2012.2198077. [Online]. Available: https://ieeexplore.ieee.org/document/6198360.

[17] Z. Ullah and J. Hur, "A Comprehensive Review of Winding Short Circuit Fault and Irreversible Demagnetization Fault Detection in PM Type Machines," *Energies*, vol. 11, no. 12, p. 3309, Nov. 2018. DOI: 10.3390/en11123309.

[18] P. Pietrzak and M. Wolkiewicz, "Comparison of Selected Methods for the Stator Winding Condition Monitoring of a PMSM Using the Stator Phase Currents," *Energies*, vol. 14, no. 6, Mar. 2021. DOI: 10.3390/en14061630.

Paper D

Improved Quadratic Time-frequency Distributions for Detecting Inter-turn Short Circuits of PMSM in transient States

Sveinung Attestog, Huynh Van Khang, Kjell G. Robbersmyr

This paper has been published as:

S. Attestog, H. V. Khang and K. G. Robbersmyr, "Improved Quadratic Time-frequency Distributions for Detecting Inter-turn Short Circuits of PMSMs in Transient States," 2020 International Conference on Electrical Machines (ICEM), Gothenburg, Sweden, 2020, pp. 1461-1467, doi: 10.1109/ICEM49940.2020.9271050.

D.1 Abstract

This paper aims to improve quadratic time-frequency distributions to adapt condition monitoring of electrical machines in transient states. Short-Time Fourier transform (STFT) has been a baseline signal processing technique for detecting fault characteristic frequencies. However, limits of window sizes due to loss of frequency- or time-resolution, make it hard to capture rapid changes in frequencies. Within this study, Choi-Williams and Wigner-Ville distributions are proposed to effectively detect peaks at characteristic frequencies while still maintaining low computation time. The improved quadratic time-frequency distributions allow for generating spectrograms of a longer lasting data signal and capturing multi-component signals with a better separation of the components than STFT. Further, the time resolution of the spectrograms generated by the proposed method is not affected by the window size. The effectiveness of the proposed methods is numerically verified from the data of an in-house test setup.

D.2 Introduction

Permanent magnet synchronous motors (PMSMs) are compact and highly efficient, making them attractive in electric powertrains for wind turbines and electric vehicles, which operate dynamically with variable speed and torque. Moreover, the powertrains are intensively exposed to mechanical-, and electrical stress in harsh environments and thermal cycling due to the dynamic operation. Consequently, detection and prevention of the faults in such powertrains are more important and challenging. In condition-based maintenance the machines are monitored over time, which allows to determine when the next maintenance is needed. Implemented correctly will reduce unexpected downtimes and costs.

Condition monitoring for electrical machines in dynamic operation requires the analysis of non-stationary signals. Short-time Fourier transform (STFT) is often used for this purpose. The resolution of the time-frequency representation, or spectrogram, is dependent on the window size. A smaller time window results in a high time resolution and fewer lines of resolution on the frequency axis. On the other hand, larger window sizes cause a lower time resolution. Over the years, multiple techniques have been developed, i.e., Wavelet transform [1] and quadratic time-frequency distribution (TFD), to address the computation burden and resolution. Quadratic TFD or Cohen Class function has been used in quantum physics and Heisenberg's uncertainty principle [2]. This family of functions includes Wigner-Ville (WVD), Choi-Williams (CWD), Zhao-Atlas-Marks (ZAM), and Rihaczek distributions. The difference among them is their kernel function. The advantage of these distributions is that they can capture the transient behavior of a signal, and time resolution is not affected by the length of the time sample. This property makes quadratic TFDs attractive in many applications besides fault detection of electrical motors, i.e., optical sensor, radar sensor, and wireless communication [3]–[5].

WVD is one of the oldest distributions and fast to compute. The demerit of this distribution is the presence of cross-terms. Additional peaks and patterns occur when applied to a signal with multiple components. Pseudo WVD or combining WVD with the

Gabor distribution can be a solution to address this challenge [6], [7]. Alternatively, an improved eigenvalue decomposition-based approach for reducing the cross-term was proposed in [8]. Minimizing the cross-term can also be done by changing the kernel function, giving a different Cohen class function. Towards condition monitoring for PMSMs, CWD was used for feature extraction in a demagnetization fault detection scheme [9]. The fault indicator was based on a box-counting fractal dimension. The spectrogram is divided into squares by a grid. The number of squares, where the signal is present, is counted. A demagnetization fault increases the number of boxes due to a more chaotic signal.

Although considerable researches have been devoted to enhance the accuracy of quadratic TFDs [6]–[13], limited research has focused on improving computation time of time-frequency representations or spectrograms [14]. The spectrograms were limited to shorter time samples. The largest time sample used in a bilinear TFD was found in [7], which was 2.7 s with sampling frequency 1.5 kHz. The increasing computation time with longer sample arrays restricts the application of quadratic TFDs in condition monitoring. This paper aims to propose an improved quadratic TFDs to make quadratic TFDs better suitable for condition monitoring of electrical machines in transient states while reducing the computational burden.

D.3 Mathematical background

D.3.1 Cohen Class Function

The general equation for Cohen class distribution function can be written as function of time t and frequency ω.

$$C(t,\omega) = \frac{1}{2\pi}\int_{-\infty}^{\infty}\int_{-\infty}^{\infty} A(\theta,\tau)\phi(\theta,\tau)e^{-j\theta t - j\tau\omega}d\theta d\tau \tag{D.1}$$

where $A(\theta,\tau)$ is the ambiguity function

$$A(\theta,\tau) = \frac{1}{2\pi}\int_{-\infty}^{\infty} R(t,\tau)e^{j\theta t}dt \tag{D.2}$$

$R(t,\tau)$ is the auto correlation function, which is defined as

$$R(t,\tau) = s^*(t-\frac{\tau}{2})s(t+\frac{\tau}{2}) \tag{D.3}$$

where τ is running time. The analytic signal $s(t)$ is defined as

$$s(t) = x(t) + jH(x(t)) \tag{D.4}$$

where the real part $x(t)$ is the original signal and the imaginary part $H(x(t))$ is the Hilbert transform of the original signal.

$$H(x(t)) = \frac{1}{\pi}\int_{-\infty}^{\infty}\frac{x(\tau)}{t-\tau}d\tau \tag{D.5}$$

The integrals in (D.1) and (D.2) are Fourier and inverse Fourier transformations:

$$\mathcal{F}_{t\to\omega}(f(t)) = \int_{-\infty}^{\infty} f(t)e^{-j\omega t}dt \tag{D.6}$$

$$\mathcal{F}^{-1}_{\omega\to t}(F(\omega)) = \int_{-\infty}^{\infty} F(\omega)e^{j\omega t}d\omega \tag{D.7}$$

The indexes $t \to \omega$ and $\omega \to t$ are added for clarifying what domains the data is switched between with the Fourier transformations. The general equation of Cohen class function, defined by (D.1) and (D.2), is rewritten to

$$C(t,\omega) = \mathcal{F}_{\tau\to\omega}\mathcal{F}_{\theta\to t}\left(\phi(\theta,\tau)\mathcal{F}^{-1}_{t\to\theta}\left(R(t,\tau)\right)\right) \tag{D.8}$$

The frequency domains θ and ω are different. The θ-domain is where the filtering by the kernel function is applied, while ω is the frequency domain of the resulting TFD.

The kernel function $\phi(\theta,\tau)$ is the main difference between the Cohen class functions. The simplest kernel functions is

$$\phi_{WVD}(\theta,\tau) = 1 \tag{D.9}$$

This gives the WVD, which can be written as

$$C(t,\omega) = \mathcal{F}_{\tau\to\omega}R(t,\tau) \tag{D.10}$$

The main problem of WVD is the cross-term when the signal $x(t)$ consists of multiple components. The most commonly used TFDs, that minimizes the cross-term, are CWD and ZAM, in which the kernel function is defined as:

$$\phi_{CWD}(\theta,\tau) = e^{-\frac{(\theta\tau)^2}{\sigma}} \tag{D.11}$$

and

$$\phi_{ZAM}(\theta,\tau) = \frac{\sin(\pi\theta\tau)}{\pi\theta\tau}e^{\frac{-2\pi\tau^2}{\sigma}} \tag{D.12}$$

Other notations of these kernel functions substitute σ with $\frac{1}{\alpha}$. Keeping σ is preferred, since reducing σ minimises the cross terms, while α has an inverse relation. Both $\phi_{CWD}(\theta,\tau)$ and $\phi_{ZAM}(\theta,\tau)$ become equivalent to $\phi_{WVD}(\theta,\tau)$ when σ goes toward ∞.

The integrals of the Cohen class distribution functions are defined from $-\infty$ to ∞. The next section will describe how to obtain the spectrograms for signals, that lasts for a finite period, with Fast Fourier Transform (FFT).

D.3.2 Discrete form

First apply the window function $d(n)$ to a measurement sample array $x(n)$. The selected window function is a hanning window.

$$d(n) = \frac{1}{2} + \frac{1}{2}\cos\left(2\pi\frac{n}{N}\right) \tag{D.13}$$

where N is the element size of $x(n)$ and n is the integer defined in the range $\left[-\frac{N}{2}, \frac{N}{2} - 1\right]$. The Hilbert transform is applied for obtaining the analytical signal $s(n)$ and a zero is appended,

$$s(n) = \begin{bmatrix} x(n) + jH\left(x(n)\right) \\ 0 \end{bmatrix}. \tag{D.14}$$

Then the elements of $s(n)$ need to be organized in the auto correlation matrix $R\left(n_t, n_\tau\right)$. The row vector n_τ and column vector n_t are defined as,

$$n_\tau = \begin{bmatrix} -\frac{N}{2} & \cdots & \frac{N}{2} - 1 \end{bmatrix} \tag{D.15}$$

and

$$n_t = \begin{bmatrix} -\frac{N}{2} & \cdots & \frac{N}{2} - 1 \end{bmatrix}^T \tag{D.16}$$

$R\left(n_t, n_\tau\right)$ is now written as,

$$R(n_t, n_\tau) = s^*(n_t - n_\tau) \odot s(n_t + n_\tau) \tag{D.17}$$

Note that the multiplications performed in (D.17) is a Hadamard product. About a half of the entries is not defined, because the sum or difference between n_t and n_τ is outside of the definition range of $x(n)$, $\left[-\frac{N}{2}, \frac{N}{2} - 1\right]$. These entries are set to 0. One way to solve this problem (in a code) is to set all entries, that are not defined in $R\left(n_t, n_\tau\right)$, equal to the last entry of $s(n)$, which is 0.

The ambiguity function is obtained by an inverse FFT from n_t-domain to n_θ-domain.

$$A\left(n_\theta, n_\tau\right) = \mathrm{FFT}^{-1}_{n_t \to n_\theta}\left(R(n_t, n_\tau)\right) \tag{D.18}$$

The characteristic function $M\left(n_\theta, n_\tau\right)$ equals the element wise product (Hadamard product) between the ambiguity function and the kernel function.

$$M\left(n_\theta, n_\tau\right) = \phi(n_\theta, n_\tau) \odot A(n_\theta, n_\tau) \tag{D.19}$$

The final TFD is obtained by a FFT from n_θ-domain back to n_t-domain and then by a FFT from n_τ-domain to n_ω-domain

$$C(n_t, n_\omega) = \mathrm{FFT}_{n_\tau \to n_\omega}\left(\mathrm{FFT}_{n_\theta \to n_t}\left(M\left(n_\theta, n_\tau\right)\right)\right) \tag{D.20}$$

Both window function and kernel function have been applied to the signal $x(n)$. Reducing σ for a CWD minimizes the cross-terms but spreads it across all frequencies e.g., raises the noise floor. It appears as vertical lines in a CWD with horizontal time axis and vertical frequency axis. The peaks of the frequency components are still present on top of the noise floor. This effect was filtered out by subtracting the hundredths smallest values of $C(n_t, n_\omega)$ for each time instant n_t.

D.4 Proposed Quadratic Time-Frequency Distribution

The essential parameters include the sampling frequency (f_s), time window (T), and overlap (OL), which are selected at 1 kHz, 1 s, and 20 %, respectively, in this work. Figure D.1 shows the flowchart of the proposed method with steps as follows.

1. Extract a sample from the original array from entry n_1 to n_2. The initial values of n_1 and n_2 are 1 and f_sT, respectively.

2. Execute the signal processing described in Section II on this sample and obtain the quadratic TFD.

3. Cut off the first 20 % and last 20 % of the spectrogram (OL). In the case, for the first second the spectrogram from 0.2 s to 0.8 s is extracted and put into the final plot.

4. Add the product of the OL and f_sT to n_1 to n_2 and repeat the process. In the second iteration, the next sample extracted is from 0.8 s to 1.8 s. The third interval will be from 1.6 s to 2.6 s.

5. Repeat until end of signal

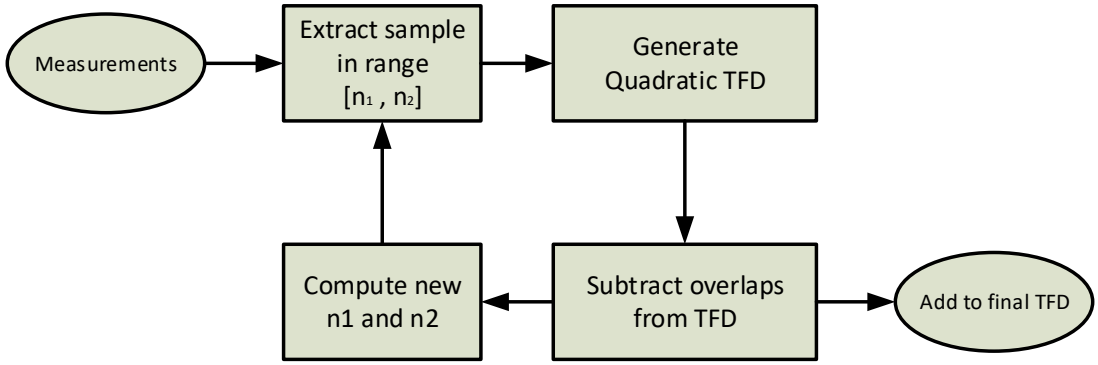

Figure D.1: Flowchart of the proposed quadratic TFD

D.5 Numerical test

In this section, the performance of the proposed quadratic TFDs is numerically investigated and compared with that of using STFT. In this numerical example, a signal with 5 frequency components used and was defined as:

$$x(t) = \sum_{k=1}^{5} \sin\left(2\pi k\left(\frac{5}{c}\sin\left(ct\right) + 25t\right)\right). \tag{D.21}$$

The signal includes sinusoidal components with frequency modulation. The instantaneous frequency of the signal component, where $k = 1$ and $c = 1$ $\frac{\text{rad}}{\text{s}}$, is a sinusoidal function with amplitude of 1, frequency of $\frac{1}{2\pi}$ Hz and bias of 25 Hz. The constant c is set to 1 $\frac{\text{rad}}{\text{s}}$. Figs. D.2a and D.2b show the spectrograms generated with CWD and STFT, respectively. The window size was set 1 s with 20 % overlap. CWD was computed with $\sigma = 0.1$. Both algorithms capture all five signal components as described by (D.21). c was increased to 2 $\frac{\text{rad}}{\text{s}}$. The signal of (D.21) was separable in the CWD, but not separable in the spectrogram generated by STFT. (See Figure D.3a and Figure D.3b) The resolution improves when the window size is reduced to 0.1 s for STFT, but the signal component is

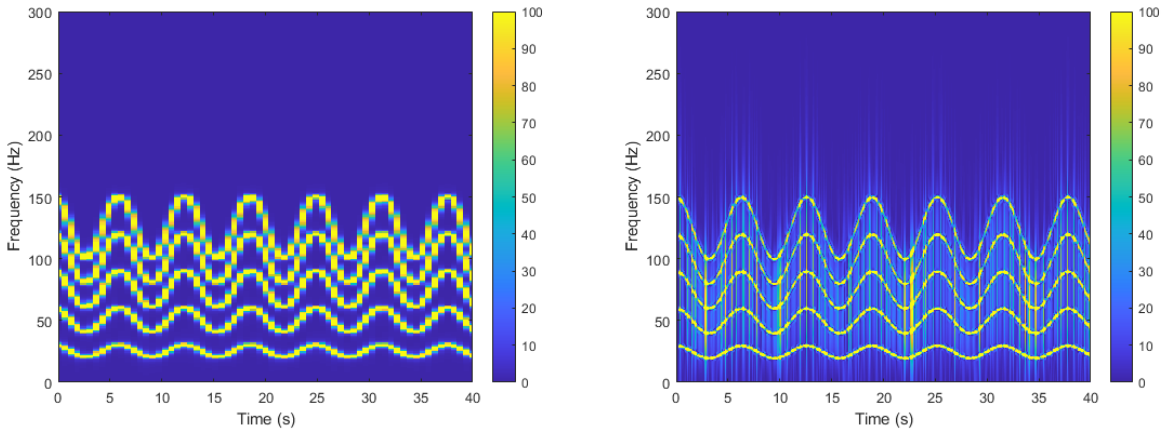

(a) (b)

Figure D.2: Numerical example - $c = 1$ and window 1 s - (a) STFT and (b) CWD

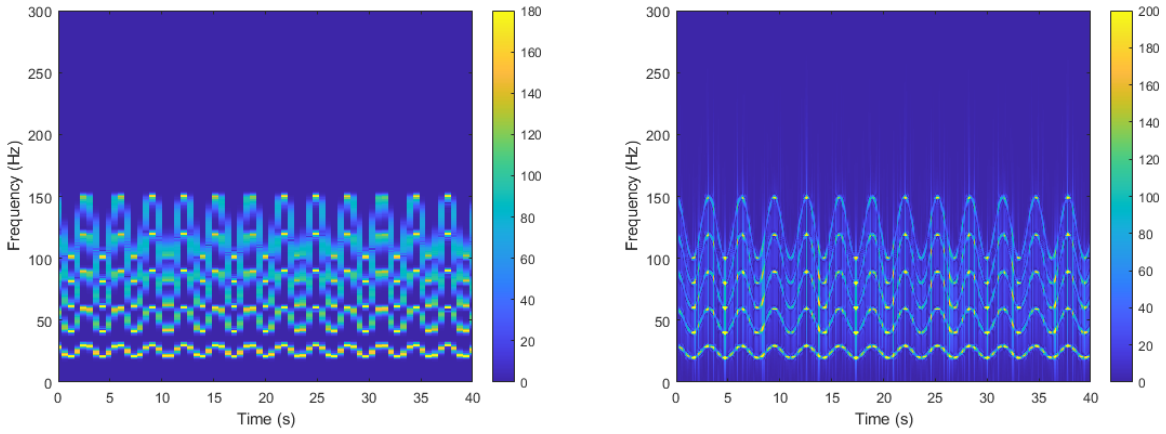

(a) (b)

Figure D.3: Numerical example - $c = 2$ and window 1 s - (a) STFT and (b) CWD

still hard to separate. The contours of the signal components in the CWD spectrogram seem to be thinner and have a smoother shape.

Decreasing window size to 0.1 s reduces the computation time for CWD from 16.5 s to 1.3 s, while the computation time for STFT is increased from 0.014 s to 0.040 s. The performance is considered acceptable for both methods since the total time for the measurement array was 120 s. The reduction in computation time for CWD is obtained since the CWD solves smaller matrices after each iteration. The algorithm solves a 100×100 matrix with a window size of 0.1 s and a 1000×1000 matrix with a window size of 1 s. The sampling rate is 1 kHz. Both CWD and STFT need to perform more iterations due to a smaller window. Another interesting finding is that increasing the window size for CWD does not affect the time resolution of the spectrogram. Changes in frequency can still be captured by CWD, while all the signal components will get merged in the STFT at too larger window sizes. However, the window size only needs to be sufficiently large for the CWD. Smaller window size will give problems with lines of resolution on the frequency axis. Note that a larger window size increases the computation time.

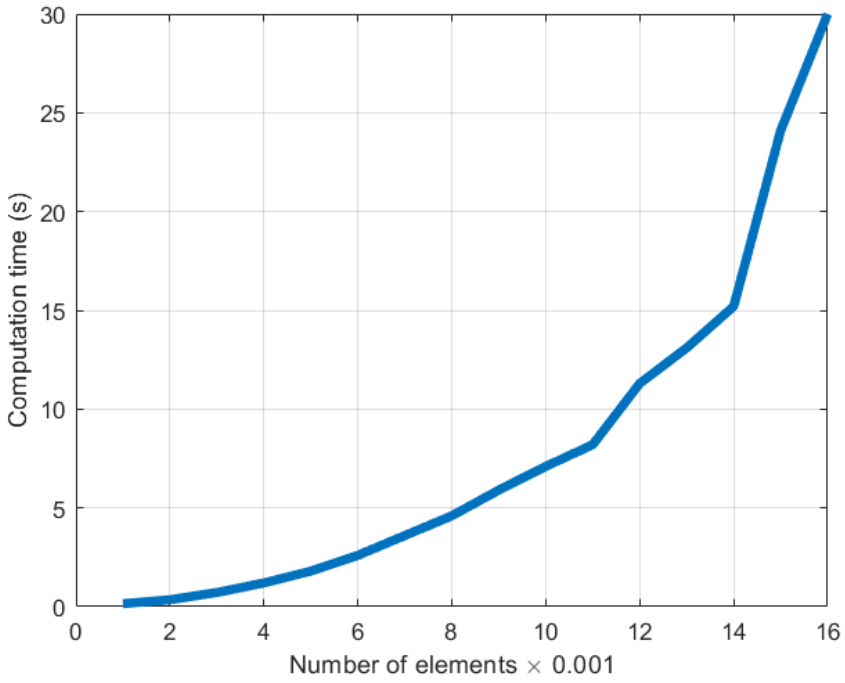

Figure D.4: Computation time versus number of elements in array - CWD

Figure D.4 shows the computation time for executing one iteration of the proposed algorithm presented versus the element size of the input sample. The overlap is set to 0 %. If the input array has an element size of 10000, it will take 7.5 s to solve. An array of 10000 elements can have a total time of 1 s with sample rate of 10 kHz or 10 s with sample rate of 1 kHz. The second sample would be possible in condition monitoring, because the total time would is larger than the computation time.

The replacement of values in the matrices of $n_t - n_\tau$ and $n_t + n_\tau$ is one of the time consuming operations. This is solved with if-statements, where half of the entries end up as 0 in $R(n_t, n_\tau)$. One possibility for reducing computation complexity is to avoid computing parts of the kernel function and auto-correlation matrix because those entries have an insignificant effect on the final TFD. This is explored in detail in [14]. The complexity of FFT (and inverse FFT) applied to a vector with N elements is $O(N \log(N))$. Both $R(n_t, n_\tau)$ and $M(n_\theta, n_\tau)$ are square matrices with N rows and N columns. Inverse FFT is executed once, and FFT is executed twice on $N \times N$ matrices. Therefore, the computational complicity of all these transformations is $O(3N^2 \log(N))$, which explains why the computational complexity increase exponentially in Figure D.4. The performance of the algorithm can can be improved with faster computer or a more efficient code.

D.6 Experimental results and Discussions

The experimental setup consists of two 2.5 kW, 16 poles PMSMs as shown in Figure D.5, in which one operates as a motor while another motor operates as a generator coupled to a resistive load. An inter-turn winding short circuit fault with 10 % severity is seeded

in the motor. The setup is tested on two different speed profiles in both healthy and faulty conditions. The first one is a multi-step speed-profile between standstill to 375 rpm and back down to a full stop. The second speed-profile is an unpredictable speed-profile where the speed increases and decreases around 250 rpm in an irregular manner. The experimental setup is described in detail in [15].

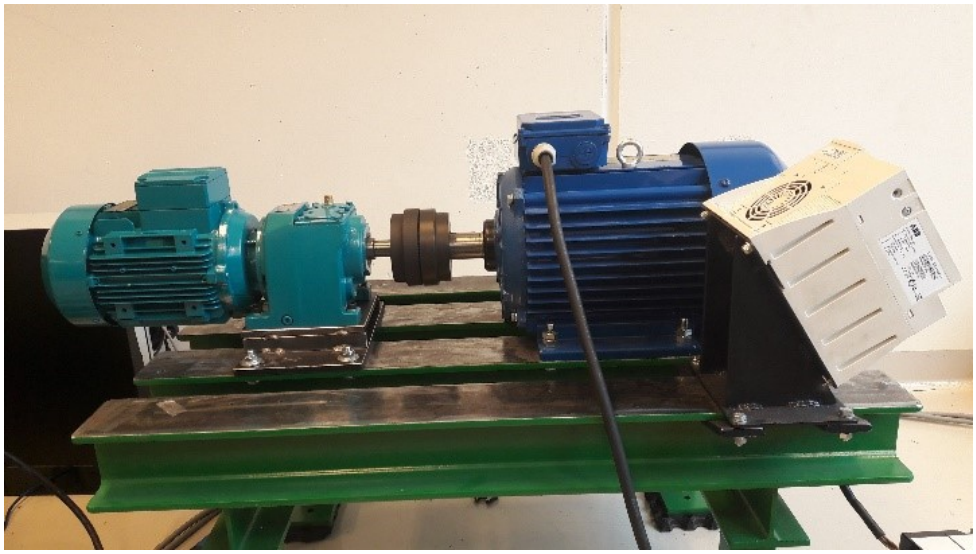

Figure D.5: The in-house experimental setup.

Figure D.6a shows the spectrogram generated by STFT for a phase current of the PMSM in the healthy case. Sampling rate and window size are 1 kHz and 1 s, respectively. The hanning window function was applied to the window with an overlap of 20 %. STFT is used as a benchmark to compare with the spectrograms generated by CWD and WVD. Figure D.6b and D.6c show the spectrograms generated from CWD and WVD. The kernel function for CWD has $\sigma = 10^{-7}$. The harmonic peaks were captured and proved that CWD is capable of capturing harmonic peaks. The fundamental frequency is much more dominant in CWD as compared to the STFT. This may be due to the extremely small σ. One attempt to solve this issue was done by applying an element-wise square root of the CWD, but this makes the spectrograms noisier. The additional filtering by subtracting the hundredths smallest value for each instant in time improved the quality of the spectrogram. The WVD-based spectrograms have additional peaks, but other peaks are not visible on the spectrograms. This is caused by the cross-term and the limits on the color axis.

Figure D.7a, D.7b and D.7c show the spectrograms obtained by STFT, CWD, and WVD of the phase current for the same PMSM operating under an inter-turn short circuit. Both STFT and CWD was able to pick up the second harmonic, which is an indicator for electrical faults. WVD seems to pick up all the integer harmonics. Similar results are shown in Figure D.8a, D.8b and D.8c, which show the spectrograms for the second speed profile generated by STFT, CWD, and WVD, respectively. These experimental results proved that CWD can pick up the same harmonic peaks as STFT. The fundamental component is much more dominant in the CWD. It was discussed earlier in the numerical example, how the quadratic TFDs would perform better with more rapid speed changes.

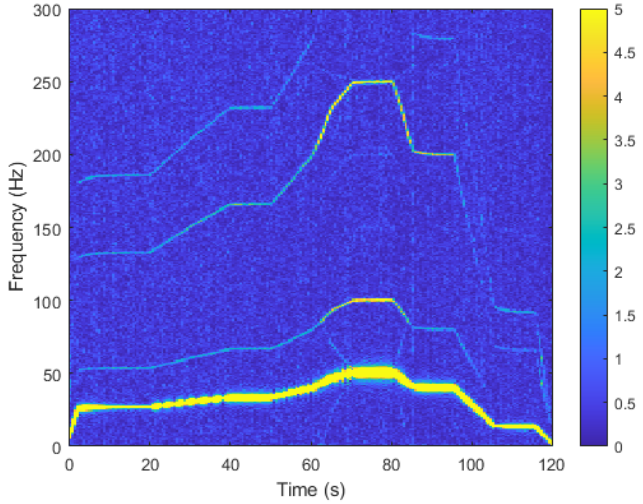

(a)

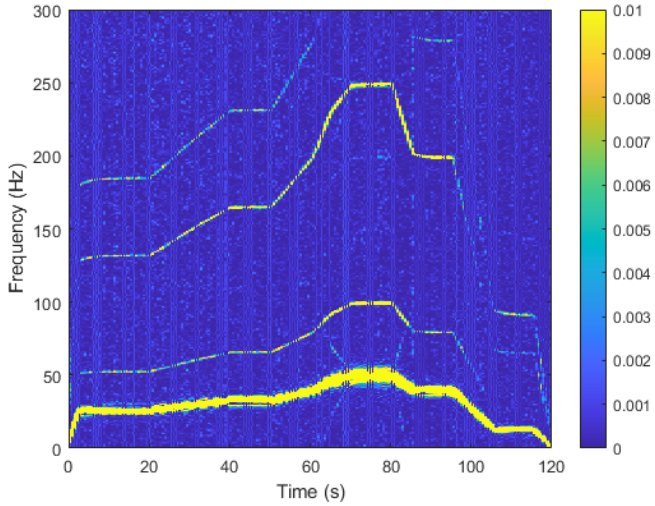

(b)

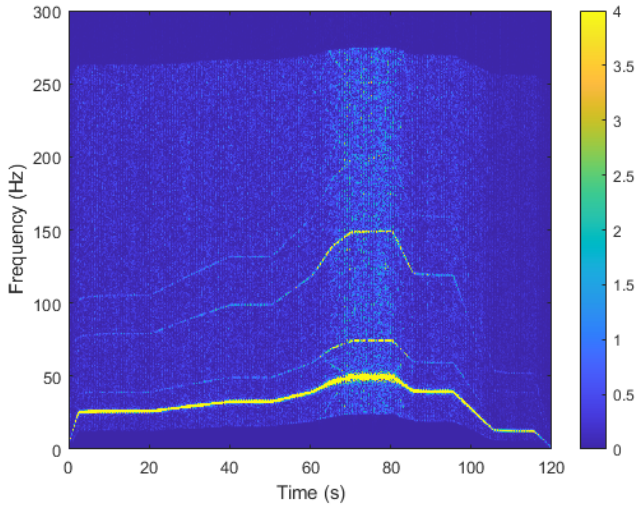

(c)

Figure D.6: Spectrograms of phase current of healthy PMSM operating with the first speed profile, (a) STFT, (b) CWD and (c) WVD

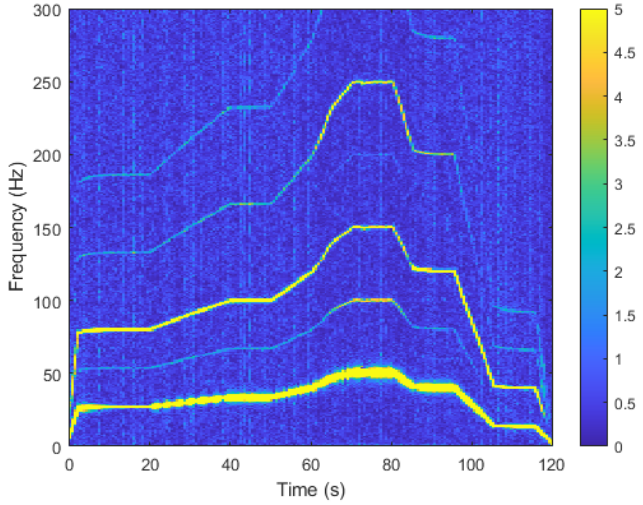

(a)

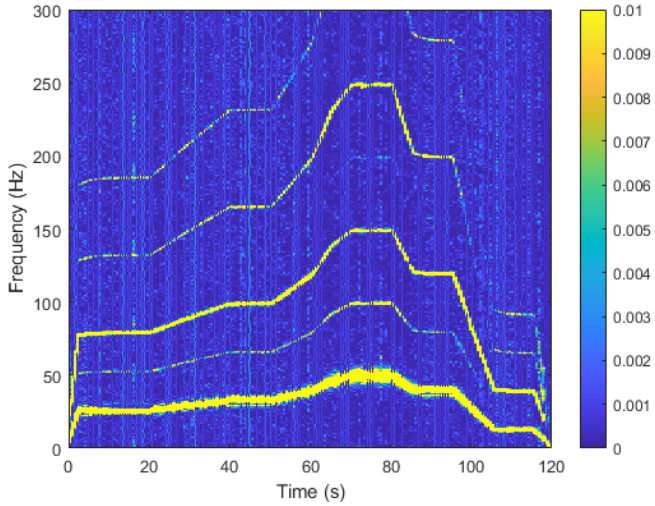

(b)

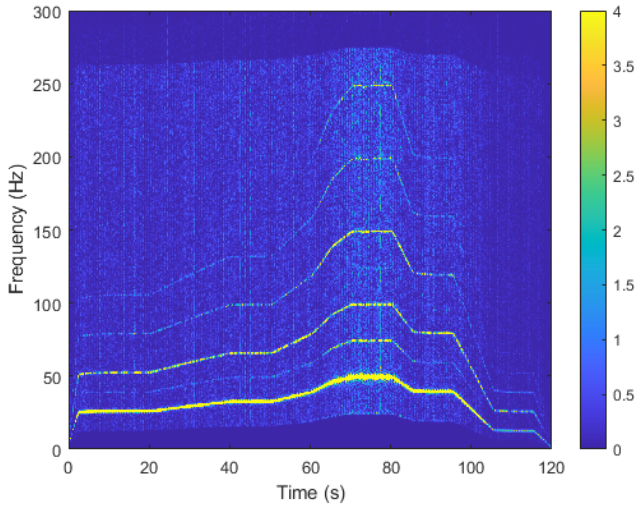

(c)

Figure D.7: Spectrograms of phase current of PMSM with 10 % ITSC operating with the first speed profile, (a) STFT, (b) CWD and (c) WVD

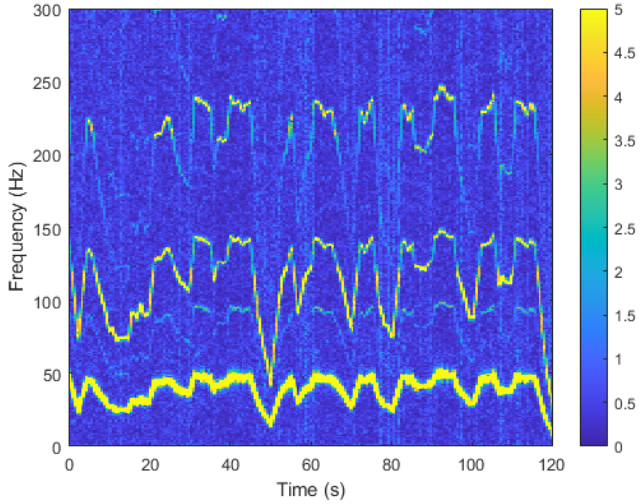

(a)

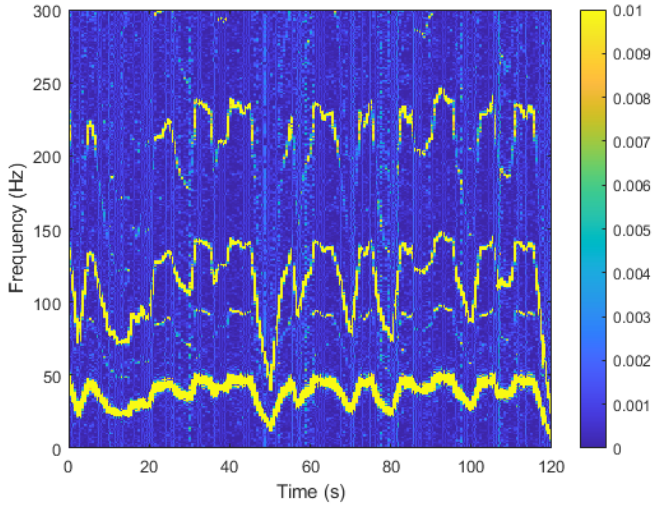

(b)

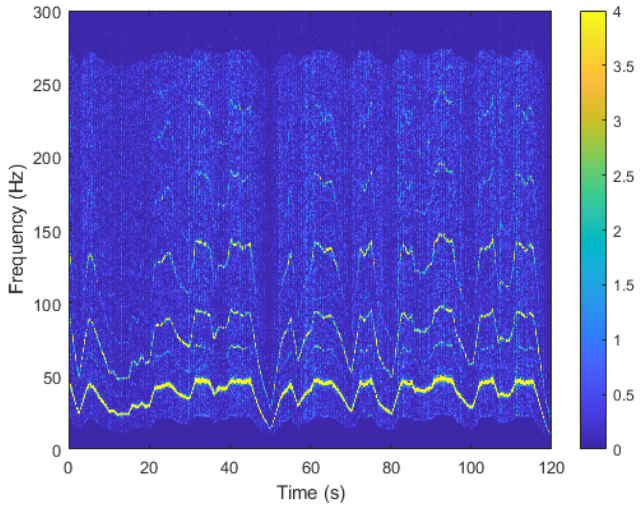

(c)

Figure D.8: Spectrograms of phase current of PMSM with 10 % ITSC operating with the second speed profile, (a) STFT, (b) CWD and (c) WVD

The second and third harmonics have merged in the first 10 s and around 50 s on the spectrograms using STFT and CWD as shown in Figure D.8a and Figure D.8b, respectively. The reason for this issue is that they are separable in the WVD (See Figure D.8c). Multiplying the fundamental frequency with integers would also lead to the same conclusion.

The spectrograms computed from the experimental data shows that the quadratic TFD can capture the signal, but the current set-up does not give any additional information compared to STFT. But further analysis shows that the signal components in the CWD have sharper peaks. The spectrogram generated from the second speed profile was divided into three frequency bands as listed in Table I. The first, third and fifth harmonics are present and dominant in these bands. The time average kurtosis comparison between CWD and STFT is presented in Table I. CWD have a larger kurtosis in all three frequency bands, which indicates that it got higher and sharper central peaks.

Table D.1: Average kurtosis over frequency bands in the spectrgram generated by STFT and CWD

Frequency band	CWD	STFT
0 Hz to 50 Hz	414.0	20.5
50 Hz to 150 Hz	9.6	2.6
150 Hz to 300 Hz	4.0	2.1

D.7 Conclusion

In this paper, we have proposed a solution to improve quadratic TFD for analyzing non-stationary signals. The proposed method allows for generating spectrograms with CWD and WVD for longer-lasting signals, as compared to the existing methods. The numerical test showed that CWD could generate spectrograms with better separation of multiple components than STFT if the frequency modulation is too large. Within the framework, the time resolution is unaffected by window size, but frequency resolution sets a minimum limit on the window. Larger windows increase the computation time and set a maximum limit. The test on the experimental data proved that the proposed method could capture the signal components on data with noise. The time average kurtosis for generating spectrograms by CWD was larger than that of STFT for the first, third and fifth harmonics of the signal. This indicates that CWD generates spectrograms with sharper peaks.

Future work will include trying out other distribution functions that will overcome the problems of the CWD, and make the fundamental frequency less dominant. The WVD has a problem with cross-terms, but is much faster than other Cohen class functions. Alternatively, a pseudo WVD could be implemented instead, which would reduce cross-terms and maintain high computation speed and resolution.

References

[1] M. Heydarzadeh, M. Zafarani, M. Nourani, and B. Akin, "A wavelet-based fault diagnosis approach for permanent magnet synchronous motors," *IEEE Transactions on Energy Conversion*, vol. 34, no. 2, pp. 761–772, Jun. 2019.

[2] L. Cohen, "Time-frequency distributions-a review," *Proceedings of the IEEE*, vol. 77, no. 7, pp. 941–981, Jul. 1989.

[3] Y. Yu, L. Luo, B. Li, K. Soga, and J. Yan, "Quadratic time-frequency transforms-based brillouin optical time-domain reflectometry," *IEEE Sensors Journal*, vol. 17, no. 20, pp. 6622–6626, Aug. 2017.

[4] J. Gao, L. Shen, S. W. F. Ye, and R. Zhangn, "Multi-feature radar signal modulation recognition based on improved PSO algorithm," *The Journal of Engineering*, vol. 2019, no. 19, pp. 5588–5592, Jun. 2019.

[5] T. Wang, J. Liang, and X. Liu, "Soil Moisture Retrieval Algorithm Based on TFA and CNN," *IEEE Access*, vol. 7, pp. 597–604, 2019.

[6] Y. S. Shin and J. Jeon, "Pseudo Wigner-Ville Time-Frequency Distribution and its Application to machinery condition monitoring," *Shock and Vibration*, vol. 1, pp. 65–76, 1993.

[7] A. L. Martinez-Herrera, L. M. Ledesma-Carrillo, M. Lopez-Ramirez, S. Salazar-Colores, E. Cabal-Yepez, and A. Garcia-Perez, "Gabor and the Wigner-Ville transforms for broken rotor bars detection in induction motors," in *2014 International Conference on Electronics, Communications and Computers (CONIELECOMP), Cholula*, May 2014, pp. 83–87.

[8] R. Sharma and R. B. Pachori, "Improved Eigenvalue Decomposition-Based Approach for Reducing Cross-Terms in Wigner–Ville Distribution," *Circuits, Systems, and Signal Processing*, vol. 37, no. 8, pp. 3330–3350, 2018.

[9] M. Delgado Prieto, A. Garcia Espinosa, J.-R. Riba Ruiz, J. C. Urresty, and J. A. Ortega, "Feature extraction of demagnetization faults in permanent-magnet synchronous motors based on box-counting fractal dimension," *IEEE Transactions on Industrial Electronics*, vol. 58, no. 5, pp. 1594–1605, May 2011.

[10] S. Rajagopalan, J. A. Restrepo, J. M. Aller, T. G. Habetler, and R. G. Harley, "Nonstationary motor fault detection using recent quadratic time–frequency representations," *IEEE Transactions on Industry Applications*, vol. 44, no. 3, pp. 735–744, May 2008.

[11] J. Zhang, H. Gao, Q. Liu, and C. Grebe, "A new real-time signal processing approach for frequency-varying machinery," *Journal of Vibration and Control*, vol. 24, no. 11, pp. 2359–2368, 2018.

[12] Y. Guan, M. Liang, and D. S. Necsulescu, "Velocity synchronous bilinear distribution for planetary gearbox fault diagnosis under non-stationary conditions," *Journal of Sound and Vibration*, vol. 443, pp. 212–229, 2019.

[13] W. Liu and X. Guo, "Detection of transient power quality disturbances based EMD combined with Choi-Williams distribution," in *2012 IEEE International Conference on Automation and Logistics*, pp. 588–591.

[14] B. Hollinger Kenneth, *Code optimization for the Choi-Williams distribution for ELINT applications*, Dec. 2009. [Online]. Available: `https://calhoun.nps.edu/handle/10945/4422`.

[15] J. S. L. Senanayaka, V. K. Huynh, and K. G. Robbersmyr, "Fault detection and classification of permanent magnet synchronous motor in variable load and speed conditions using order tracking and machine learning," *Journal of Physics: Conference Series*, vol. 1037, no. 3, 2018.

Paper E

Mixed Fault Classification of Sensorless PMSM Drive in Dynamic Operations Based on External Stray Flux Sensors

Sveinung Attestog, Jagath Sri Lal Senanayaka, Huynh Van Khang, Kjell G. Robbersmyr

This paper has been published as:

S. Attestog, J. S. L. Senanayaka, H. Van Khang, and K. G. Robbersmyr, "Mixed Fault Classification of Sensorless PMSM Drive in Dynamic Operations Based on External Stray Flux Sensors," Sensors, vol. 22, no. 3, p. 1216, Feb. 2022, doi: 10.3390/s22031216.

E.1 Abstract

This paper aims to classify local demagnetisation and inter-turn short-circuit (ITSC) on position sensorless permanent magnet synchronous motors (PMSM) in transient states based on external stray flux and learning classifier. Within the framework, four supervised machine learning tools were tested: ensemble decision tree (EDT), k-nearest neighbours (KNN), support vector machine (SVM), and feedforward neural network (FNN). All algorithms are trained on datasets from one operational profile but tested on other different operation profiles. Their input features or spectrograms are computed from resampled time-series data based on the estimated position of the rotor from one stray flux sensor through an optimisation problem. This eliminates the need for the position sensors, allowing for the fault classification of sensorless PMSM drives using only two external stray flux sensors alone. Both SVM and FNN algorithms could identify a single fault of the magnet defect with an accuracy higher than 95% in transient states. For mixed faults, the FNN-based algorithm could identify ITSC in parallel-strands stator winding and local partial demagnetisation with an accuracy of 87.1%.

E.2 Introduction

Fault diagnosis in permanent magnet synchronous motors (PMSM) has always received a lot of attention, aiming at increasing the safety level in dynamic and critical applications or preventing large economical losses due to unexpected downtime [1]. Unlike industrial productions, PMSMs in wind turbines and electric vehicles are intensively exposed to dust, mechanical, chemical, and thermal stresses in harsh environments and thermal cycling due to the dynamic operations. This causes an inter-turn short-circuit (ITSC) in the stator windings and demagnetisation on rotor permanent magnets (PM) of PMSMs, resulting in reduced efficiency and increased cogging torque [2]. The ITSC is a common fault in all motor types, e.g., induction motor and reluctance motor. However, demagnetisation is a fault that is unique to permanent magnet motors. A uniform demagnetisation affects all magnets equally and significantly reduces the overall back electromagnetic motive force (BEMF). A local demagnetisation only affects a specific region of rotor magnets. The complexity of machine structure, variable speeds, and loads render fault diagnosis challenges due to sensor requirements and nonstationary signals, attracting significant research that has tackled ITSC and demagnetisation in industry and academia in recent years, which is briefly discussed hereafter.

E.2.1 Related Works

Most research on ITSC implements the short-circuit in a single-strand stator winding. The ITSC in such windings can be detected based on characteristic frequencies in the current measurement. However, stator windings in PMSM can have multiple strands in parallel. Such stator windings have lower stator resistance and inductance, but the maximum output of the BEMF is reduced. The impact of ITSC in multi-strand windings on current signals is less compared to its single-strand counterpart. Multiple strands in one phase

with an ITSC may be unaffected by it. The fault signature will be different if the ITSC is on a single stand or between two strands. Van Der Geest et al. [3] have numerically analysed a PMSM with three parallel strands in the stator to study the effect of ITSC on the copper losses. The authors proposed a fault detector, which was the fundamental component of the difference between machine neutral voltage and the estimated inverter neutral voltage based on three equal impedance. The method has been tested on both a high-speed PMSM prototype and an off-the-shelf PMSM. It was not possible to implement ITSC on the prototype; therefore, two additional turns were wound around two stator teeth to resemble an ITSC. The research does check the performance of the fault detector in case of "open strand fault", partial demagnetisation, and misalignment in simulation. It was found that the fault indicator was most sensitive to ITSC fault and could detect it with a severity level down to 0.4%. However, it is not clearly specified if the ITSC is applied to all strands or just a single strand. Furthermore, it is unclear whether the extra turns were added to a single strand or to the end terminal. The fault indicator was tested in steady state operation, but at different speeds. The loads in their experiments were either no-load or at the rated condition. No variable speed or load profiles were used to test the detector.

Zhu et al. [4] investigated a partial demagnetisation fault, which was assumed to be applied uniformly on all magnets. The rotor was demagnetised by increasing the internal temperature by overloading. The current level of demagnetisation was estimated based on the measured BEMF in two study cases, where the magnets had lost 17% and 33% of their original strength. The merit of this method is that it does not cause any physical damage or imbalance in the rotor, but the demagnetisation is implemented uniformly. The Vold–Kalman filtering for an order tracking was used to detect demagnetisation alone in a PMSM. Kao et al. [5] proposed a diagnosis algorithm, combining discrete wavelet transform and convolution neural network (CNN), to separate between local demagnetisation and bearing faults. Two strategies for demagnetisation were implemented: first replacing a piece of the magnet with aluminium, and learning how to weaken the strength of the magnet. The paper does not address the second method: how to weaken the magnet. However, validating this approach for detecting demagnetisation is not convincing, since there is an imbalance if the replacement material does not have the same density. The fault classifier proposed in [5] is based on one-dimensional CNN, being trained for demagnetisation fault and bearing fault, but the authors did not investigate the possibility for mixed fault context. The classifier was trained and tested for 20 different constant speed settings, but there is no variable speed profile in this work.

Iglesias-Martinez et. al. [6] investigated the use of bi-coherence and a fuzzy C-means algorithm for detecting winding asymmetries in induction motors. External coil sensors with 1000 turns and an external diameter of 8 cm were placed in proximity to the motor, measuring radial, tangential, and axial components of the stray flux. The stray flux signals were recorded during the start-up of the motor; then, they were used in a fuzzy C-means machine learning fault classifier, resulting in an accuracy of about 90%. Zamudio-Ramirez et. al. [7] proposed also smart sensors for the online detection of individual and combined faults in induction motors, such as broken rotor bar and misalignment. The sensor solution consists of three hall sensors oriented towards the three Cartesian directions. Their

analysis concluded that the axial and radial stray flux components were the most effective in the transient analysis. The classification was performed with linear discriminant analysis and feedforward neural network (FNN), where the time-frequency representations were computed from the MUSIC algorithm during startup. The classifiers were trained by data from different mechanical faults such as broken rotor bar and misalignment, but mixed faults were missing in the study. The neural network was trained on measurements from startup duration alone, without other operations.

Gurusamy et al. [8] conducted a theoretical study on how loading would affect the fundamental and third harmonic of the measured stray flux based on finite element analysis. The information of stray flux was extracted from selected points in the finite-element analysis. The results showcased how the harmonics would change in magnitude, depending on the location of the fault. Simulations were verified with experimental work. The third harmonic of the stray flux was proposed as the fault indicator, since it was less affected by loading conditions than the fundamental component. However, the third harmonic may indicate many kinds of asymmetries in the magnetic circuit. Furthermore, the ITSC detector was only tested for constant speed or load operations.

E.2.2 Contribution

Conventional methods of detecting faults in stator winding and PMs of PMSMs methods focus on off-line tests, steady-state operations, and require a high number of available sensors in the drives. However, PMSMs are always controlled and dynamically operated based on the driver's demands. Furthermore, modifying the existing drive system for automatic fault detection must be avoided in critical systems and applications, where sensorless controls are preferred due to reliability or reduced maintenance cost. Stray flux has recently gained popularity in the literature for fault detection of ITSC, demagnetisation, and mechanical faults due to its sensitivity and is simple to install outside of a drive system. Existing research focuses on model or signal-based algorithms, requiring multiple stray flux sensors and speed measurements for detecting faults in variable speed conditions. Furthermore, seeded demagnetised magnets were inappropriately implemented in the existing research, causing imbalances or without an overheat demagnetisation. To the author's knowledge, most existing machine learning-based fault classifications are trained and tested on the same datasets or the same operational profiles, rendering a challenge of trustworthiness on other datasets or working conditions. To address the mentioned challenges, this paper aims to achieve the following:

1. Increase the robustness of potential machine learning classifiers against transient operating conditions and different operation profiles by resampling at a fixed angular increment.

2. Eliminate the need of position sensors in the resampling process (order tracking).

3. Introduce a heat treatment method for inducing local partial demagnetisation fault.

4. Train the machine learning algorithms, ensemble decision tree (EDT), k-nearest neighbour (KNN), support vector machine (SVM), and feedforward neural network

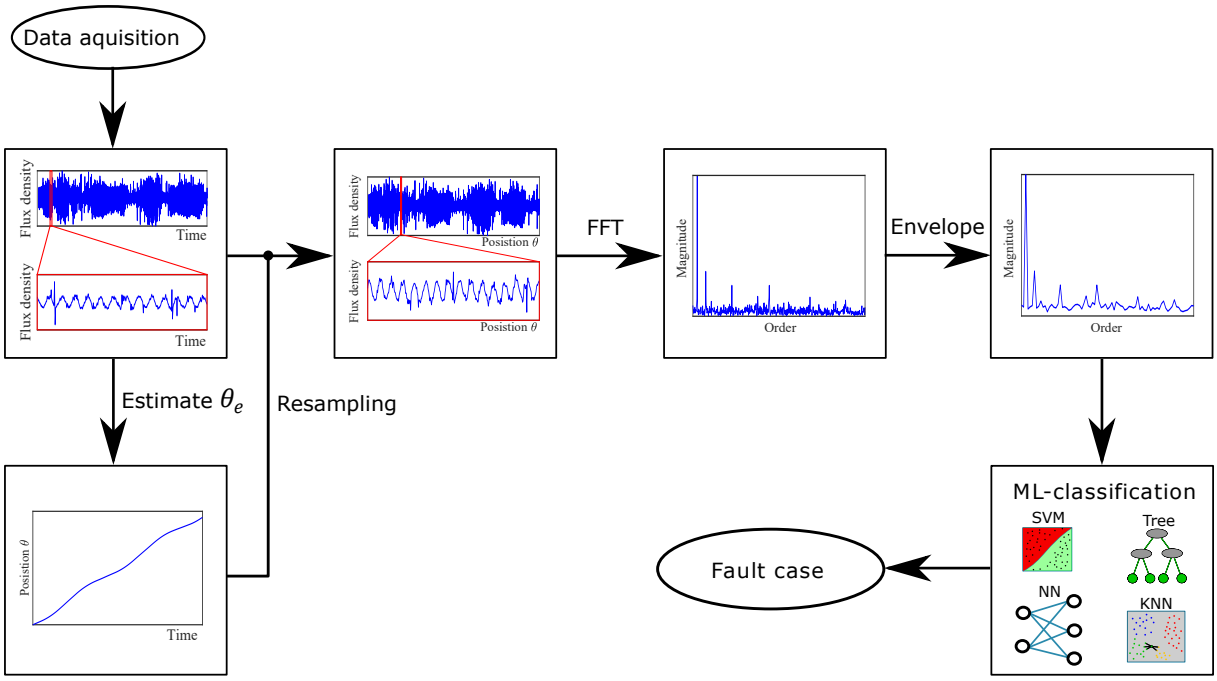

Figure E.1: Block diagram of preparation of features

(FNN) and compare their performance in different operation profiles and with or without the presence of mixed faults in the datasets.

5. Investigate the variation of the classifier accuracy based on features computed from data collected by stray flux, current, and torque signals.

6. Recommend minimum length of data sample for an accurate fault classification.

The rest of this paper is organised as follows: Section E.3 describes the proposed technique for fault diagnosis under stationary as well as nonstationary conditions, which was followed by a description of how the fault was implemented in Section E.4. Section E.5 describes the experimental setup of the in-house test bench. The results are presented and discussed in Section E.6. This paper ends with concluding remarks in Section E.7.

E.3 Methodology

The block diagram in Figure E.1 shows the proposed pre-treatment of measurements for computing features before passing it through a machine learning classifier. First, data samples were collected and labelled based on their fault case and operation condition. The rotor position was estimated with an optimisation problem. The estimated position was used for resampling of the original datasets, with data points sampled at a fixed time increment, to datasets sampled at a fixed angular increment. The resampled datasets were split into smaller samples, which contain a fixed number of rotor revolutions. The second step is to compute the spectrograms of the resampled datasets with Fast Fourier Transform (FFT), which is normalised based on the fundamental frequency. This gives a fundamental frequency spike with an order number equal to 1 and a magnitude of

1. Therefore, any fault classification approach based on analysing these spectrograms needs to study the composition of the harmonics. Third, an envelope of the spectrogram was obtained by splitting the spectrogram into intervals with a length of 0.5 order centred around the half harmonics [0.5, 1, 1.5,... , 39.5, 40] and then finding the maximum in each interval. This simple method produces an envelope of the spectrogram, which includes the harmonic peaks with fewer entries. In addition, the pre-treatment will order normalise the spectrogram and make classification more robust against speed change. The resulting envelopes of the spectrograms are chosen as the selected features for classifications, being trained and tested on EDT, KNN, SVM, and FNN.

E.3.1 Resampling Time-Series Data

Measured signals in PMSM, e.g., flux, current, and voltage are cyclical and ideally have a sinusoidal shape. In the case of a four-pole motor, every two cycles in these measurements represent one revolution of the rotor. Normally, datasets are sampled at constant time intervals. There will be more data points per cycle at lower speeds. For example, there are 400 data points per cycle if a four-pole motor is running at 750 rpm with a sampling frequency of 10 kHz. The number decreases to 100 data points per cycle when the motor is running at 3000 rpm. This imbalance of samples per cycle is the main cause for the peaks spreading over a wide range of frequencies in the spectrogram of signals with time-varying frequencies, which is computed by FFT. A solution to this is to resample the data from equal time steps to equal angular steps [9].

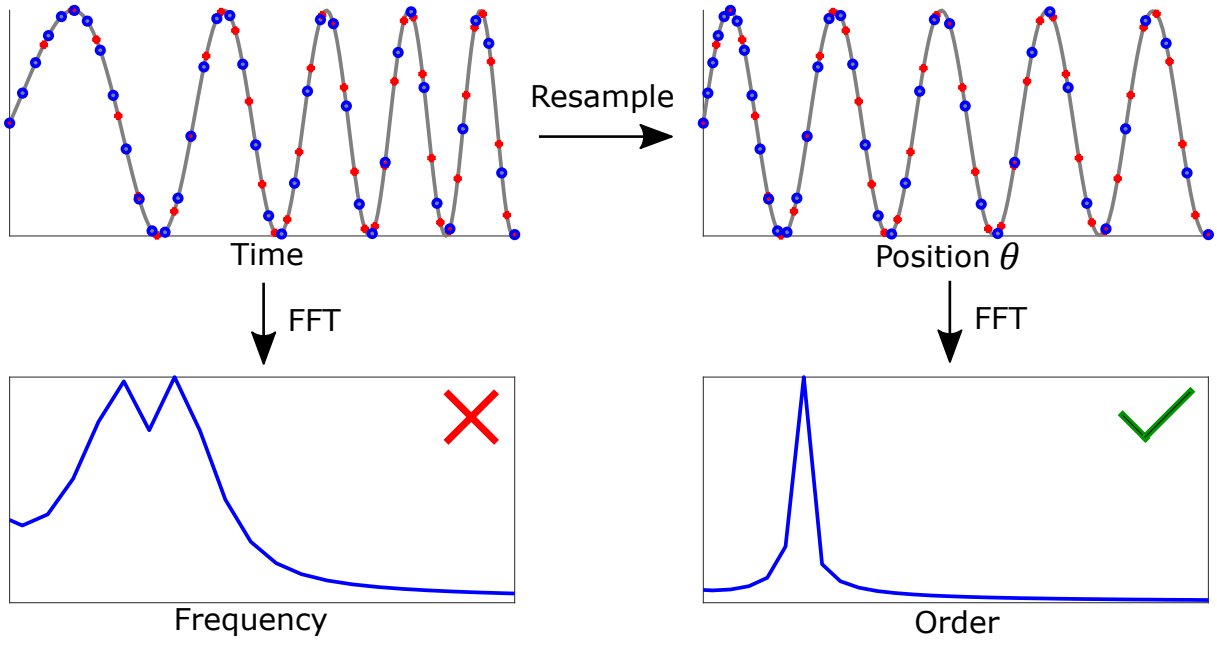

Figure E.2: Visualising the benefit of the resampling process from time- to θ-domain.

Figure E.2 shows the results of the resampling process with a chirp function. The blue rings represent samples from the original dataset, where the data points are spaced at an equal time distance. Figure E.2 highlights that more samples are concentrated at the first interval, when the instantaneous frequency is at its lowest. The red points represent the

resampled dataset with the equal angular distance, where every interval have the same number of samples regardless of frequency. The resampling process can be viewed as a transformation from time-domain to θ-domain. After the transformation, the datasets can be split into intervals defined by a fixed number of cycles instead of a fixed time interval. Longer samples, regardless of being defined by time intervals or cycles, will increase the order resolution in the spectrograms and improve the confidence in the present peaks. The minimum number of cycles needed for computing features will be discussed in the results.

E.3.2 Estimation of Position

The resampling process requires the information of the rotor position or position sensor [10]. However, being dependent on encoders, resolvers, or tachometers will exclude the applicability in sensorless PMSM drives, since these sensors are not available. Removing a position sensor will improve the system reliability and enhance the performance of any fault classification method. Etien et al. [11] proposed a nonlinear adaptive algorithm with phase-locked loop and orthogonal signal generators. This method is suited for online detection but does require tuning a PI controller. Lu et al. [12] computed the phase from a filtered current signal, which is turned into a unipolar signal by an absolute function. The signal is divided into frames, which is every half cycle of the sine function. The phase angle is computed from the inverse sine of the ratio between the instantaneous value of the function within the current frame and the maximum value of the previous frame. This method is more prone to noise, because of the few key data points defining the maximum value of each frame. The method suggested in this paper is to find the fundamental frequency via an optimisation problem. Hou et al. [13] proposed ridge regression for obtaining instantaneous frequencies in time-frequency representation. Then, this method requires wavelet or short-time Fourier transform. The suggested method does not need such algorithms for estimating the fundamental frequency. Assuming the speed changes is negligible in a short time period (0.1 s is used in this study), the fundamental component of the signal can be defined as follows:

$$h(t) = \sin(2\pi f_1 t + \ \theta\ ) \tag{E.1}$$

where f_1 is the fundamental frequency and θ is the phase angle. The fundamental frequency can be obtained via FFT, but short-time periods are needed for an accurate estimate, which negatively affects the frequency resolution. Instead, the fundamental frequency is estimated by the optimisation problem:

$$[f_1, \theta] = \underset{f_1,\theta}{\arg\min} \left((x(t) - h(t))^2 \right). \tag{E.2}$$

The range for the optimal value of f_1 can be narrowed down between the standstill and nominal speed, i.e., $f_1 \in [0, 100]$ Hz. The value of the objective function in (E.2) repeats itself when θ is increased from 0 to 2π, keeping the f_1 constant. The modulo operator is used such that $\theta \in [0, 2\pi]$. Steps to estimate the fundamental component in the stray flux signal are described as follows.

1. Extract a small time sample with period T from the original time-series data.
2. Compute the objective function for frequencies in the interval $[0, 100]$ Hz with an incremental step of 5 Hz. The optimal θ for a given f_1 is found by the Golden Section Search in the interval $[0, 2\pi]$. The values for f_1 and θ, that yield the smallest value of (E.2) are the initial guesses in step 3.
3. Find the optimal solution for f_1 and θ by the Simplex Search method in [14] with the initial guesses given in step 2.
4. Repeat step 1 to 3 for the next time step until the end of the time sample.

The output of the estimator is dependent on all data points in the sample of each iteration. Therefore, it would be less prone to noise and require no tuning. One weakness to this approach for obtaining the fundamental frequency is a local convergence. Signals with an immoderate signal-to-noise ratio will tend to reach 0 Hz instead of the desired solution. One approach to avoid this problem is to increase the lower boundary in the brute force analysis in step 2, e.g., 10 Hz.

E.3.3 Machine Learning Methods

This section aims to investigate the performance fault classifications of features computed from stray flux measurements. The following supervised machine learning algorithms are investigated: DT, KNN SVM, and FNN. Each sensor produces an envelope of the spectrogram with 41 elements; thus, the number of inputs is the product between 41 and the number of sensor measurements added to compute the features.

E.3.3.1 Ensemble Decision Tree

The "trees" in decision tree classification starts at the first node known as the trunk, then it branches out to more if-else statements. The final nodes of the tree are called leaves, which get numeric values in the case of regression tree and discrete categories in case of classification tree. An EDT consists of a forest with smaller decision tress called "stumps". They usually only have one node with two leafs each. The "stumps" are weak learners on their own, but combined ones can predict with high accuracy where the class is decided with a majority vote. However, the votes from each "stump" got a weight, which is obtained from training. The EDT in this study uses the AdaBoost method for training with 100 training cycles with the learning rate of 1. The maximum number of splits per tree is set at 1, and each leaf has a minimum of 1 observation [15].

E.3.3.2 K-Nearest Neighbours

KNN is one of the simplest supervised machine learning algorithms, but it is still an effective tool. The principle of the classification process is that new observations are categorised based on the previous observations closest to them. The number of neighbours, k, is used to decide the class of the new observation. It is adjusted to make the classifier more robust and less likely to overfit. The votes from the closest neighbours are counted,

and the class with the highest number of votes dictates the outcome of the classifier [16]. In this paper, k was set to 15, which was obtained via trial-and-error during training. The distance is computed with Euclidean distance, and the potential ties in four-class classification are settled by the label of the nearest neighbour among the tied groups. Ties are not possible in fault detection (two-class classification), since k is an odd number. Each of the features is standardised by centring and scaling with respect to their mean and standard deviation.

E.3.3.3 Support Vector Machine

In an SVM, the input data are mapped into a high-dimensional feature space using a kernel function. The objective is to maximise the margin between the classes and give the best separation of the training data [17]. In this paper, the linear kernel function was used. The nature of SVM is to classify between two datasets. These methods are called "one-versus-all" and "one-versus-one". The first method uses multiple SVMs where each one determines if an observation belongs to their respective class. Ideally, only one SVM will identify the observation as their own class, which dictates the outcome of the classifier. The second type of multi-class SVM was used in this study. Multiple SVMs are trained to separate between two classes, which is unique to each SVM. A decision is reached with a plurality vote. Each of the features is standardised by centring and scaling with respect to their mean and standard deviation.

E.3.3.4 Feedforward Neural Network

The mathematical model [7] for the output y in each neuron in an FNN is given as

$$y = f\left(\sum_{n=1}^{N} w_n x_n + b\right) \tag{E.3}$$

where w_n and b are the weights and bias applied to the inputs x_n, and $f(\cdot)$ is the activation function. The rectified linear unit (ReLU) activation function was selected. A block diagram of the FNN used in this paper is shown in Figure E.3, consisting of two fully connected layers. The first one contains 100 neurons, while the other is equal to the number of classes. In case of fault detection, it is 2, and it is 4 for classification with mixed faults. It also has a batch normalisation layer, which makes it faster and more stable. The last two layers are the softmax layer and the classification layer. The network is trained with an adaptive moment estimation [18] with a learning rate of 0.001, gradient decay of 0.9, squared gradient decay factor of 0.99, and denominator offset of 10^{-8}. The mini-batch size and number of epochs are set to 16 and 10, respectively.

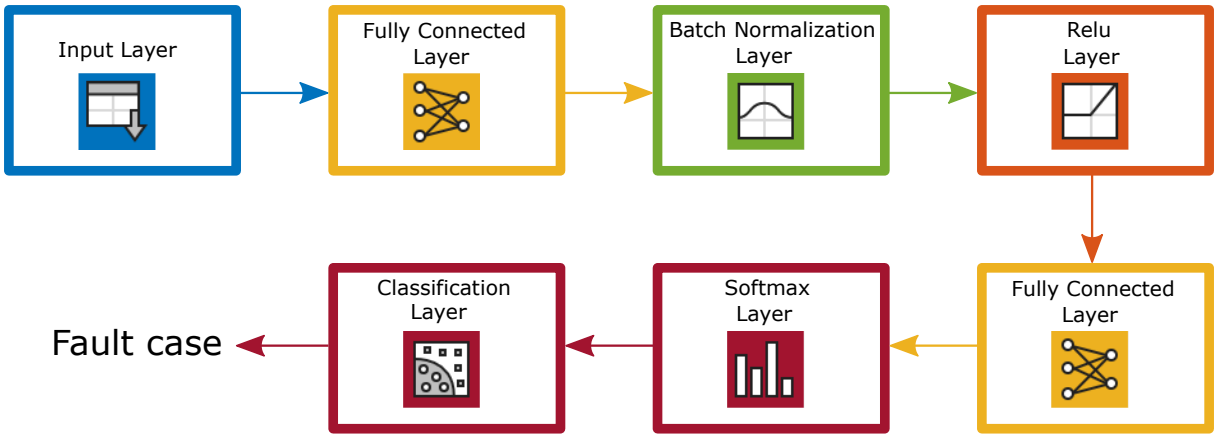

Figure E.3: Block diagram of FNN used for fault classification

E.4 Implementation of Faults

E.4.1 Implementing Local Demagnetisation

Demagnetisation faults in permanent magnet motors are usually implemented by removing parts of the magnets [19] and replacing them with a non-magnetic material [20]. This is to counteract the imbalance in the rotor. Another option is to install weaker magnets in the rotor through manufacturers [21]. The mentioned implementations do not mimic the demagnetisation due to thermal cycling in dynamic operations of sensorless PMSM drives. This study presents a demagnetisation process by heat treatment. The temperature distribution on magnets is not uniform. The investigations performed by Fernandez et al. [22] and Reigosa et al. [23] showcased how the temperature is distributed under different applied currents in thermal equilibrium. The study was applied on PMSM with interior magnets, where they concluded that the hottest spot on average over time is in the middle of the magnet. Thus, this region is most likely to be affected by demagnetisation due to overloading.

Several attempts for local demagnetisation were executed involving an electric discharge machine, blow torch, and heat gun. None of the solutions can achieve a satisfactory result, where one magnet became partially demagnetised without causing significant physical damage to the rotor. Note that these methods were tested on a separate rotor that was not used in the final test. The best option, to our knowledge, is to heat one side of the rotor on a 1500 W electric cooking plate made of iron. A solid aluminium block with the dimensions of 200 mm $\times$ 90 mm $\times$ 20 mm was placed between the rotor and the cooking plate due to its low permeability. This ensures a safe placement and removal of the rotor on the hot cooking plate. A wet towel was placed on the rotor to cool the other poles. The heat treatment is shown in Figure E.4. The aluminium block reached temperatures up to 232 °C. The rotor was left on the hot surface for 5 minutes. Thermal paste is used to improve the heat transfer between the objects.

The magnetic field around the rotor was measured before and after the thermal treatment, as shown in Figure E.5 with an Extech SDL900 magnetic field meter. Note that the measurements after the heat treatment were done after the rotor had cooled down

to the ambient temperature. The wooden frame allowed the rotor to rotate, kept its rotor axis horizontal, and prevented any translational movement. The measured magnetic field strength surrounding the rotor decreases with distance. Therefore, the hall sensor in SDL900 was kept at a constant distance of 3 mm from the rotor surface.

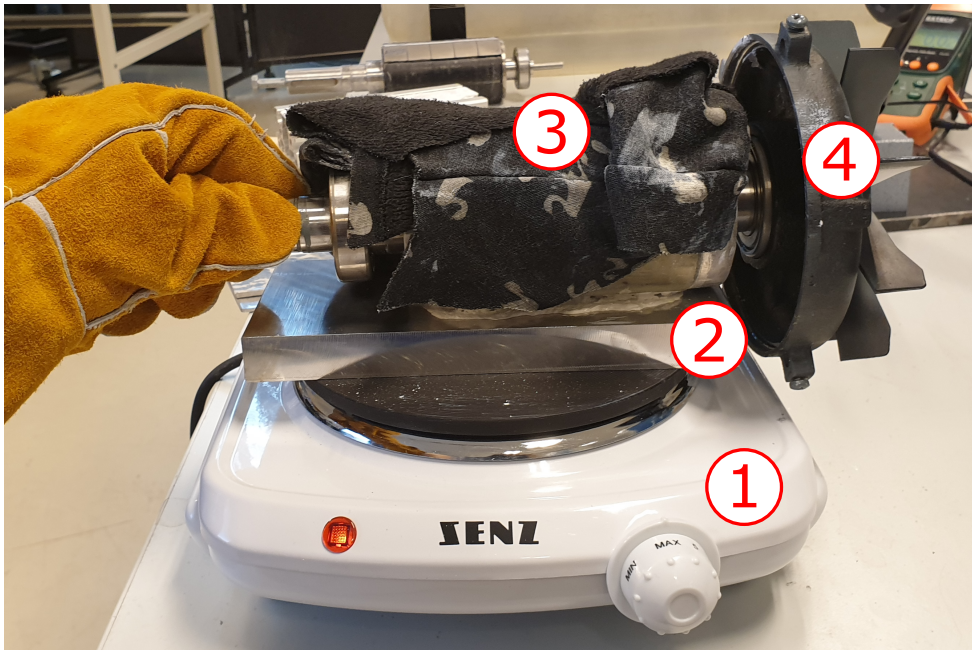

Figure E.4: Thermal treatment setup consisting of (1) cooking plate, (2) solid aluminium block, (3) wet towel, and (4) the rotor

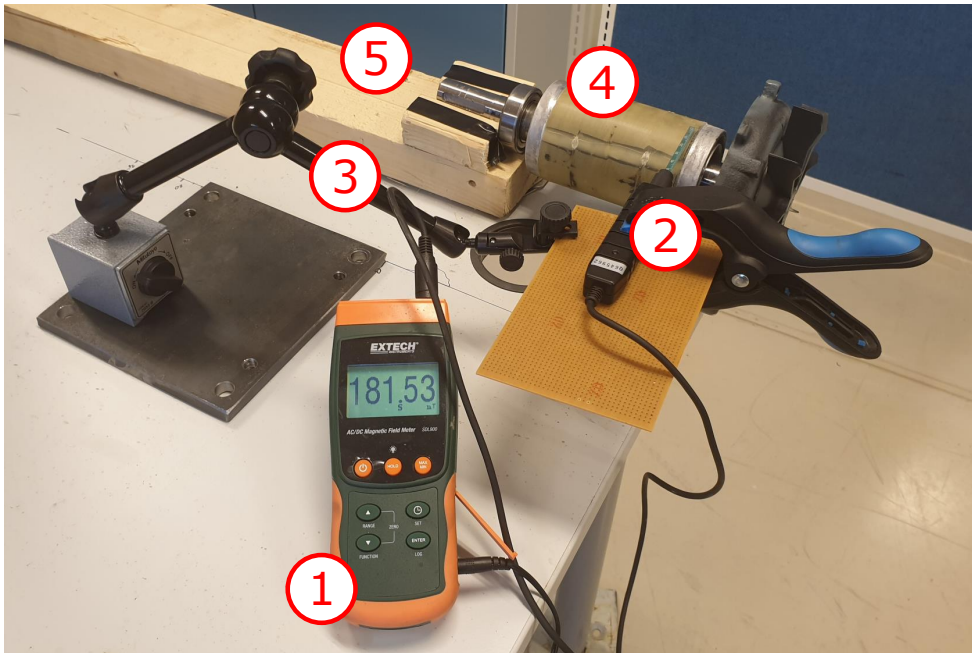

Figure E.5: Setup for magnet strength measurement: (1) Extech magnetic AC/DC magnetic field meter, (2) measurement rod, (3) universal magnetic stand, (4) PM rotor, and (5) wooden frame

Figure E.6 shows the measured magnetic field surrounding the rotor before and after the heat treatment. The measurement was repeated three times to reduce the measurement error. The North poles are indicated by positive value with the South ones are negative. It can be seen that the rotor after the heat treatment has a slight decrease of magnetic strength at two points on one pole. Further investigations reveal that those two spots lost up to 30% of their original field strength.

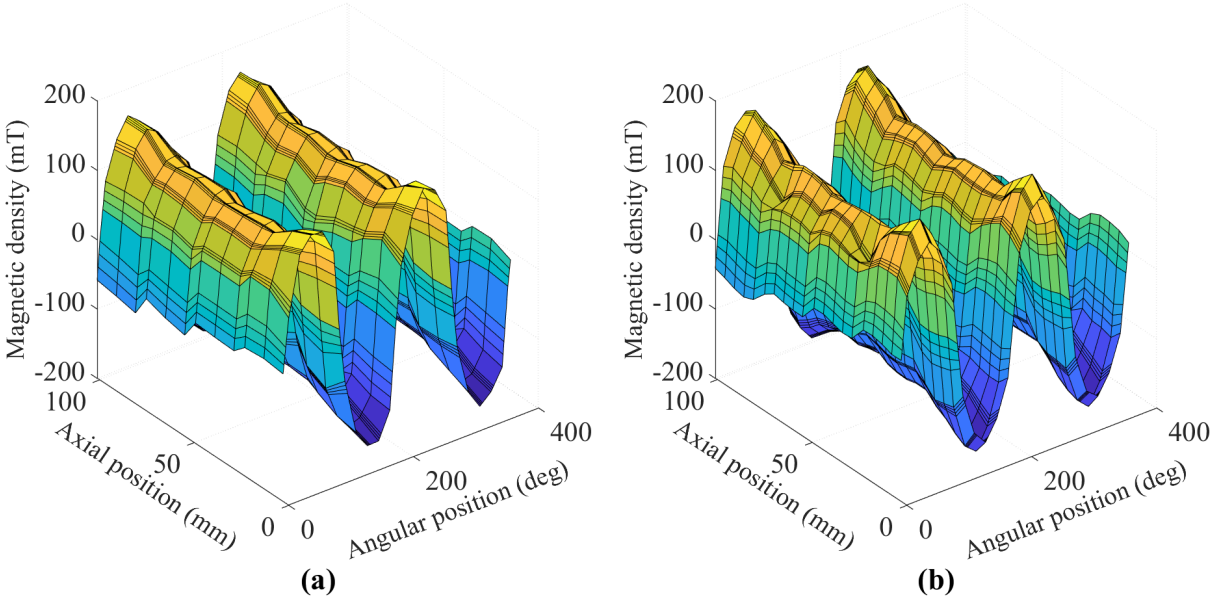

Figure E.6: Side-by-side comparison of measured magnetic field strength of the permanent magnet rotor (a) before and (b) after the heat treatment

E.4.2 Implementing Short Circuit Fault

In the studied PMSM, each phase winding has three strands in parallel. The advantage of this configuration is a reduced overall phase resistor and phase inductance. The drawback is a smaller BEMF. A simple analysis of the expected DC resistance measured by a multimeter was conducted. The inductance is ignored, since it does not affect the measured resistance in steady state.

It is assumed that the resistance of each strand is R_{S}. Four taps were implemented in one phase of the PMSM. The taps are shorted with the input voltage terminal U. This arrangement ensures that no short-circuit occurs between two parallel strands. Resistances between a tap and the end terminals were measured for each tap. A single multimeter can often measure resistance, but the accuracy is limited by the low current induced by the multimeter. Figure E.7 shows the sensitive resistance measurement setup. A current source of 1 A is used, which is significantly less than the nominal current 6 A of the studied PMSM. The strand, where a tap is placed, is assumed to be split into two resistors R_1 and R_2. The measured equivalent resistance R_{mea} between a tap in the middle of the coil and the end or end terminals is defined as below.

$$R_{\mathrm{mea}} = \mu_{\mathrm{f}} \left(1 - \frac{2}{3}\mu_{\mathrm{f}}\right) R_{\mathrm{S}}, \tag{E.4}$$

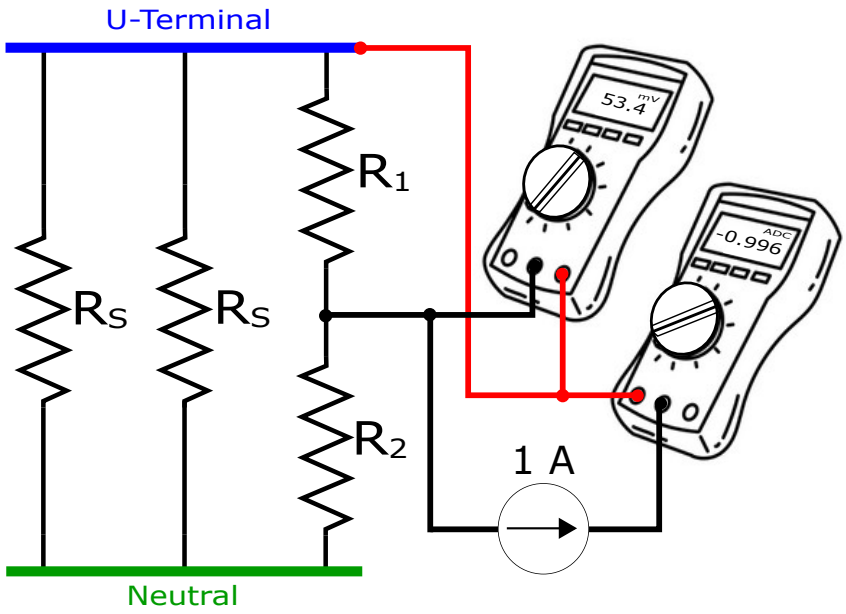

Figure E.7: Sketch illustrating the setup for accurate resistance measurement

where μ_f is the number of turns between the tap and the end terminals divided by the total number of turns in the coil. The solution for μ_f is the second-order equation :

$$\mu_f = \frac{3}{4} \pm \frac{1}{2}\sqrt{\frac{9}{4} - 6\frac{R_{\text{Mea}}}{R_S}}. \tag{E.5}$$

The valid answer from (E.5) is identified based on the location of the tap relative to the end terminals. If the tap is expected to be close to the U-terminal, it is reasonable to assume that $\mu_f < \frac{3}{4}$. It is also reasonable to assume that $\mu_f > \frac{3}{4}$ between the tap and neutral. The ITSC severity of 5% was used in this study.

E.5 Experiment and Data Collection

E.5.1 In-House Test Bench

A schematic diagram of the test setup is shown in Figure E.8, including a 400 V three-phase drive and the Microlabbox operated with an office laptop. The hall sensors measuring the stray flux were solid-state sensors of type SS495A. The output of these sensors are ratio-metric and linear within the range $[-67, 67]$ mT and has a sensitivity of 31.25 $\frac{mV}{mT}$. Two sensors were soldered to a veroboard and wired to the Microlabbox, which delivered power to the sensors and recorded the stray flux. One of the sensors was bent 90°, such that it could measure both the tangential and radial component of the stray flux. Two sets of sensors were placed in proximity to the motor at the top and on the side. Furthermore, the current sensors are located inside a cabinet to the top right corner of Figure E.9 to measure the input phase currents. The study motor has no position sensors; therefore, the encoder on the generator measure s the rotor position to validate the suggested method of position estimation.

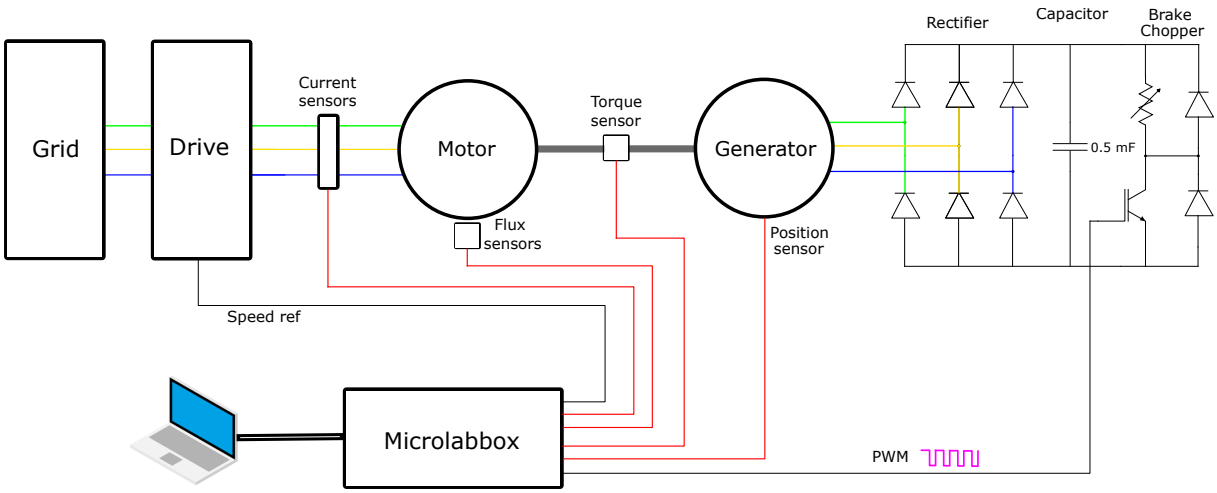

Figure E.8: Schematic diagram of test bench.

Table E.1: Nameplate parameters for IE5-PS2R 90 L.

Parameter	Value
Output power	3 kW
Nominal speed	3000 rpm
Number of poles	4
Nominal current	6.0 A
Nominal voltage	315 V
Phase resistance	0.6 Ω
Phase inductance	6 mH

Demagnetisation fault is introduced by replacing the rotor with no magnet defects with a rotor that went through the heat treatment process described in Section E.4.1 . Both rotors belong to the same type of PMSMs: IE5-PS2R 100 L, with their key parameters given in Table E.1. ITSC faults are induced by wiring the external taps implemented in the PMSM. A fault resistor (1 Ω) is used for mimicking the remaining insulation in an ITSC and limiting the short circuit current. The motor is coupled to a generator with a torque transducer in between. Both the encoder and torque transducer are powered by a 24 V DC-supply. The output of the generator is rectified with a three-phase full-bridge rectifier. Two 1000 μF capacitors are connected in series across the output terminal of the rectifier, which removes the ripples of the DC output. The reason for two capacitors in series is that the output of the rectifier at nominal speed does exceed the voltage rating of the capacitor (400 V). The equivalent capacitance is 500 μF, but this is still sufficient to remove the voltage ripples. The brake chopper is regulated by a pulse width modulation (PWM) signal from the Microlabbox, which needs to be amplified by a factor of 4 due to insufficient voltage amplitude from the Microlabbox. The op-amp is powered by a 12 V DC supply. In an ideal system, the duty cycle would be proportional to the reciprocal of the motor speed. However, due to losses and imperfections, a look-up table is generated for the duty cycle , which dictates the required duty cycle for achieving a requested load in the speed range between 1000 and 2000 rpm.

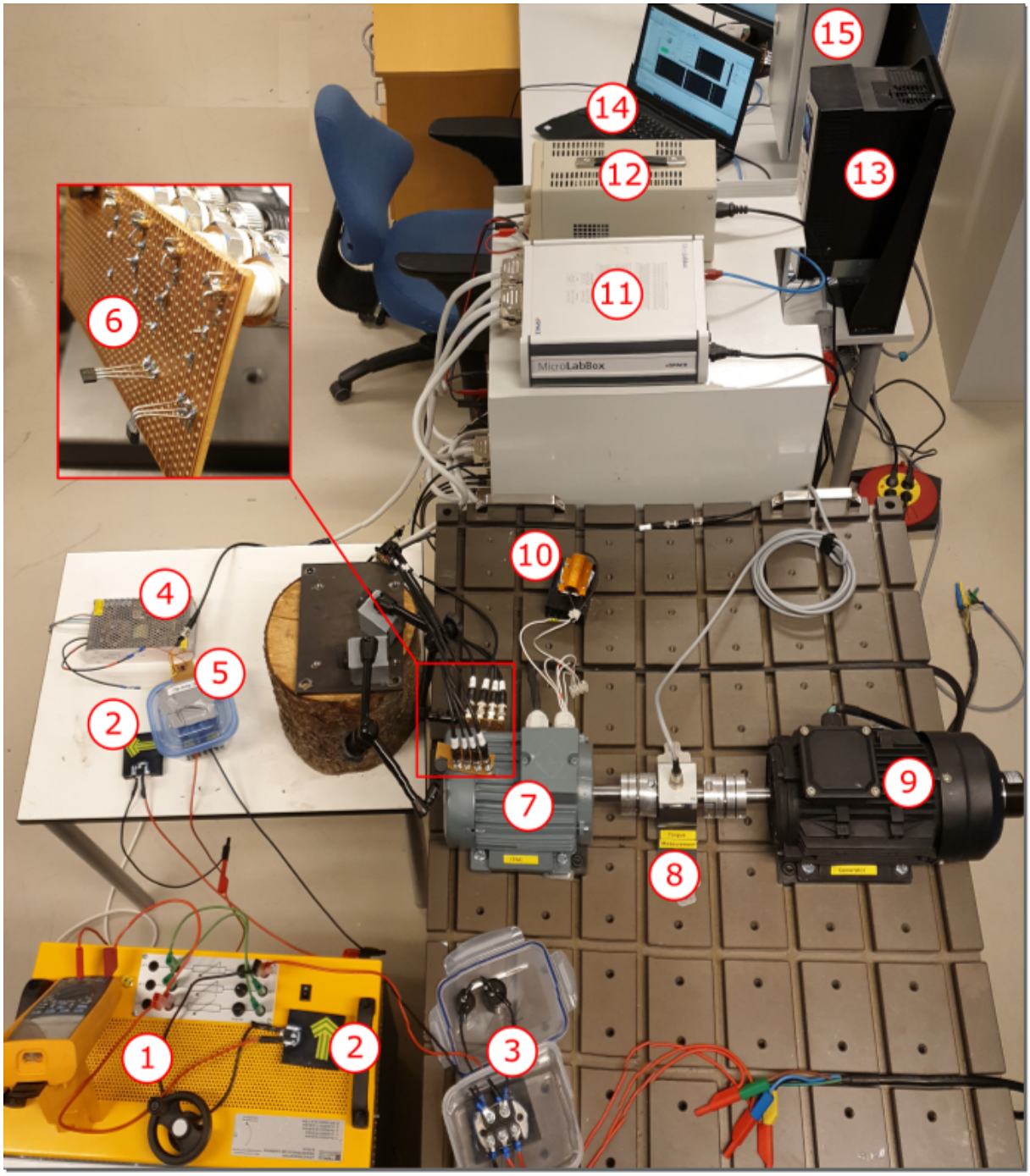

Figure E.9: Overview of the test bench with (1) resistor bank, (2) flyback diode, (3) three-phase rectifier with capacitor bank, (4) 12 V DC supply, (5) IGBT brake chopper with op amp, (6) hall sensors, (7) PMSM, (8) torque sensor, (9) generator, (10) fault resistor, (11) Microlabbox, (12) 24 V DC-supply, (13) ABB drive, (14) office laptop, and (15) cabinet containing the current sensors

E.5.2 Description of Collected Datasets

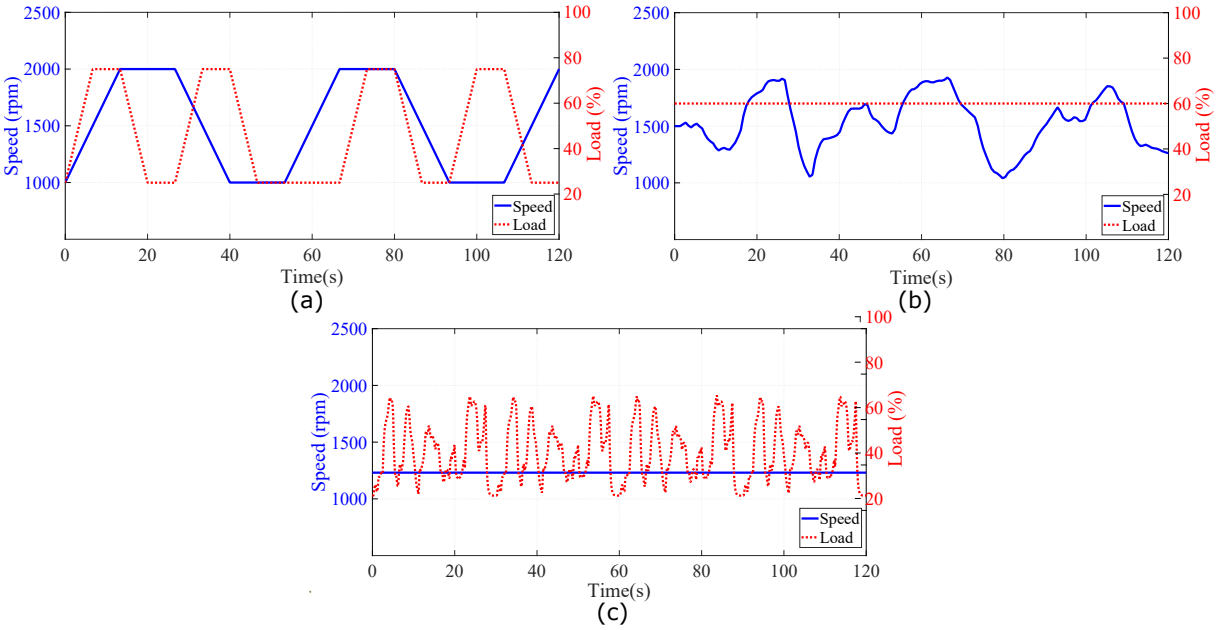

Figure E.10: Visual representation of the three operation profiles: (**a**) Profile 1—Variable load and variable speed. (**b**) Profile 2—Constant load and variable speed and (**c**) Profile 3—Variable load and constant speed.

Stray flux was measured for three different nonstationary operating conditions with a sampling rate of 10 kHz. The rotor position, input current, and torque were measured for all three profiles. Observation used for training and testing in the ML tools is computed from smaller samples. They are from three operation profiles, which are split based on a fixed number of revolutions of the rotor. The output of the resampling process obtained 400 samples per revolution. Section E.6 will use the term "cycles", which is double the number of revolutions of the rotor. Profile 1 contains a regular pattern, where the speed ramps up and down between 1000 and 2000 rpm. The load changes between 25% and 75% of the full load. The profile shown in Figure E.10a includes combinations of increases and decreases of the load when the speed is increasing, decreasing, or constant. The second operation profile in Figure E.10b keeps the reference speed constant at 1200 rpm, but the load changes with a pattern, which is randomly generated and repeats itself every 30 s. The last profile keeps the load steady at 60%, and the reference speed profile was also generated with random numbers. It is plotted in Figure E.10c. The total period is 120 s for all three profiles. In the remainder of this paper, these profiles will be referred to as Profile 1, Profile 2, and Profile 3.

Data collection of all conditions of the PMSM was repeated for all mentioned profiles in the following fault condition: There were healthy conditions, ITSC with 5% severity, local partial demagnetisation, and a mixed faulty case of ITSC and demagnetisation.

E.6 Result and Discussion

E.6.1 Position Estimation

The purpose of estimating the rotor position is to remove the need for any position information or sensor in the fault classification and make the classifiers robust against speed changes. A fault classifier scheme using stray flux alone would be easier to implement in existing sensorless PMSM drives , since an external flux sensor can be placed in proximity of the PMSM. The optimisation problem, which estimated the speed, was able to estimate the electrical position θ_e from a flux signal with an average relative error of less than 0.5%. Therefore, the position measurements were replaced by the estimated position for the resampling process. The estimated electrical angle position and the measured value from the encoder are plotted in Figure E.11.

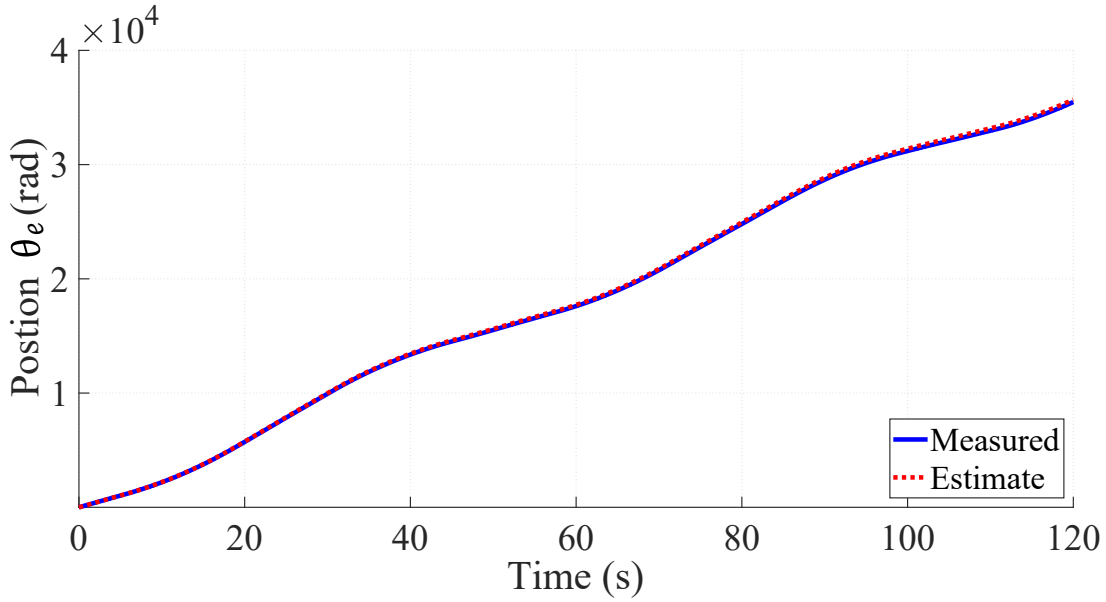

Figure E.11: Comparing estimated θ_e with measured θ_e

E.6.2 Comparing Physical Parameters

The performance of the four learning classifiers, EDT, KNN, SVM, and FNN, is investigated. The recorded data of operation Profile 1 with regular change in speed and load is split in 80% for training and 20% for testing. The observation in Profile 1 is shuffled randomly before the split to prevent over-fitting of the classifiers. After training, all algorithms were tested on the whole datasets of Profile 2 and Profile 3 , which were also shuffled, and the remaining observation from Profile 1. The performance of algorithms is varied depending on the training data. Therefore, the average achieved accuracy and training time are obtained by a Monte Carlo analysis, where the algorithm is repeatedly trained and tested 100 times. The training time is reported in Table E.2 . All the algorithms had a training time less than 3 s. However, the computation times of EDT and FNN of the first and second orders of magnitude are larger than the other two.

Table E.2: Training time of the machine learners

Number of Classes	EDT	KNN	SVM	FNN
2	0.60 s	0.011 s	0.084 s	1.3 s
4	2.8 s	0.010 s	0.12 s	2.1 s

The letters "τ", "I", and "ϕ" in Figures E.12–E.14 refer to the use of torque, current, and stray flux signals for training the algorithms, respectively. The number refers to how many sensors were used to compute the features in each observation. For the torque signal, there is only one transducer coupled between the motor and generator. Three current sensors or one sensor per phase are used to collect current signals. There are four hall sensors in the setup, which can record the radial and tangential components in proximity of the motor through data acquisition . In the comparison study between physical parameters, only one pair of hall sensors is used.

For single faults, all four machine learning algorithms were trained on Profile 1 in the cases of only local demagnetisation or ITSC fault (severity 5%). The achieved accuracy of the classifiers is on the y-axes in Figure E.12 and Figure E.13 with a range between 50% and 100%. This highlights the differences in performance of the classifiers trained with different physical measurements and operation profiles. In case of ITSC fault, all classifiers obtain an accuracy less than 70% with the current and torque measurements. It appears that these physical parameters are not sensitive to ITSC. This phenomenon can be explained based on the configuration of the stator winding with three parallel strands. The short-circuit tap s are connected to the phase terminal, which is a common point for all three strands. The other end of the short-circuit was soldered to a single strand, making the remaining strands in parallel unaffected. Therefore, the 5% ITSC fault has less impact on the motor torque or total phase current, which is the sum of all the currents in the three strands. However, the hall sensors are significantly more sensitive to the presence of the ITSC fault. The algorithms EDT, SVM, and FNN can reach an average accuracy over 90% when testing on data of Profile 1 . The purpose of the pre-treatment of the time-series datasets is to make the machine learning algorithms more robust against transient operating conditions. The strength of this process is further demonstrated by testing the machine learner on Profile 2 and Profile 3. None of the machine learners have been train with samples from these operation profiles. The accuracy of the ITSC detector drops from around 95% to around 85%, with SVM and FNN having the highest accuracy. The drop in accuracy implies that there is some over-fitting, and the machine learners can be confused by new unexpected operating conditions. However, the accuracy of 85% is still considered respectable. This is the accuracy when testing on one operation profile, which the machine learners have not been trained for, and an ITSC fault with 5% severity on one out of three parallel strands in a PMSM is less severe as compared to the case of one strand per phase. KNN has the lowest accuracy in this case study. It is hardly better than random chance when being trained on features computed from only torque or current data and tested on Profile 2 and Profile 3. Data from stray flux sensors on the other hand achieve an average accuracy of around 80%.

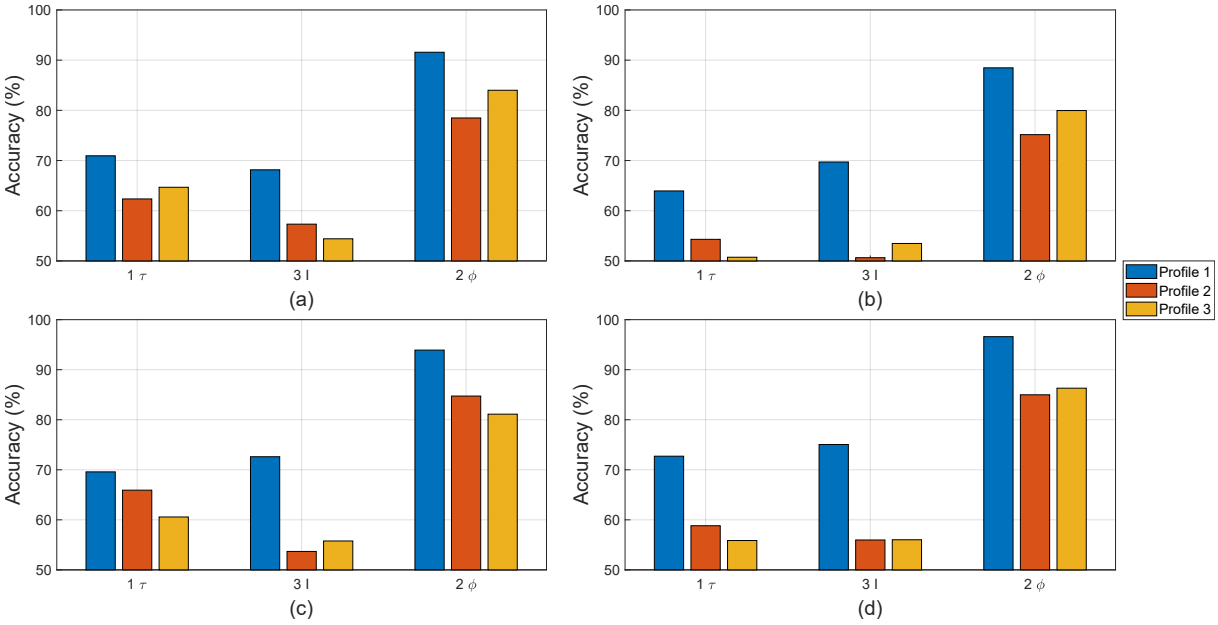

Figure E.12: Detection accuracy with ITSC alone obtained by (**a**) EDT, (**b**) KNN, (**c**) SVM, and (**d**) FNN

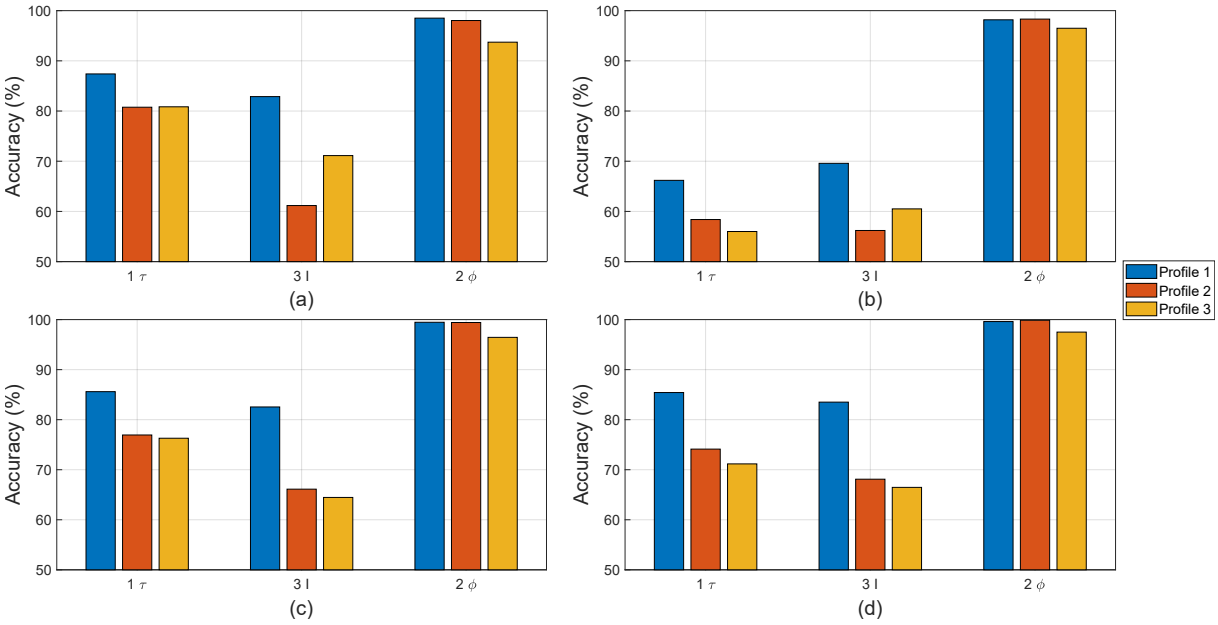

Figure E.13: Detection accuracy with demagnetisation alone obtained by (**a**) EDT, (**b**) KNN, (**c**) SVM, and (**d**) FNN

For the single fault of local demagnetisation, all four classifiers can reach an accuracy larger than 90% with features computed from stray fluxes, as shown Figure E.13. It is noted that the data from stray flux sensors allows all four classifiers to detect the local demagnetisation with an accuracy of above 90%. The accuracy does not drop significantly when being tested on the unseen operation profiles (Profile 2 and Profile 3). This indicates that the asymmetry caused by local demagnetisation is detectable, and the classifiers become robust to unseen load and speed changes for identifying these signatures. The

performance of the machine learners drops significantly if the current or torque data are used instead of computing the input features. The KNN-based classifiers have overall the worst accuracy among the tested algorithms. However, the accuracy achieved with features computed from stray flux is on par with the rest.

For the mixed fault, the machine learning algorithms are not only trained for fault detection but also for discrimination between local demagnetisation and ITSC. In this study, there are four classes: no-fault, only local demagnetisation fault, only ITSC fault, or mixed fault. There is an equal number of observations in each fault case; thus, the y-axes in all of the bar plots in Figure E.14 are limited to above 25%. The EDT, SVM, and FNN-based classifier have the highest accuracy among the studied algorithms. The accuracy of all the classifiers can be increased by using more data for training, e.g., if all four hall sensors are included. The KNN -based classifier has an accuracy of just above 25% when being trained and tested using current or torque data on Profile 2 and Profile 3. In addition, the mixed fault does deteriorate the performance of the tested algorithms if they were trained on separate faults. This indicated that the fault signatures of local demagnetisation and ITSC in their incipient state are difficult to separate. However, the tested algorithms using stay flux signals can improve the performance in detecting these magnetic asymmetry.

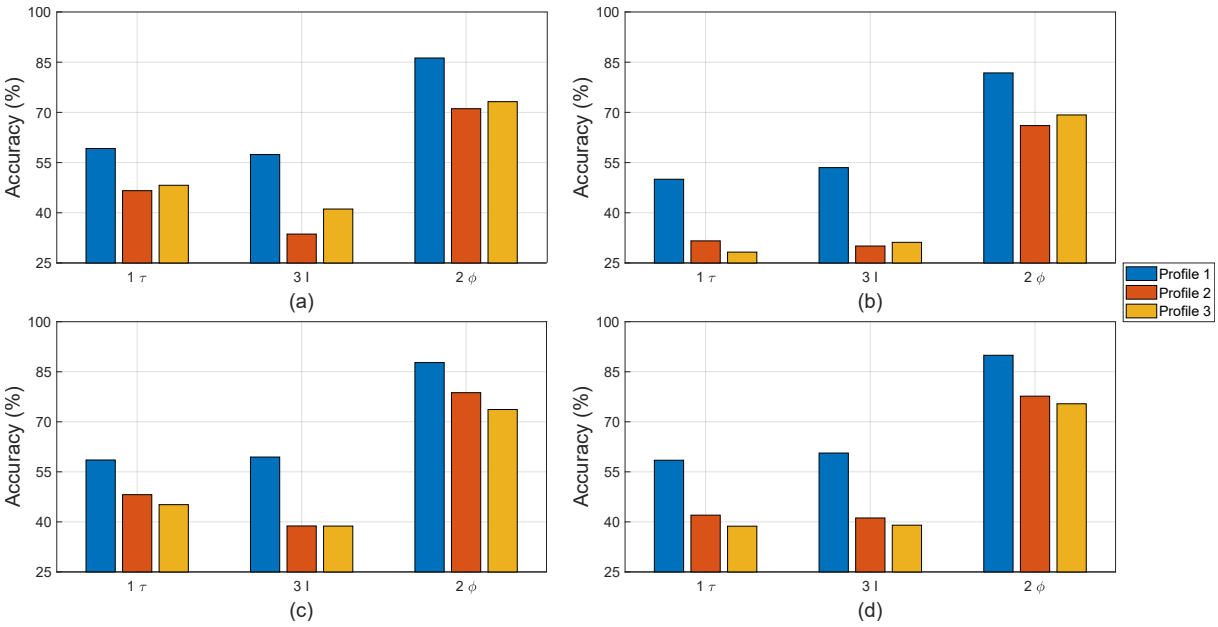

Figure E.14: Classification accuracy with mixed fault obtained by (**a**) EDT, (**b**) KNN, (**c**) SVM, and (**d**) FNN.

All the average accuracies are plotted in Figure E.12 to Figure E.14 and reported in Table E.3. The columns blow "Demagnetisation" and "ITSC" are in case of single fault. In case of demagnetisation, all algorithms achieve an accuracy of above 90% , which is highlighted in bold. The last three columns under the label "Mixed" refer to the mixed fault of demagnetisation and ITSC.

Table E.3: Average classification accuracy (%) for detecting demagnetisation, ITSC, and mixed fault case.

Machine	Operation	Demagnetisation			ITSC			Mixed		
Learner	Profile	1 τ	3 I	2 ϕ	1 τ	3 I	2 ϕ	1 τ	3 I	2 ϕ
SVM	1	85.6	82.5	**99.5**	69.6	72.6	**93.9**	58.5	59.4	87.8
	2	76.9	66.1	**99.4**	65.9	53.7	84.7	48.2	38.8	78.7
	3	76.3	64.5	**96.4**	60.6	55.8	81.1	45.2	38.7	73.7
KNN	1	66.2	69.6	**98.2**	63.9	69.7	88.5	50.0	53.5	81.8
	2	58.4	56.2	**98.3**	54.3	50.6	75.2	31.6	30.1	66.1
	3	56.0	60.5	**96.5**	50.7	53.5	80.0	28.2	31.2	69.2
EDT	1	87.4	82.9	**98.5**	70.9	68.2	**91.6**	59.2	57.4	86.3
	2	80.8	61.2	**98.0**	62.3	57.3	78.5	46.6	33.6	71.1
	3	80.8	71.1	**93.7**	64.7	54.4	84.0	48.2	41.1	73.2
FNN	1	85.4	83.5	**99.6**	72.7	75.1	**96.6**	58.5	60.6	89.9
	2	74.1	68.1	**99.9**	58.8	56.0	85.0	42.0	41.2	77.7
	3	71.2	66.5	**97.5**	55.9	56.0	86.3	38.7	39.0	75.4

E.6.3 Required Samples for Fault Classification

Normally, the length of samples used as input for FFTs is measured in time. Since the time-series data have been resampled due to the transient operation condition, the length of each sample is defined by the number of cycles. Stray flux and current signals measured from a PMSM are cyclical due to their sinusoidal nature. One cycle is defined as one period of the fundamental frequency in the measurement. It is equal to double the number of rotor revolutions in the case of four-pole motors. The frequency or order resolution of the spectrogram computed by FFT depends on the length of the sample; thus, a longer sample would give more confidence in the presence of peaks. A longer sample will also equate to a longer measuring period, which depends on the motor speed. For example, 30 revolutions (60 cycles) of a four-pole PMSM running at 3000 rpm are equal to a measurement period of 0.6 s, but this will increase to 2.4 s when the motor is running at 750 rpm. Therefore, it is of interest to find the minimum number of cycles required for accurate fault detection.

Figure E.15 shows line plots of the detection accuracy of local demagnetisation achieved by the FNN classifier, which has the highest accuracy at different numbers of cycles used to compute the spectrogram. The achieved accuracies were invested in cases when the features were being computed using data from one torque sensor (1 τ), three current sensors (3 I), two hall sensors (2 ϕ), and four hall sensors (4 ϕ). Combination of the three different physical parameters was also tested, but none of them gave a significant improvement as compared to the case of using four flux sensors. The accuracy in all four cases showcased in Figure E.15 is increased if using data from more cycles. However, only the two cases using stray flux data do converge. The accuracy converge if using four-flux sensors data of 20 cycles and two hall sensors data of between 30 and 40 cycles. The FNN-based classifier takes longer to converge, implying that unseen speed changes may

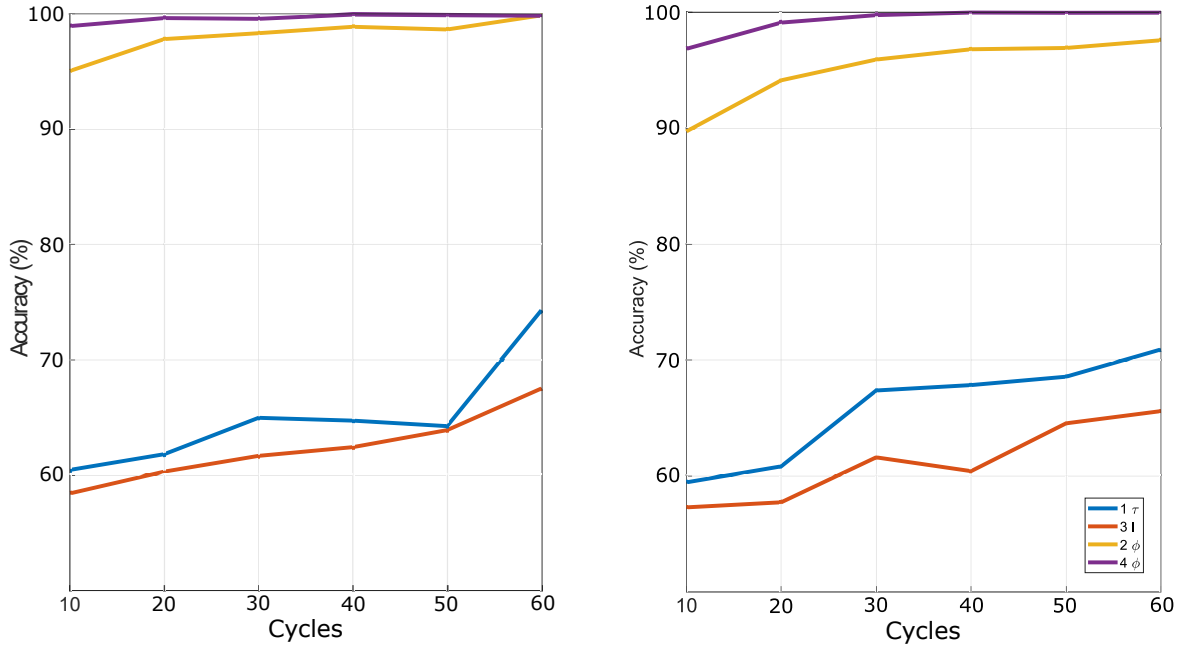

(a) (b)

Figure E.15: Performance of FNN-classifier for detecting local demagnetisation alone with spectrograms computed from different numbers of cycles in operations of (**a**) Profile 2 and (**b**) Profile 3.

still offer a challenge in training machine learning classifier. It is recommended that one pair of flux sensors of at least 20 cycles, measuring tangential and radial components, should be used for a reliable identification of magnet defects. If the data have a length of 20 cycles, i.e., 10 rotor revolutions of the rotor, then the required measurement time for computing one set of features is 0.8 s when the motor operates at 750 rpm or 0.2 s when it works at 3000 rpm. The fault classifiers will perform better if being trained on features computed from longer datasets, but they will take longer to acquire the first sample. The required computing time of the next dataset of features can be significantly reduced if the dataset for the next set of features is overlapped with the previous one.

E.7 Conclusion

This paper presents a scheme of fault classification for single and mixed faults of a sensorless PMSM drive in dynamic operations using two external stray flux sensors alone. An order tracking method based on position estimation is proposed for resampling the measurement before generating features for machine learning algorithms. This eliminates the need for position sensors and makes the learning classifiers more robust to speed changes. The fault classifiers are trained using data from Profile 1, but they achieve high accuracy for detecting magnet defect or ITSC faults when tested on the datasets in Profiles 2 and Profile 3. This work also introduces a method of inducing local demagnetisation through heat treatments.

The comparative study shows that current and torque signals are not sensitive enough to detect the faults in the studied PMSM. However, data from two external stray flux sensors allow the classifiers to detect faults significantly better, although all learning classifiers are less robust to new speed profiles when trained for ITSC faults. FNN achieved the highest accuracy of the learning classifiers test in this study. It is recommended that the measurement period is set to a minimum of 10 rotor revolutions for computing one set of features without a significant loss of accuracy.

References

[1] J. Lee, S. Moon, H. Jeong, and S. W. Kim, "Robust Diagnosis Method Based on Parameter Estimation for an Interturn Short-Circuit Fault in Multipole PMSM under High-Speed Operation," *Sensors*, vol. 15, no. 11, pp. 29 452–29 466, 2015. DOI: 10.3390/s151129452.

[2] E. A. Bhuiyan, M. M. A. Akhand, S. K. Das, *et al.*, "A survey on fault diagnosis and fault tolerant methodologies for permanent magnet synchronous machines," eng, *International journal of automation and computing*, vol. 17, no. 6, pp. 763–787, 2020.

[3] M. Van Der Geest, H. Polinder, J. A. Ferreira, A. Veltman, J. J. Wolmarans, and N. Tsiara, "Analysis and neutral voltage-based detection of interturn faults in high-speed permanent-magnet machines with parallel strands," *IEEE Transactions on Industrial Electronics*, vol. 62, no. 6, pp. 3862–3873, 2015. DOI: 10.1109/TIE.2015.2402641.

[4] M. Zhu, B. Yang, W. Hu, G. Feng, and N. C. Kar, "Vold-Kalman Filtering Order Tracking Based Rotor Demagnetization Detection in PMSM," *IEEE Transactions on Industry Applications*, vol. 55, no. 6, pp. 5768–5778, 2019. DOI: 10.1109/TIA.2019.2932692.

[5] I. H. Kao, W. J. Wang, Y. H. Lai, and J. W. Perng, "Analysis of Permanent Magnet Synchronous Motor Fault Diagnosis Based on Learning," *IEEE Transactions on Instrumentation and Measurement*, vol. 68, no. 2, pp. 310–324, 2019. DOI: 10.1109/TIM.2018.2847800.

[6] M. E. Iglesias-Martinez, J. Antonino-Daviu, P. Fernandez de Cordoba, J. A. Conejero, and L. Dunai, "Automatic Classification of Winding Asymmetries in Wound Rotor Induction Motors based on Bicoherence and Fuzzy C-Means Algorithms of Stray Flux Signals," *IEEE Transactions on Industry Applications*, vol. 9994, no. c, pp. 1–11, 2021. DOI: 10.1109/TIA.2021.3108413.

[7] I. Zamudio-Ramirez, J. A. Ramirez-Nunez, J. Antonino-Daviu, *et al.*, "Automatic Diagnosis of Electromechanical Faults in Induction Motors Based on the Transient Analysis of the Stray Flux via MUSIC Methods," *IEEE Transactions on Industry Applications*, vol. 56, no. 4, pp. 3604–3613, 2020. DOI: 10.1109/TIA.2020.2988002.

[8] V. Gurusamy, E. Bostanci, C. Li, Y. Qi, and B. Akin, "A Stray Magnetic Flux-Based Robust Diagnosis Method for Detection and Location of Interturn Short Circuit Fault in PMSM," *IEEE Transactions on Instrumentation and Measurement*, vol. 70, 2021. DOI: 10.1109/TIM.2020.3013128.

[9] J. S. L. Senanayaka, H. V. Khang, and K. G. Robbersmyr, "Fault detection and classification of permanent magnet synchronous motor in variable load and speed conditions using order tracking and machine learning," *Journal of Physics: Conference Series*, vol. 1037, no. 3, 2018. DOI: 10.1088/1742-6596/1037/3/032028.

[10] ——, "Multiple classifiers and data fusion for robust diagnosis of gearbox mixed faults," *IEEE Transactions on Industrial Informatics*, vol. 15, no. 8, pp. 4569–4579, 2019. DOI: 10.1109/TII.2018.2883357.

[11] E. Etien, A. Allouche, L. Rambault, T. Doget, S. Cauet, and A. Sakout, "A tacholess order analysis method for pmsg mechanical fault detection with varying speeds," *Electronics*, vol. 10, no. 4, 2021. [Online]. Available: https://www.mdpi.com/2079-9292/10/4/418.

[12] S. Lu, Q. He, and J. Zhao, "Bearing fault diagnosis of a permanent magnet synchronous motor via a fast and online order analysis method in an embedded system," *Mechanical Systems and Signal Processing*, vol. 113, pp. 36–49, 2018, SI: IMETI-MechElectro. DOI: https://doi.org/10.1016/j.ymssp.2017.02.046.

[13] B. Hou, Y. Wang, B. Tang, Y. Qin, Y. Chen, and Y. Chen, "A tacholess order tracking method for wind turbine planetary gearbox fault detection," *Measurement*, vol. 138, pp. 266–277, 2019. DOI: https://doi.org/10.1016/j.measurement.2019.02.010.

[14] J. C. Lagarias, J. A. Reeds, M. H. Wright, and P. E. Wright, "Convergence properties of the nelder–mead simplex method in low dimensions," *SIAM Journal on Optimization*, vol. 9, no. 1, pp. 112–147, 1998. DOI: 10.1137/S1052623496303470. eprint: https://doi.org/10.1137/S1052623496303470.

[15] J. C. Quiroz, N. Mariun, M. R. Mehrjou, M. Izadi, N. Misron, and M. A. Mohd Radzi, "Fault detection of broken rotor bar in ls-pmsm using random forests," *Measurement*, vol. 116, pp. 273–280, Feb. 2018. DOI: https://doi.org/10.1016/j.measurement.2017.11.004.

[16] P. Pietrzak and M. Wolkiewicz, "On-line detection and classification of PMSM stator winding faults based on stator current symmetrical components analysis and the KNN algorithm," *Electronics*, vol. 10, no. 15, 2021. DOI: 10.3390/electronics10151786. [Online]. Available: https://www.mdpi.com/2079-9292/10/15/1786.

[17] J. S. L. Senanayaka, H. V. Khang, and K. G. Robbersmyr, "Toward self-supervised feature learning for online diagnosis of multiple faults in electric powertrains," *IEEE Transactions on Industrial Informatics*, vol. 17, no. 6, pp. 3772–3781, 2021. DOI: 10.1109/TII.2020.3014422.

[18] Z. Li, Y. Xu, and X. Jiang, "Pattern recognition of dc partial discharge on xlpe cable based on adam-dbn," *Energies*, vol. 13, no. 17, 2020. DOI: 10.3390/en13174566. [Online]. Available: https://www.mdpi.com/1996-1073/13/17/4566.

[19] Y. Park, D. Fernandez, S. B. Lee, *et al.*, "Online Detection of Rotor Eccentricity and Demagnetization Faults in PMSMs Based on Hall-Effect Field Sensor Measurements," *IEEE Transactions on Industry Applications*, vol. 55, no. 3, pp. 2499–2509, Dec. 2019. DOI: 10.1109/TIA.2018.2886772.

[20] S. Moon, J. Lee, H. Jeong, and S. W. Kim, "Demagnetization Fault Diagnosis of a PMSM Based on Structure Analysis of Motor Inductance," *IEEE Transactions on Industrial Electronics*, vol. 63, no. 6, pp. 3795–3803, Feb. 2016. DOI: 10.1109/TIE.2016.2530046.

[21] J. R. Riba Ruiz, J. A. Rosero, A. Garcia Espinosa, and L. Romeral, "Detection of demagnetization faults in permanent-Magnet synchronous motors under nonstationary conditions," *IEEE Transactions on Magnetics*, vol. 45, no. 7, pp. 2961–2969, 2009. DOI: 10.1109/TMAG.2009.2015942.

[22] D. Fernandez, D. Reigosa, T. Tanimoto, T. Kato, and F. Briz, "Wireless permanent magnet temperature & field distribution measurement system for IPMSMs," *2015 IEEE Energy Conversion Congress and Exposition, ECCE 2015*, pp. 3996–4003, Sep. 2015. DOI: 10.1109/ECCE.2015.7310224.

[23] D. D. Reigosa, D. Fernandez, T. Tanimoto, T. Kato, and F. Briz, "Permanent-Magnet Temperature Distribution Estimation in Permanent-Magnet Synchronous Machines Using Back Electromotive Force Harmonics," *IEEE Transactions on Industry Applications*, vol. 52, no. 4, pp. 3093–3103, Mar. 2016. DOI: 10.1109/TIA.2016.2536579.

Paper F

Robust Active Learning Multiple Fault Diagnosis of Sensorless PMSM Drives in Dynamic Operations Under Imbalanced Datasets

Sveinung Attestog, Jagath Sri Lal Senanayaka, Huynh Van Khang, Kjell G. Robbersmyr

This paper has been published as:

S. Attestog, J. S. L. Senanayaka, H. Van Khang, and K. G. Robbersmyr, "Robust Active Learning Multiple Fault Diagnosis of Sensorless PMSM Drives in Dynamic Operations Under Imbalanced Datasets", IEEE Transactions on Industrial Informatics (under revision).

F.1 Abstract

This paper proposes an active learning scheme to detect multiple faults in permanent magnet synchronous motors in dynamic operations without using historical labelled faulty training data. The proposed method combines the self-supervised anomaly detector based on local outlier factor (LOF) and a deep Q-network (DQN) supervised reinforcement learner to classify inter-turn short-circuit, local demagnetisation and mixed faults. The first fault, which is detected by LOF and verified by an expert during maintenance, is used as training data for the DQN classifier. From that point onward, LOF anomaly detector and DQN fault classifiers are working in tandem in identification of new faults, which require an expert intervention when either of them identifies a fault. The robustness of the scheme against dynamic operations, mixed fault and imbalanced training datasets is validated via a comparative study using stray flux data from an in-house test setup.

F.2 Introduction

Permanent magnet synchronous motors (PMSM) in off-shore wind turbines and electric vehicles are intensively exposed to mechanical and thermal stresses in dynamic operations with thermal cycling. These result in inter-turn short-circuit (ITSC), and local demagnetisation fault (DF) [1]. A local demagnetisation only affects a small region of rotor magnets in early states, and induces a magnetic asymmetry in contrast to uniform DF, which downgrade all magnets equally. Detecting and identifying these faults in incipient stages allow for life prolonging operation or planned maintenance, reducing costs and production down-times [2]–[4].

Fault detection and identification (FDI) methods for electrical machines have been extensively developed and categorised as: model-, signal- and machine learning (ML) based methods [5]. The model-based methods aim to identify fault signatures by estimating hard-to-measure parameters and computing a residual between a suggested model and measurements. This approach relies on the accurate information of physical parameters in the model or detailed dimensions of machines, which are difficult to acquire in reality [6]. Signal processing methods detect a fault based on fault-related characteristic frequencies. These methods are simple but are only applicable to single fault diagnosis. Further, missing a fault characteristic frequency does not guarantee that a machine is completely healthy. ML based methods have recently gained popularity since they are less demanding on prior knowledge of a machine [7].

To address the lack of labelled faulty data issues, anomaly detection has been used in various studies [8], [9]. These anomaly detectors and one-class classifiers (OCCs) train on the observation from the healthy cases. A trained OCC can quantify the deviation of a new data sample from the healthy samples. A large deviation from a healthy sample is considered as a faulty case. Krawczyk et. al. [10] separate the OCCs into four categories namely; (1) Density-based methods e.g. local outlier factor (LOF) [11], (2) Reconstruction-based methods such as auto-encoder [12] and contrastive learning [13], (3) Boundary-based methods e.g., one-class SVM [8], (4) Ensemble-based methods which combine OCCs to form a more flexible data description model [10]. It is important to

use a proper comparative study to find the best OCC type for a given anomaly detection application. However,to the authors' knowledge, finding the best OCC method for detecting anomaly in PMSMs has not been studied in the literature.

Another method to tackle the lack of labelled faulty data is using active learning (AL). It is a set of semi-supervised learners [14], [15], which are used to accelerate the labelling process of partially labelled dataset. They are trained on the labelled samples and tests on the unlabelled samples. The prediction with the lowest confidence is passed to an expert, who "actively" labels the dataset for the ML-based detection. An AL is often called a cooperative learner when it significantly alleviates the labelling task for the expert. Alternatively, a self-supervised anomaly detector can be implemented in an AL scheme. Senananyaka et. al. [8] proposed a FDI development scheme without using historical data from operating faulty motors. Within the study, a self-supervised one-class SVM is first used to detect the anomaly. However, this OCC defines healthy domain based on its kernel function and may include regions of low competence. It will have a high rate of false negatives (FN) if the healthy and faulty classes overlap. The second part of the presented FDI scheme is a convolutional neural network (CNN) classifier, which is trained by samples identified by the one-class SVM and validated by an expert. Further development of such a FDI will create a more competent CNN with knowledge of faults, that have occurred. The authors in [8] trained and tested the FDI scheme on a balanced dataset alone. However, obtaining a balanced dataset for ML-based fault diagnosis methods is not feasible from PMSMs in offshore wind turbines. Developing a novel fault diagnosis must take the imbalance in datasets into consideration.

Imbalance in a dataset is often measured by the ratio (λ) between negative (healthy) and positive (faulty) samples. The problem of imbalance data set is amplified due to noise, overlap between classes, and if one class is represented by multiple clusters [16]. A common method for "rebalancing" the imbalanced data set is to oversample the minority class and undersample the majority class. Both of these processes can be executed by random sampling. However, the minority class also has an option for generating new synthetic samples with different variations of synthetic minority oversampling technique (SMOTE) or extraction maximisation imputation-based class imbalanced learning [17]. Zhang et. al. [12] proposed a self-supervised feature learning scheme for bearing fault in steady state with less than 50 labelled training samples per class. A CNN is trained with augmented data to match the computed pseudo labels, which consist of statistical features and features extracted from an auto-encoder. This allows for rich feature mining from a small number of positive samples. However, the existing studies could deal with imbalanced datasets for detecting single faults alone in steady states while using a lot of historical data at faulty conditions.

This study aims to develop a novel scheme of mixed fault diagnosis in sensorless PMSM drives under dynamic operations while addressing the problems of imbalanced datasets using limited samples from faulty conditions. Within the framework, an anomaly detector is developed based on a LOF to define more complex domains in healthy cases to tackle overlapping classes. The proposed scheme is proven to be robust against dynamic operations at different operation profiles by resampling at a fixed angular increment without using any position sensor. This suggested scheme, using external flux sensors alone, allows

for developing a plug-and-play automatic fault detection without modifying the existing drive systems in critical or offshore applications, where sensorless controls are preferred due to reliability or reduced maintenance cost.

F.3 Proposed Fault Diagnosis Scheme

The proposed FDI scheme shown in Figure F.1 is developed based on an online fault diagnosis scheme in [8]. The pretreatment after data collections involves resampling of the original time-series data at a fixed angular increment. The rotor position is estimated from one stray flux measurement with an optimisation problem, being detailed in Section III. The resampled data is split into intervals of 30 revolutions, which are converted to the frequency domain by fast-Fourier transform (FFT). The spectrograms are normalised with respect to both amplitude and frequency of the fundamental component. Then, the spectrograms are enveloped by splitting the spectrogram into intervals with a length of 0.5 order centred around the half harmonics (0.5, 1, 1.5, ...) to find the maximum in each interval. This saves the storage space while maintaining the information on the half harmonics. The pretreatment makes the FDI scheme robust against transient operation condition and can be implemented in sensorless drives.

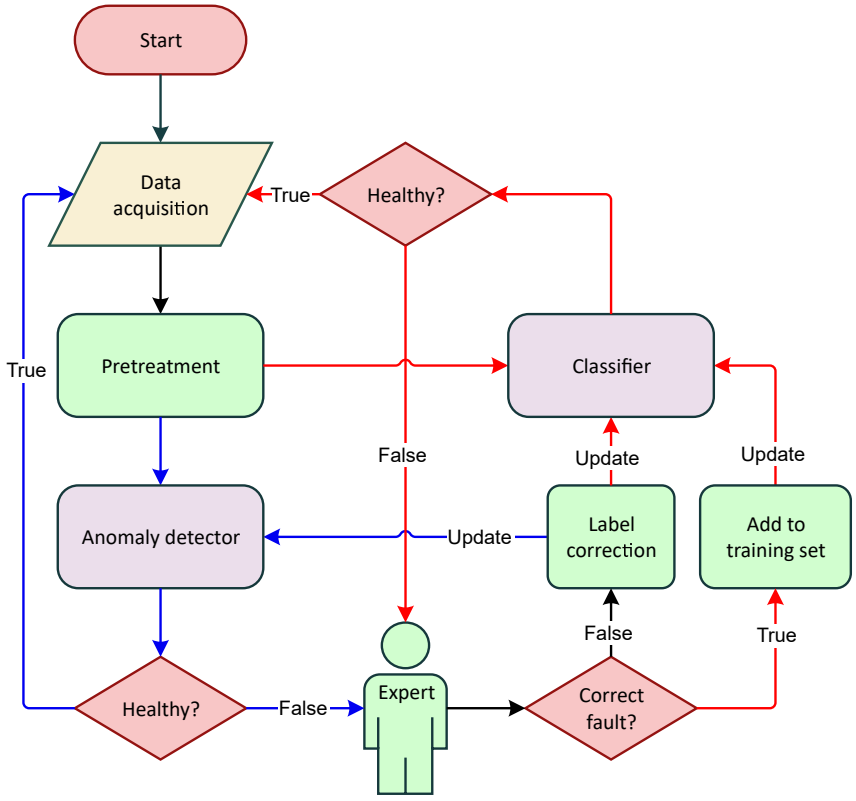

Figure F.1: Flowchart of the proposed FDI scheme. Note: Arrows coloured in red, blue and black represent information flow related to classifier, detector or both; Green objects represent processes/actions; purple boxes represent detector and classifier, red diamonds represent decisions

The FDI scheme starts with detecting anomaly using a self-supervised anomaly de-

tector, since historical data at faulty is not available. If the anomaly detector gives a false positive (FP), which is determined by an expert, it then needs to be updated with these FPs to learn the new region of healthy case. True positive samples marks the end of the first stage of the FDI scheme since the samples of faulty case are now available for training of the fault classifier. The second stage keeps the fault detector, but it works alongside with the fault classifier. An investigation by an expert is required when either the detector or classifier identifies a fault. If a fault is detected and classified as a previously discovered fault, the fault search can be narrowed down during maintenance. Note that in the first iteration of stage 2, the classifier only knows of one fault. However, more data during operations will result in a more knowledgeable and confident FDI, which can speed up the maintenance process, reducing unexpected downtime and cost. The detailed description of the FDI is given in Algorithm 1.

Algorithm 1 Detailed description of FDI scheme

```
Require: Healthy case data set, threshold, maintenance expert
  while No discovered faulty cases do
      Compute Anomaly score with OCC
      if Anomaly criterion = TRUE then:
          Expert investigation
          if Fault = TRUE then:
              Perform maintenance
              Label newly discovered fault and train classifier
          else if Fault = FALSE then
              Update OCC
          end if
      end if
  end while
  while At least one discovered fault class do
      Compute Anomaly score with OCC
      Predict fault class with classifier
      if A fault is detected by classifer or OCC then:
          Expert investigation
          if Fault = TRUE then:
              Perform maintenance
              if Fault = New then
                  Label new fault and update classifier
              else if Fault = Old then
                  Label new fault samples and update classifier
              end if
          else if Fault = FALSE then
              Updata OCC
          end if
      end if
  end while
```

F.3.1 Anomaly detection

The existing anomaly detectors using self-supervised learners need samples from healthy cases to identify any anomalies, which later can be labelled by an expert for initiating the training of a fault classifier in a later stage. The suggested one-class SVM in [8] is replicated, and 10 % of the training data is assumed to be outliers. The drawback with this OCC is its assumption of defining the region of healthy case with the kernal function. Regions of low competence may be included to increase the chance of FN. To address this demerit, a density based method LOF in [11] is used in this work to replace the one-class SVM. Like the k-nearest neighbours, the pair-wise distance between all the samples in the training dataset needs to be computed. This will make the LOF computationally heavy when the library of samples in the healthy case become too large. This problem can be solved by selective samplings [18].

The samples in datasets are grouped into clusters. An outlier can be isolated by a threshold value of the average distance to its nearest neighbours. However, the samples of the healthy dataset do not necessarily have a uniform density in its cluster in feature space. Thus anomalies can be closer to a cluster, depending on the region in the feature space [11]. LOF isolates outliers based on the sample density $\rho_{\mathbf{samp}}$ in feature space.

$$\rho_{\text{samp}}(P) = \left(\frac{1}{k} \sum_{n=1}^{k} d(P, o_n) \right)^{-1} \tag{F.1}$$

where k is an integer, $d(P, o_n)$ is the pair-wise Euclidean distance between point P and its nearest neighbours o_n. Then the sample density of each of the neighbour points o_n ($\rho_{\text{samp}}(o_n)$) needs to be computed. LOF is here defined as:

$$\text{LOF}(P) = \frac{1}{k} \sum_{n=1}^{k} \frac{\rho_{\text{samp}}(o_n)}{\rho_{\text{samp}}(P)} \tag{F.2}$$

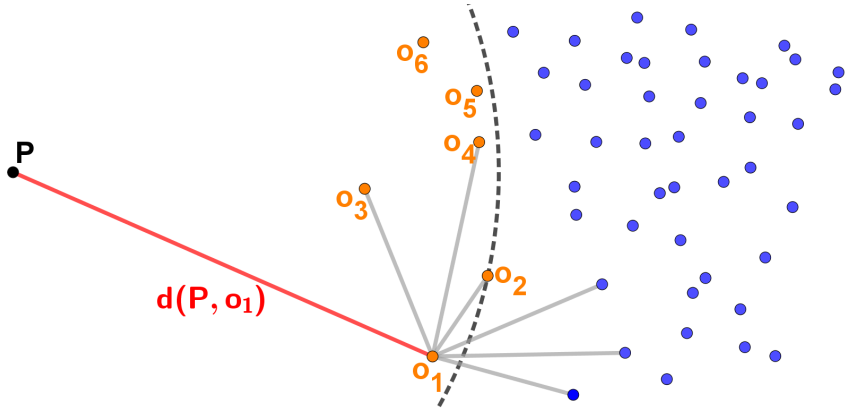

Figure F.2: Illustration of LOF in a 2D-feature space with P (black), o_n (orange), $d(P, o_1)$ (red), distance between o_1 to its nearest neighbours (gray), and rest of samples in the cluster (blue)

Figure F.2 illustrates the principle of LOF. The sixth nearest neighbours for point P are coloured in orange, while the rest of the dataset is coloured in blue. Point o_1 is

used as an example, where o_1 and its sixth nearest neighbours have grey connections. An anomaly is detected if LOF is greater than a set threshold. This implies that the new observation P is located in a region, which is a too "sparsely" populated region in feature space.

F.3.2 Fault identification

After the anomaly detection, the multiple fault identifications are implemented by a reinforcement learning (RL) based classifier in this study. RL has already proven its effectiveness in information theory, simulation-based optimisation, control theory and statistics [19], [20] and developed for bearing fault diagnosis alone [21] while the imbalance issues were not addressed. The proposed RL scheme based on a double deep Q-network (DQN) in [22] will be compared with the recently developed using a CNN architecture for fault identification in [8]. The problem with the existing CNN classifier is that it is not suited for imbalance datasets. The proposed DQN fault classifier can compensate the imbalance datasets without any oversampling. RL usually uses the analogy of teaching the agent to play a game. In the fault classification, the RL agent plays a "quiz game". It is formulated in form of 1D arrays as features, where the agent needs to give a response on classification. The Q-learning aims to set up a Q-table that contains the policy to maximise a reward depending on the input. In DQN, the Q-table is replaced with a neural network. Figure F.3 illustrates the interaction between the DQN agent and its environment. The illustration inside the DQN shows the layers of the critic network with four layer: Input layer (243 nodes), fully connected layer (100 nodes), ReLU activation function layer and the second fully-connected layer. The number of nodes in the final layers is equal to number classes in the training data.

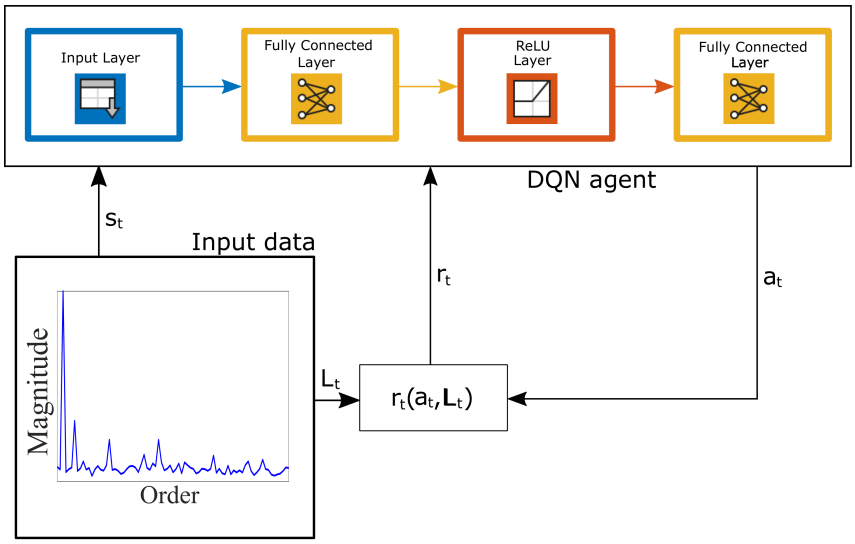

Figure F.3: Block diagram of DQN interacting with the environment

The action of the agent is associated with the label of the training dataset. If there is only two classes in the training set, it is sufficient to define the action space as $A = \{0, 1\}$. In this study, the action space is defined as $A = \{[0, 0], [0, 1], [1, 0], [1, 1]\}$. The entries in

A represent healthy or no fault (NF), DF, ITSC and mixed fault (MF), respectively. MF is the mix of DF and ITSC. The encoding of the labels is for the DQN only, which needs to be decoded after the prediction.

The reward function [22] is weighted based on the ratio between negative (healthy case) and positive (faulty case) samples.

$$r_t = \begin{cases} 1, & a_t = L_t = \text{Healthy} \\ -1, & a_t \neq L_t = \text{Healthy} \\ \lambda, & a_t = L_t = \text{Faulty} \\ -\lambda, & a_t \neq L_t = \text{Faulty} \end{cases} \tag{F.3}$$

The performance of a classifier to identify positive samples will decline when the imbalance ratio λ is increased. Eventually, the network will classify every sample as negative regardless of input. This phenomenon is called a collapse and is caused by the fact that the negative samples receive a greater sway in the training of the network since they are in majority. The role of r_t is to tackle the trend towards a collapse by balancing the weights of the negative and positive samples in the training process. The training process of the DQN is described in Algorithm 2 [23], where Θ is the parameter critic and τ is the smoothing factor for updating the target critic, which has the parameter Θ_t. There is no terminal state for S_{t+1}.

Algorithm 2 Training Algorithm for DQN

Require: Positive and negative samples
  for N_{epi} episode **do**
    Pick a random sample s_1 from the training set
    for N_{step}-1 steps **do**
      if Exploration **then**
        Pick a random action a_t from A
      else
        $a_t = \max_{a_t} = Q(s_t, a_t|\Theta)$
      end if
      Execute a_t and observe the reward r_t
      Randomly pick s_{t+1} from training set
      Store the experience (s_t, a_t, r_t, s_{t+1})
      Compute and store the value function:
      $y_t = r_t + \gamma \arg\max_{a_t} Q_t(s_{t+1}, a_{t+1}|\Theta_t)$.
      Compute the loss for a mini-batch with M samples:
      $L = \frac{1}{M}\sum_{t=1}^{M}\left(y_t - Q(s_t, a_t|\Theta)\right)^2$
      Update the critic by one-step minimisation
      Update the target critic parameters: $\Theta_t = \tau\Theta + (1-\tau)\Theta$
      Update the decaying probability for exploration
      Repeat
    end for
  end for

F.4 Experimental setup and data collection

F.4.1 In-house test bench

The studied four-pole, 2.2 kW PMSM is coupled to a generator with a torque transducer in between as shown in Figure F.4. The output of the generator is rectified by a three-phase full-bridge rectifier with a 500 μF capacitor bank, being connected across the output terminals, to remove the ripples of the DC output. The brake chopper is regulated by a PWM signal, which needs to be amplified by a factor of 4 due to the voltage amplitude insufficiency from the Microlabbox. The PWM signal is defined by the duty cycle, which is an ideal system that would be proportional to the reciprocal of the motor speed. However, due to losses and imperfections, a look-up table is generated for the duty cycle. It dictates the required duty cycle for achieving a requested load in the speed range between 1000 rpm and 2000 rpm.

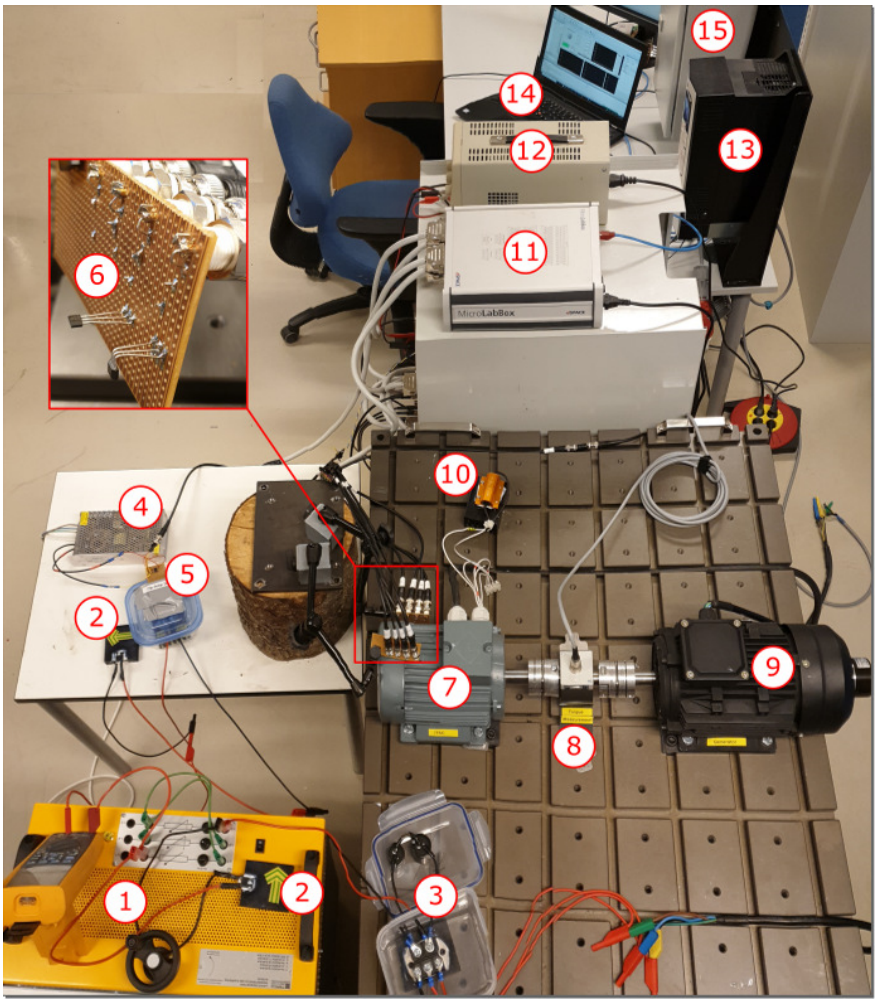

Figure F.4: Overview of the test bench with (1) resistor bank, (2) flyback diode, (3) three-phase rectifier with capacitor bank, (4) 12 V DC-supply, (5) IGBT brake chopper with OP-Amp, (6) hall sensors, (7) PMSM, (8) torque transducer, (9) generator, (10) short circuit resistor, (11) Microlabbox, (12) 24 V DC-supply, (13) ABB drive, (14) office laptop and (15) cabinet containing the current sensors

The solid state hall sensors, Type SS495A, measure the stray flux. The output of these sensors is linear and ratio-metric within the range [-67, 67] mT and has a sensitivity of 31.25 $\frac{mV}{mT}$. Two sensors were soldered to a Veroboard and wired to the Microlabbox, which delivers power to the sensors and records the measurement. The sensors could measure both tangential and radial components of the stray flux. Two sets of sensors were placed in proximity to the PMSM at the top and on the side.

F.4.2 Description of collected datasets

Stray fluxes are measured for three different non-stationary operating conditions with a sampling rate of 10 kHz. The time-series data is resampled with 400 samples per rotor revolution and split into samples with a length of 30 revolutions. Each sample is transformed into the frequency domain to produce the features for each observation used for training and testing of the proposed algorithm. The test setup is operated with the the three operation profiles shown in Figure F.5. Profile 1 consists a regular pattern, where the speed ramps up and down between 1000 rpm and 2000 rpm, and the load changes between 25 % and 75 % of the full load. Profile 2, which keeps the load constant at 60 % of the full load, while the speed changes with a randomly generated speed profile. Profile 3 keeps the speed constant at 1200 rpm, and then the load is randomly generated, where it repeats itself every 30 s. Stray flux measurement was collected from the PMSM operating in all mentioned profiles in the following fault condition: NF, ITSC with 5 % severity, local partial DF, and a MF case with both ITSC and DF. The DF is induced by one pole on a hot plate where two spots in the middle on one North pole have lost 30 % of original magnetic strength. The studied PMSM has 3 parallel strands, thus the severity is a estimated value of the shorted turns between the phase terminal on a single strand while the two other strands are unaffected. The ITSC is induced with a 1 Ω short circuit resistor, for mimicking the remaining insulation coating in the ITSC.

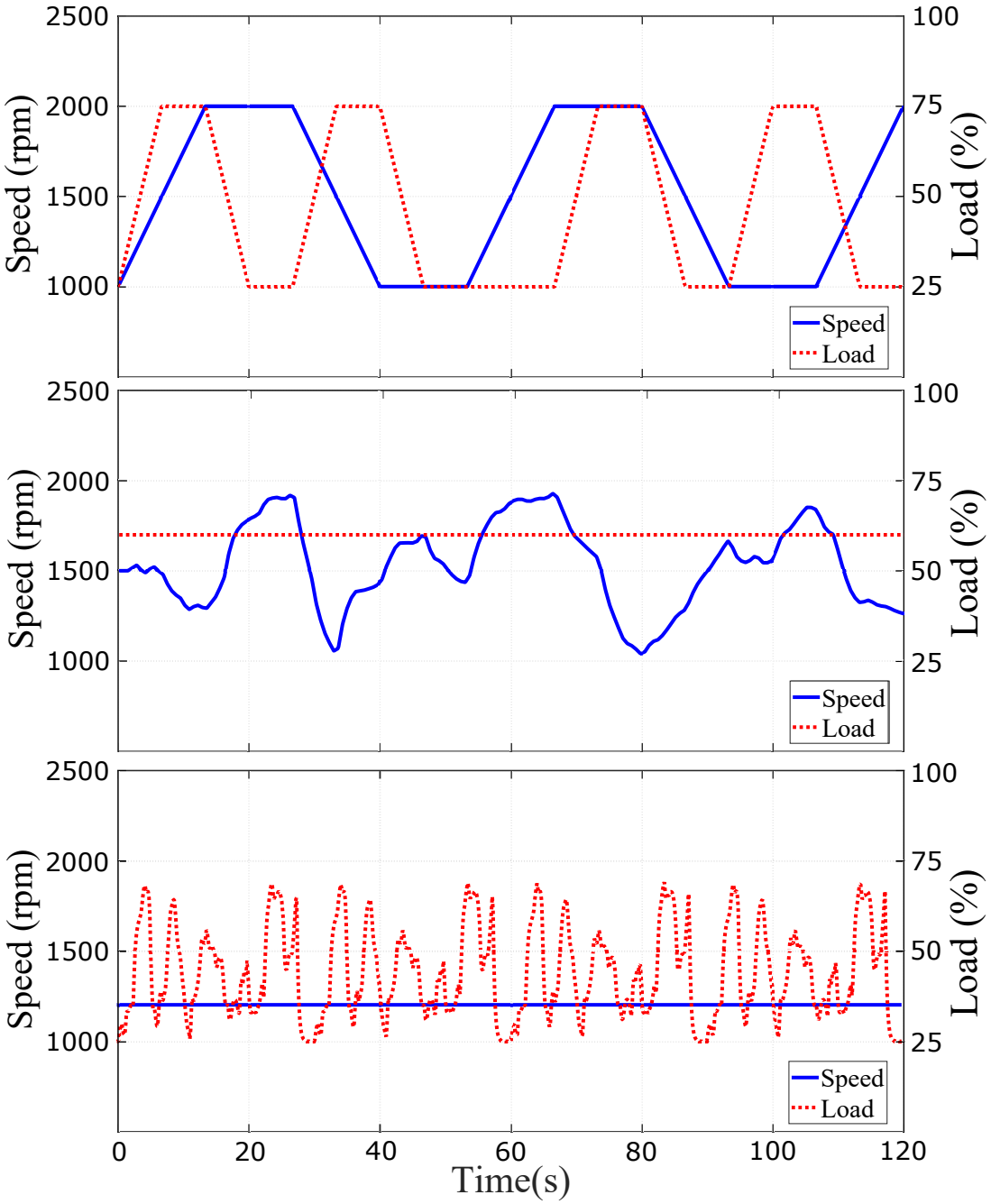

Figure F.5: The three studied operation profiles: (top) Profile 1 with variable load and variable speed, (middle) Profile 2 with constant load and variable speed, and (bottom) Profile 3 with variable load and constant speed

F.5 Results and Discussions

F.5.1 Performance of anomaly detection

The one-class SVM and LOF need to define their respected criterion for anomaly identification. The sensitivity of the one-class SVM is defined by the outlier fraction, where the portion of outliers in the training dataset is set to 10 %. The output of the trained one-class SVM under testing is a numeric score, which is less than 0 in case of an anomaly as suggested in [8]. The LOF does require trial and error to determine a suitable threshold. A value close to 1 will make the detector more sensitive but has the risk of increasing the FP rate. The threshold for LOF was set to 1.1, which means that a new point is classified as an anomaly/fault if the regions of its k^{th} nearest neighbours are on average of 10 % denser than the region of the new point. The parameter k is set to 5.

The one-class SVM and LOF classifiers are first trained on the healthy datasets from Profile 1 with the result shown in Tabel F.1 and Table F.2. The healthy dataset was split by 83.3 % (250 samples) for training and 16.7 % (50 samples) for testing. All the samples from each the faulty cases from any operation profile are used for testing (900 samples in total). Initially, the training set includes only samples from Profile 1. The performance of the one-class SVM has an accuracy of 84 % when tested on the same profile during training. The accuracy of the one-class SVM anomaly detector proposed in [8], when testing on each of the fault cases, varies between 57 % and 98.3 %. The proposed LOF algorithm, on the other hand, predicts all the fault cases as anomalies almost perfectly. However, the proposed LOF has a high FP rate. To address this issue, more samples in the healthy dataset from Profiles 2 (50 samples) and 3 (50 samples) are added to the training data to improve in the proposed FDI scheme with AL. As a result, the accuracy of the proposed LOF anomaly detector improves constantly when more samples are added. The compared one-class SVM detector suffers from the newly added data samples, where its accuracy in healthy cases improves, but FN rate increases. This proves that the proposed LOF anomaly detector could effectively identify anomalies better than the existing one when more knowledge of healthy cases is added during normal operations.

F.5.2 Training times of fault classifiers

To compare the computational effectiveness of the proposed DQN fault classifier and existing one, the average training times of DQN and the CNN benchmark are reported in Table F.3 while increasing the imbalance in datasets. The classifiers were trained with two classes (healthy and faulty), and with all four classes of healthy, DF, ITSC and MF. The training time for the DQN stays close to constant around two minutes while the training time of the CNN declines when increasing the imbalance as reported in Table F.3. The imbalance ratio λ is increased by removing samples in the faulty case. Number of steps in each of the episode in the DQN is set to 400, which would explain why the training time does not change. The CNN-based classifier on the other hand uses all available samples in each step in the training. It is noted that the imbalance of the training dataset in case of four-class is computed by the imbalance of each respected fault class. The ratio between healthy and each faulty case is considered as a more relevant metric in the compensation

Table F.1: Accuracy of one-class SVM outlier detector

Fault test case	Test	Extra samples from Profile 2 and 3					
(Criterion)	Pro.	0	50	100	150	200	250
Healthy	1	84.0	82.0	80.0	80.0	80.0	80.0
(Score $\geqslant 0$)	2	80.0	98.0	98.0	98.0	98.0	98.0
	3	46.0	70.0	80.0	80.0	84.0	90.0
DF	1	71.7	55.3	56.0	56.0	51.7	53.0
(Score < 0)	2	57.0	46.0	45.7	44.3	41.0	41.0
	3	84.0	58.3	54.7	51.0	44.7	44.3
ITSC	1	82.3	55.3	53.7	53.0	46.3	45.7
(Score < 0)	2	90.7	54.3	48.0	39.7	22.7	21.7
	3	98.3	77.0	74.7	67.0	59.0	57.0
MF	1	66.7	44.0	46.0	43.0	39.7	38.7
(Score < 0)	2	73.3	32.0	30.3	23.7	16.3	15.0
	3	93.0	62.3	58.7	51.7	42.7	37.0

Table F.2: Accuracy of LOF outlier detector

Fault test case	Test	Extra samples from Profile 2 and 3					
(Criterion)	Pro.	0	50	100	150	200	250
Healthy	1	86.0	86.0	88.0	88.0	80.0	98.0
(LOF $\leqslant 1.1$)	2	14.0	72.0	94.0	80.0	86.0	84.0
	3	8.0	52.0	88.0	80.0	82.0	90.0
DF	1	100	100	98.0	98.0	100	100
(LOF > 1.1)	2	100	98.0	100	100	100	100
	3	100	92.0	94.0	94.0	98.0	98.0
ITSC	1	100	100	100	100	100	100
(LOF > 1.1)	2	100	100	100	100	100	100
	3	100	100	100	94.0	100	100
MF	1	100	98.0	100	96.0	100	100
(LOF > 1.1)	2	100	94.0	96.0	100	100	98.0
	3	100	92.0	84.0	92.0	96.0	96.0

Table F.3: Recorded training time of DQN and CNN

Imb.	DQN		CNN	
ratio	2 classes	4 classes	2 classes	4 classes
1	133.5	125.0	279.1	525.7
1.25	131.9	123.0	233.6	437.9
1.67	132.1	120.5	209.6	348.7
2.5	131.1	122.2	187.2	284.8
5	129.4	122.0	163.2	196.4
10	129.6	124.0	140.7	155.3
15	126.5	118.4	141.1	154.9
30	127.1	119.7	142.9	139.3

described in the reward function. This study, equal imbalance (Imb.) ratios λ are applied for each fault case.

F.5.3 Performance of two-class classifiers

The proposed DQN and existing CNN fault classifiers are trained to identify a specific single fault, namely DF or ITSC. Table F.4 list the results when the DQN and the CNN classifiers are trained to identify these faults. Note, the accuracy results of the fault classifiers are listed in Table F.4, in which green-coloured numbers show the high accuracy results of over 98 % and red-coloured numbers indicate low accuracy results of less than 50 %. This is to highlight the main trends of the results. The terms of positive and negative samples will hereafter be interchangeably used with faulty and healthy case, respectively. The imbalance is increased by reducing the number of positive samples in the training dataset. All negative samples from the PMSM operating with Profile 1 are used for training, but 50 of these samples are randomly picked for testing. 50 test samples are randomly sampled from each faulty case and are sampled from the samples that are not a part of the training dataset, when $\lambda > 1$. It is noted that this selection is only applied for the testing dataset from Profile 1. All samples from Profile 2 and Profile 3 are used for testing (300 samples per class per profile). The performance of the DQN and CNN classifiers are compared with the metrics, true positive rate (TPR) and true negative rate (TNR).

In the case of DF, only the samples of the motor with an induced local demagnetisation are used as the positive training samples. The proposed DQN and existing CNN classifiers are tested on all four-fault cases, namely DF, ITSC, MF and NF or healthy, to investigate what the two other faulty datasets (ITSC and MF) can be classified. The fault signatures of MF may share common characteristics with both of DF and ITSC. Therefore, it is possible for the MF samples to be classified as a fault by the classifier trained for detecting DF or ITSC, which is why Table F.4 reports TPR for MF. Ideally, ITSC fault will not be classified as a fault by the classifiers trained for DF and vice versa. This is why Table F.4 reports TNR for the fault classifier were not trained before being used in testing.

The proposed DQN classifier and CNN achieve a TPR higher than 90 % for the fault

Table F.4: Comparing TPR and TNR of DQN and CNN classifiers when trained for identifying either DF or ITSC

		Local Demagnetisation								Inter-turn short circuit							
		DQN				CNN				DQN				CNN			
Test Pro.	Imb. ratio	TPR DF	TNR NF	TPR MF	TNR ITSC	TPR DF	TNR NF	TPR MF	TNR ITSC	TPR ITSC	TNR NF	TPR MF	TNR DF	TPR ITSC	TNR NF	TPR MF	TNR DF
1	1	100	99.9	95.8	100	97.2	98.4	73.7	99.9	98.5	97.9	12.8	99.4	95.4	96.6	2.9	99.8
	1.25	100	99.9	97.6	99.8	96.3	98.1	71.2	99.9	95.7	97.2	9.4	99.6	93.2	93.6	6.7	98.6
	1.67	100	99.7	99.6	100	95.8	98.9	71.0	100	97.1	98.1	11.5	98.8	89.1	97.9	5.8	98.8
	2.5	100	99.9	99.5	98.8	95.5	99.3	69.8	99.9	98.2	96.5	14.9	98.4	81.6	97.9	1.6	99.9
	5	100	98.7	99.6	99.1	92.9	98.6	64.3	99.9	96.4	95.6	14.7	98.9	67.6	96.9	2.1	99.8
	10	100	96.1	99.9	97.9	82.1	99.8	49.8	100	96.2	92.8	19.0	97.7	55.4	96.7	3.0	99.7
	15	99.9	93.4	99.6	95.8	69.4	97.5	35.8	99.7	93.4	90.3	15.7	98.5	43.5	99.7	2.0	99.5
	30	100	88.6	100	93.1	46.9	99.8	23.9	99.9	90.1	84.7	27.2	95.5	23.6	99.7	0.2	100
2	1	99.4	100	95.8	99.9	92.3	93.4	74.3	99.4	91.4	85.1	28.9	95.4	80.0	94.0	3.0	99.9
	1.25	99.6	99.9	97.9	100	94.8	93.7	77.1	99.5	92.7	85.1	24.6	96.6	77.8	91.0	4.8	99.7
	1.67	99.9	99.6	98.8	100	95.3	93.2	75.8	99.4	90.0	85.7	24.9	96.2	72.8	95.1	4.4	99.6
	2.5	99.8	99.1	99.5	99.7	95.2	94.8	75.9	99.4	94.6	77.9	35.1	92.3	65.0	95.9	2.0	100
	5	99.9	97.9	99.6	99.3	91.3	95.0	65.8	99.5	94.4	72.5	35.7	91.2	47.4	96.4	1.7	99.9
	10	99.9	91.6	99.8	96.4	75.4	97.5	47.3	99.9	88.0	69.9	35.1	91.7	37.6	96.3	1.4	99.8
	15	100	85.0	99.9	93.8	66.7	93.2	37.6	98.6	84.6	68.8	30.7	91.2	23.4	99.4	0.6	99.8
	30	100	72.8	100	89.8	49.1	97.6	32.2	99.3	79.6	72.3	33.2	88.0	13.2	99.5	0.3	100
3	1	97.9	99.9	89.0	100	99.0	97.1	91.6	100	82.0	91.6	12.4	99.3	76.1	94.6	5.4	99.1
	1.25	97.8	99.9	90.9	100	98.5	95.4	90.8	99.7	83.2	90.2	10.1	99.3	81.0	87.9	11.8	96.9
	1.67	98.9	99.8	94.0	99.9	99.1	96.4	93.7	100	83.8	90.1	10.9	99.3	76.9	94.6	9.4	96.6
	2.5	99.5	98.2	96.5	99.5	98.3	98.0	88.1	99.8	85.9	87.7	11.4	99.0	64.4	97.1	2.0	99.9
	5	99.6	97.0	97.5	98.9	97.5	97.6	85.9	99.8	86.6	84.8	11.4	98.8	53.9	95.3	2.0	99.8
	10	99.8	93.1	98.4	97.8	88.4	99.6	71.0	100	86.9	80.2	14.1	98.8	39.1	95.9	1.9	99.1
	15	99.7	88.4	98.4	96.3	78.0	96.3	57.2	98.6	85.2	79.0	13.3	98.2	22.5	98.4	2.6	99.0
	30	99.8	82.2	99.1	95.1	46.8	99.6	30.8	100	83.9	73.2	20.5	95.0	18.2	99.3	0.4	100

cases they are trained before testing when $\lambda = 1$. The lowest TPRs for the proposed DQN and compared CNN classifier are 82.0 % and 76.1 %, respectively when they were trained for ITSC dataset and tested on profile 3 with a constant speed and variable loads. The DQN classifier maintains a TPR of above 97.8 % when trained and tested for DF. However, the TNR for the healthy case is dropping to 72.8 %. The CNN classifier improves its TNR for the healthy case when the increasing the imbalance of the datasets . Fewer FPs is normally a positive quality in a classifier, but TPR for the CNN drops to below 50 % when increasing the imbalance in a dataset. The accuracy trend for the CNN classifier is reduced significantly when all samples are classified as healthy cases. The proposed DQN clasifier, on the other hand, reduces the possibility of FN, but has overcompensated slightly and increased FPs. Neither FP nor FN is desirable in FDI. However, both FN and FP rates can be compensated in the proposed AL scheme by correcting relabel by an expert, and the proposed DQN fault classifier has a second option with the weighted reward function.

The MF case includes both DF and ITSC. Therefore, there is a possibility that this fault case can be classified as one of those faults. This is in the context of fault classifiers, that are trained for identifying the presence of a specific fault. The test result reveals that both DQN and CNN classifiers, which are trained for DF, and it identifies MF as a fault. The TPR reported under MF is lower as compared to the case, where the classifiers are trained and tested on the same fault case. The TPR for the CNN classifier is also reduced when increasing the imbalance in datasets. Neither DQN nor CNN classifier identifies MF

as a fault when they are trained to identify ITSC fault. This result indicates that there is a high possibility that DF and MF may share the same fault signatures. The fault classifier, being trained on all four-fault cases included in this study, may find it difficult to distinguish between DF and MF.

F.5.4 Performance of four-class classifier

The proposed DQN and CNN fault classifiers are further trained with all four fault classes: DF, ITSC, MF and NF. Figure F.6 shows the hit rates of the DQN and CNN fault classifiers using test dataset in Profile 3. This includes the TNR and TPR, which were discussed in Section IV.C. The overall accuracy is also added in Figure F.6. It equals the average of the four hit rates, since the test dataset is balanced between the four classes. The proposed DQN and CNN fault classifiers suffer from being trained for all four faults. They start with an overall accuracy of 75 %, then decrease with respect to the imbalance of the dataset. Note each fault class has equal λ, which is the imbalance ratio given on the axis. The performance of the CNN is worse than the DQN, since its accuracy declines at a larger rate with a trend towards a collapse. Its hit rate for healthy case, i.e. NF, is increased towards 100 % due to this trend.

Each fault class can be incorrectly classified into three classes. This in total gives 12 miss for a four-class classifier. Figure F.7 plots the miss rates for both DQN and CNN fault classifiers, which were not close to 0. The comparison still uses the test dataset from Profile 3. It is noting that the first and last letters in the labels denote the predicted and true classes, respectively. Figure F.7a reveals that the proposed DQN fault classifier is confused between DF and MF, which were predicted in the analysis of the two-class classifiers. The DQN classifier confuses ITSC with NF and MF, while NF is generally confused with all of the other health classes. This demonstrates that the reward function may have overcompensated and needs to be adjusted. A combine decision between fault classifier and anomaly detector may also reduce the rate of FPs since Table F.2 reports a high accuracy for LOF. The CNN fault classifier does not misclassify NF with any of the fault classes. The confusion between DF and MF do decrease when increasing the imbalance, but these fault classes starts to be predicted as NF instead. Almost all samples from fault case ITSC are misclassified as NF.

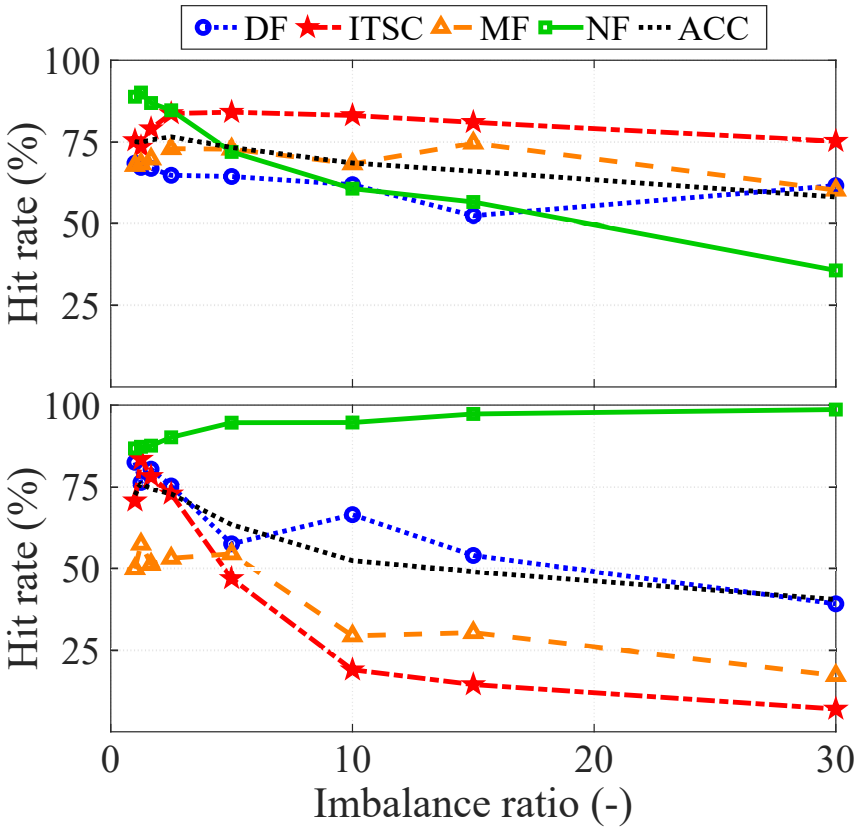

Figure F.6: Hit rates of DQN (top) and CNN (bottom) fault classifiers

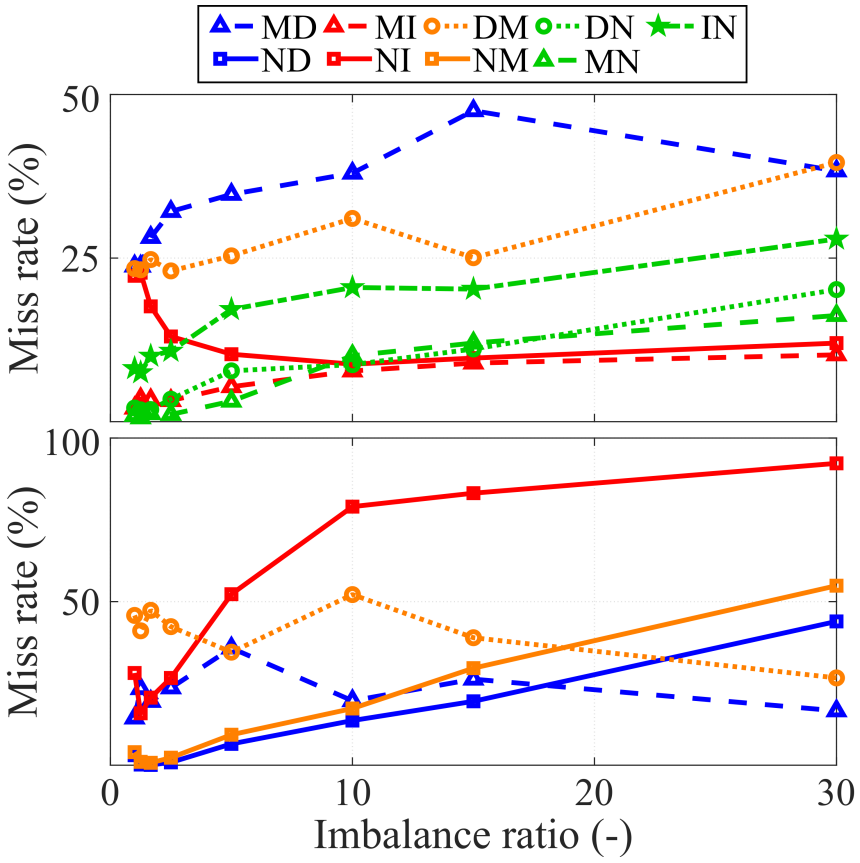

Figure F.7: Miss rates of DQN (top) and CNN (bottom) fault classifiers

F.6 Conclusion

This study proposed a fault diagnosis scheme trained and tested with both transient operating condition and mixed faults, where labelled training samples were initially unavailable. The training and testing dataset are collected by stray fluxes from the in-house test setup. The proposed method order-normalises the spectrogram by resampling the time-series data at a fixed angular increment to make it more robust against dynamic operations. The rotor position is estimated with a single external stray flux sensor, which allows for an automatic fault diagnosis of sensorless PMSM drivetrains without modifying the existing drives. The local outlier factor anomaly detector was only trained on samples from Profile 1, which gave a high false positive rate. Nevertheless, the proposed active learning framework allows for improving prediction accuracy when adding new healthy case samples. Newly discovered health classes are used to train the proposed DQN classifiers at different imbalance ratios. The comparative study shows that the DQN fault classifier is more robust than the existing CNN fault classifier, and can even have overcompensated the weight of the minority class.

References

[1] Y. Qi, E. Bostanci, V. Gurusamy, and B. Akin, "A Comprehensive Analysis of Short-Circuit Current Behavior in PMSM Interturn Short-Circuit Faults," *IEEE Transactions on Power Electronics*, vol. 33, no. 12, pp. 10 784–10 793, Dec. 2018. DOI: 10.1109/TPEL.2018.2809668.

[2] L. Wu, Y. Du, Z. Chen, Y. Guo, H. Wen, and Y. Fang, "Influence of Load Characteristics on Three-Phase Short Circuit and Demagnetization of Surface-Mounted PM Synchronous Motor," *IEEE Transactions on Industry Applications*, vol. 56, no. 3, pp. 2427–2440, Jan. 2020. DOI: 10.1109/TIA.2020.2968036.

[3] M. E. Iglesias Martínez, J. A. Antonino-Daviu, P. F. de Córdoba, J. A. Conejero, and L. Dunai, "Automatic Classification of Winding Asymmetries in Wound Rotor Induction Motors Based on Bicoherence and Fuzzy C-Means Algorithms of Stray Flux Signals," *IEEE Transactions on Industry Applications*, vol. 57, no. 6, pp. 5876–5886, Nov. 2021. DOI: 10.1109/TIA.2021.3108413.

[4] I. Zamudio-Ramirez, R. A. Osornio-Rios, J. A. Antonino-Daviu, H. Razik, and R. d. J. Romero-Troncoso, "Magnetic Flux Analysis for the Condition Monitoring of Electric Machines: A Review," *IEEE Transactions on Industrial Informatics*, vol. 18, no. 5, pp. 2895–2908, May 2022. DOI: 10.1109/TII.2021.3070581.

[5] E. A. Bhuiyan, M. M. A. Akhand, S. K. Das, and et. al., "A Survey on Fault Diagnosis and Fault Tolerant Methodologies for Permanent Magnet Synchronous Machines," *Int. J. Autom. Comput.*, vol. 17, no. 6, pp. 763–787, Nov. 2020. DOI: 10.1007/s11633-020-1250-3.

[6] Y. Qi, E. Bostanci, M. Zafarani, and B. Akin, "Severity Estimation of Interturn Short Circuit Fault for PMSM," *IEEE Transactions on Industrial Electronics*, vol. 66, no. 9, pp. 7260–7269, Sep. 2019. DOI: 10.1109/tie.2018.2879281.

[7] D. Neupane and J. Seok, "Bearing Fault Detection and Diagnosis Using Case Western Reserve University Dataset With Deep Learning Approaches: A Review," *IEEE Access*, vol. 8, pp. 93 155–93 178, Apr. 2020. DOI: 10.1109/ACCESS.2020.2990528.

[8] J. S. L. Senanayaka, H. V. Khang, and K. G. Robbersmyr, "Toward Self-Supervised Feature Learning for Online Diagnosis of Multiple Faults in Electric Powertrains," *IEEE Transactions on Industrial Informatics*, vol. 17, no. 6, pp. 3772–3781, Aug. 2021. DOI: 10.1109/TII.2020.3014422.

[9] C.-F. Tsai and W.-C. Lin, "Feature Selection and Ensemble Learning Techniques in One-Class Classifiers: An Empirical Study of Two-Class Imbalanced Datasets," *IEEE Access*, vol. 9, pp. 13 717–13 726, Jan. 2021. DOI: 10.1109/ACCESS.2021.3051969.

[10] B. Krawczyk, M. Galar, M. Woźniak, H. Bustince, and F. Herrera, "Dynamic Ensemble Selection for Multi-Class Classification with One-Class Classifiers," *Pattern Recognition*, vol. 83, pp. 34–51, Nov. 2018. DOI: 10.1016/j.patcog.2018.05.015.

[11] S. Liu, Y. Zhao, Z. Lin, *et al.*, "Data-Driven Event Detection of Power Systems Based on Unequal-Interval Reduction of PMU Data and Local Outlier Factor," *IEEE Transactions on Smart Grid*, vol. 11, no. 2, pp. 1630–1643, Mar. 2020. DOI: 10.1109/TSG.2019.2941565.

[12] T. Zhang, J. Chen, S. He, and Z. Zhou, "Prior Knowledge-Augmented Self-Supervised Feature Learning for Few-shot Intelligent Fault Diagnosis of Machines," *IEEE Transactions on Industrial Electronics*, pp. 10 573–10 584, Jan. 2022. DOI: 10.1109/TIE.2022.3140403.

[13] Y. Ding, J. Zhuang, P. Ding, and M. Jia, "Self-Supervised Pretraining via Contrast Learning for Intelligent Incipient Fault Detection of Bearings," *Reliability Engineering and System Safety*, vol. 218, p. 108 126, Feb. 2022. DOI: https://doi.org/10.1016/j.ress.2021.108126.

[14] C. Huang, "Featured Anomaly Detection Methods and Applications," Doctor of Philosophy in Computer Science, University of Exeter, 2018, pp. 115–124. [Online]. Available: https://ore.exeter.ac.uk/repository/%20bitstream/handle/10871/34351/HuangC.pdf?sequence=1.

[15] M. Chen, K. Zhu, R. Wang, and D. Niyato, "Active Learning-Based Fault Diagnosis in Self-Organizing Cellular Networks," *IEEE Communications Letters*, vol. 24, no. 8, pp. 1734–1737, Aug. 2020. DOI: 10.1109/LCOMM.2020.2991449.

[16] Y. Lu, Y.-M. Cheung, and Y. Y. Tang, "Bayes Imbalance Impact Index: A Measure of Class Imbalanced Data Set for Classification Problem," *IEEE Transactions on Neural Networks and Learning Systems*, vol. 31, no. 9, pp. 3525–3539, Nov. 2020. DOI: 10.1109/TNNLS.2019.2944962.

[17] R. Razavi-Far, M. Farajzadeh-Zanjani, and M. Saif, "An Integrated Class-Imbalanced Learning Scheme for Diagnosing Bearing Defects in Induction Motors," *IEEE Transactions on Industrial Informatics*, vol. 13, no. 6, pp. 2758–2769, Sep. 2017. DOI: 10.1109/TII.2017.2755064.

[18] M. E. Khoda, T. Imam, J. Kamruzzaman, I. Gondal, and A. Rahman, "Robust Malware Defense in Industrial IoT Applications Using Machine Learning with Selective Adversarial Samples," *IEEE Transactions on Industry Applications*, vol. 56, no. 4, pp. 4415–4424, Aug. 2020. DOI: 10.1109/TIA.2019.2958530.

[19] B. Jang, M. Kim, G. Harerimana, and J. W. Kim, "Q-Learning Algorithms: A Comprehensive Classification and Applications," *IEEE Access*, vol. 7, pp. 133 653–133 667, Sep. 2019. DOI: 10.1109/access.2019.2941229.

[20] Z. Song, J. Yang, X. Mei, T. Tao, and M. Xu, "Deep Reinforcement Learning for Permanent Magnet Synchronous Motor Speed Control Systems," *Neural Computing and Applications*, vol. 33, no. 10, pp. 5409–5418, May 2021. DOI: 10.1007/s00521-020-05352-1.

[21] L. Wen, X. Li, and L. Gao, "A New Reinforcement Learning Based Learning Rate Scheduler for Convolutional Neural Network in Fault Classification," *IEEE Transactions on Industrial Electronics*, vol. 68, no. 12, pp. 12 890–12 900, Dec. 2021. DOI: 10.1109/tie.2020.3044808.

[22] E. Lin, Q. Chen, and X. Qi, "Deep Reinforcement Learning for Imbalanced Classification," *Applied Intelligence*, vol. 50, no. 8, pp. 2488–2502, Mar. 2020. DOI: 10.1007/s10489-020-01637-z.

[23] Y. Zhang, Z. Zhang, Q. Yang, D. An, D. Li, and C. Li, "EV Charging Bidding by Multi-DQN Reinforcement Learning in Electricity Auction Market," *Neurocomputing*, vol. 397, pp. 404–414, Jul. 2020. DOI: https://doi.org/10.1016/j.neucom.2019.08.106.